Experimental Study of The Through-Thickness Strength of Laminated Composites

A thesis submitted to the Department of Engineering Science of the University of Oxford as partial fulfilment of the requirements for the degree of Doctor of Philosophy

By

Guiyong Cui

St Anne's College

Oxford

Michaelmas Term 1994

Abstract

Guiyong Cui D.Phil.

St Anne's College Michaelmas Term 1994

Experimental Study of The Through-Thickness Strength of Laminated Composites

Complicated structures made of fibre reinforced laminates will suffer the failure of delamination which is the main through-thickness failure mode and is usually caused by the combined through-thickness stress state. Three tests, namely the oblique test, the waisted C-specimen test and the notched beam test, have been developed to reveal the failure activities under the combined stress state of in-plane normal stress, through-thickness normal stress and interlaminar shear, and, as a part of the big project, to establish a 3-D failure map in the coordinates of the three stress components. All tests have been analyzed either numerically by FEM or experimentally by Moire interferometry technique.

The experimental results have shown that the failure behaviours of laminates are far more complicated than and very different from the traditional metallic materials which can usually be described by phenomenological failure criteria. The phenomenological criteria attempt has been tried and further confirmed that a full experimental understanding is the most important. Moreover, fractographic analysis by SEM has also been conducted to support the test results.

Finally the Weibull statistics method has been used to treat the stress gradient effect in the different test geometries while establishing the failure map. It has proved to be a very efficient instrument.

Preface

This thesis is an account of the work carried out by the author in the Department of Engineering Science of the University of Oxford under the supervision of Dr. Carlos Ruiz.

The research described here is original, although the work of others has been drawn upon freely, with due acknowledgement in the text. No part of this thesis has been submitted for a degree at any other university.

Acknowledgements

First and foremost, I would like to express my sincere thanks to Dr Carlos Ruiz for his help, guidance and consistent encouragement in the supervision of the project.

I am also indebted to Dr. Gunnar Hognestad, Dr Hongzhi Zhong for their friendly help in my experiment and calculation; to Dr. L. Boniface for her generous offer of the recipe for manufacturing G/epoxy panel.

Thanks are due to Messrs. Peter Hardy and Philip Webb for the assistance in the Laboratory.

My thanks also go to Rolls-Royce plc for the sponsorship of the research project.

I sincerely thank the Education Committee of P.R. China and the British Council who provide the financial support through the SBFSS award for me to study here.

Last but not least, I would express my thanks to my wife, Zhe Zhang, without her consistent love I would not have finished my degree.

To my parents and my wife

Contents

Chapter 1

INTRODUCTION

1.1 BACKGROUND

Laminated fibre reinforced polymer matrix composite (laminate) materials are amongst the most advanced materials to have undergone rapid development in the last decades. Their wide range of uses in various engineering disciplines, especially in the aircraft industry due to their high specific strength and high specific stiffness, have called for substantial fundamental and applied research.

As with classical monolithic materials, the failure and strength of laminate materials is always an interesting topic which has attracted considerable research in both the micro and the macroscopic aspects. Yet the heterogeneous and anisotropic features of laminate materials have brought much more complicated problems than metals and alloys. A lot of work has been done on the in-plane strength of the individual laminae of laminated structures based on the widely used Classical Lamination Theory (CLT), which assumes that there are no interlaminar stresses (Jones, 1975). The strength of a laminate is geometrically described by that of each lamina but this yields sufficiently accurate results only for thin composite plates (Noor, 1989).

Interlaminar stresses do, however, exist even if a laminate is only subjected to in-plane loading (Pipes,1971). It is believed that because the laminate has a weakness in the through-thickness direction, the out-of-plane or interlaminar stresses can result in the separation of two adjacent

plies. This failure mode, known as delamination, could reduce the failure strength and the stiffness of the laminate well below that predicted by in-plane failure criteria, and below that which can be achieved if only in-plane mechanisms are present.

With increasing use of thicker and more complicated geometries of laminated composite structures and components, a thorough understanding of the through-thickness strength is urgently needed in engineering design, coupled with a comprehensive database of mechanical properties. In surveying the research work done in this field until now, it is found that nearly all investigations are concerned with either theoretical and numerical modelling of interlaminar stresses (Noor, 1989; Whitcomb, 1983; Chang, 1989; Reddy, 1990; Lu, 1992) or simple interlaminar strength measurement (Ho, 1991; Hiel, 1991; Hognestad, 1993). The real nature of delamination, which is encountered often under a complicated combined stress state in engineering structures, has not yet been explored by any experiments.

This investigation focuses on the through-thickness strength of polymer laminates with woven reinforcement subjected to combined stresses, in order to explore the failure mechanisms and establish failure maps and practical design criteria.

1.2 DETERMINATION OF THROUGH-THICKNESS STRENGTH

The most commonly used form of polymer composite is a laminate consisting of two or more laminae reinforced with fibres in a single direction (UD) or with a woven material (FABRIC). The laminate is loaded mainly in the plane of the laminate and therefore the through-thickness stress is much lower than the in-plane stress components.

For each lamina, in the principal materials coordinate system (1, 2, 3) as shown in Fig. 1.1, the governing constitutive equations are,

$$\begin{pmatrix} \sigma_1 \\ \sigma_2 \\ \sigma_3 \\ \tau_{23} \\ \tau_{31} \\ \tau_{12} \end{pmatrix} = \begin{bmatrix} C_{11} C_{12} C_{13} C_{14} C_{15} C_{16} \\ C_{12} C_{22} C_{23} C_{24} C_{25} C_{26} \\ C_{13} C_{23} C_{33} C_{34} C_{35} C_{36} \\ C_{14} C_{24} C_{34} C_{44} C_{45} C_{46} \\ C_{15} C_{25} C_{35} C_{45} C_{55} C_{56} \\ C_{16} C_{26} C_{36} C_{46} C_{56} C_{66} \end{bmatrix} \begin{pmatrix} \epsilon_1 \\ \epsilon_2 \\ \epsilon_3 \\ \gamma_{23} \\ \gamma_{31} \\ \gamma_{12} \end{pmatrix}$$

where, C_{ij} is the stiffness matrix;

or simply by assuming a state of plane stress,

$$\begin{pmatrix} \sigma_1 \\ \sigma_2 \\ \tau_{12} \end{pmatrix} = \begin{bmatrix} Q_{11} & Q_{12} & 0 \\ Q_{12} & Q_{22} & 0 \\ 0 & 0 & Q_{66} \end{bmatrix} \begin{pmatrix} \epsilon_1 \\ \epsilon_2 \\ \gamma_{12} \end{pmatrix}$$

where, Q_{ij} is the reduced stiffness matrix.

Even for a simple laminate, the stress and strain distributions are very complicated. As shown in Fig. 1.2 (a),(b), the anisotropic or at least orthotropic feature of each lamina results in the stress/strain distribution in lamina A being different from that in lamina B. Applying a shear stress may cause different strains in each lamina (Fig.1.2 (c)) or a uniform shear strain may be caused by different stresses in each lamina (Fig.1.2 (d)). The existence of interfaces brings sudden changes in properties and hence singularities in strain and stress distribution. This makes the determination of the interlaminar stresses directly from the constitutive equations a very difficult task.

In view of the difficulties in characterizing fully and accurately the interlaminar stresses, the experimental characterization concentrates on ascertaining the through-thickness strength under "simple" conditions. The current tests for characterizing through-thickness strength can be mainly grouped into two sets, depending on whether the strain energy release rate or the critical stress (or strain) are measured. In the first case, the approach is based on classical fracture mechanics, in the second it is based on stress and strain analysis.

1.2.1 Fracture Mechanics Approach

This approach to characterize delamination behaviour is based upon the measurement of the interlaminar fracture toughness (G_c), i.e. the critical strain energy release rate for the initiation and propagation of a pre-existing crack in the laminate.

The concept of strain energy release rate was first proposed by Griffith (1920) as,

$$G = \frac{\partial U}{\partial (ba)}$$

where a is the crack size, b the crack width and U the strain energy. For isotropic materials it is believed that, for a given existing crack, the propagation of the crack depends on G_c, the energy per unit area required for creating a new crack surface, which is a pure material property regardless of load, specimen geometry and crack length.

The experimental determination of G_c can be categorized according to Mode I, Mode II and Mixed-mode I/II fracture failure modes.

Mode I:

The most popular method for measuring Mode I fracture toughness (G_{Ic}) is the Double Cantilever Beam (DCB) test (Fig. 1.3(a)) (Davies, 1989). The data recorded in DCB tests are load, displacement and corresponding crack length. Although there are many other ways to calculate G_{Ic} such as the empirical compliance method (Berry,1963) and the area method (Hashemi,1990), the calculation from simple strength of materials considerations with stress singularities being ignored is still commonly used. The justification for this sweeping simplification is that since the stress singularity moves with the crack, the change in strain energy as the crack grows is therefore assumed to be due only to the variation in the general stress field(Latter, 1991). The simple beam theory analysis result, and some of the modifications based upon it are,

Elementary expression

$$U = \frac{1}{2}P2\Delta = \frac{4P^2a^3}{E_1bh^3}, \qquad G_{Ic} = \frac{12a^2P^2}{E_1b^2h^3} \tag{1-1.a}$$

Timoshenko (shear deformation)

$$G_{Ic} = \frac{12a^2P^2}{E_1b^2h^3}\left[1+\frac{1}{10}\frac{E_1}{G_{13}}\left(\frac{h}{a}\right)^2\right] \tag{1-1.b}$$

Kanninen correction(1974)

$$G_{Ic} = \frac{12a^2P^2}{E_1b^2h^3}\left[1+\chi\left(\frac{h}{a}\right)^2\right] \tag{1-1.c}$$

where, for isotropic materials χ=0.67 and for orthotropic materials Williams(1989) proposed,

$$\chi = \sqrt{\frac{1}{11}\frac{E_1}{G_{13}}\left[3-2\left(\frac{\Gamma}{1+\Gamma}\right)^2\right]}$$

where,

$$\Gamma=\frac{\sqrt{E_1E_3}}{0.85G_{13}}$$

Mode II:

The commonly used tests for measuring G_{IIc} include the End-Notch Flexure (ENF) test (Fig.1.3(b)) and the End-Loaded Split (ELS) test (Fig.1.3(c)). Again the simple beam analysis result and the modifications are,

Elementary expression for ENF

$$G_{IIc} = \frac{9a^2P^2}{16b^2h^3E_1} \qquad (1\text{-}2.a)$$

Carlsson (1986) (shear deformation) for ENF

$$G_{IIc} = \frac{9a^2P^2}{16b^2h^3E_1}\left(1+0.2\frac{E_1}{G_{13}}\left(\frac{h}{a}\right)^2\right) \qquad (1\text{-}2.b)$$

Elementary expression for ELS

$$G_{IIc} = \frac{9a^2P^2}{4b^2h^3E_1} \qquad (1\text{-}3)$$

Mixed Mode I/II:

Since delamination cracking is a complex failure phenomenon involving interlaminar shearing (Mode I) as well as out-of-plane peeling (Mode II), efforts were made on mixed-mode delamination testing (Reeder,1990; Hashemi,1991; Hutchinson,1992; Kinloch,1993). Among those, the Mixed Mode Bending (MMB) test was the most popular, proposed by Reeder(1990) (Fig. 1.4). According to the principle of stress superposition MMB was actually a simple combination of DCB and ENF (Fig. 1.5).

Part (a) of Fig 1.5 shows the MMB loading expressed in terms of the applied load P, the loading lever length c, and the specimen half-span L. As shown in part (b) of Fig. 1.5, the mode I component of this loading is

$$P_I = \left(\frac{3c-L}{4L}\right)P$$

Substituting P_I in Eqn.(1-1.a) leads to the following equation for G_{Ic} of the MMB test.

$$G_{Ic} = \frac{3a^2P^2}{4b^2h^3L^2E_1}(3c-L)^2 \qquad (1\text{-}4)$$

Part (c) of Fig 1.5 shows the mode II portion of the MMB loading. Note that the right-hand loading has been divided equally between the two equal-stiffness arms of the specimen. This is equivalent to the conventional loading of the ENF test. For the ENF test, the mode II bending load is

$$P_{II} = \left(\frac{c+L}{L}\right)P$$

Substituting for P_{II} in Eqn.(1-2.a), the corresponding equation for G_{IIc} of the MMB test is

$$G_{IIc} = \frac{9a^2P^2}{16b^2h^3L^2E_1}(c+L)^2 \qquad (1\text{-}5)$$

Dividing Eqn.(1-4) by Eqn.(1-5), the G_I/G_{II} ratio for the MMB test can be expressed as

$$\frac{G_{Ic}}{G_{IIc}} = \frac{4}{3}\left[\frac{(3c-L)}{(c+L)}\right]^2 \qquad c>\frac{L}{3} \qquad (1\text{-}6)$$

Therefore the MMB test can be used to measure delamination toughness over a wide range of mode I/II ratios as well as pure mode I and mode II.

However the question is whether or not one can obtain a pure Mode I or Mode II at a laminate interface. While the fracture mechanics failure criterion

$$\frac{G_I}{G_{Ic}} + \frac{G_{II}}{G_{IIc}} = 1$$

was claimed to be in good agreement with experimental data (Johnson,1987; Hashemi,1991), other experimental results indicated that G_{Ic} and G_{IIc} suffered from wide scattering.

DCB test results for C/epoxy specimens by Davies(1990) showed large variations. Average values of G_{Ic} around 130 J/m^2 with standard deviation of between 12 and 43 J/m^2 were obtained. Guedra (1987) distinguished between G_{Ic} at initiation, at maximum load and at crack arrest, and found that G_{Ic} depended on the crack length, Fig.1.6. Zhu (1993) found from tests with hybrid glass/carbon epoxy laminates that the values of G_{Ic} varied from 229 to 1003 J/m^2, using the DCB specimen, dependent on crack lengths between 35 and 174 mm.

Barsoum (1989) pointed out that the values of G_{IIc} for T300/5208 material varied between 150 to 1200 J/m^2, which far exceeds acceptable statistical variations for use as a design property. It was explained that the calculations of G_{II} have an unknown proportion of G_I in each test, which leads to the large scatter in the data. The results of a series of tests have been reported by Davies(1991). DCB, ENF and ELS configurations were tested with the following general conclusions:

-Mode I propagation is fairly reproducible, with G_{Ic} ranging between 150 and 250 J/m^2.

-Mode I initiation is strongly dependent on the starter defect. A 60 m thick starter film was regarded as excessively thick. Values of G_{Ic} between 100 and 220 J/m^2 were recorded.

-Mode II tests in which the crack grew from a mode I pre-crack gave values of G_{IIc} between 450 and 900 J/m^2. When the starter was a film, G_{IIc} varied between 1000 and 1700 J/m^2.

Based on an assessment of published literature and on his own work at Oxford UTC, Ruiz (1994) pointed out that the critical strain energy release rate for delamination cannot be regarded as a mechanical property of the composite system, since it depends on factors such as size and shape of specimens, testing method and procedure followed for the analysis of data, crack starter, slow crack growth, etc. Therefore it still remains as an open question, whether G_{Ic} and G_{IIc} are meaningful material properties (Barsoum,1989).

1.2.2 Critical Stress or Strain Approach

Critical stress or strain criteria are based on a combination of uniaxial or multiaxial stresses or strains, usually an invariant. When the combined stress or strain reaches a critical value, the onset of delamination is assumed to occur. The criteria may be regarded as phenomenological since they do not explain the real failure modes, they merely describe them.

The failure criteria currently used for laminates mainly refer to the in-plane strength. They include first ply failure criterion (FPF) and last ply failure criterion (LPF), which are based

on the hypothesis that a laminate fails when only one ply fractures with the rest of the plies intact (FPF), or when the last intact ply has finally fractured (LPF). That is to say that the in-plane strength of a laminate is solely dependent on that of each lamina and the interlaminar stresses and through-thickness failures (delamination) are not considered. The most generally used lamina failure models can mainly be grouped into three categories (Jones,1975).

1) Maximum stress theory and maximum strain theory, in which the stresses (or strains) in the principal material direction must be less than the respective strengths, otherwise failure is said to have occurred. Obviously there are actually three subcriteria for a lamina and there is no interaction between modes of failure in the maximum stress theory, while there is some relation between the strains ε_1 and ε_2 by Poisson's ratio in maximum strain theory.

2) Tsai-Hill Theory, which is based on a yield criterion for anisotropic materials proposed by Hill (1956) and developed by Tsai for lamina. The Tsai-Hill theory is actually an extension of the von Mises isotropic yield criterion. The von Mises criterion, in turn, can be related to the amount of energy that is used to distort the body (2nd invariant) rather than to change the volume. However, the problem is that distortion cannot be separated from dilatation in orthotropic materials. Thus the amount of distortion energy may not be directly related to failure as it was for many isotropic materials.

3) Tsai-Wu Tensor Theory. Tsai and Wu (1971) postulated that a failure surface in stress space exists in the form,

$$F_i\sigma_i+F_{ij}\sigma_i\sigma_j=1 \qquad i,j=1,....,6 \tag{1-7}$$

wherein F_i and F_{ij} are strength tensors of the second and fourth rank respectively, and the usual contracted stress notation is used except that $\sigma_4 = \tau_{23}$, $\sigma_5 = \tau_{31}$ and $\sigma_6 = \tau_{12}$.

Equation (1-7) is a quadratic in which the higher order terms are ignored for simplicity. It is possible to choose more terms such as the cubic tensor polynomial failure criterion proposed by Tennyson(1978) and Jiang(1989).

For an orthotropic lamina under plane stress condition,

$$F_1\sigma_1+F_2\sigma_2+F_6\sigma_6+F_{11}\sigma_1^2+F_{22}\sigma_2^2+F_{66}\sigma_6^2+2F_{12}\sigma_1\sigma_2=1 \tag{1-8}$$

Some of the components of the strength tensors in Eqn.(1-8) can be defined in terms of the engineering strength,

$$F_1=\frac{1}{X_t}+\frac{1}{X_c} \qquad F_6=0$$

$$F_{11}=-\frac{1}{X_tX_c} \qquad F_{66}=\frac{1}{S^2} \tag{1-9}$$

$$F_2=\frac{1}{Y_t}+\frac{1}{Y_c}$$

$$F_{22}=-\frac{1}{Y_tY_c}$$

wherein, X_t (X_c) and Y_t (Y_c) are tensile (compressive) engineering strengths in 1 and 2 directions respectively, and S is the shear strength in 1-2 plane.

The interactive tensor strength F_{12} can be determined by a biaxial test.

Referring to the through-thickness strength, although a lot of work has been done on how to determine the interlaminar stresses, very little has been done about the failure criteria to predict initiation of delamination. The difficulty is the experimental characterization of a 3-D, or even a through-thickness 2-D, combined stress state, which is required to obtain a phenomenological failure criterion, such as the biaxial test required for determining F_{12} of the Tsai-Wu theory in the case of in-plane strength.

Some tests to characterize through-thickness properties in terms of the critical stress or strain criteria are:

a) Iosipescu Shear Test

Since it was originally developed for the measurement of shear strength of metals by Nicolace Iosipescu in the 1960's, the Iosipescu shear test has been widely used for determining the in-plane shear modulus and strength of composite materials (Ho, 1991; Lee, 1990). Fig. 1.7 shows a loaded Iosipescu specimen with corresponding shear force and bending moment diagrams. It is clear that a pure shear force, without bending moment, is applied at the middle section of the specimen, where it is waisted from top and bottom. The notch angles are chosen as 90^0 so that the notch faces are parallel to the 45^0 principal stresses. It was thought that this would avoid stress concentrations at the notch roots (Iosipescu,1967).

The Iosipescu shear test was used at Oxford University to measure the interlaminar shear properties with specimens made of 0°/90° fabric laminate. Fig.1.8 shows a test set-up by

Hognestad (1993). Numerical analysis was done to find the stress distribution along the throat section, and it was found that a sharper notch angle gave a higher stress concentration and that above 80^0 no stress concentration was present (Fig.1.9). Xing (1992) examined the strain field around the test section of the Iosipescu specimen using the moiré interferometry technique. This is a coherent-light optical method characterized by subwavelength displacement sensitivity, high spatial resolution, high signal-to-noise ratio and very large displacement range. Therefore the complete state of strain on the specimen surface -- the normal strains and the shear strain -- is determined easily from the displacement field (Post,1991). It was found by Xing that on the test section there was an approximately uniform shear strain distribution, which indicates a uniform shear stress distribution, for the woven laminate specimen (Fig.1.10). However it was also pointed out that the specimen is very easily distorted by various factors such as the stress concentration at loading points, and that torsion and bending moment resulted from misalignment. Therefore great care had to be paid to the loading and the alignment of specimen and fixtures in order to achieve a pure and uniform shear stress.

b) Curved Beam Test

The fact that through-thickness stresses, developed when curved composite laminates are subjected to flexural loading in the plane of curvature, have induced the interlaminar failure was initially addressed in the University of Delaware's Design Guide Encyclopedia (Kedward, 1980) and then was experimentally demonstrated by Lagace and Weems (1986). Kedward, Wilson and McLean (1989) examined the generic curved beam, plate and cylindrical tube configurations, at which significant interlaminar tensile stress (ILTS) has developed, using finite element methods, classical elasticity theory and a simplified strength of materials approach. The acceptability and utility of latter approach is assessed by drawing comparisons

with the former two approaches. This, to some extent, confirmed the curved beam test as a quite standard test for assessing the ILTS of composite laminates. Fig.1.11 shows the work in NASA by Hiel, Sumich and Chappell (1991), who proposed two kinds of curved beam specimen configuration (semi-circular and elliptical) to determine the ILTS of a composite laminate subjected to end tensile loads which open up the curvature and induce damage by delamination. The plies of both configurations were orientated around the circumferential direction (100% 0° layup) in order to eliminate the free edge ILTS intensification. The maximum ILTS within the laminate at the apex of each specimen was calculated by classical elasticity (continuum) theory and finite element analysis respectively. The results showed that the static failure load for the semicircular specimen was highly sensitive to flaw content and the elliptical specimen demonstrated unusually high failure strength, indicating the presence of phenomena requiring further study. Wu (1993) also tested and calculated the through-thickness stresses generated in curved laminates by bending moments.

The work at Oxford University (Hognestad,1993) used C-specimens made of fabric reinforced laminate ($0^0/90^0$) subjected to tensile loads as shown in Fig. 1.12. It was found that the C-specimen test is a good method for measuring through-thickness strength of laminates under combined stress, and for the C-specimen made of fabric laminated composite, the stress distribution could be described by classical continuum mechanics (Timoshenko, 1970):

$$\sigma_r = -4\frac{Pe}{N_1}\left(\frac{a^2b^2}{r^2}\ln\frac{b}{a}+b^2\ln\frac{r}{b}+a^2\ln\frac{a}{r}\right)-\frac{P}{N_2}\sin\theta\left[r+\frac{a^2b^2}{r^3}-\frac{(a^2+b^2)}{r}\right]$$

$$\sigma_t = -4\frac{Pe}{N_1}\left(-\frac{a^2b^2}{r^2}\ln\frac{b}{a}+b^2\ln\frac{r}{b}+a^2\ln\frac{a}{r}+b^2-a^2\right)-$$

$$-\frac{P}{N_2}\sin\theta\left[3r-\frac{a^2b^2}{r^3}-\frac{(a^2+b^2)}{r}\right]$$

$$\tau_{rt} = \frac{P}{N_2}\cos\theta\left[r+\frac{a^2b^2}{r^3}-\frac{(a^2+b^2)}{r}\right] \qquad (1\text{-}10)$$

where,

$$N_1 = (b^2-a^2)^2-4a^2b^2\left(\ln\frac{b}{a}\right)^2$$

$$N_2 = a^2-b^2+(a^2+b^2)\ln\frac{b}{a}$$

FEM analysis was found to agree with the analytical solution following Timoshenko. Since the most probable position of failure is the apex of the C-specimen, a pair of interlaminar tensile stress and tangential stress, without shear stress, can be obtained. The experimental results showed that delamination was affected not only by interlaminar normal stress but also by in-plane tensile/compressive stress.

1.2.3 Limitation of Current Work: Failure Maps

Current work is limited to the determination of delamination toughness (G_c) or to tests in either pure shear or tension + tangential stress testing. This is not enough for engineering design. Crack growth might occur too late to prevent a disaster because it is based on the analysis of existing cracks. In practice, what is really needed is a failure map or criterion to select admissible design stress in the dimensioning of engineering components.

In order to establish a failure map based on combined stresses at failure, experimental data obtained under a variety of stress states is needed. It is obviously envisaged that a failure map including all stress components related to the through-thickness strength is impossible; instead we choose the in-plane normal stress σ_1, interlaminar shear stress τ_{13} and through-thickness normal stress σ_3 as the most important factors contributing to delamination. This simplification could be easily justified since peeling (σ_3) and tearing (τ_{13}) stresses lead to delamination, and the effect of σ_1 on the through-thickness strength has been experimentally confirmed by Hognestad (1993).

Fig. 1.13 shows the stress space of σ_1 -σ_3 - τ_{13}, which is divided into four quadrants, namely I, II, III and IV because the shear strength in the principal material directions is seen to be independent of differences in tensile and compressive behaviour, viz. the shear stress whether "positive" or "negative" has the same maximum value. This statement is rationalized by observation of Fig.1.14 wherein positive and negative interlaminar shear stresses are applied to a laminate. Here a shear stress is denoted as positive when its moment about the centre of the element is clockwise (Singer, 1951). Therefore the tests to be conducted will be designed to "fill" and investigate each quadrant of the stress space. They include,

a) Oblique Test

The specimen is shown in Fig.1.15. It is obvious that a $\sigma_1(+)$ -$\sigma_3(+)$ - τ_{13}(quadrant I) or a $\sigma_1(-)$ - $\sigma_3(-)$ - τ_{13}(quadrant III) stress state can be obtained whilst imposing a tensile or compressive load.

b) Waisted C-specimen Test

As a modification of the plain C-specimen, the controlled failure at the waisted section of the specimen will add an interlaminar shear to σ_1 - σ_3 according to classical elastic theory (Fig.

1.16). Therefore a $\sigma_1(+)$ -$\sigma_3(+)$ - τ_{13}(quadrant I) or a $\sigma_1(-)$ - $\sigma_3(+)$ - τ_{13}(quadrant II) stress state can be obtained.

c) Central Notched Beam under Four-Point Bending Test

For a beam with a central notch under four-point bending, a combined $\sigma_1(+)$ -$\sigma_3(+)$ - τ_{13} (quadrant I) stress state is found along the notch surface (Fig. 1.17). It is also found that, by changing the depth of the notch, the magnitude of each stress component can be controlled and therefore failure can be caused predominately by one or two of the stress components.

Finally, it should be stated that, for simplicity and consistency, all test specimens will be woven laminate with pure 0°/90° lay-up.

1.3 STRUCTURE OF THE THESIS

In this investigation, the through-thickness strength of fibre reinforced polymer matrix laminates is studied by means of three tests, namely the oblique test, the waisted C-specimen test and the notched beam test. These are designed in order to establish a 3-D failure map in the coordinates of in-plane stress σ_1, interlaminar normal stress σ_3 and interlaminar shear stress τ_{13}, as well as to understand the failure mechanisms of delamination. The three tests are described respectively in Chapters 2, 3 and 4. All the test geometries are analyzed by either numerical or experimental means to ensure that they are subjected to a known stress state. Two kinds of material systems have been tested, namely carbon fabric reinforced epoxy matrix laminate (C/epoxy) and glass fabric reinforced epoxy matrix laminate (G/epoxy). The C/epoxy is a widely used industrial material, and the experimental results are intended to be of direct application to design. The G/epoxy is basically a laboratory material. It is hoped that the

transparency of the G/epoxy may help to detect the onset of any cracks so as not only to verify that the failures are caused by the known stress state rather than by manufacturing or other defects, but also to reveal visually the failure mechanisms. Besides the failure stresses taken from the various stress states of each test, the broken specimens' surfaces are examined by scanning electron microscope (SEM) technique to reveal the micro-structural features of failure under different stress states.

A general interpretation of the results from Chapters 2, 3 and 4 is carried out in Chapter 5, where the experimental accuracy is assessed and all the results are correlated. As the phenomenological failure criterion has been well used in in-plane stress prediction, a through-thickness failure criterion, based on Tsai-Wu theory, is established and compared with all the experimental results. It is found that because of the complicated failure mechanisms, which have been revealed by SEM examinations, the phenomenological failure criterion cannot predict the experimental results although there is some agreement. Therefore the full understanding of the through-thickness failure can only achieved by conducting extensive tests.

Chapter 6 deals with the problem of stress gradient effect on failure. Since the effect of the stress gradient on failure can be as high as 25~40% (Zweben, 1994), there is no point in putting all experimental results directly onto the failure map regardless of their stress gradients. Weibull statistics technique has been used to establish a methodology for modifying the results with stress gradients. Finally, in Chapter 7, conclusions are drawn on the work described in this thesis and suggestions are made for future work.

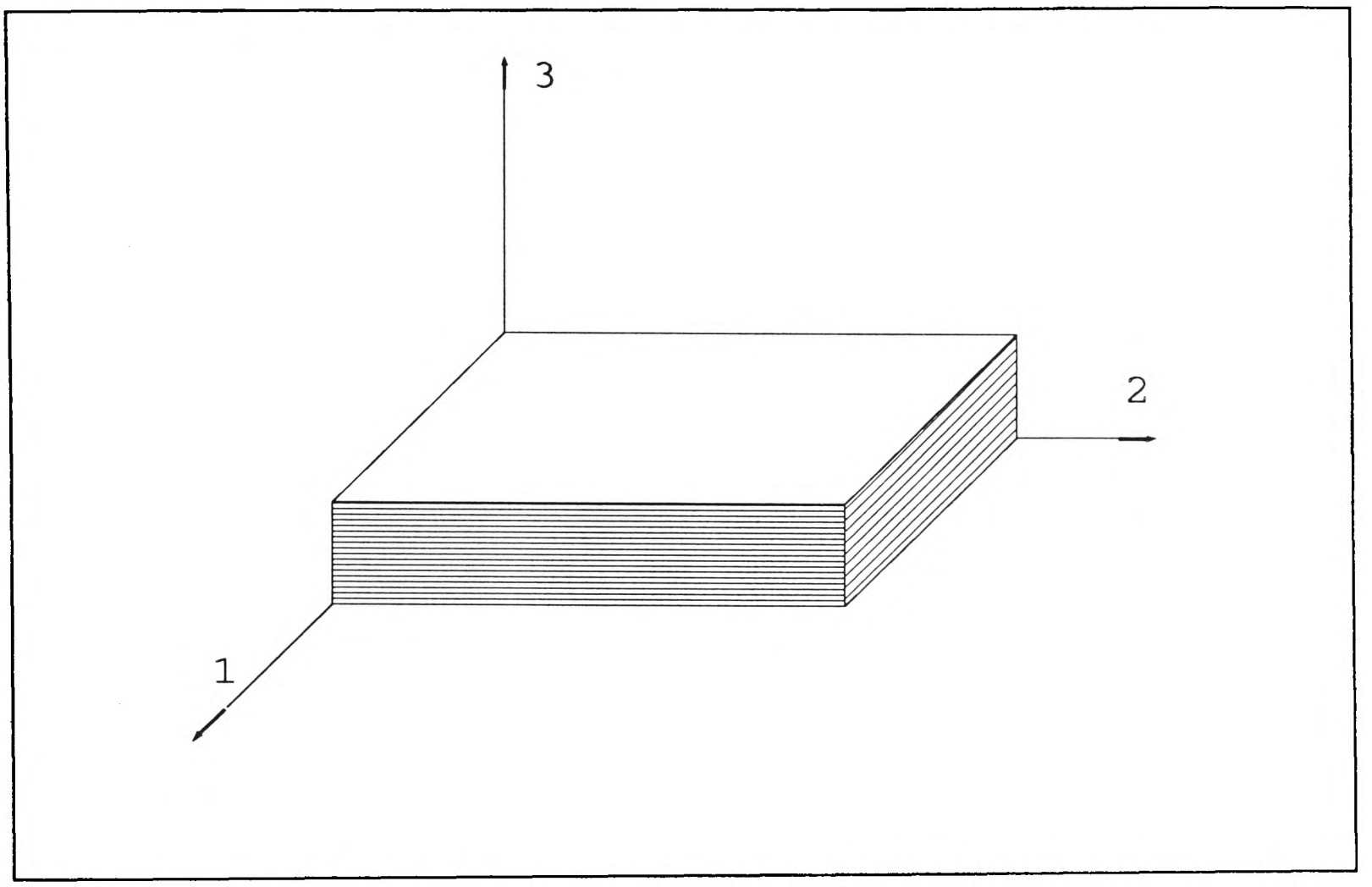

Figure 1.1 Principal Material Coordinate System

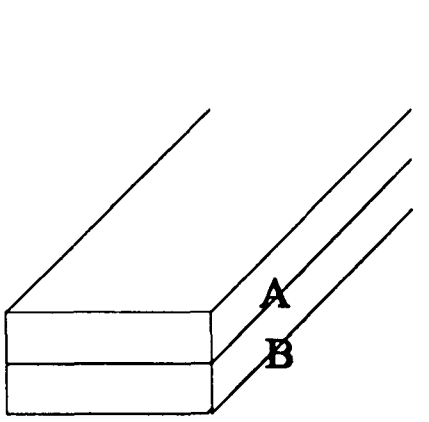

(a)

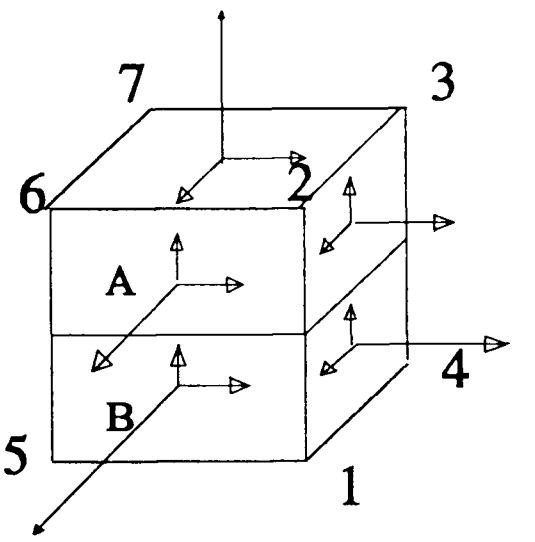

(b)

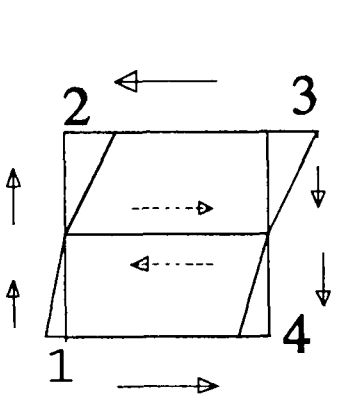

τ equal
γ different

(c)

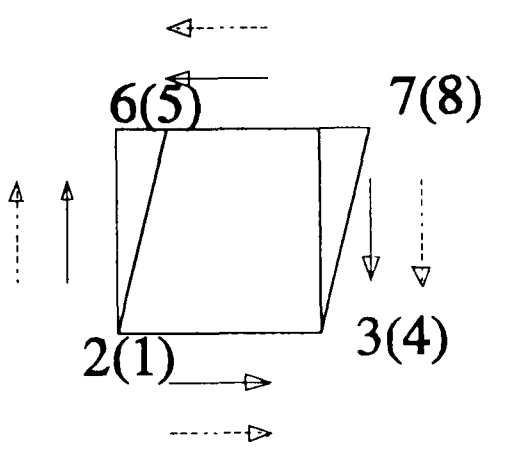

γ equal
τ different

(d)

Figure 1.2 Stress/Strain State of A Laminate

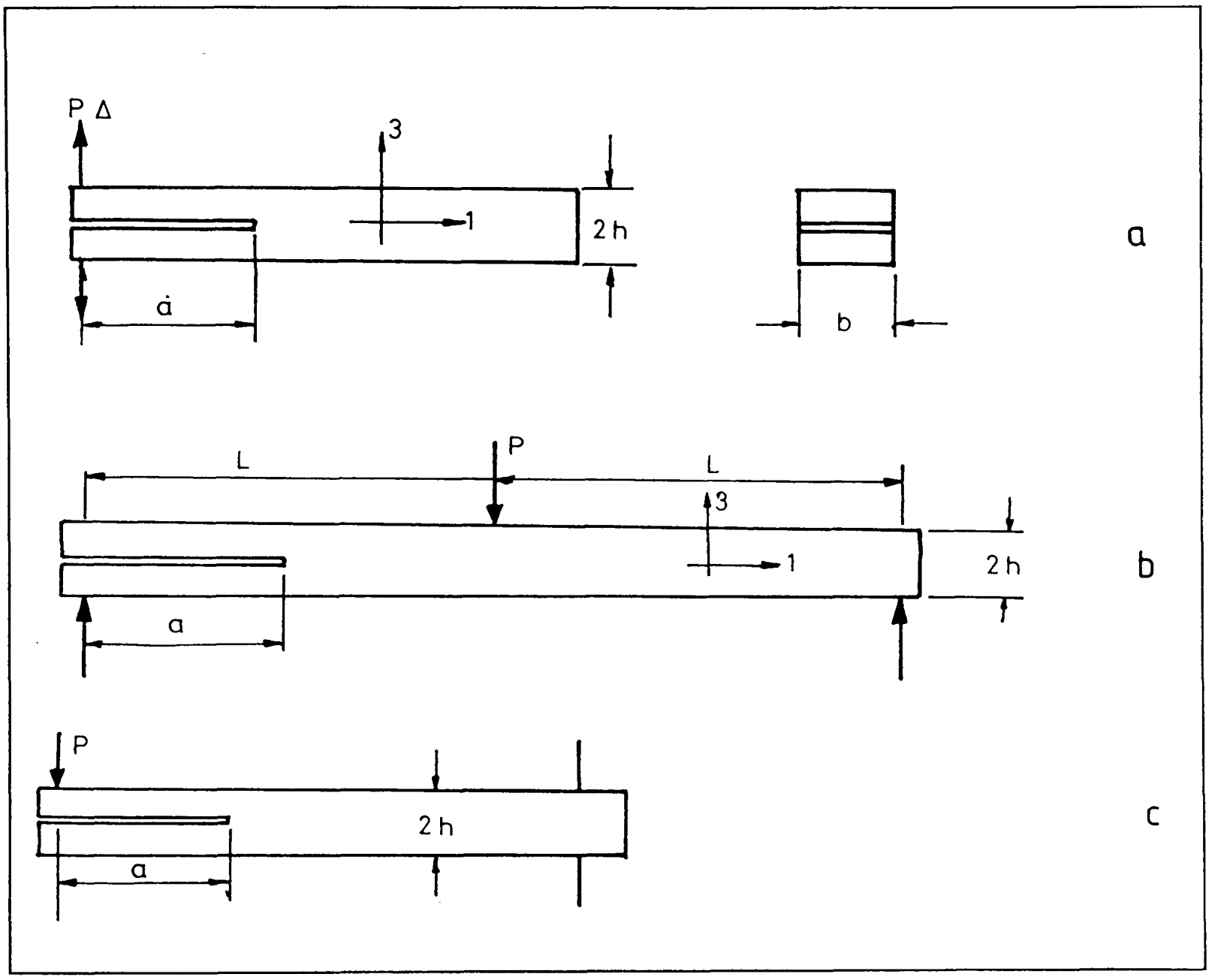

Figure 1.3 Typical Configurations for the Measurement of G_C, (a) DCB, (b) ENF, (c) ELS

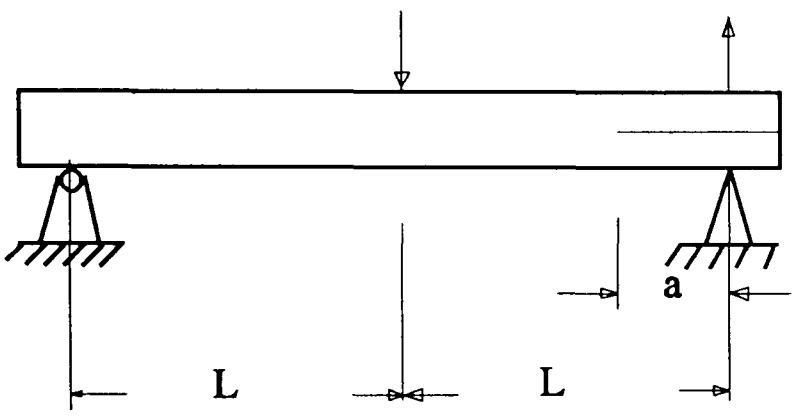

(a) Test Specimen and Loading

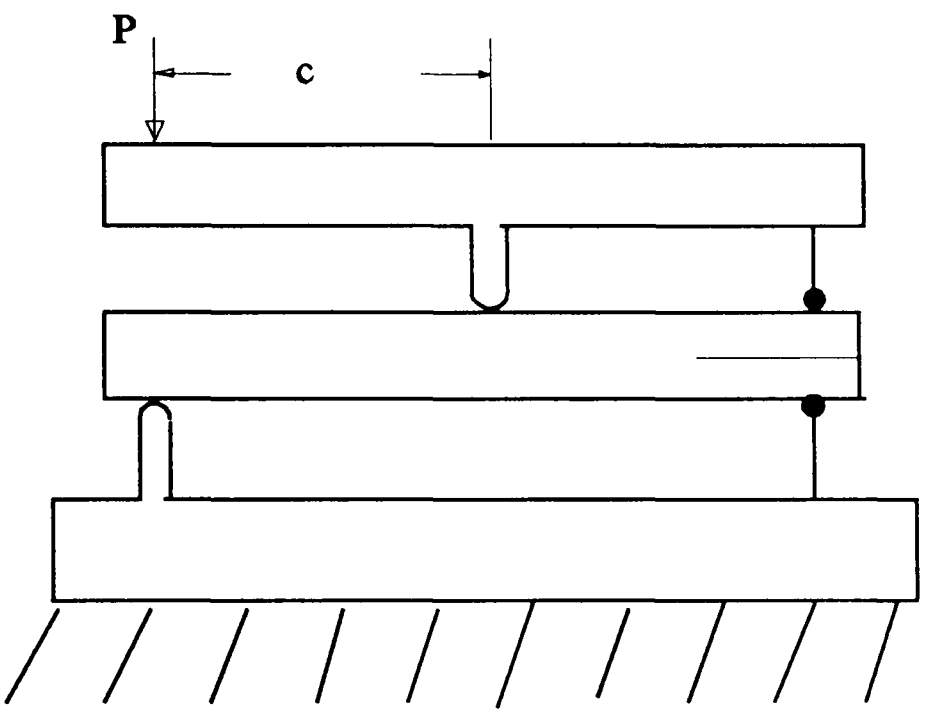

(b) Schematic Diagram of Apparatus

Figure 1.4 MMB Test

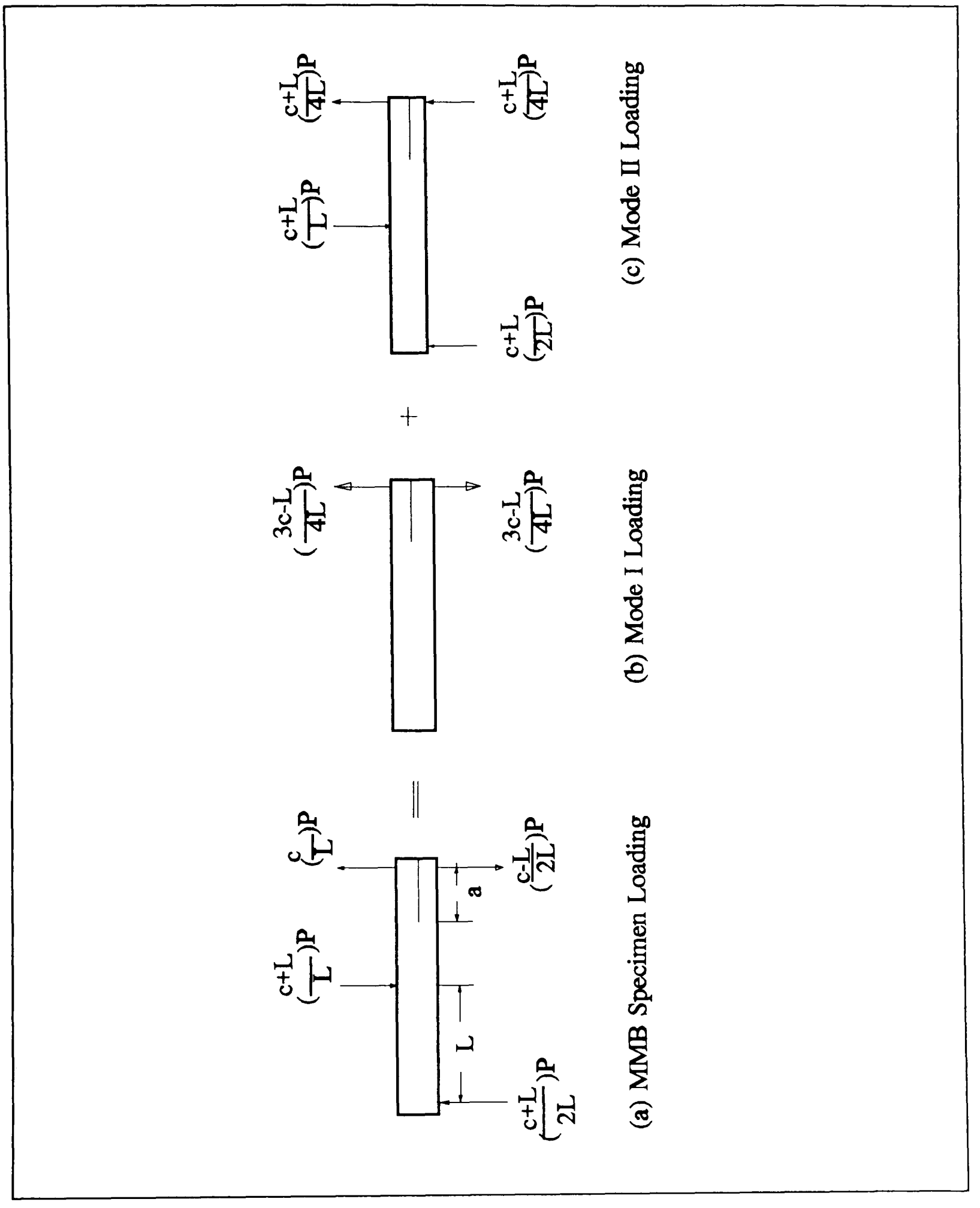

Figure 1.5 Superposition Analysis of Loading on the MMB Specimen

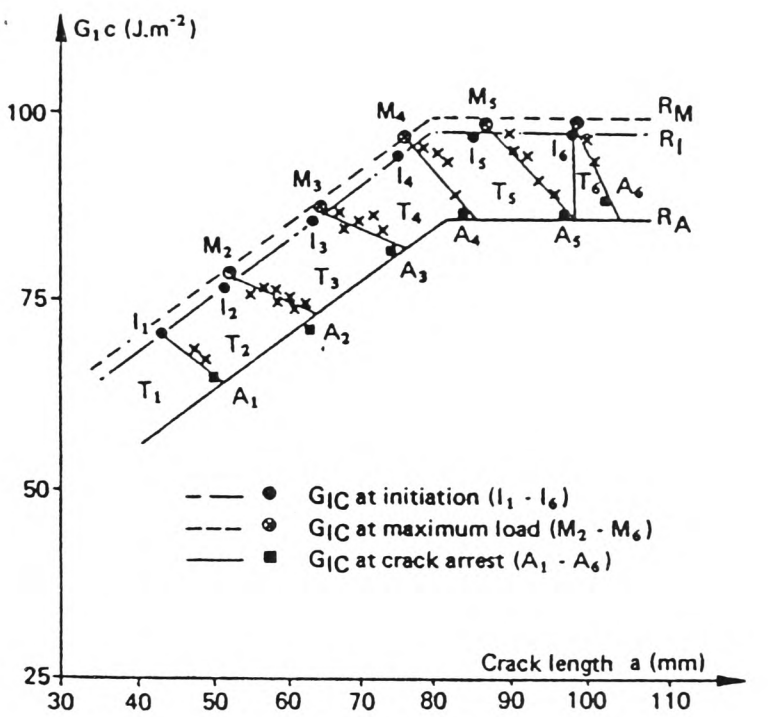

Figure 1.6 G_{IC} values for 6 loading and unloading cycles (*after* Guedra, 1987).

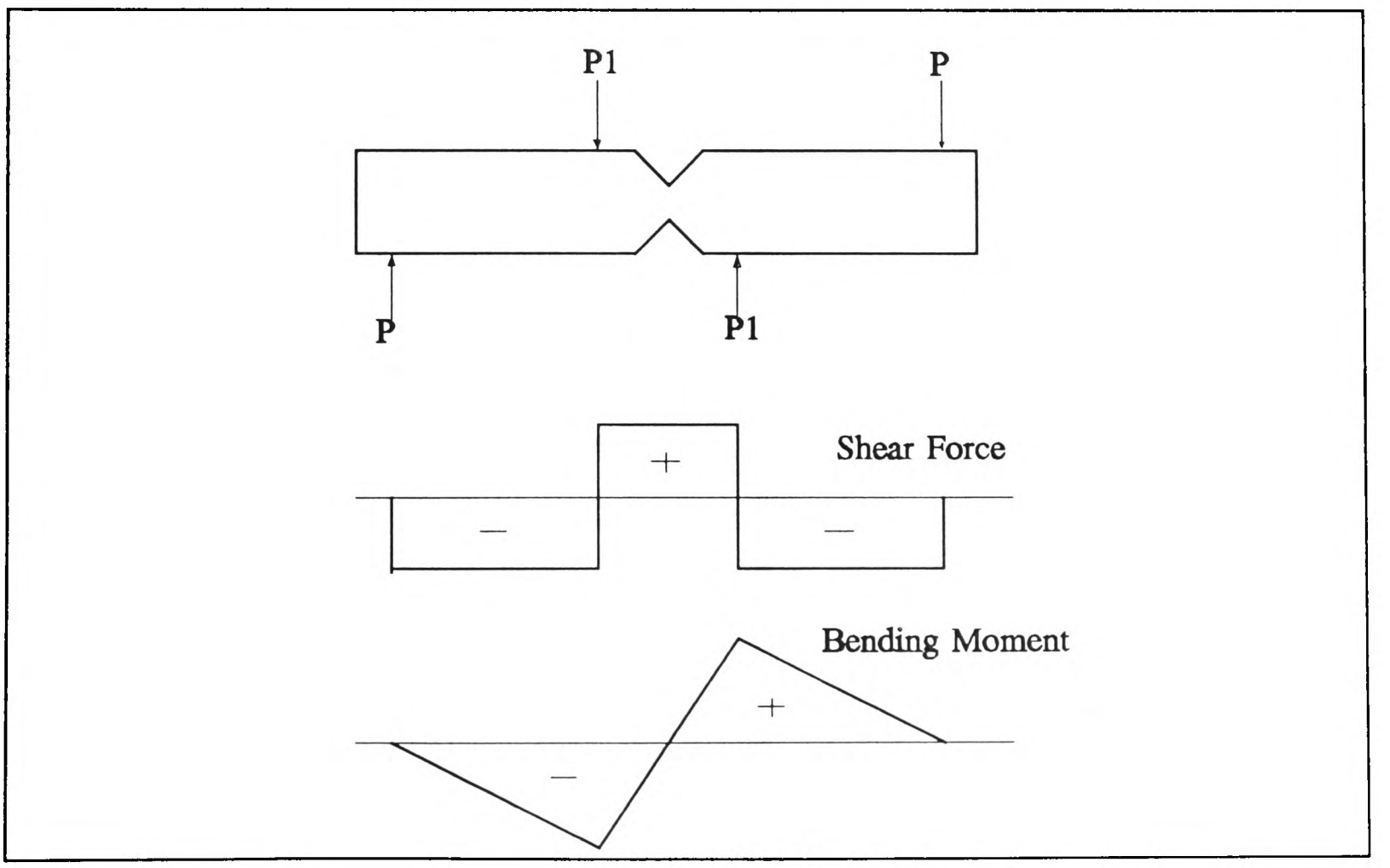

Figure 1.7 Iosipescu shear test principle.

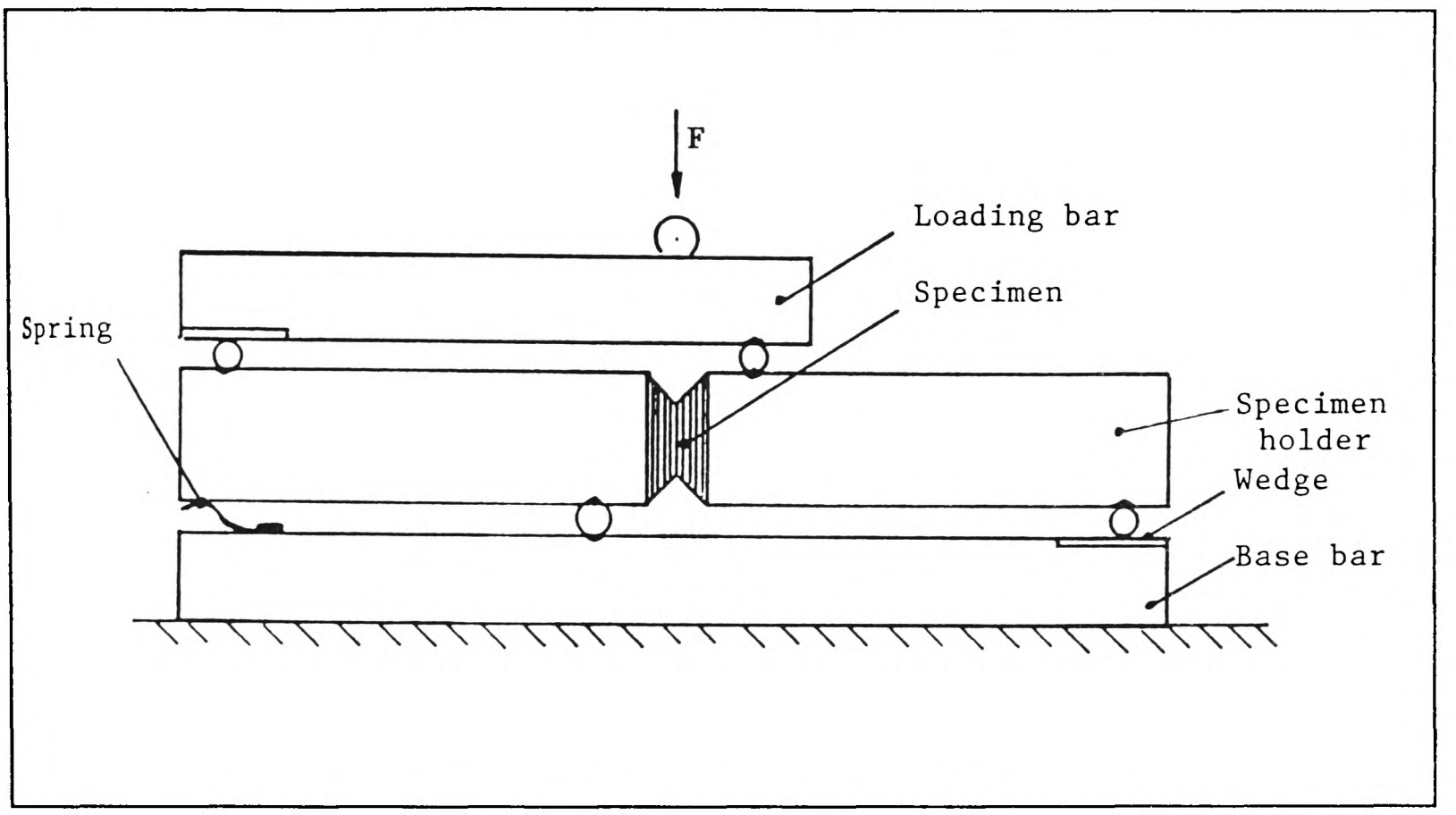

Figure 1.8 Iosipescu type shear test in 4-point anti-symmetric bending, where the laminae are parallel to the applied shear force.

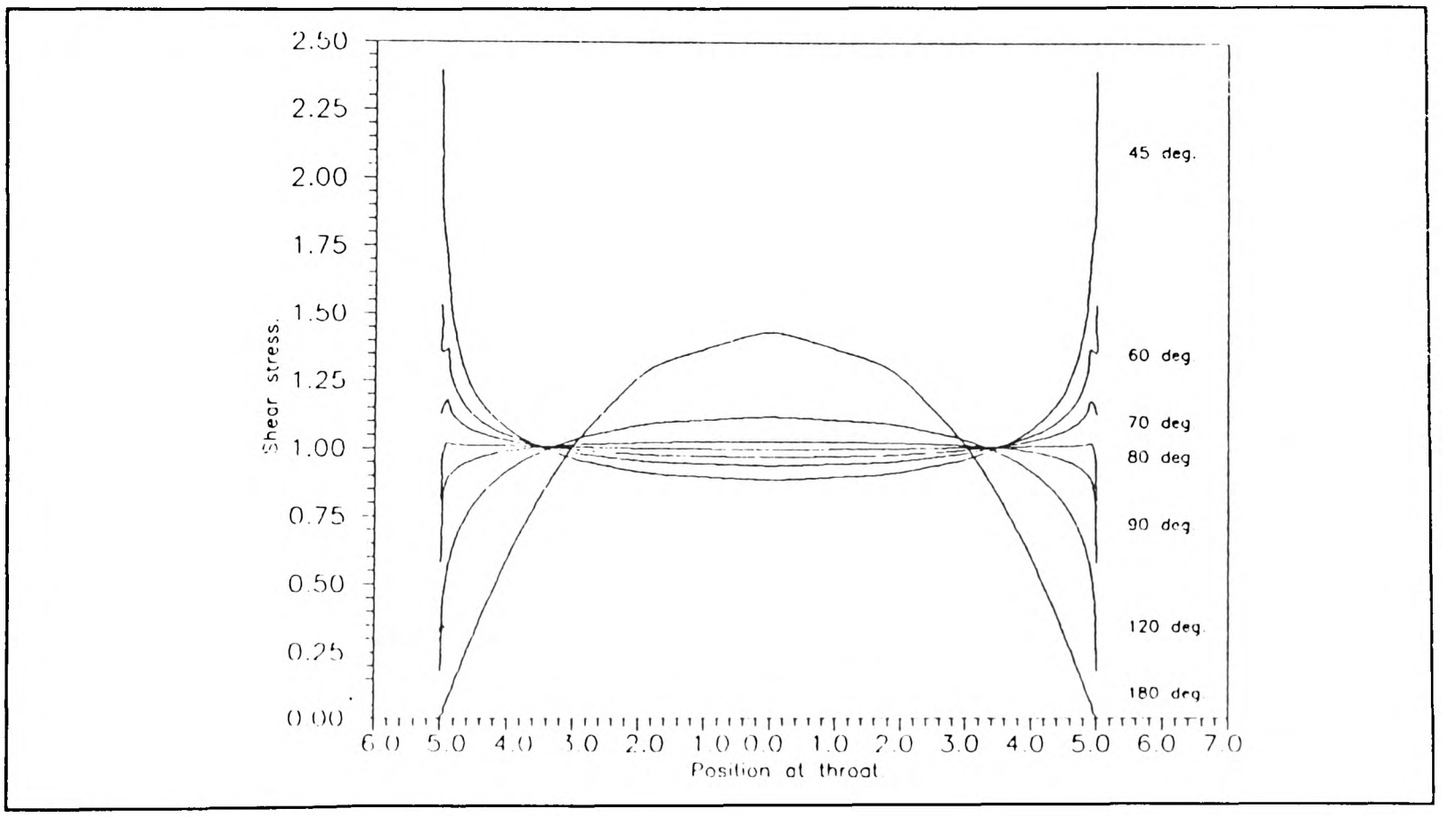

Figure 1.9 Shear stress along the throat with varying waist angle for orthotropic Iosipescu tests (*after* Hognestad, 1993).

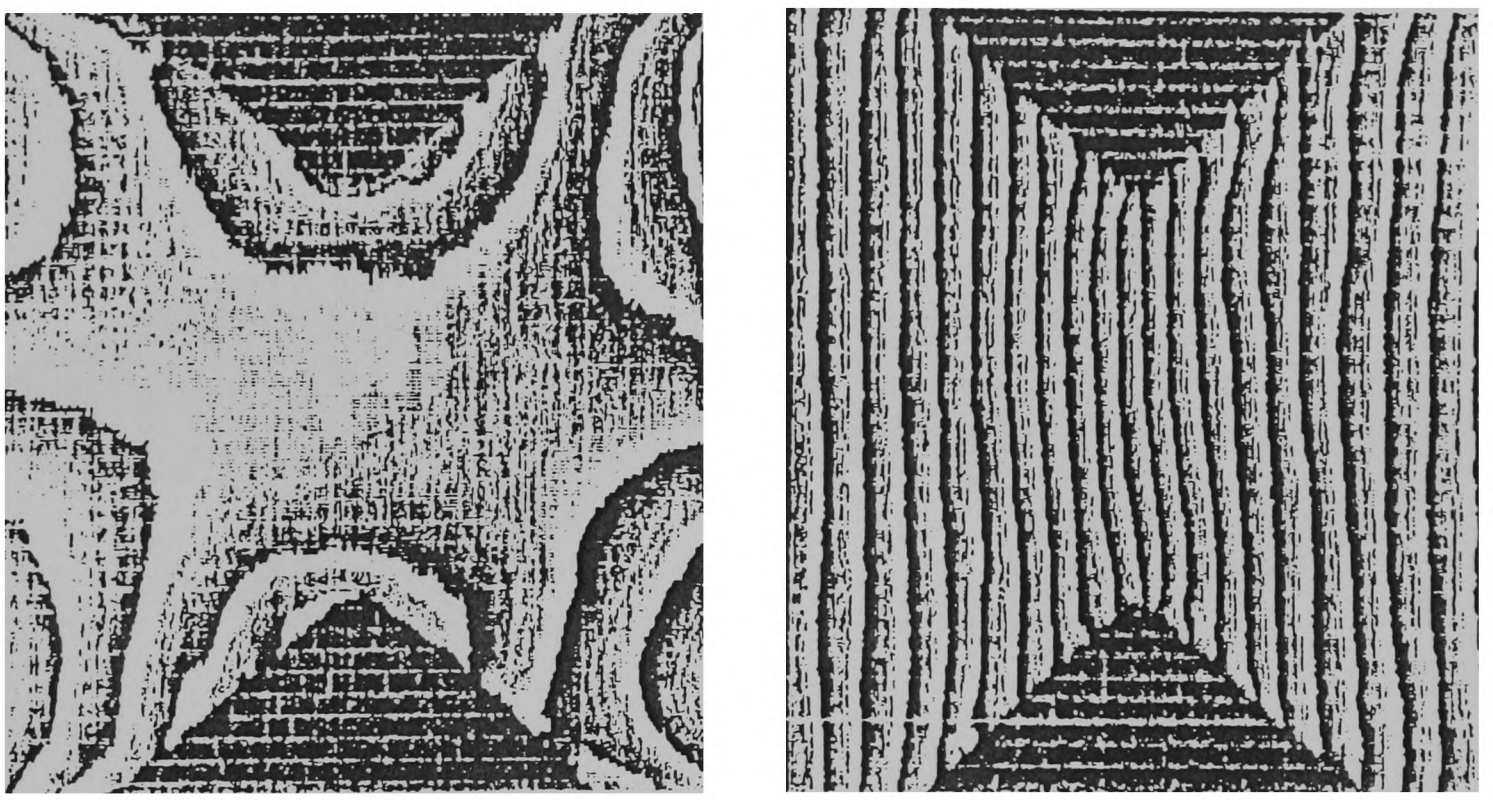

(a) (b)

Figure 1.10 Strain field under ideal conditions by Moiré interferometry technique (*after* Xing, 1992). (see next page)

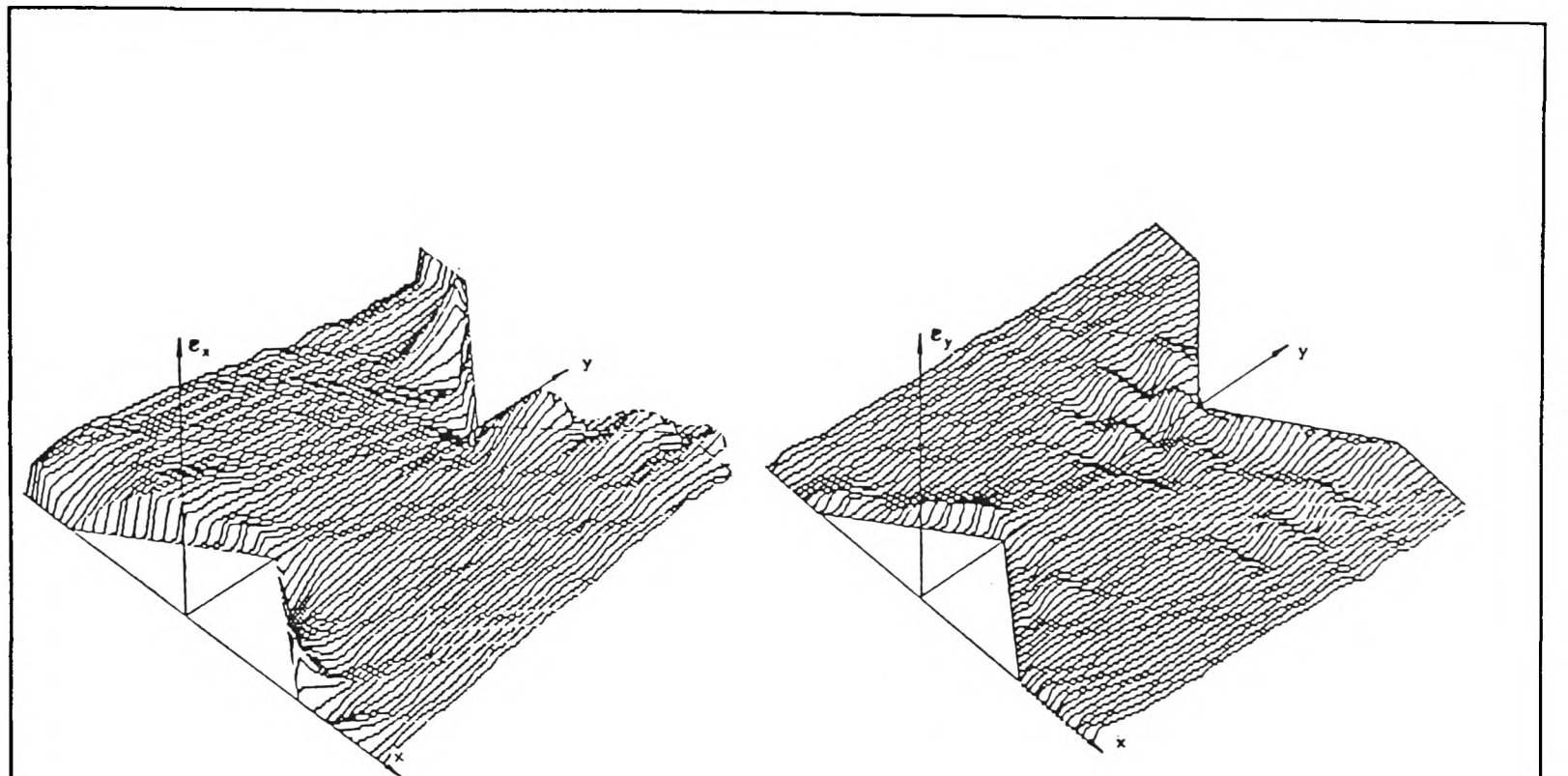

Figure 1.10 Strain field under ideal conditions, (a) U displacement fringe pattern, (b) V displacement fringe pattern, (c) 3-D map of the strain ε_x, (d) 3-D map of the strain ε_y, (e) 3-D map of the shear strain γ_{xy}, (f) distribution of the shear strain γ_{xy} along the test section.

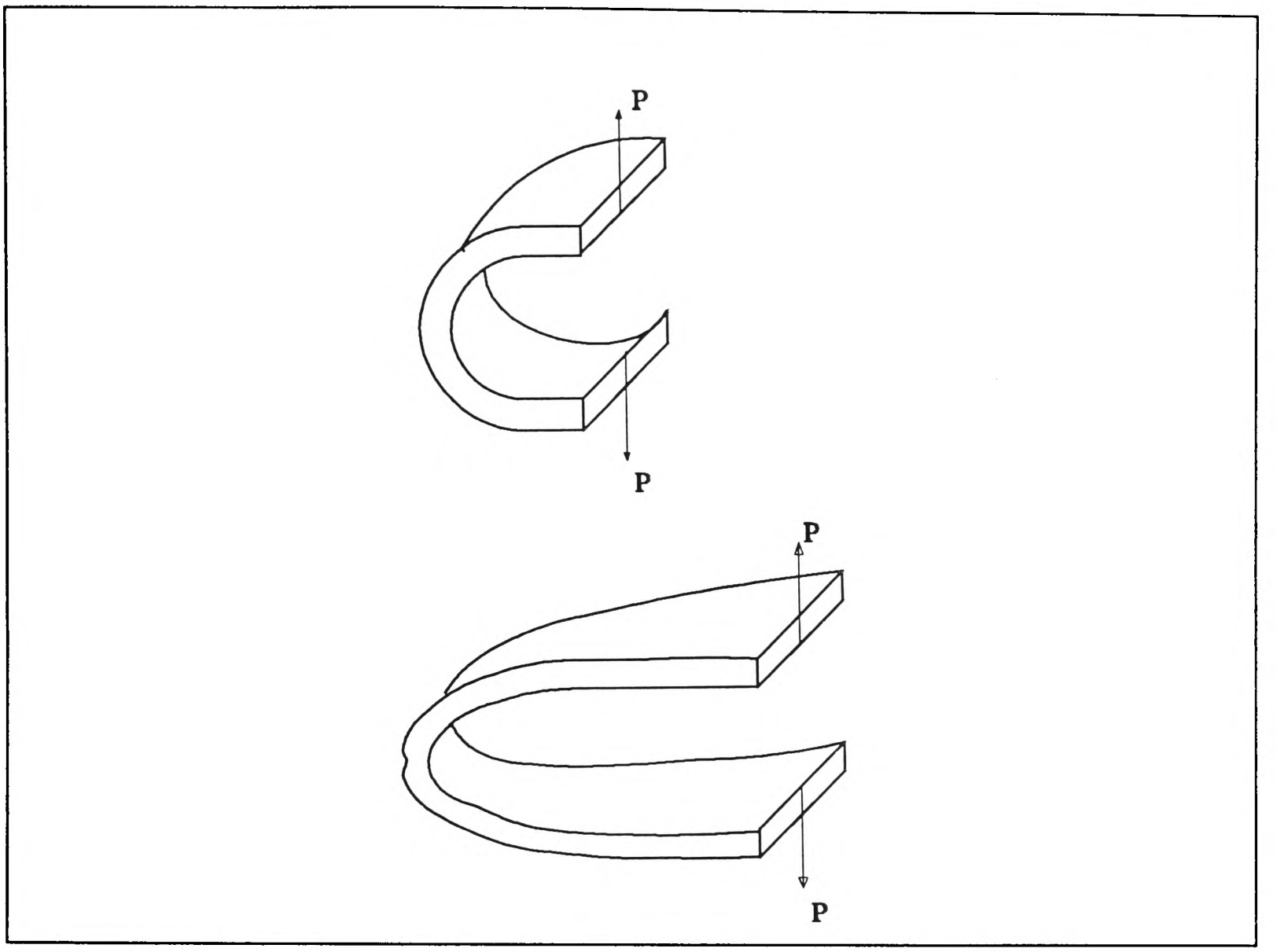

Figure 1.11 Curved beam test (*after* Hiel, 1991).

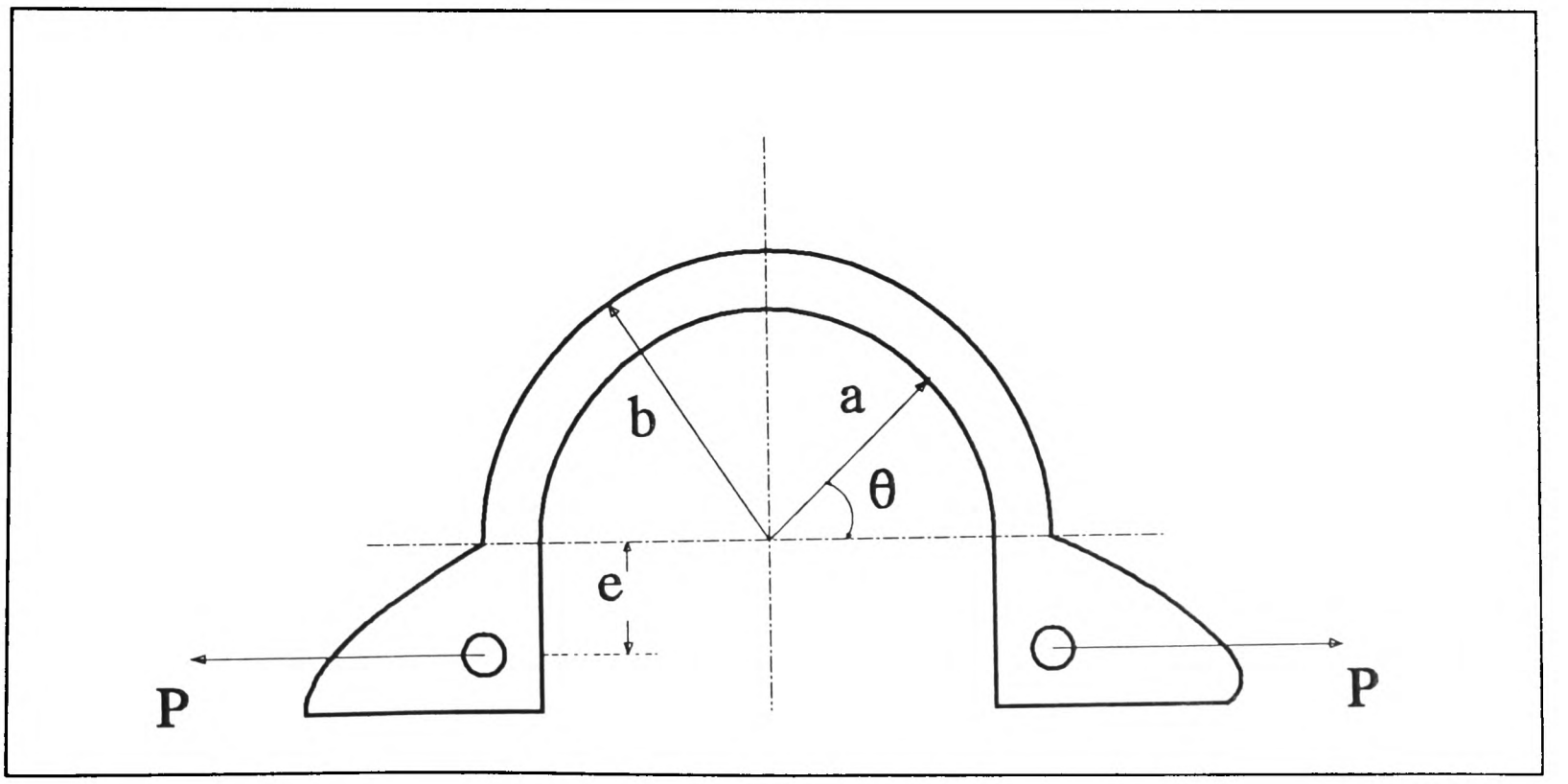

Figure 1.12 Schematic view of C-specimen test.

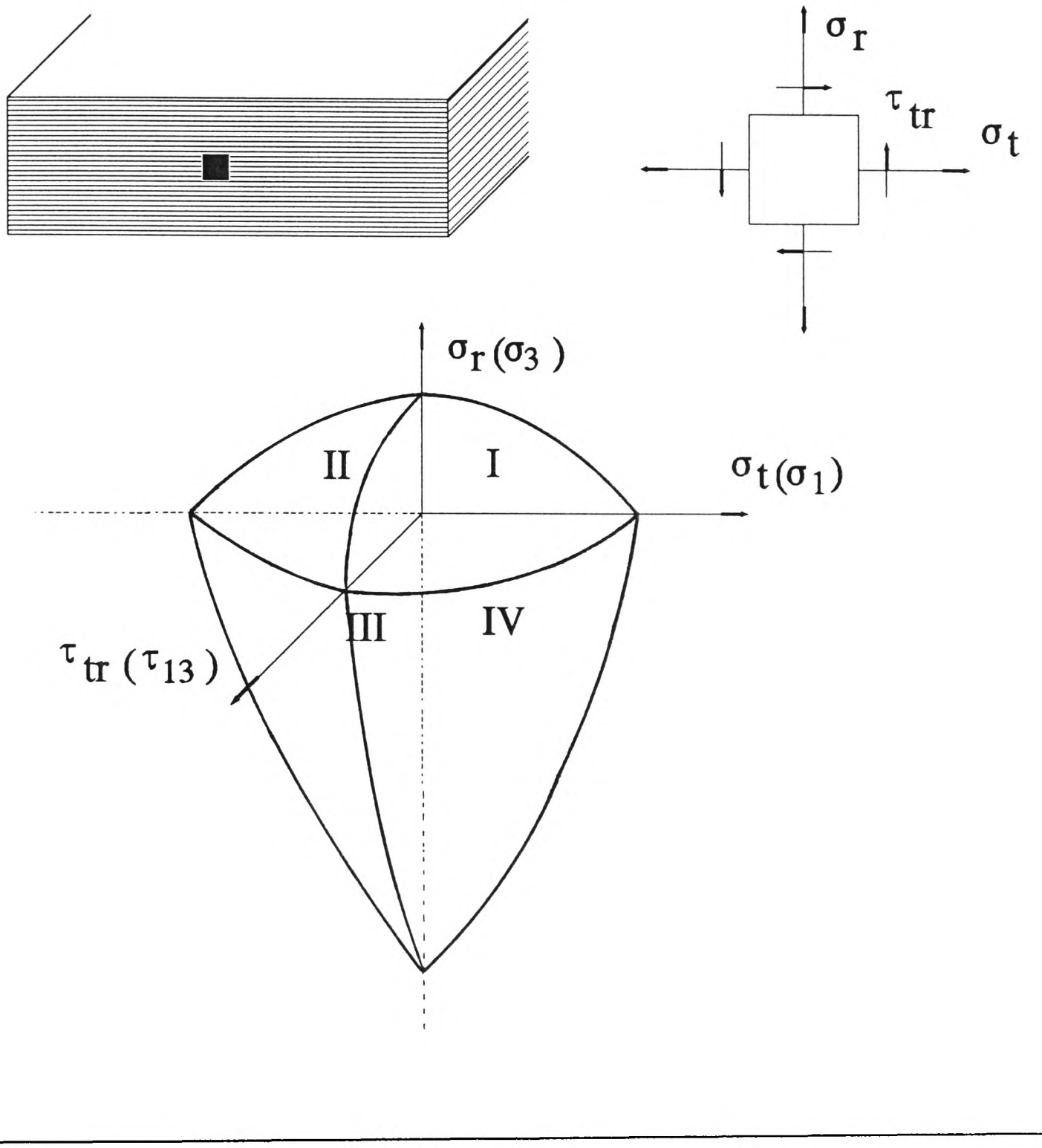

Figure 1.13 Coordinates system of failure map.

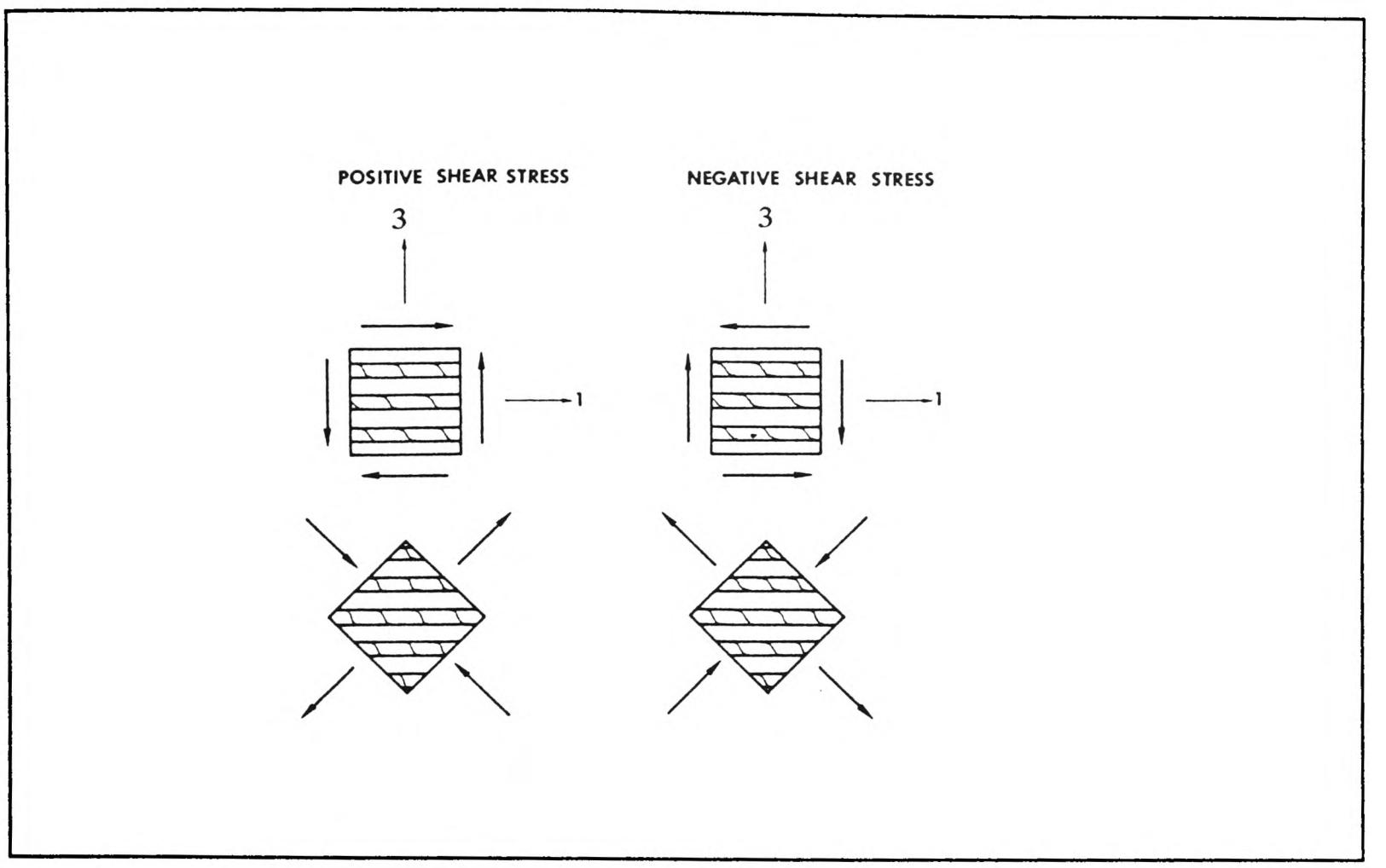

Figure 1.14 Shear stress in principal material directions.

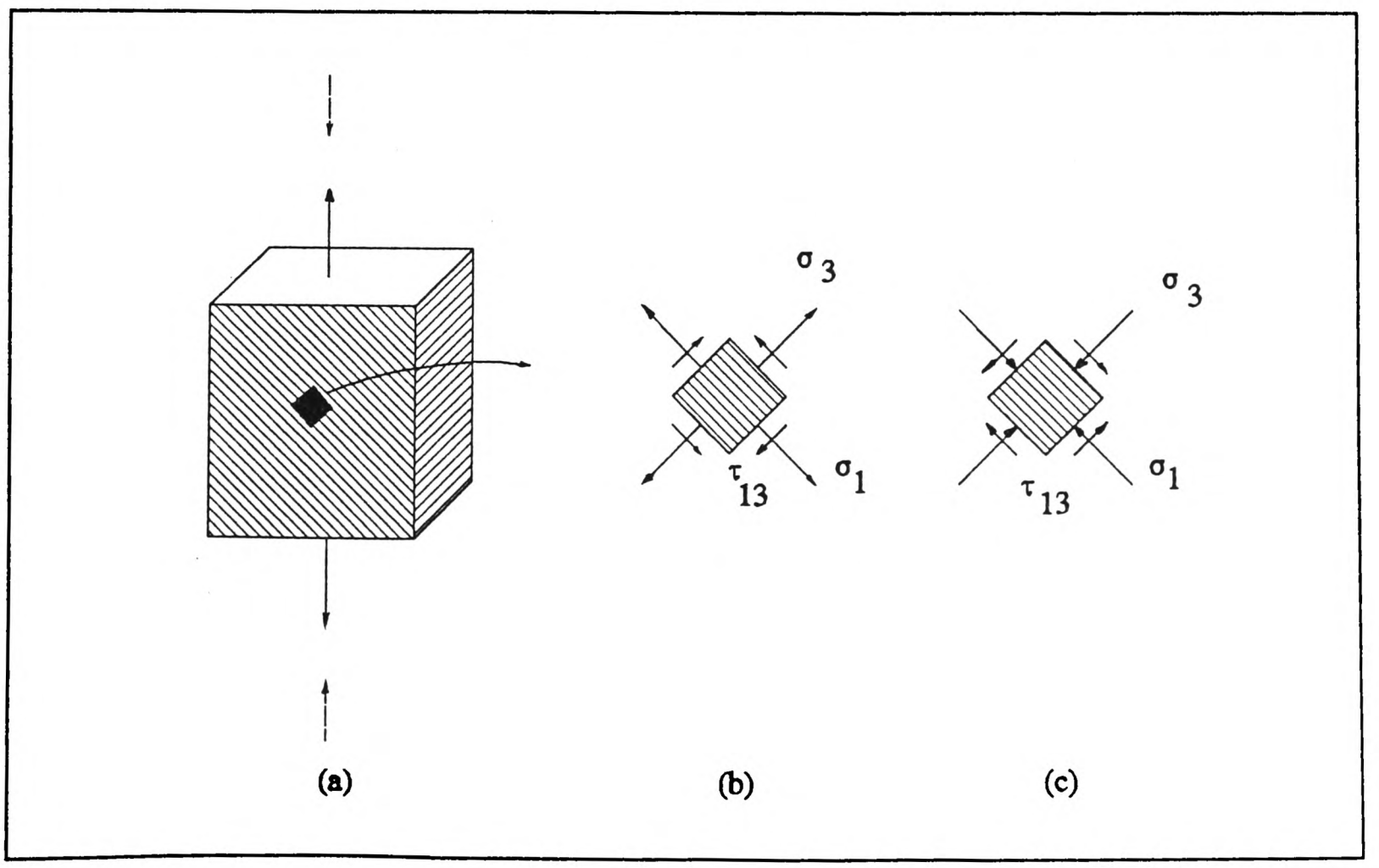

Figure 1.15 Oblique test.

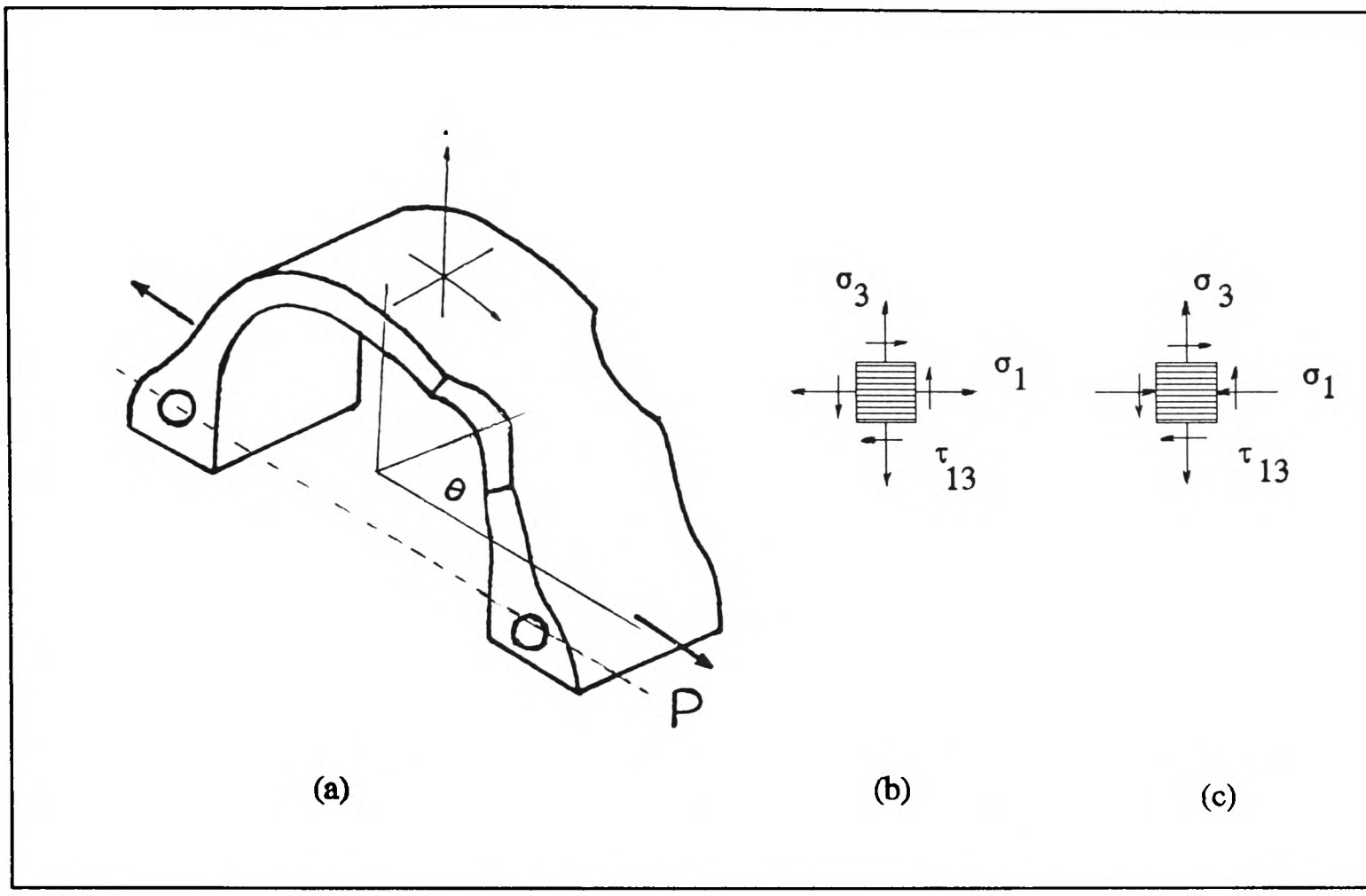

Figure 1.16 Waisted C-specimen test.

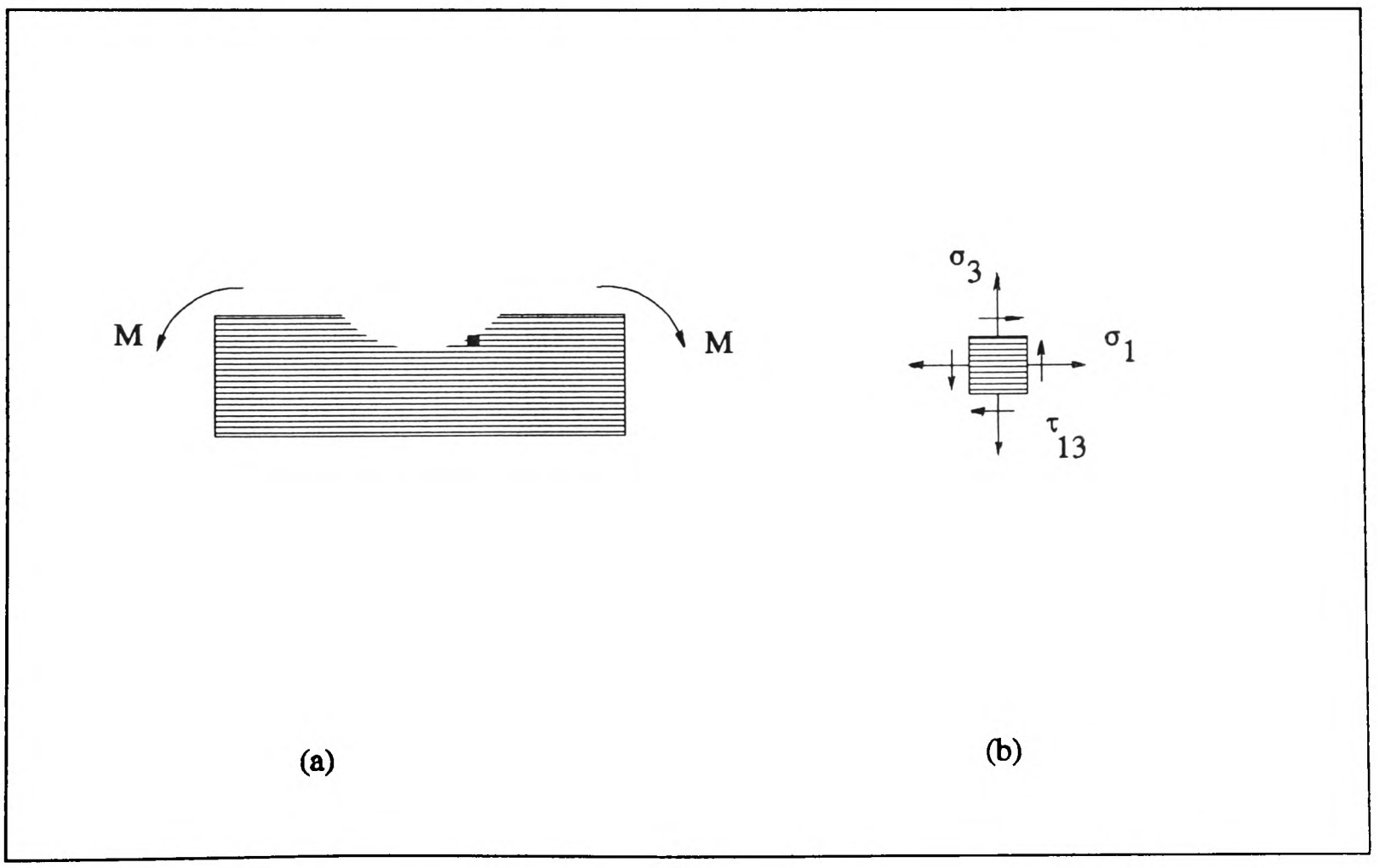

Figure 1.17 Central Notched Beam under four-point bending test.

Chapter 2

OBLIQUE UNIAXIAL LOADING TESTS

2.1 GENERAL DESCRIPTION OF THE TEST

The oblique uniaxial loading configuration is derived from the off-axis uniaxial loading test for a UD lamina as shown in Fig.2.1, where the loading axis is at an angle θ to the fibres. The stresses in the principal material directions are obtained by transformations as (Tsai, 1968),

$$\sigma_1 = \frac{\sigma}{2}(1+\cos 2\theta)$$

$$\sigma_2 = \frac{\sigma}{2}(1-\cos 2\theta) \qquad (2.1)$$

$$\tau_{12} = \frac{\sigma}{2}\sin 2\theta$$

Loading the through-thickness specimen at an angle to the plies in tension or compression, the combined through-thickness stress state consisting of $\sigma_1(+)$ - $\sigma_3(+)$ - τ_{13} or $\sigma_1(-)$ - $\sigma_3(-)$ - τ_{13} can be obtained as illustrated by Figs.2.2 & 2.3 respectively and expressed by the previous equations.

2.2 SPECIMEN

2.2.1 Materials

Two material systems were used, namely carbon fibre fabric preimpregnated with epoxy

(C/epoxy) and glass fibre fabric reinforced transparent epoxy (G/epoxy).

While woven C/epoxy composite is the most widely used material system in industry, transparent G/epoxy provides a laboratory material to investigate visually the delamination process.

2.2.2 Manufacture of Thick Laminate Panel

In order to make oblique test specimens a much thicker (about 20mm) plate was required. A thick plate not only means more work in the lab but also different manufacturing methods than for a thin plate.

a) C/epoxy

The C/epoxy laminate was made of prepregs supplied by Rolls-Royce (MSRR 9411). Eighty plies of C/epoxy prepreg were piled up and covered both on top and bottom by bleed cloths in order to get a desired fibre volume fraction, here altogether 30 plies of MSRR 9126 glass cloth bleed being used as recommended by Rolls-Royce. The prepreg bulk was firstly put into an autoclave with only pressure and vacuum (no heat) to get rid of any air bubbles (Fig.2.4). In order to achieve full wetting of the fibres by the resin for this thick panel, a specially designed autoclave curing cycle suggested by Rolls-Royce was followed (Table 2.1). The finished thick panel was examined by C-scanning[1] and a uniform quality, without conspicuous defects, was revealed (Fig.2.5) . The measured fibre fraction (V_f) (see Appendix 2A) was 50%.

[1] C-scan is a kind of ultrasonic inspection technique, which is a plan view of returned signals from a given range thickness. Conventionally, the C-scan is a binary display where the information above a certain threshold is shown in graduated shade scales (Doherty, 1987).

Table 2.1 Recommended Autoclave Cycle for Thick C/Epoxy Panel

Temperature Profile

1st Ramp from ambient temperature to 95°C at 5°C/minute.
1st Isothermal dwell at 95°C for 15 minutes.
2nd Ramp from 95 to 135°C at 2°C/minute.
2nd Isothermal dwell at 135°C for 60 minutes.
3rd Ramp from 135 to 190°C at 2°C/minute.
3rd Isothermal dwell at 190°C for 240 minutes to achieve full cure.

Pressure Profile

50 psi from start until the end of the 1st isothermal dwell.
100 psi until the start of the 2nd isothermal dwell.
200 psi until the end of the process.

b) G/epoxy

The G/epoxy laminate was made directly from glass fabric and liquid resin. The fabric was Y0227 (8 end satin) supplied by Courtaulds Advanced Materials and the resin was Stag Epoxide Resin 300 (Epikote 828) together with NMA (Nadic Methyl Anhydride) and K61B accelerator supplied by Stag Polymer & Sealants Ltd. Eighty plies of fabric were used and the manufacturing process was as follows (Boniface, 1993):

1) mix epoxide/NMA/K61B in the proportion of 100g/60g/4ml then de-gas in vacuum oven at 50°C for approximately 20-25 minutes.

2) apply resin to glass fabric (with a brush) and place laminate in vacuum chamber to wet out thoroughly at room temperature for approximately 10-15 minutes.

3) expel any residual entrapped air by squeezing excess resin using a flat blade.

4) cover with bleed cloths.

5) cure for 3 hours at 100°C in an autoclave with pressure of about 20-30 psi.

6) post-cure for 3 hours at 150°C.

The final transparent panel showed a fairly good quality without visual defects. The measured

V_f = 55%.

2.2.3 Specimen Geometry

The specimens were cut from thick laminate panels as shown in Fig.2.6 and identified by their ply angle θ relative to the loading axis.

For the compressive test, specimens were cut into a cuboid (Fig. 2.7). Only the C/epoxy material was tested in this form. Seven groups of specimens were tested with ply angles from 10.6° to 90° (see Tables 2.2, 2.3 and 2.4).

For the tensile test, specimens were machined into a dog-bone shape (Fig. 2.8) with both C/epoxy and G/epoxy material systems being used. Six groups of specimens (ply angles from 20° to 90°) were tested for each of the materials, all specimens having the same section dimensions of 5 x 5 mm. Because of the limitation of laminate plate thickness, it is difficult to make all the specimens with the same gauge length d. Instead, the gauge length changes with the ply angle so as to cover at least one ply (see Tables 2.5 and 2.6).

Aluminium tabs were glued to each end of the dogbone specimen using "EccoBond" adhesive supplied by Rolls-Royce (Fig.2.9). According to the manufacturer's recommended curing cycle, glued specimens were cured for 6 hours at 120°C.

2.3 STRESS ANALYSIS BY MOIRÉ INTERFEROMETRY

The oblique test is based on the assumption that a uniform stress distribution exists along the

plies of the specimen if a uniform load is applied. In order to verify this assumption, the Moiré interferometry technique was performed on compressive oblique specimens only, because of the considerable difficulty in conducting a Moiré interferometry test on the tensile oblique configuration. However, any conclusions from this method should apply to tensile oblique specimens also, because the gauge length is long enough to secure failure within the gauge, and the dogbone shape effect can be ignored.

The main advantages of the Moiré interferometry technique are that it can provide a whole-field measurement of in-plane displacements, and that the displacement sensitivity can be as high as submicron magnitude. Therefore it is particularly suitable for strain measurement of composite materials where local effects such as interfacial phenomena are often difficult to model using a numerical technique (Post, 1987).

The principle of Moiré interferometry is depicted in Fig. 2.10. A crossed-line diffraction grating of frequency f/2 (lines per mm) is firmly attached to the specimen. When loads are applied to the specimen, the grating moves and deforms together with the specimen surface. Two beams of coherent light, A_1 and A_2, illuminate the specimen grating obliquely from angles α and $-\alpha$, producing walls of constructive and destructive interference. These function as a reference grating, or virtual grating, of frequency f, which interacts with the horizontal set of lines of the specimen grating to form a Moire fringe pattern, which represents the displacement component in the vertical direction (y in Fig.2.10) on the specimen surface, as a contour map of equal-displacement fringes. Similarly, the displacement field in the horizontal direction (x in Fig.2.10) is produced by two coherent beams B_1 and B_2. Quantitatively, for each point in the fringe pattern,

$$U_x = \frac{1}{f} N_x \qquad U_y = \frac{1}{f} N_y$$

where u_x, u_y are components of displacement in the x and y directions respectively; N_x, N_y are fringe orders when lines of the reference grating are perpendicular to the x and y directions respectively; and f is the frequency of the reference grating. After obtaining the displacement fields the strains can be obtained by using the following equations,

$$e_y = \frac{\partial u_y}{\partial y} \quad e_x = \frac{\partial u_x}{\partial x} \quad e_{xy} = \frac{\partial u_y}{\partial x} + \frac{\partial u_x}{\partial y}$$

The test arrangement in Oxford UTC consists of a He-Ne laser light and a reference grating frequency f of 2400 lines/mm, which corresponds to a sensitivity of 0.417 m per fringe order. The fringe patterns are collected by a CCD camera using an image objective lens that performs dual functions as a decollimating lens and an objective lens: it collects all the light that emerges essentially normal to the specimen surface and it focuses the specimen surface onto the CCD image sensor consisting of a scanned array (512 X 512 pixel) of light sensitive silicon, with processing hardware to convert the scanned output to an analogue video signal format. The signals are then recorded and analyzed using an IBM or compatible PC with automated image processing software to obtain fringe patterns and three-dimensional strain maps (Poon, 1991).

Compressive oblique C/epoxy specimens were tested using the Oxford UTC setup. The method for producing the specimen grating is by a replication process illustrated in Fig.2.11, as follows: (a) An ultra-thin reflective coating of aluminium is deposited on the master mould containing a crossed-line grating. (b) A small amount of liquid epoxy adhesive is poured on

the specimen and squeezed into a thin film by pressing against the mould. (c) After curing, the mould is prised off leaving a reflective diffraction grating bonded to the surface of the specimen. The specimen tested had a ply angle of 51° and the grating was fixed in the middle of the specimen as shown in Fig.2.12. The measured Moiré Interferometry fringes are shown in Fig. 2.13. Fig.2.14 represents the calculated strain distribution maps, which show a peak and valley form caused by interface and ply respectively. However it can also be seen from these figures that the normal and shear strains are generally uniform along the ply direction, which indicate the uniform stress distributions along ply direction.

2.4 TEST PROCEDURE

The experiments were conducted using an INSTRON testing machine with load-displacement recorder to monitor the process. The cross-head speed was 1 mm/minute. It was envisaged that misalignment is a very important factor in terms of the experimental accuracy for both compressive and tensile tests. Therefore, for tensile tests, universal fixtures were used to minimise misalignment; for compressive tests, in addition to improving the dimensional accuracy of specimens, much care was paid to align the experiment set-up.

For each group of test, there are usually three specimens. However, as it is difficult to avoid pre-test damage of specimens, and in this case, the damaged specimens are rejected. But for each group the minimum number of specimens is two.

2.5 TEST RESULTS

2.5.1 Experimental Results From Compression Test

For $\theta=90^0$, the through-thickness compression strength was obtained; the test results are shown in Table 2.2. It was found that the through-thickness compressive strength was 961.1 MPa, with a standard deviation of 2.4%. The fracture surface showed a very complicated mixture of breakage of fibres and matrix (Fig.2.15(a)).

Six other groups of specimens with θ ranging from 10.6° to 80° were tested. Dimensions of the specimens are shown in Table 2.3. The experimental results for compressive failure stress vs. ply angle are shown in Table 2.4. For all the compressive oblique tests, a linear elastic deformation until failure was observed from the recorded load-displacement curves (Fig.2.16). The specimen failed abruptly, without showing any obvious pre-failure cracks. Failure consisted generally of delamination with break-down at one or several interfaces (Fig. 2.15(c,d)). The only exception was for the group 6 specimens with ply angle 80°, where failure was by delamination combined with breakage of fibres and matrix (Fig.2.15(b)).

Scanning electron microscope(SEM) examination was carried out for specimens with angle θ = 90°, 63° and 21° (Fig.2.17). It can be seen that the effect of the compressive interlaminar normal stress decreases when the angle changes from 90°, characterized by inclined matrix cracks and broken fibres, to 21^0, characterized by bare fibres and matrix debris.

2.5.2 Experimental Results from Tension Test

a) C/Epoxy

Six groups of tests were conducted with the angle θ ranging from 20° to 90°; the test results are shown in Table 2.5. Notice that when θ=90°, the pure interlaminar tensile strength was found to be 36.5 MPa, much lower than the compressive strength in Table 2.2. Load-displacement curves are shown in Fig.2.18, again revealing a linear elastic deformation prior to brittle failure. All tension specimens failed by delamination. The fracture surfaces of the specimens with angle θ=30°, 60° and 90° were examined by SEM (Fig. 2.19). From the micrographs a shear dominated failure featuring matrix voids (θ=30°) and a Mode I failure with bare fibres (θ=90°) can be recognized.

b) G/Epoxy

Six groups of specimens were tested with angle θ from 20 to 90°. The tests basically repeated those for C/epoxy. Fig. 2.20 and Table 2.6 give the load-displacement curves and test results respectively. Specimens were well illuminated during testing to observe visually any crack growth in the transparent matrix material. No pre-cracks were found before failure, which was a very sudden break down. SEM pictures were taken of the fracture surfaces of the specimens with angle θ=30°, 60° and 90° (Fig. 2.21). All pictures show very clean bare fibres, whilst the wrinkles on the resin change from being a very smooth face (θ=90°) to being very fine and dense (θ=30°).

Table 2.2 Interlaminar Compression Strength

Specimen No.	Dimensions L x W x H	Failure Load (kN)	Failure Stress (MPa)	Average Stress (MPa)	Standard Deviation
1	7.0 x 7.0 x 10.12	48.74	994.5	961.1	2.4%
2	6.97 x 6.98 x 10.12	45.73	940.0		
3	7.05 x 6.66 x 10.12	44.93	956.9		
4	7.05 x 7.05 x 10.12	47.37	953.0		

TABLE 2.3 Dimensions of Compressive Oblique Specimens

	SPEC. No.	DIMENSIONS L x W x H (mm)	PLY ANGLE (θ^0)
GROUP 1	1	10.04 x 8.19 x 9.91	10.6
	2	10.04 x 8.16 x 9.91	
	3	10.06 x 8.09 x 9.91	
GROUP 2	1	9.25 x 8.35 x 9.88	18.5
	2	9.10 x 8.50 x 9.88	
	3	8.74 x 8.43 x 9.88	
GROUP 3	1	9.50 x 7.50 x 9.82	21.0
	2	8.96 x 7.82 x 9.76	
GROUP 4	1	7.89 x 6.95 x 9.91	45.0
	2	7.64 x 6.95 x 9.91	
	3	7.89 x 6.95 x 9.91	
GROUP 5	1	8.26 x 7.13 x 9.91	63.0
	2	8.26 x 7.29 x 9.89	
	3	8.26 x 7.26 x 9.91	
GROUP 6	1	7.78 x 7.26 x 8.68	80.0
	2	7.57 x 7.10 x 9.18	
	3	7.57 x 7.08 x 9.30	

TABLE 2.4 Compressive Oblique Test Results

	SPEC. No.	PLY ANGLE (θ^0)	FAILURE LOAD (kN)	FAILURE STRESS (MPa)	AVERAGE FAILURE STRESS(MPa) AND DEVIATION	STRESS COMPONENTS(MPa)		
						σ_1	σ_3	τ_{13}
GROUP 1	1	10.6	-25.74	-313.0	-317.6 (2%)	-306.9	-10.8	57.4
	2		-26.82	-327.3				
	3		-25.45	-312.7				
GROUP 2	1	18.5	-11.62	-150.4	-207.9 (19%)	-233.8	-20.8	62.3
	2		-18.33	-237.0				
	3		-17.40	-236.2				
GROUP 3	1	21.0	-11.72	-164.5	-179.3 (8%)	-132.2	-22.4	59.2
	2		-13.60	-194.1				
GROUP 4	1	45.0	-13.42	-244.7	-248.4 (5%)	-124.1	-124.3	124.1
	2		-14.03	-264.2				
	3		-12.96	-236.3				
GROUP 5	1	63.0	-24.79	-420.9	-408.9 (6%)	-87.6	-321.3	167.5
	2		-22.72	-377.3				
	3		-25.70	-428.6				
GROUP 6	1	80.0	-41.52	-735.1	-746.4 (1%)	-20.5	-725.9	121.9
	2		-40.40	-751.7				
	3		-40.32	-752.3				

TABLE 2.5 Tensile Oblique Test Results for C/Epoxy

	SPEC. No.	GAUGE LENGTH (mm)	PLY ANGLE (θ^0)	FAILURE LOAD (kN)	AVERAGE FAILURE LOAD(kN) AND DEVIATION	FAILURE STRESS (MPa)		
						σ_1	σ_3	τ_{13}
GROUP 1	1	20	20	2.4674	2.7107 (12%)	95.8	12.7	34.8
	2			3.1959				
	3			2.4674				
GROUP 2	1	10	30	2.0585	1.9035 (8%)	57.2	19.1	30.6
	3			1.7484				
GROUP 3	1	7	45	1.6920	1.6074 (4%)	32.1	32.1	32.1
	2			1.4664				
	3			1.6638				
GROUP 4	1	5	60	1.4664	1.3755 (7%)	13.8	40.6	24.9
	2			1.2314				
	3			1.4288				
GROUP 5	1	5	75	1.0904	1.0904	2.9	40.7	10.9
GROUP 6	1	5	90	0.9118	0.9134 (0.2%)	0	36.5	0
	2			0.9149				

TABLE 2.6 Tensile Oblique Test Results for G/Epoxy

	SPEC. No.	GAUGE LENGTH (mm)	PLY ANGLE (θ^0)	FAILURE LOAD (kN)	AVERAGE FAILURE LOAD(kN) AND DEVIATION	FAILURE STRESS (MPa)		
						σ_1	σ_3	τ_{13}
GROUP 1	1	20	20	1.6203	1.8488 (9%)	65.3	8.7	23.8
	2			1.9799				
	3			1.9463				
GROUP 2	2	10	30	1.2176	1.3183 (8%)	39.6	13.2	22.9
	3			1.4190				
GROUP 3	1	7	45	1.0834	1.1074 (2%)	22.2	22.2	22.2
	2			1.1314				
GROUP 4	1	5	60	1.0019	1.0090 (2%)	10.1	30.3	17.5
	2			0.9897				
	3			1.0355				
GROUP 5	1	5	75	0.8581	0.8198 (4%)	2.2	30.6	8.2
	2			0.7862				
	3			0.8150				
GROUP 6	1	5	90	0.8102	0.7942 (2%)	0	31.8	0
	2			0.8006				
	3			0.7718				

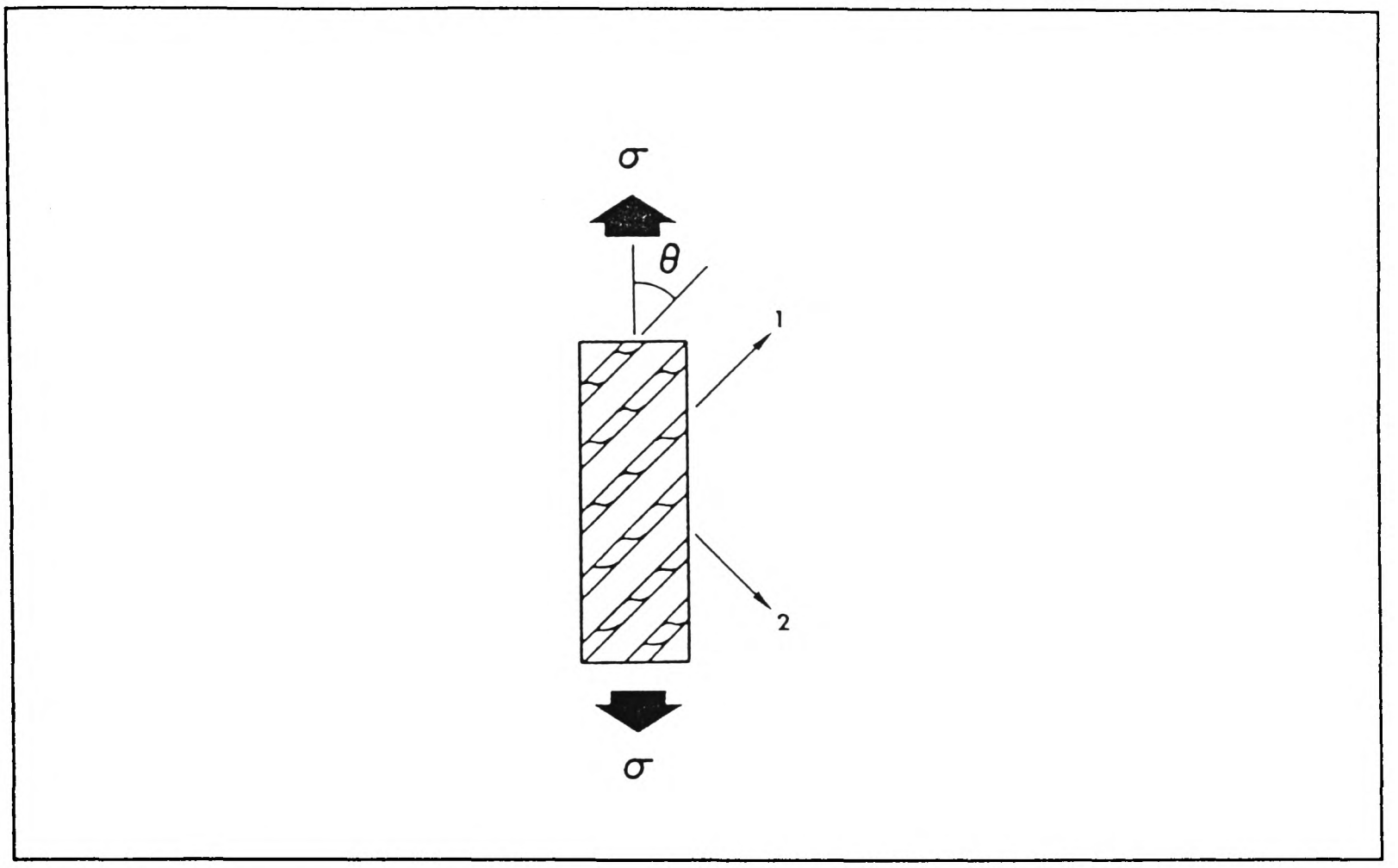

Figure 2.1 Off-axis uniaxial loading.

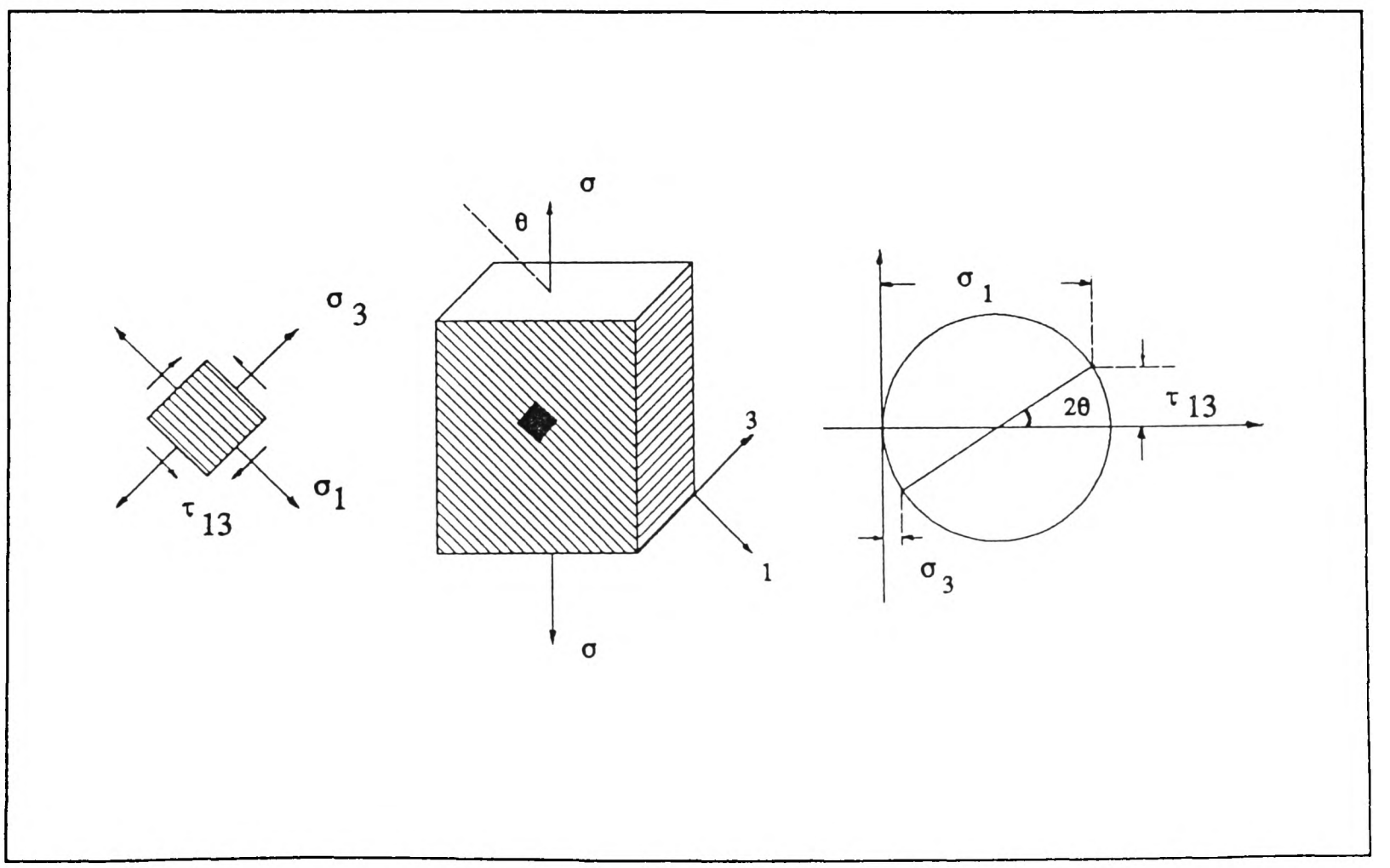

Figure 2.2 Tensile oblique test.

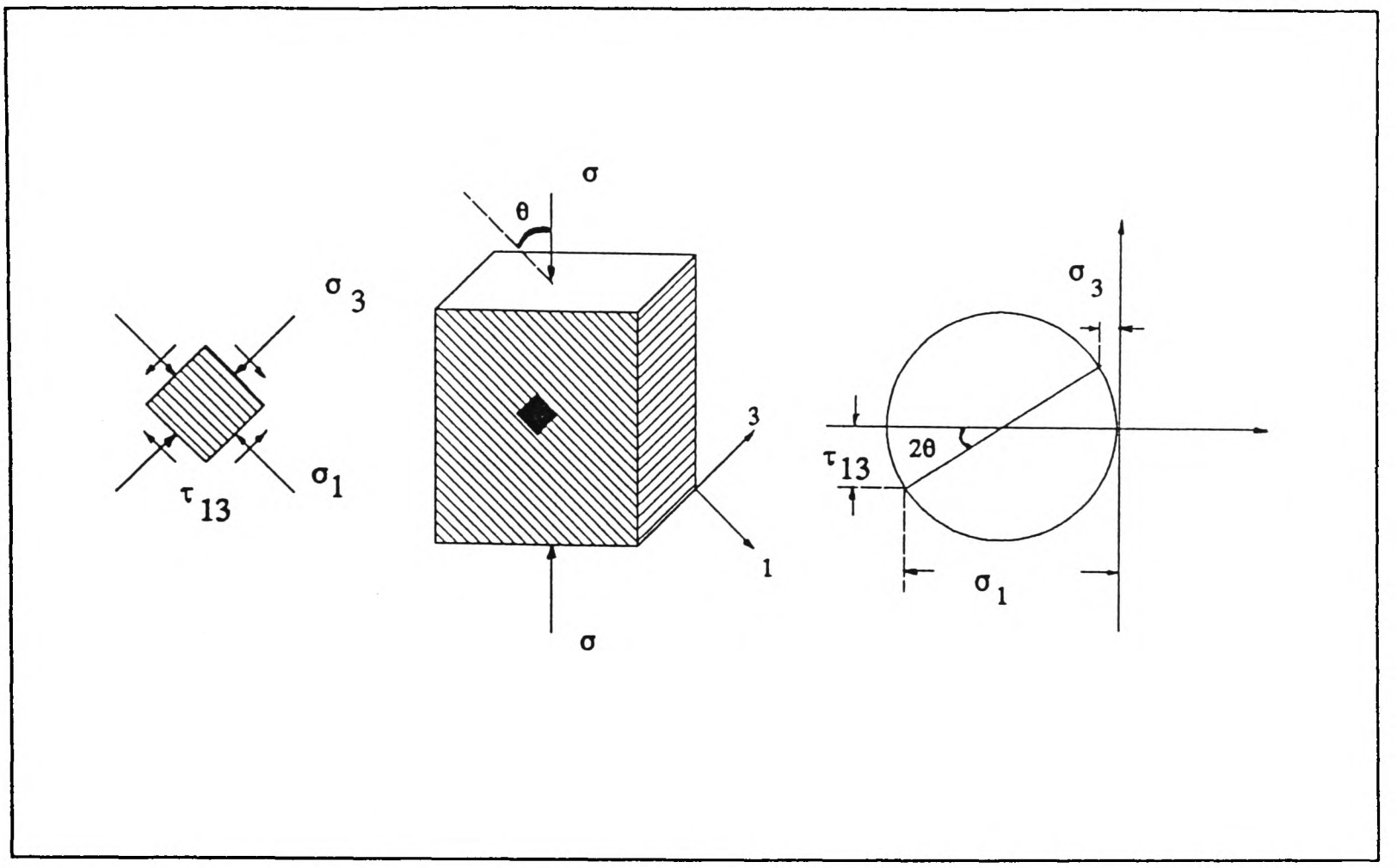

Figure 2.3 Compressive oblique test.

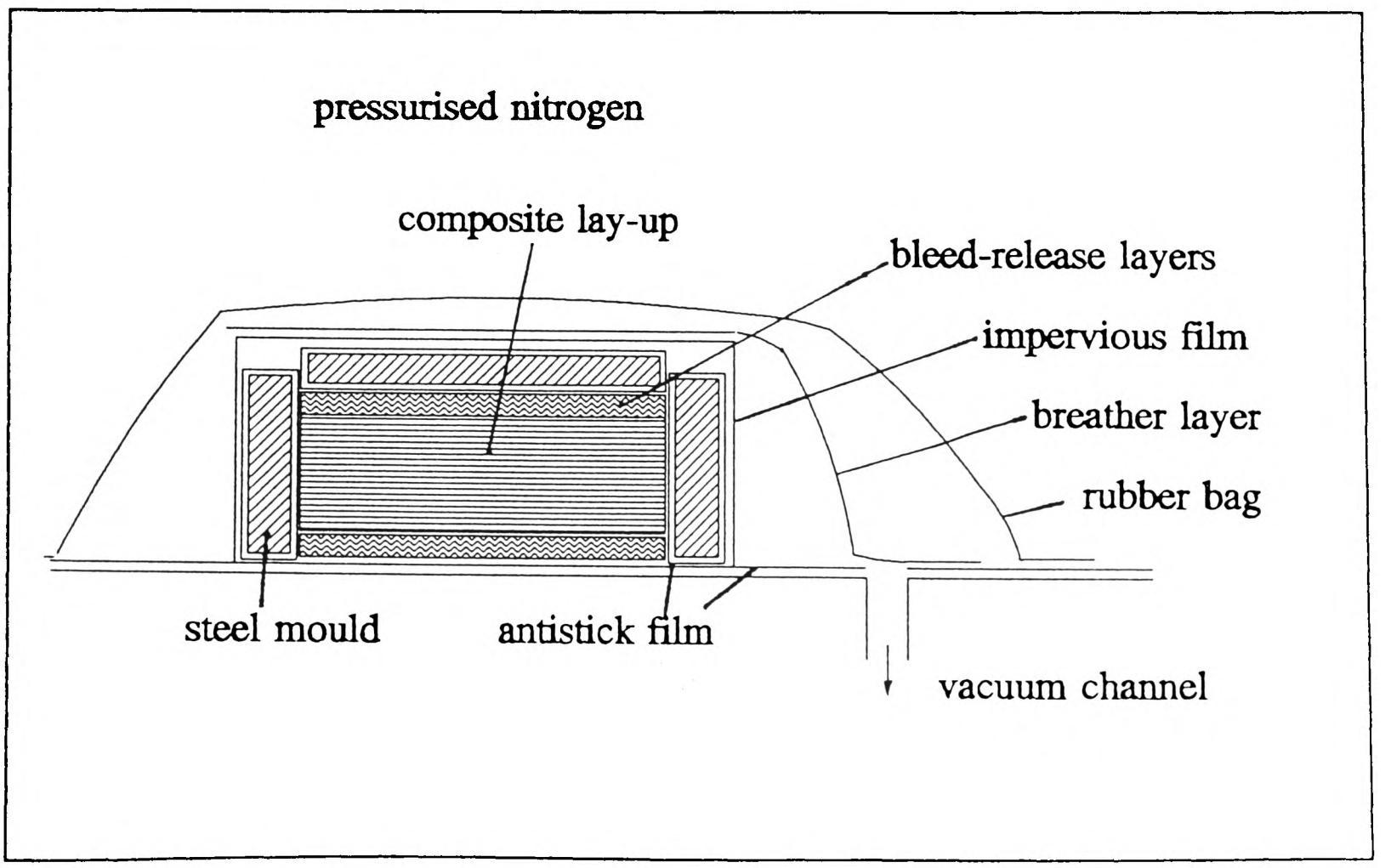

Figure 2.4 Autoclave.

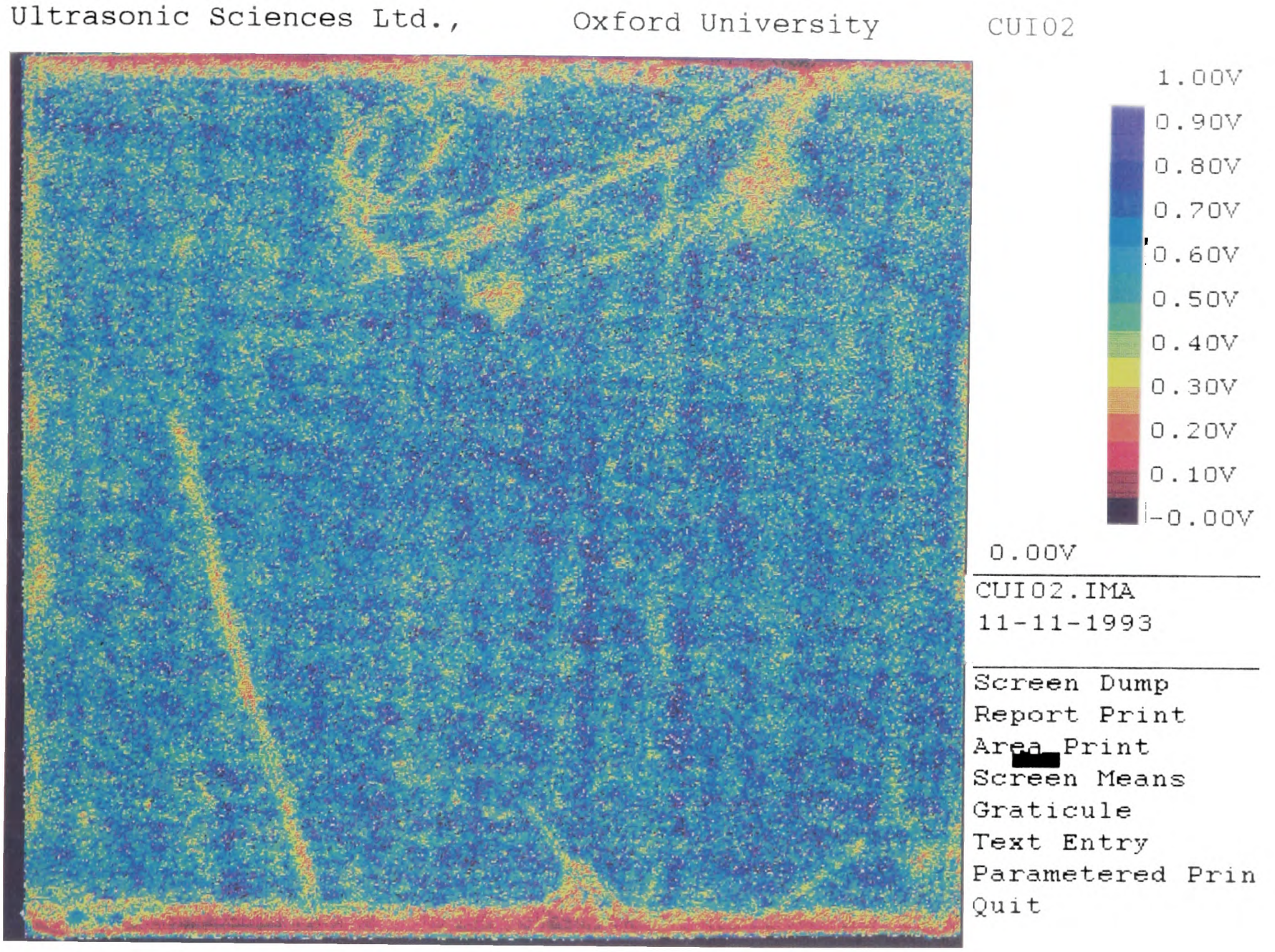

Figure 2.5 C-scanning picture of thick C/epoxy panel.

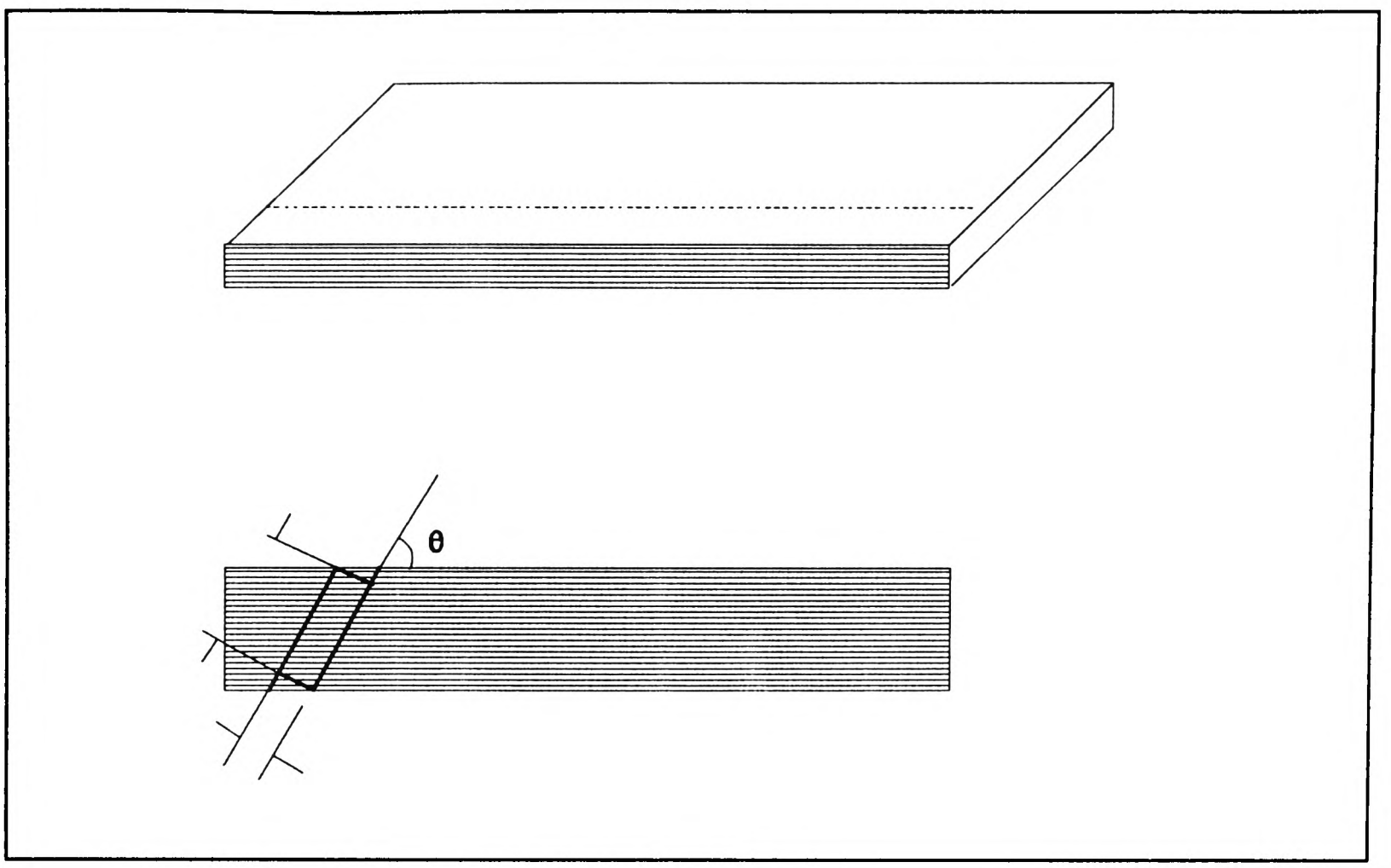

Figure 2.6 Uniaxial oblique specimen cutting from thick plate.

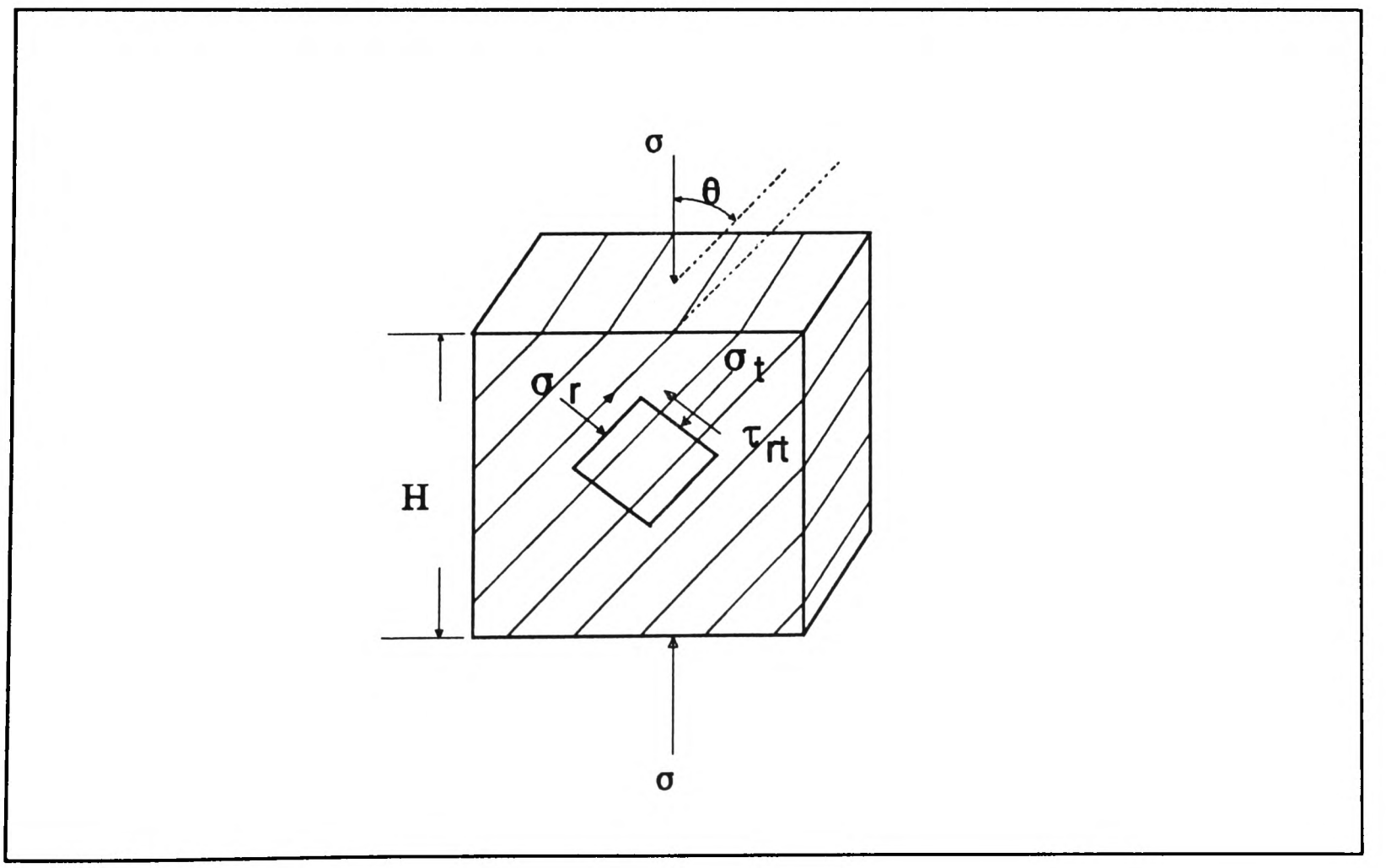

Figure 2.7 Compression oblique specimen.

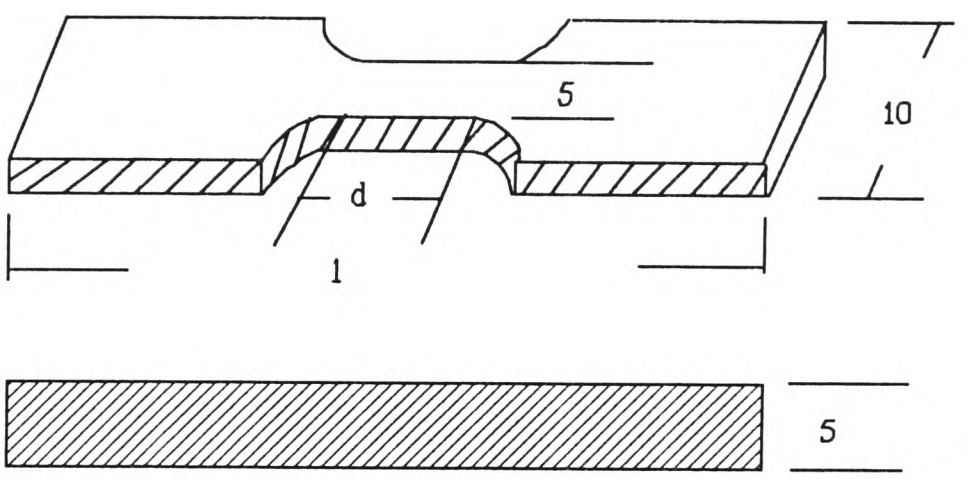

Figure 2.8 Tension oblique specimen.

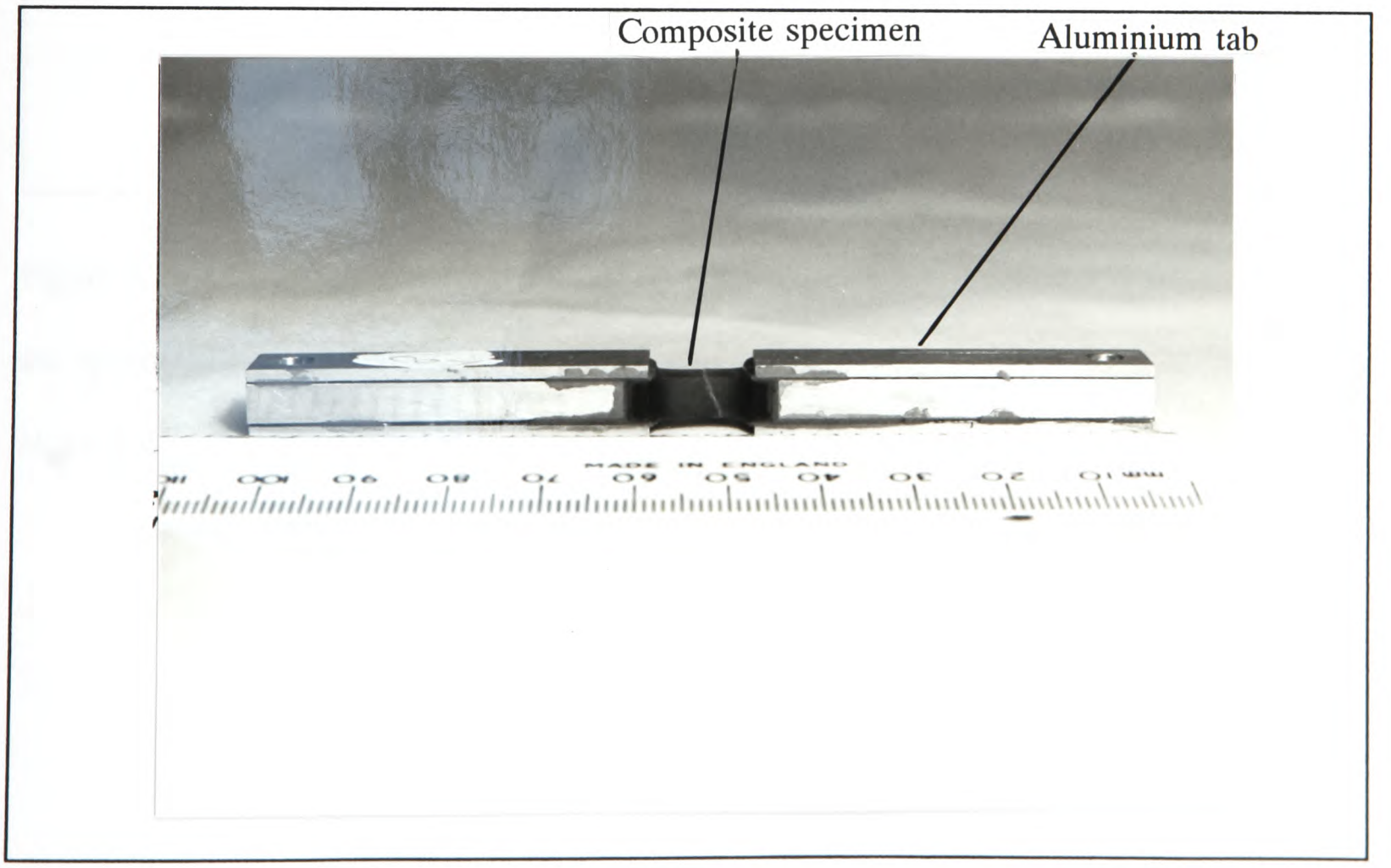

Figure 2.9 Tension oblique specimen with aluminium tabs.

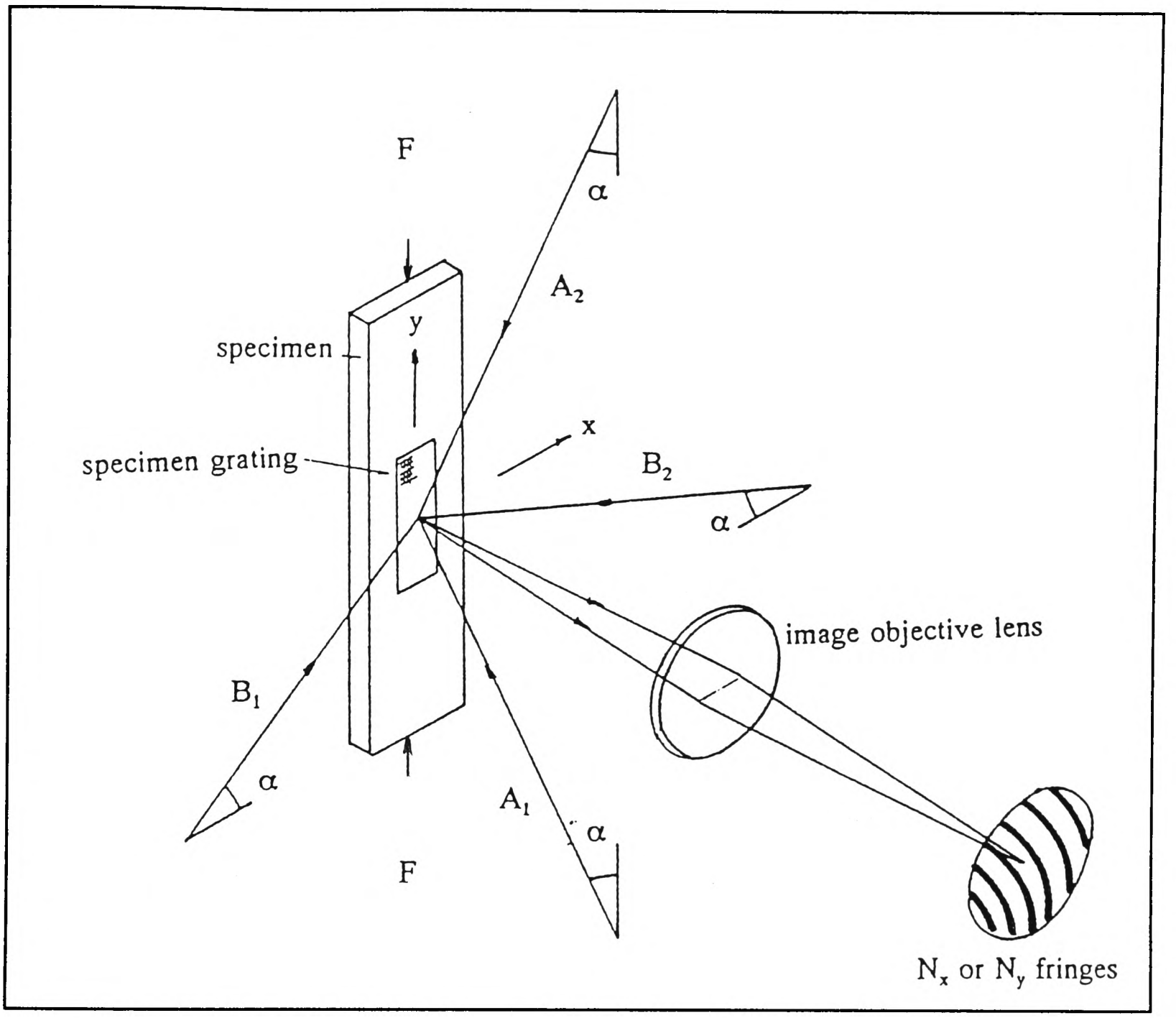

Figure 2.10 Optical system for Moire interferometry. Coherent beams A_1 and A_2 interact with the specimen grating to produce the N_y or v displacement pattern, B_1 and B_2 to produce the N_x or u displacement pattern.

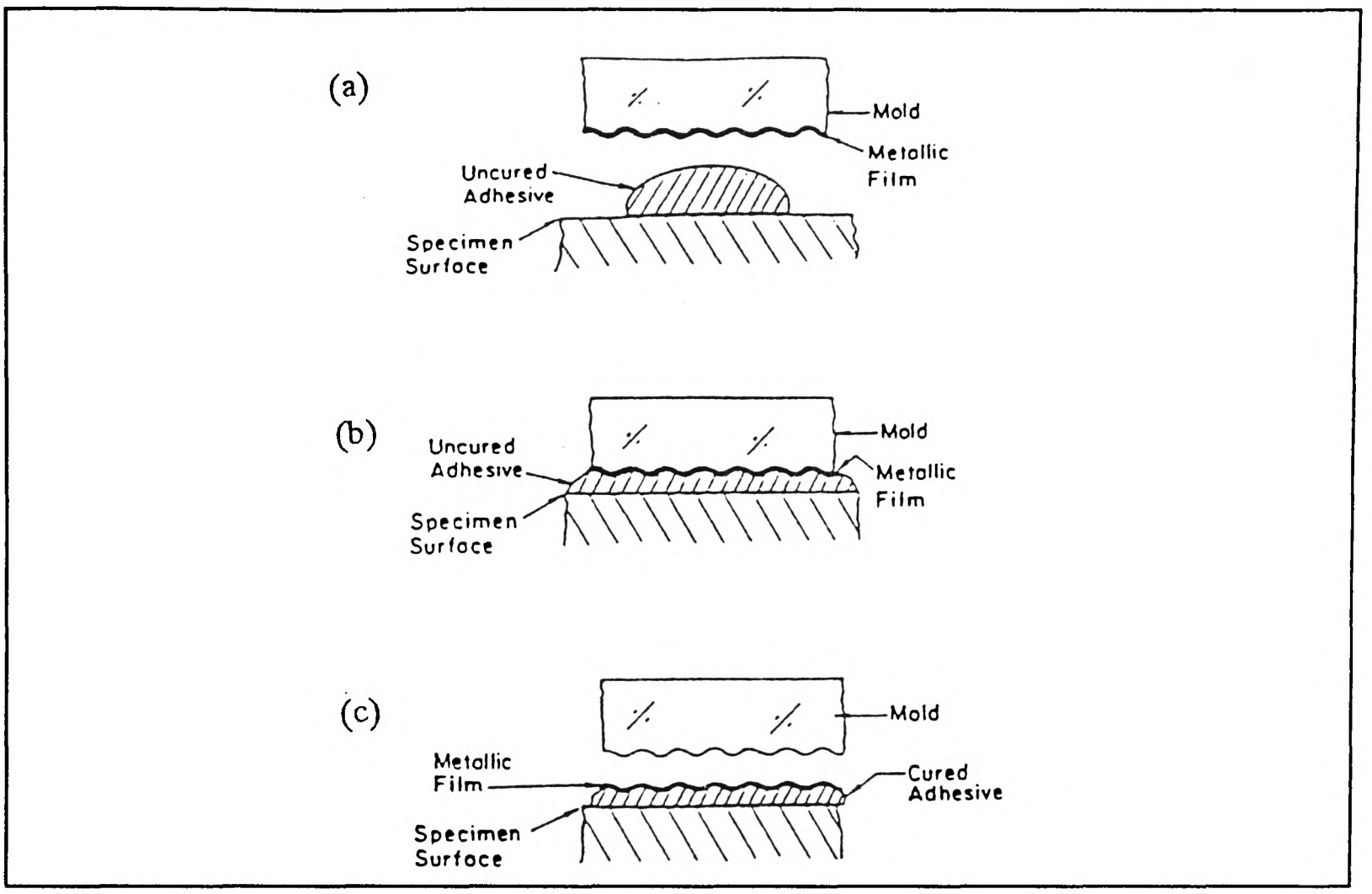

Figure 2.11 Steps in producing the specimen grating by a replication process.

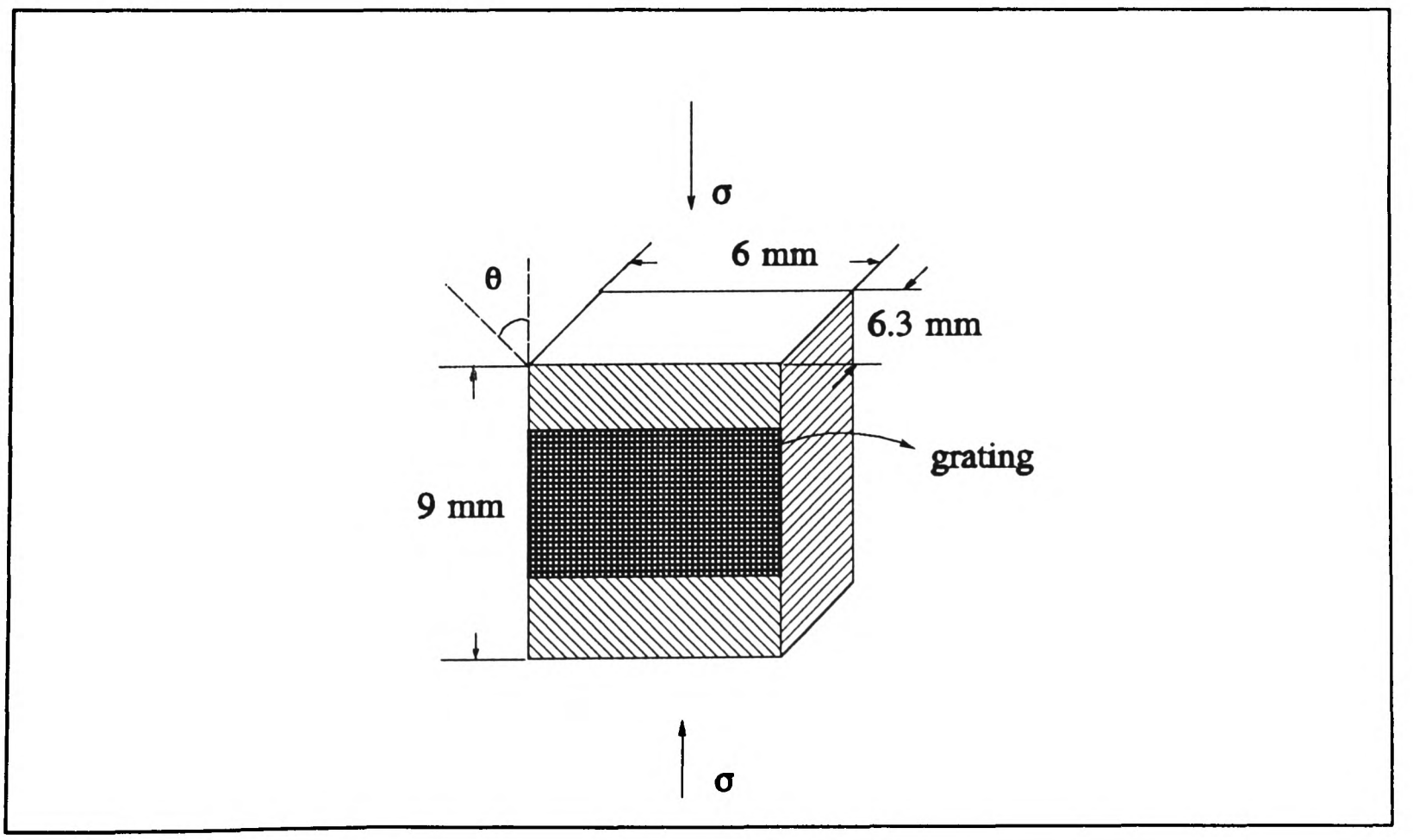

Figure 2.12 A compression oblique specimen with grating.

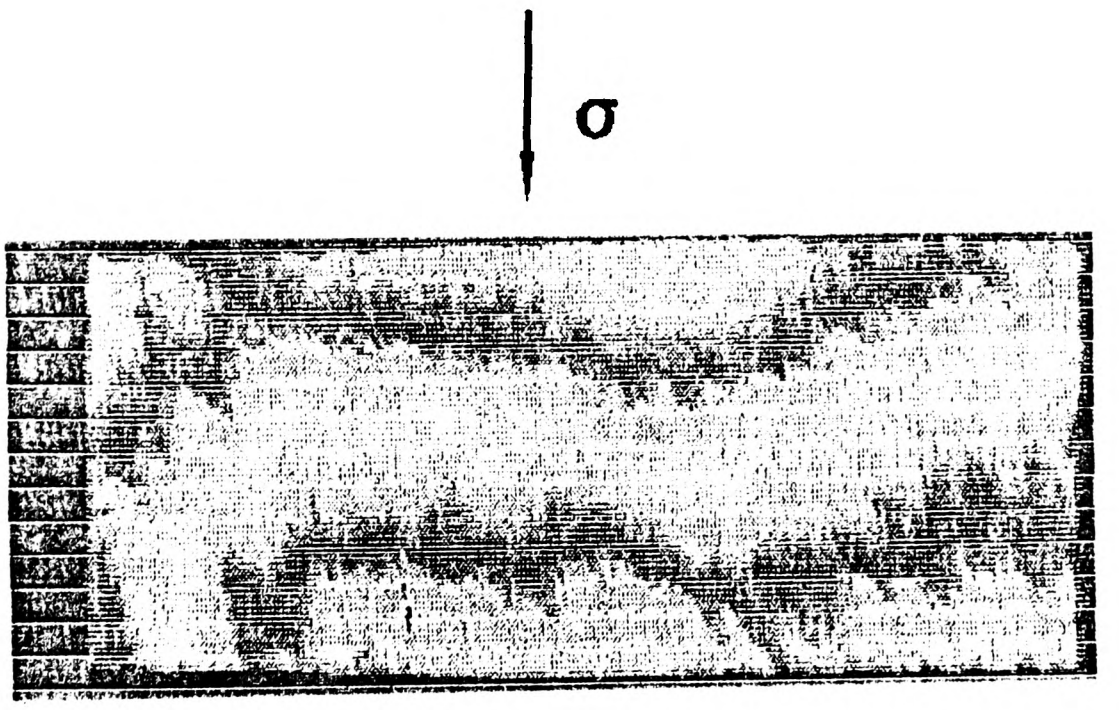

U_y (loading direction) - displacement

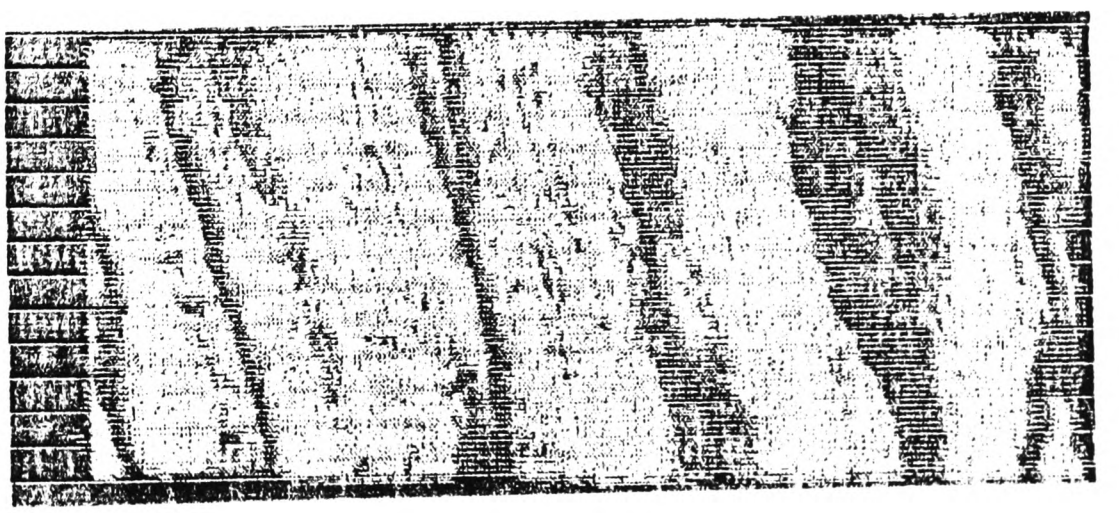

U_x - displacement

Figure 2.13 Displacement fringes of compression oblique specimen by Moire interferometry.

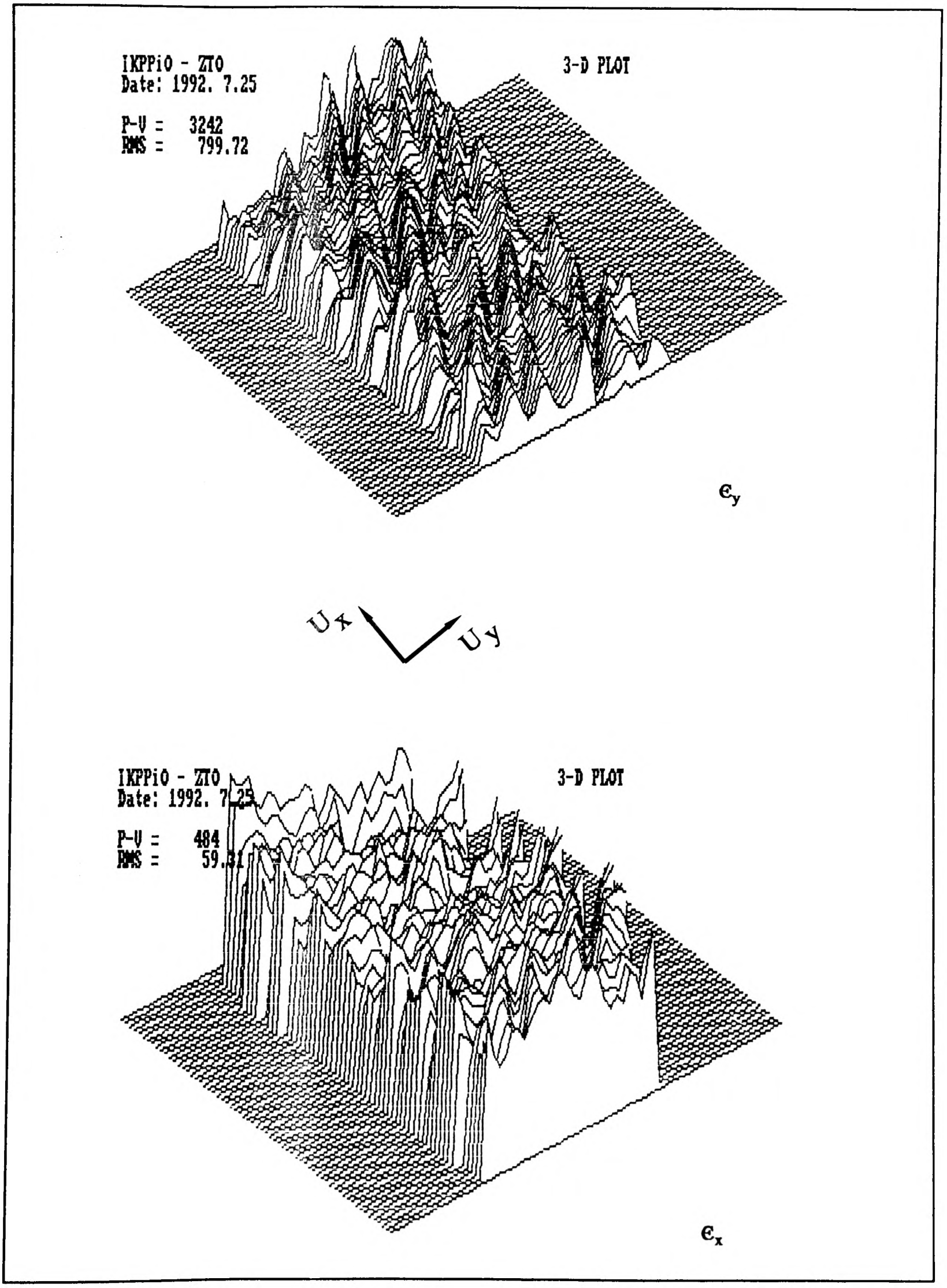
IKPPi0 - ZT0
Date: 1992. 7.25
P-V = 3242
RMS = 799.72
3-D PLOT
ϵ_y
Ux
Uy
IKPPi0 - ZT0
Date: 1992. 7.25
P-V = 484
RMS = 59.31
3-D PLOT
ϵ_x

Figure 2.14

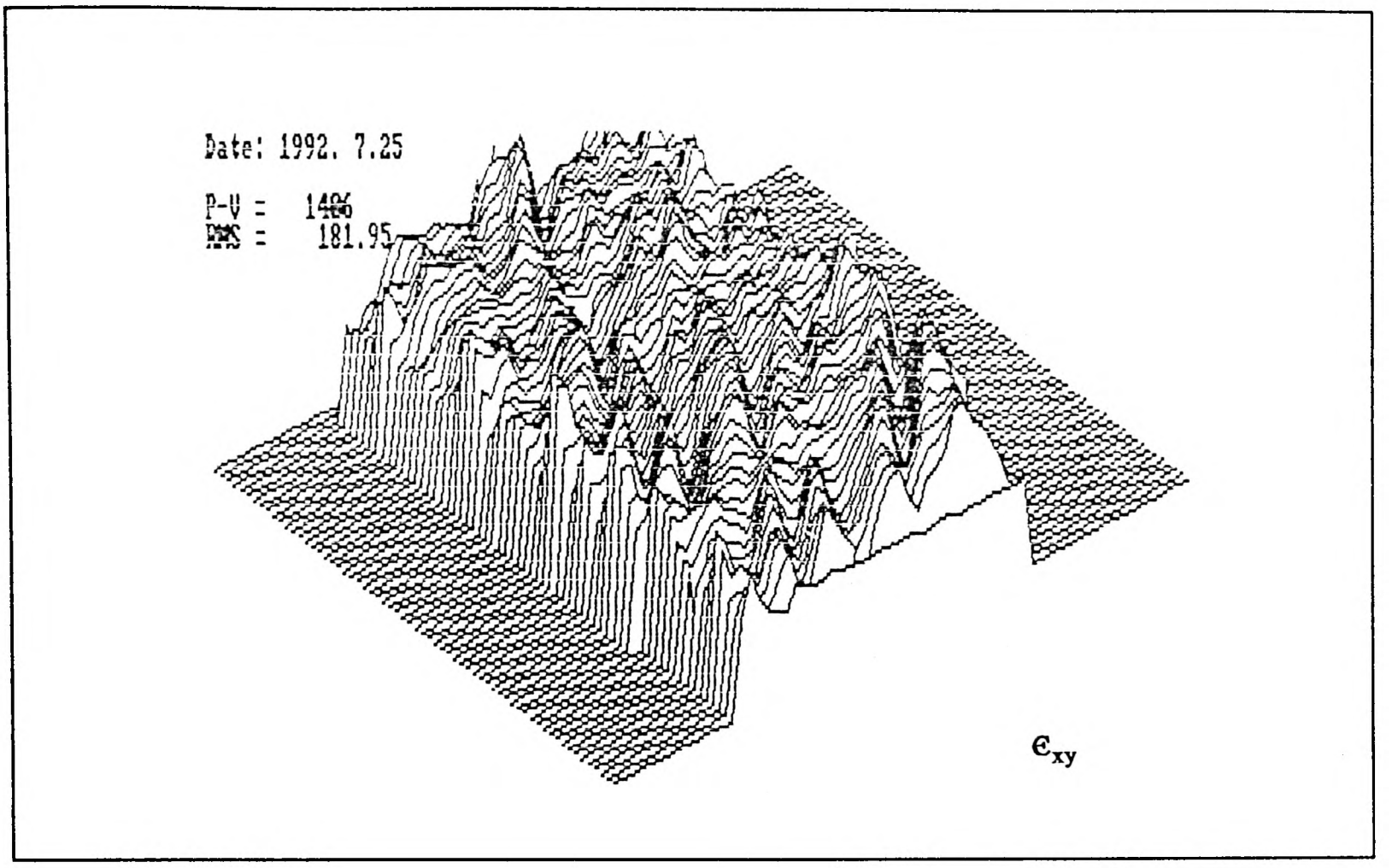

Figure 2.14 Strain distribution of compression oblique specimen by Moire interferometry.

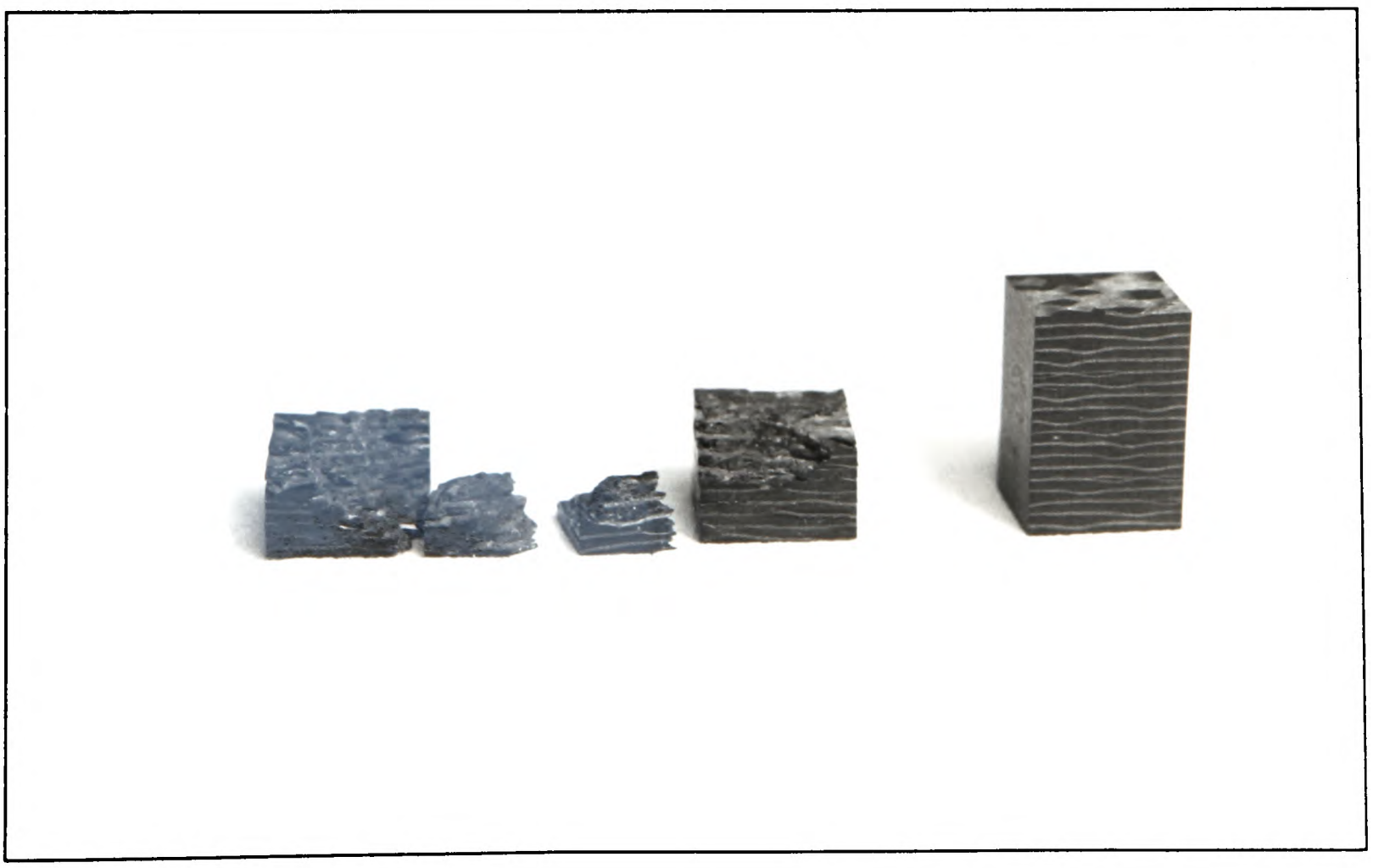

Figure 2.15 (a) $\theta=90^{\circ}$

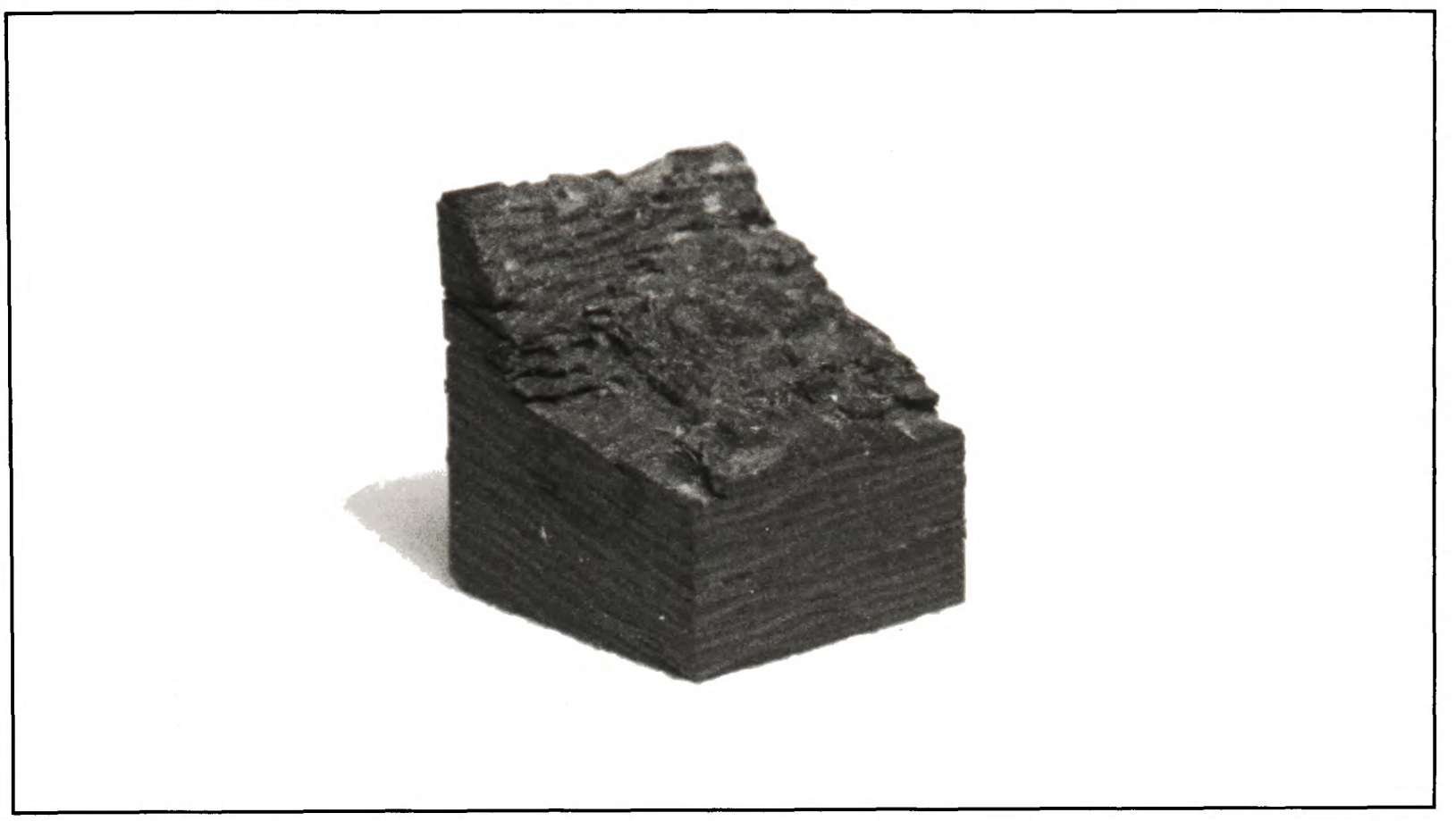

Figure 2.15 (b) $\theta=80^{o}$

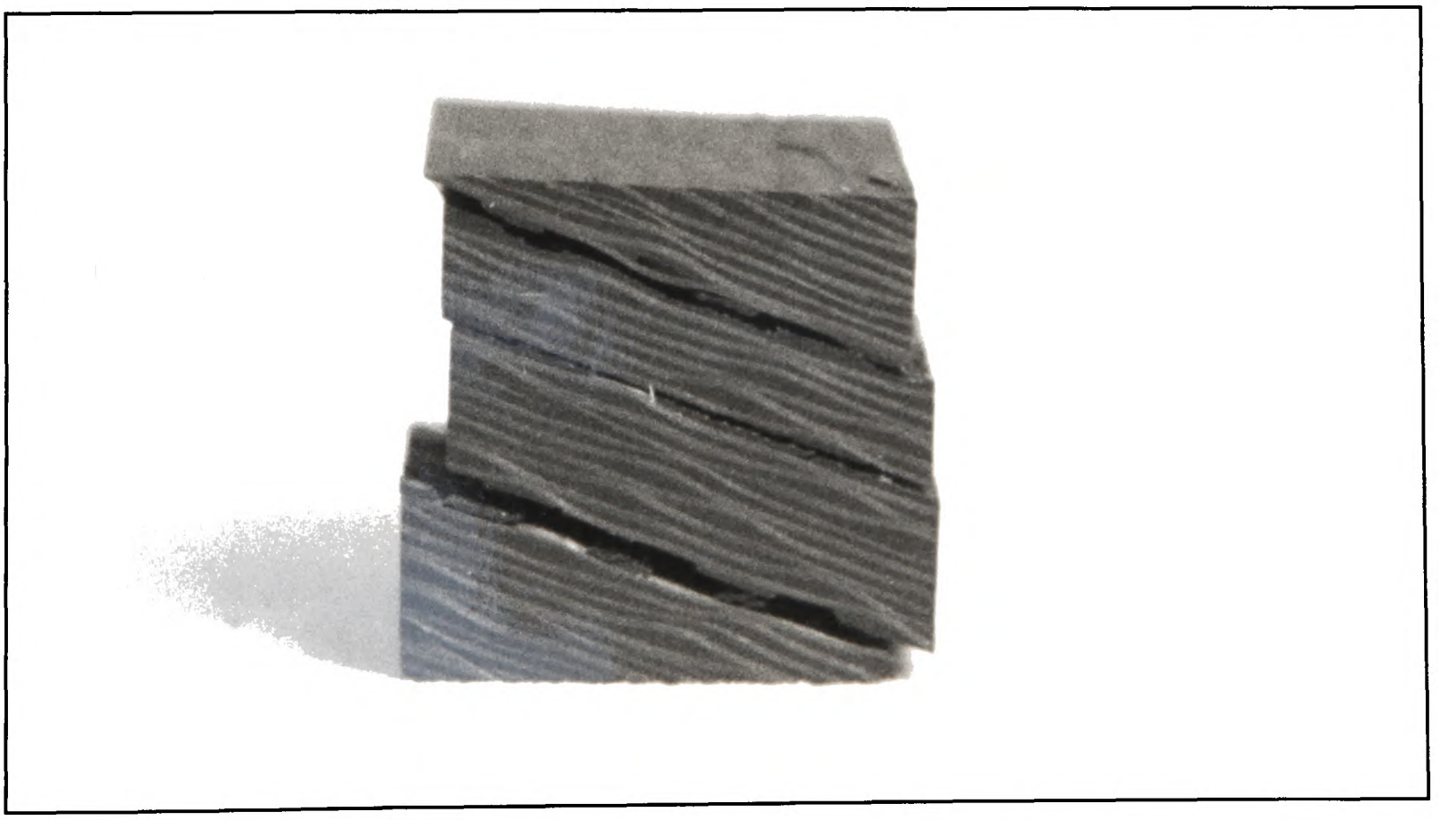

Figure 2.15 (c) $\theta<63^{0}$

The broken C/epoxy compression oblique specimens. (a) break-down of fibres and resin; (b) similar with (a); (c) delamination.

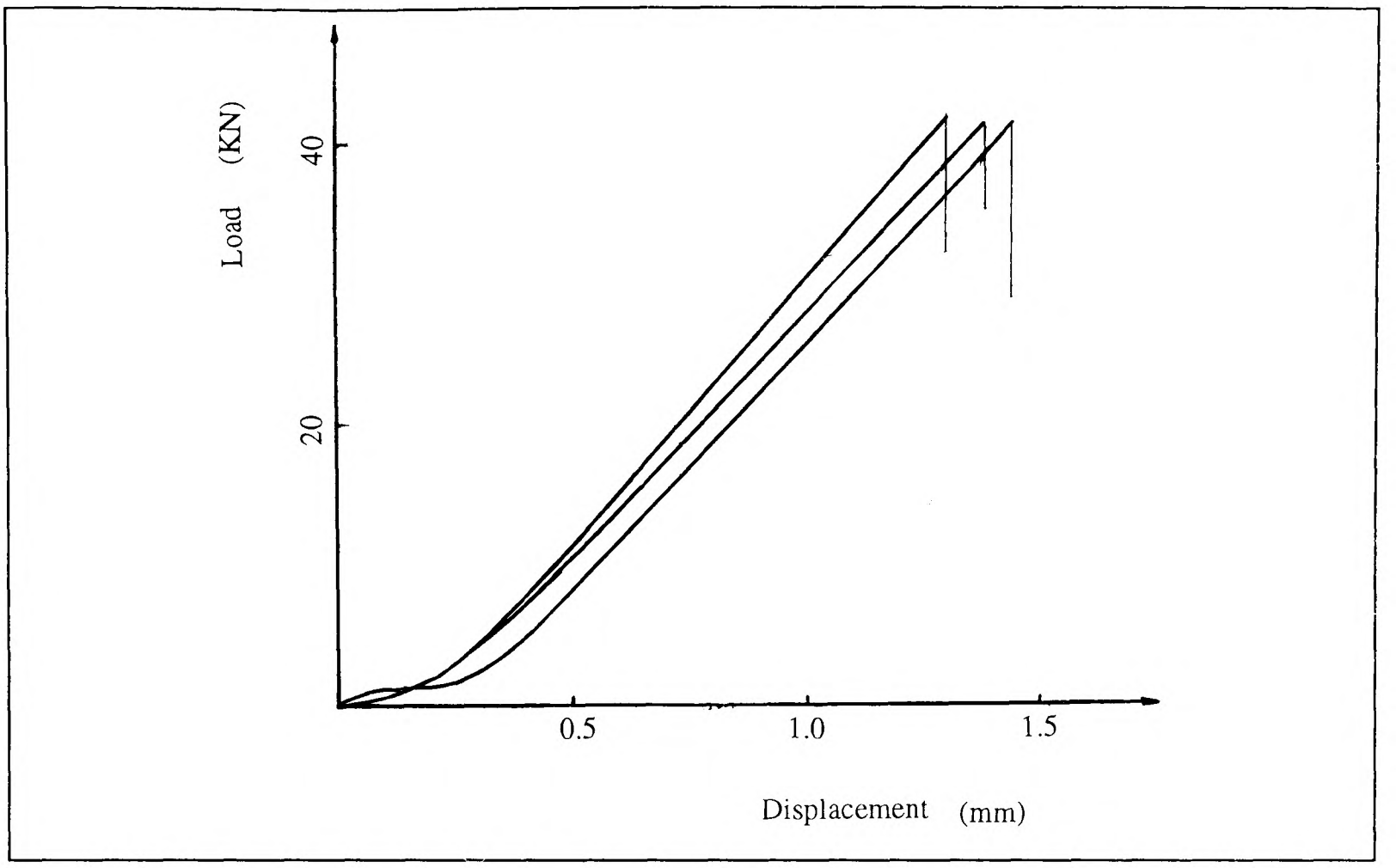

Figure 2.16 The load-displacement curves for C/epoxy compressive oblique tests (Table 2.4, group 6).

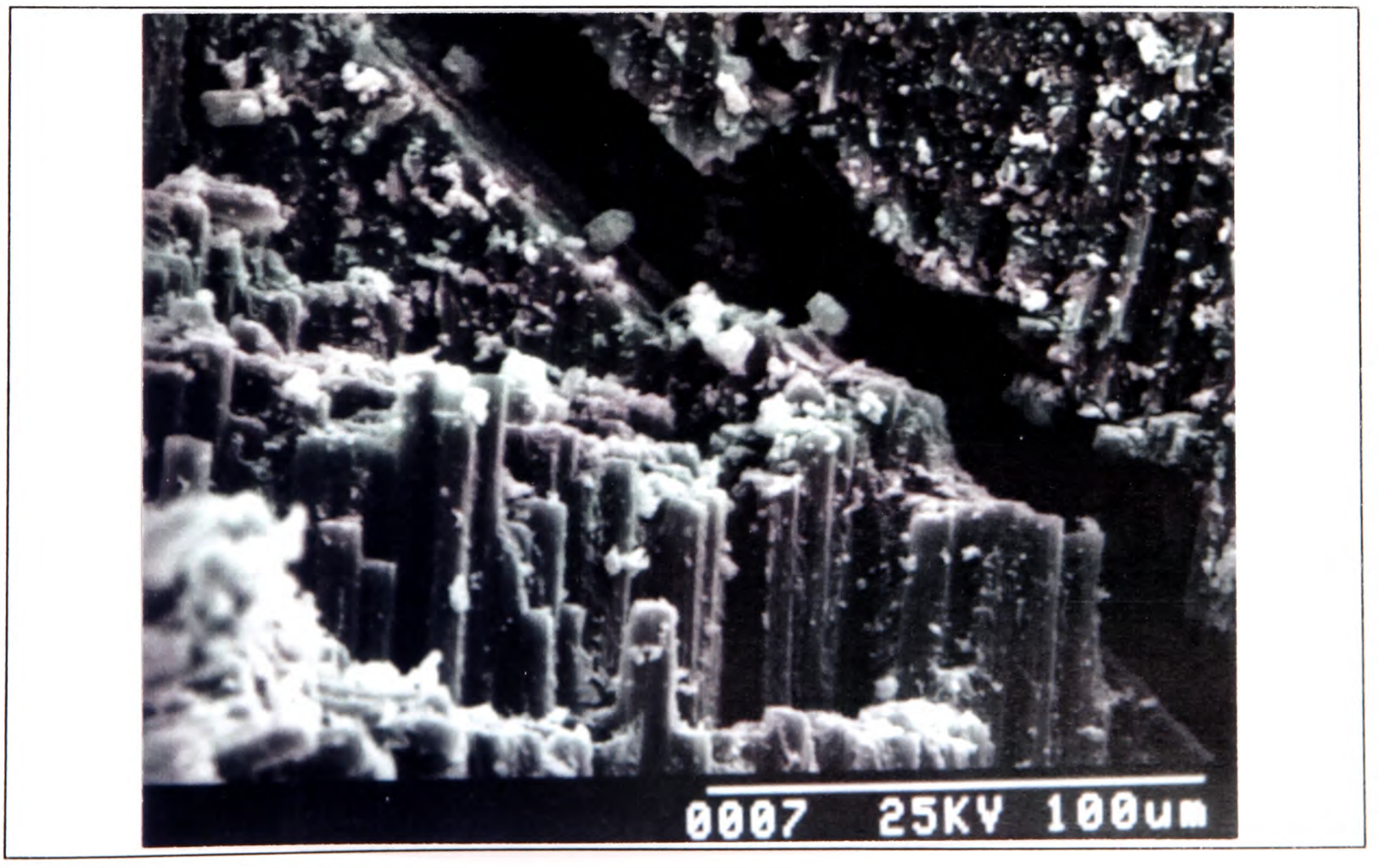

Figure 2.17 (a) $\theta=90^{o}$

Figure 2.17 (b) $\theta=60^{\circ}$

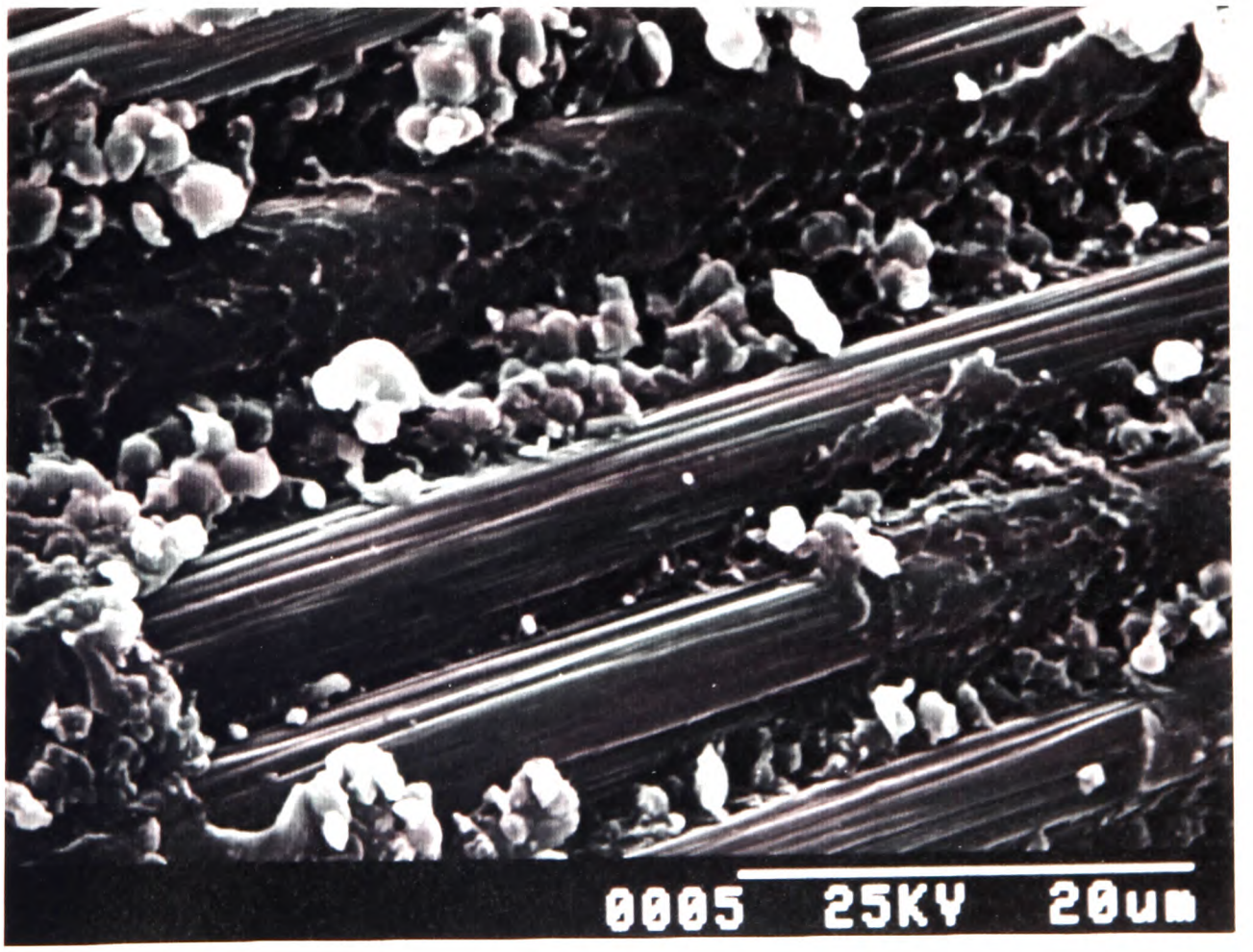

Figure 2.17 (c) $\theta=21^{\circ}$

SEM pictures for C/epoxy compressive oblique specimens.

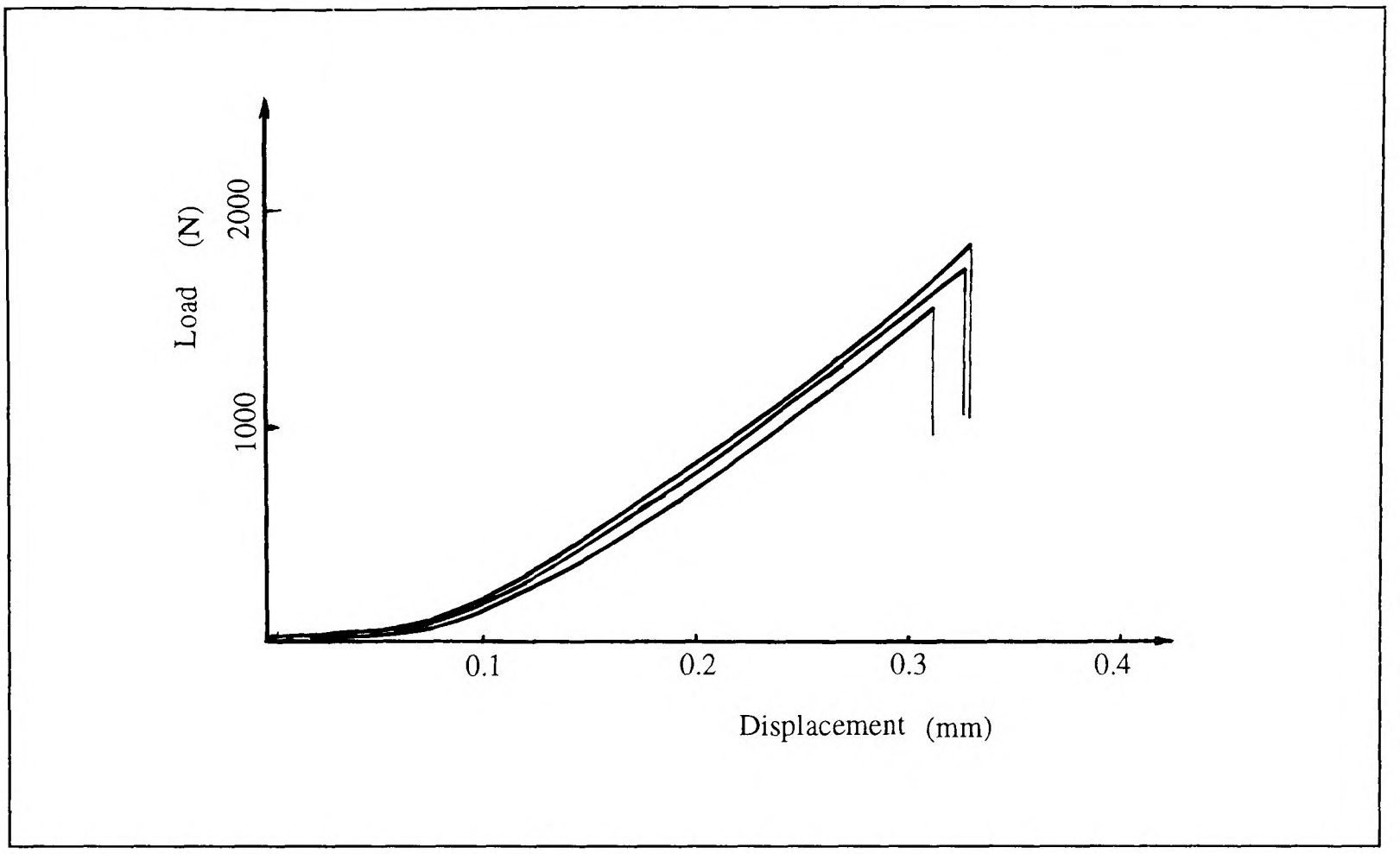

Figure 2.18 The load-displacement curves for C/epoxy tensile oblique tests (Table 2.5, group 3).

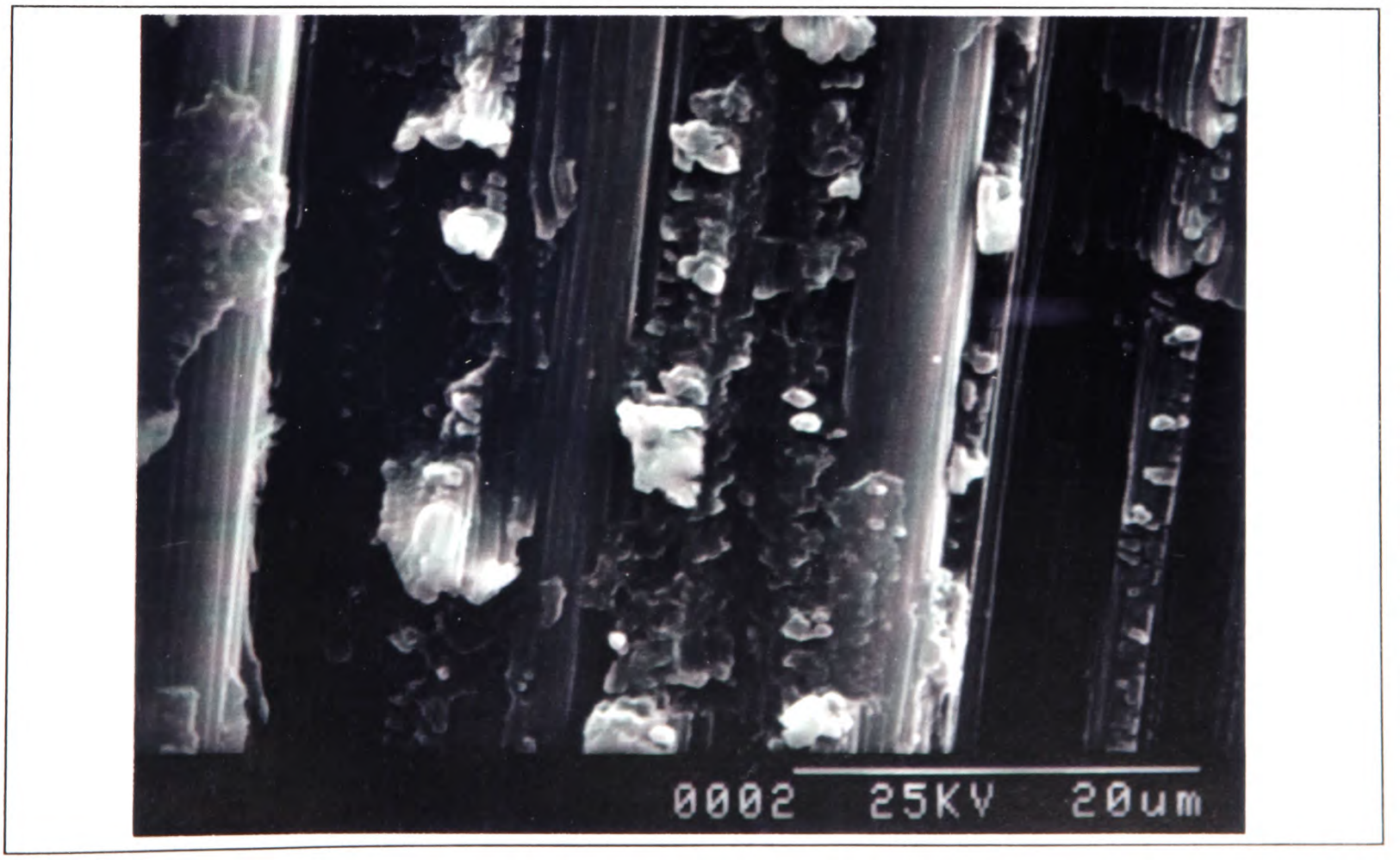

Figure 2.19 (a) $\theta=90^{o}$

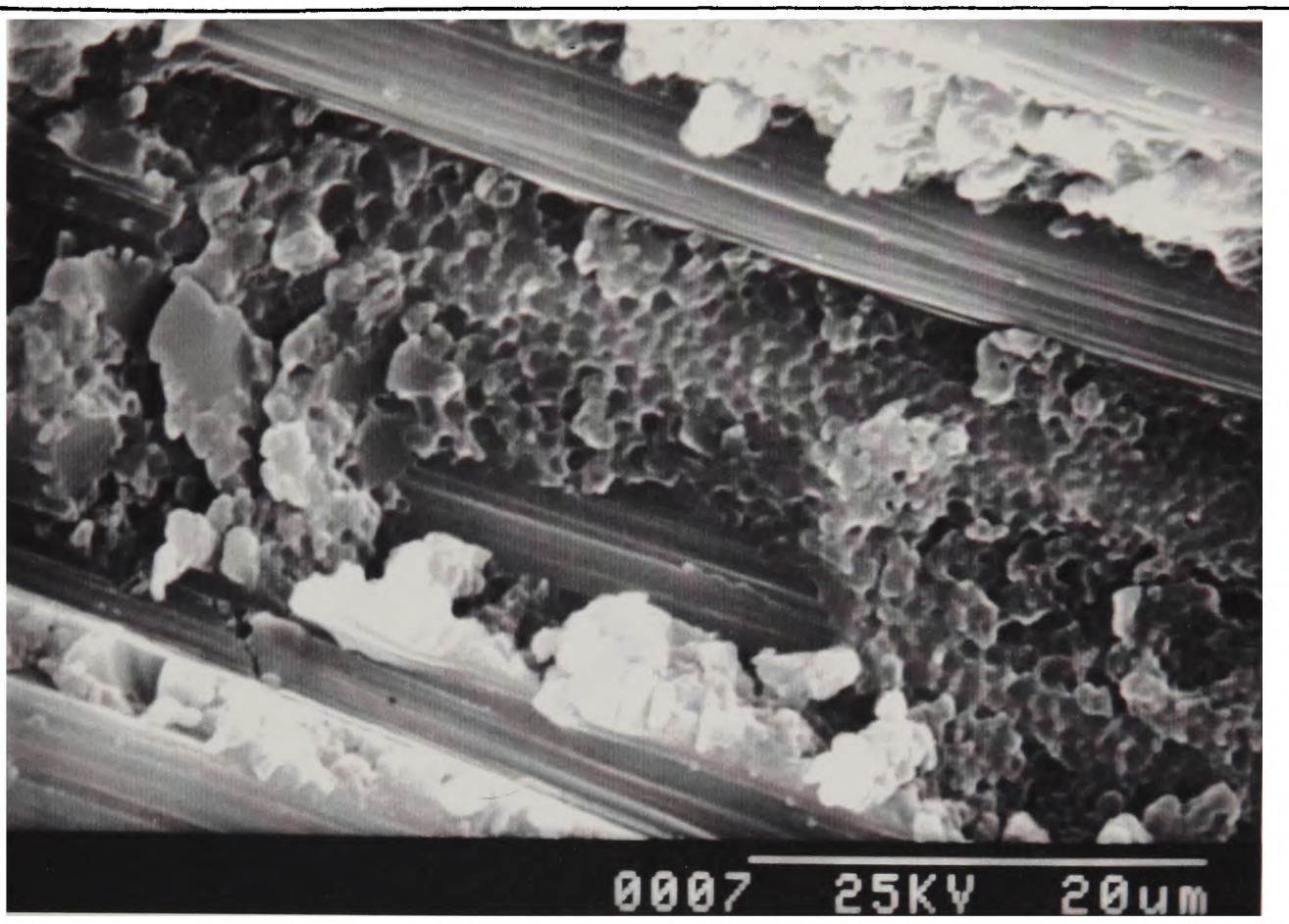

Figure 2.19 (b) $\theta=60^{\circ}$

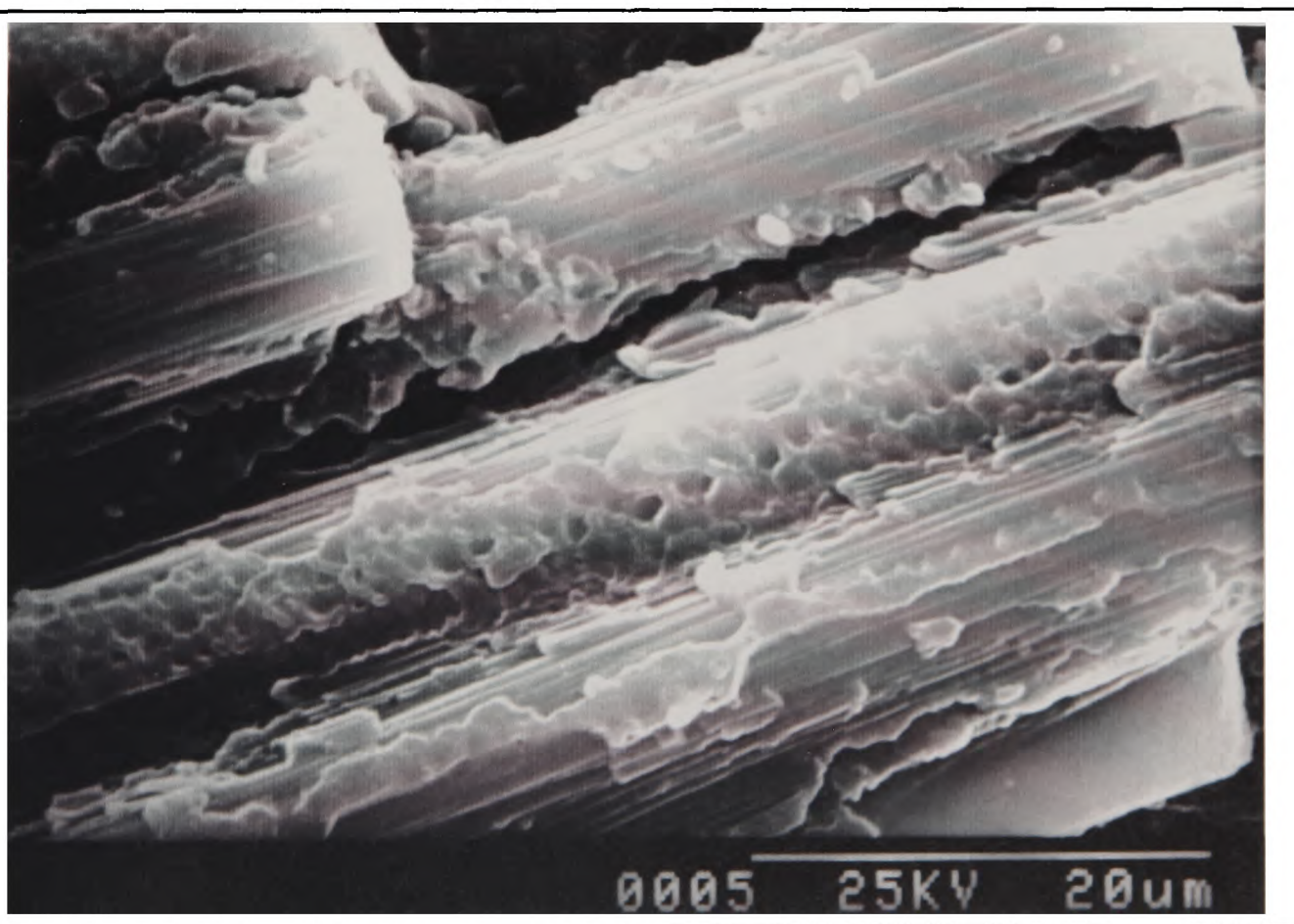

Figure 2.19 (c) $\theta=30^{\circ}$

SEM pictures for C/epoxy tensile oblique specimens.

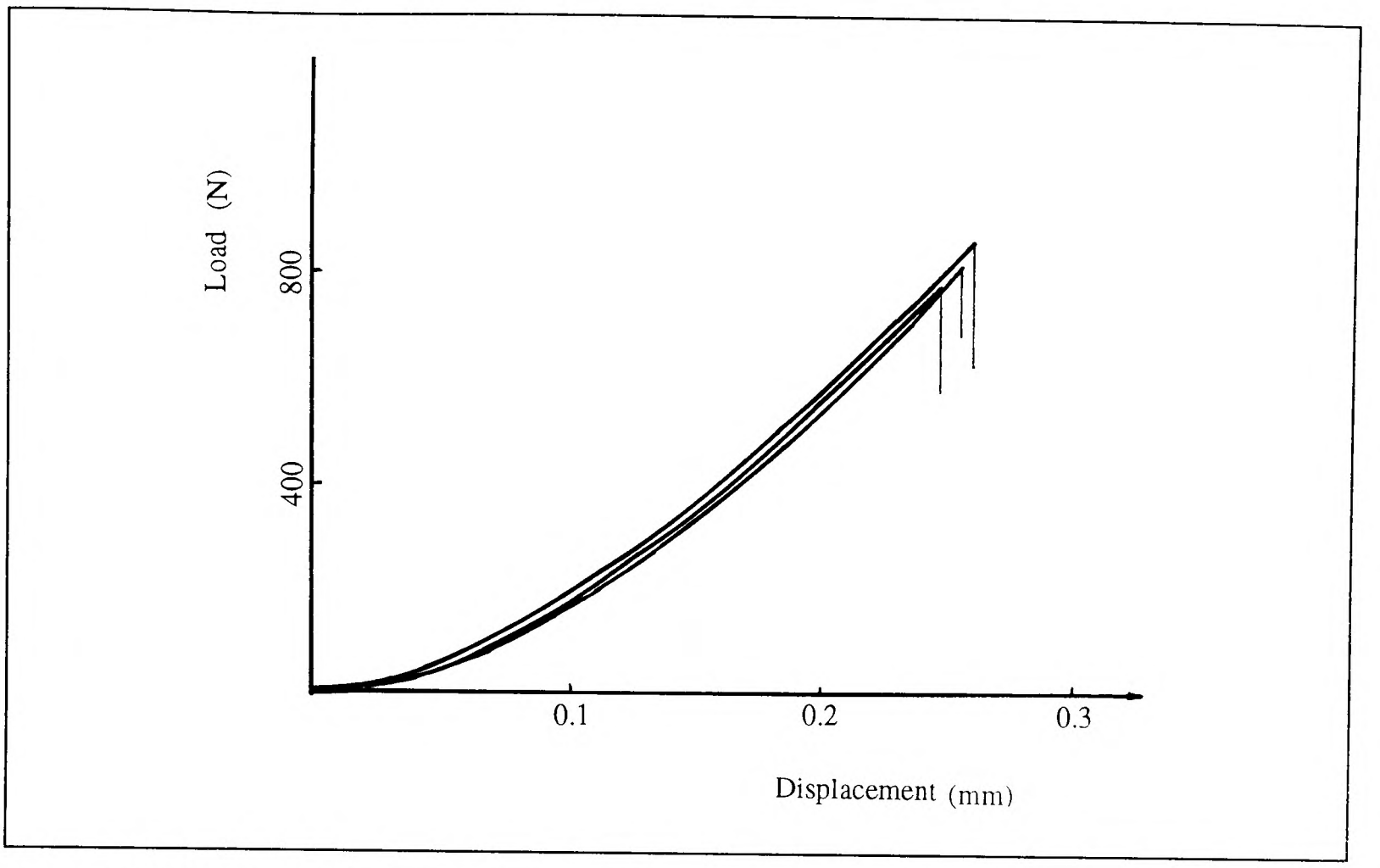

Figure 2.20 The load-displacement curves for G/epoxy tensile oblique tests (Table 2.6, group 5).

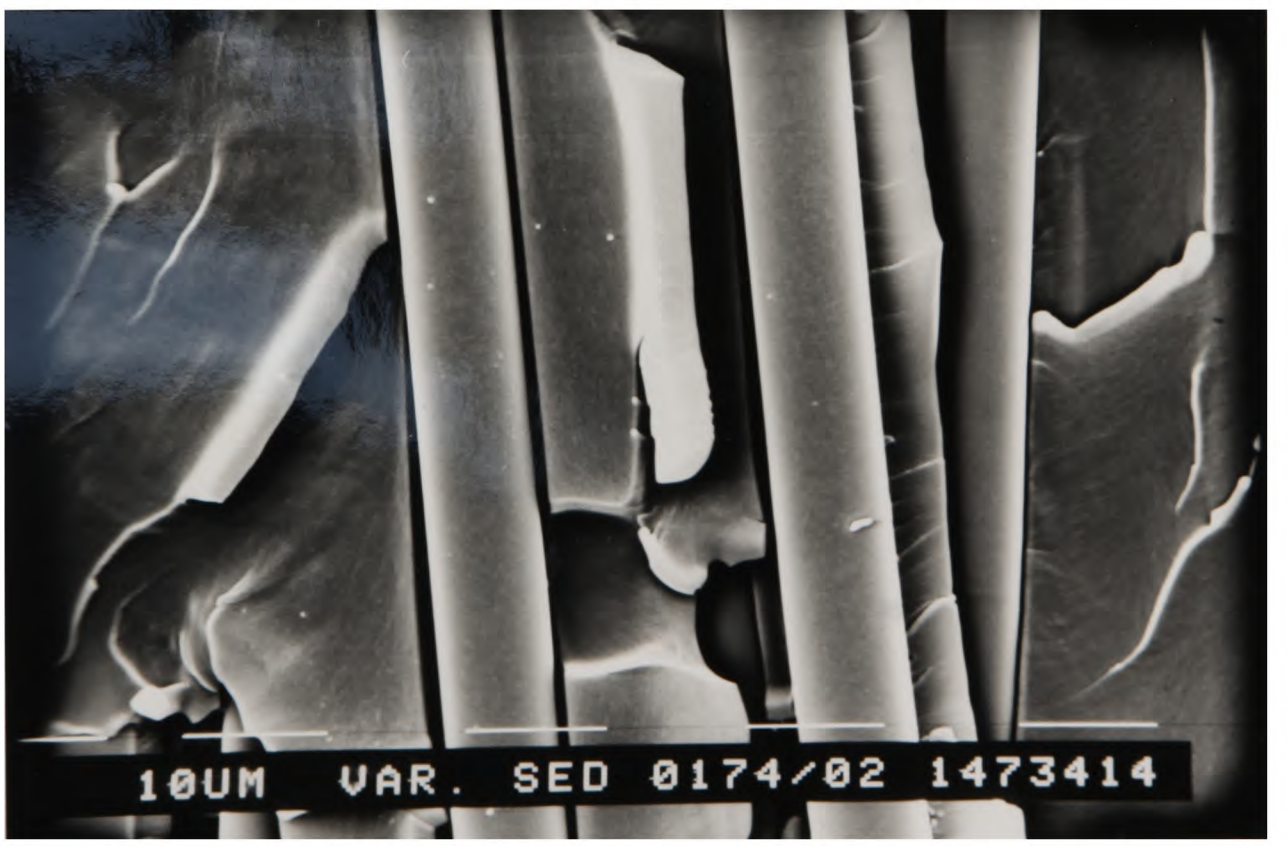

Figure 2.21 (a) $\theta=90^{o}$

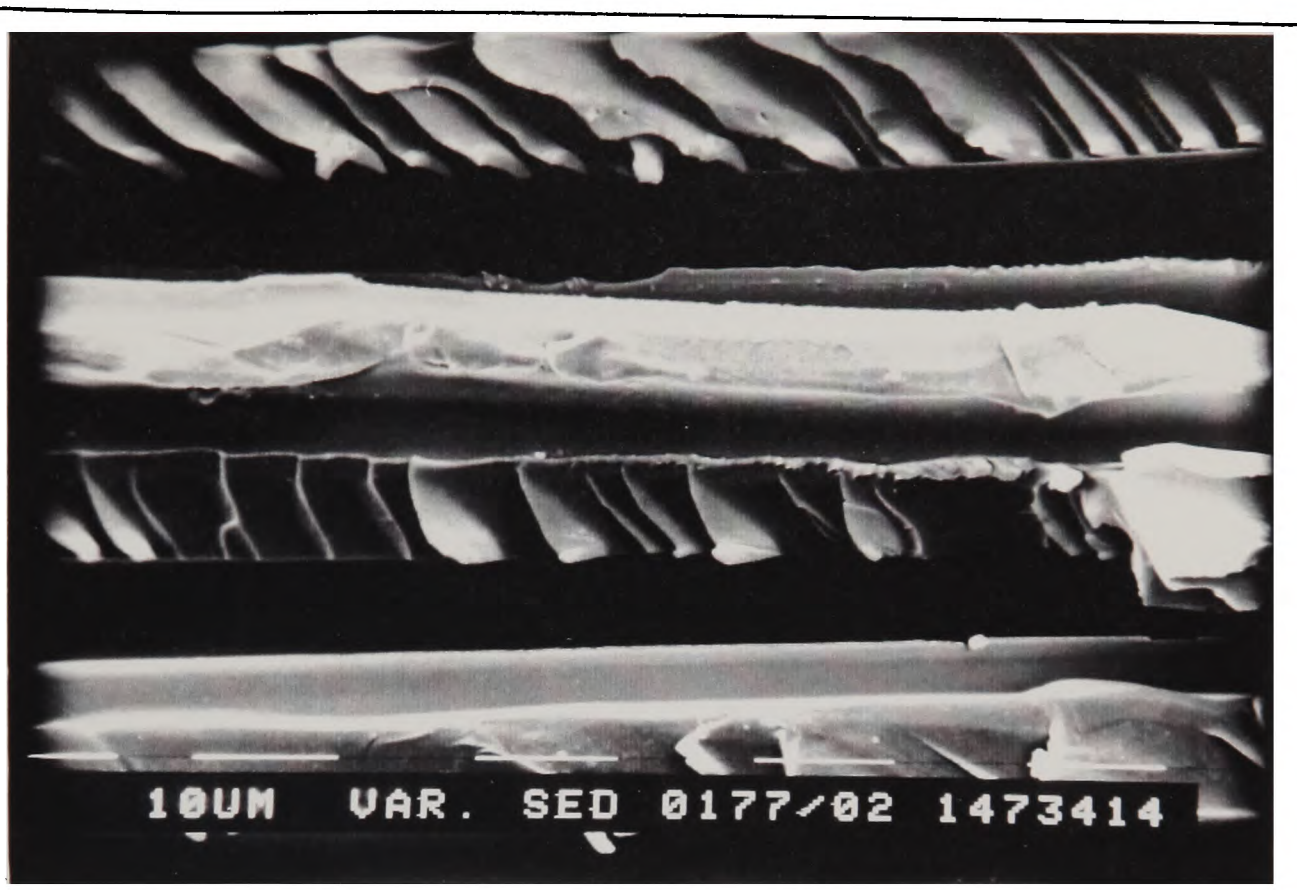

Figure 2.21 (b) $\theta=60^{\circ}$

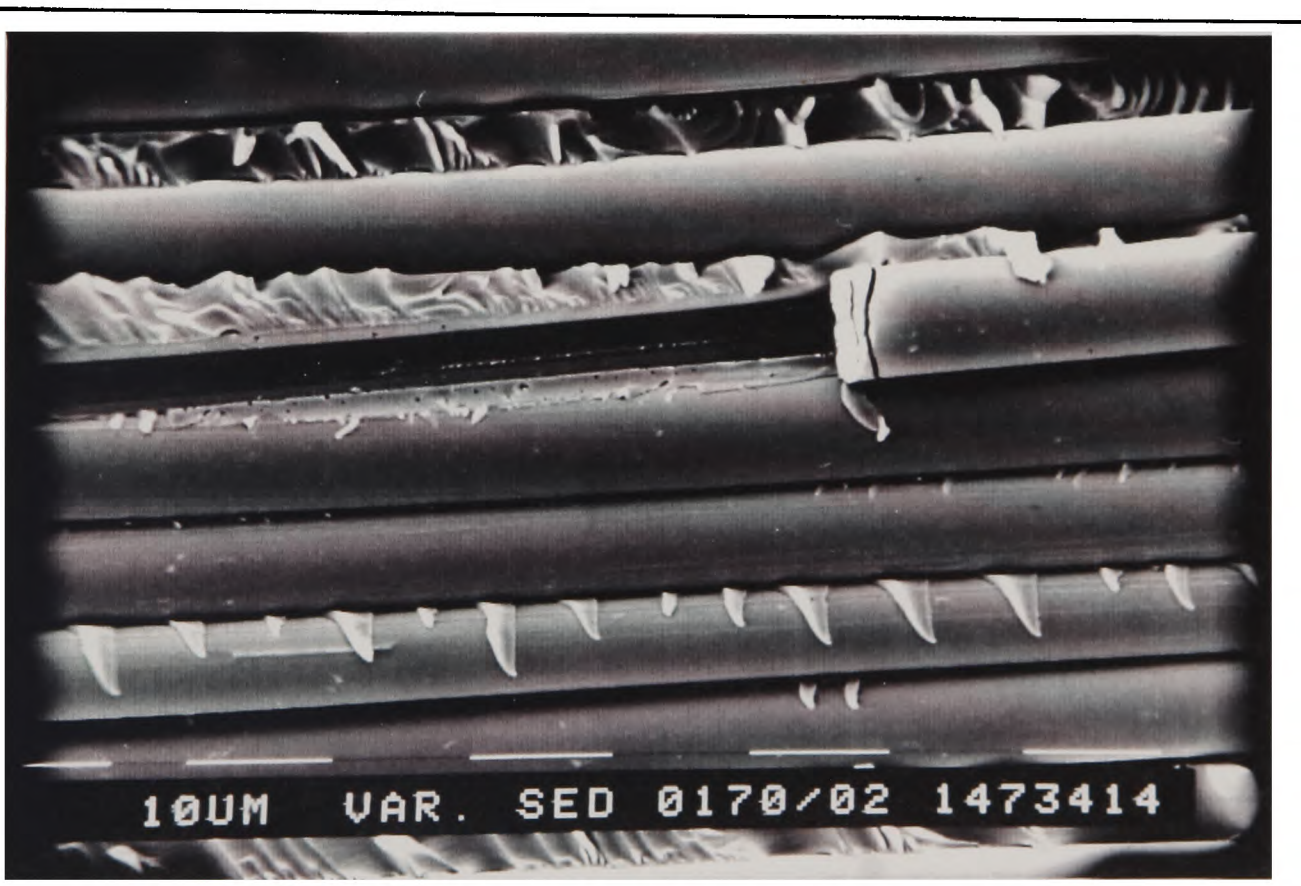

Figure 2.21 (c) $\theta=30^{\circ}$

SEM pictures for G/epoxy tensile oblique specimens.

Chapter 3

C-SPECIMEN TESTS

3.1 GENERAL DESCRIPTION OF THE TEST

The curved beam specimen (Hiel, 1991; Wu, 1993) and the C-specimen (Hognestad, 1993) have been used to model delamination failure in components containing a radiused corner, such as the knuckle in a flange (Fig. 3.1). A plain C-specimen made of woven carbon fibre reinforced composite(0°/90°) subjected to tensile loads is shown in Fig.3.2(a). As discussed in Section 1.2.2, the stress distribution, which is graphically expressed in Fig.3.2(b), is described by classical continuum mechanics (Eqn.1-10). Hognestad (1993) found that failure, in the form of interlaminar cracks, happened at the apex of the C-specimen. The cracks appeared randomly between adjacent layers across the thickness. As shown in Fig.3.2 (b), there is no interlaminar shear stress in the failure region; the state of stress consists of only combined in-plane bending and through-thickness tension. Fig.3.3 shows the experimental results from C/epoxy C-specimens by Hognestad (1993), from which it can be found that with the change of in-plane normal stress (σ_t) from compression to tension, the interlaminar tensile stress (σ_r) increases very significantly, viz. whilst σ_t increases from -500 to 200 MPa (+140%), σ_r increases from 10 to 36 MPa (+260%). This reveals the complicated effect of combined stresses on delamination of laminate composite, i.e. the interaction of interlaminar tension with either in-plane compression or tension will affect the failure mechanisms of delamination.

A very natural question will be what the delamination strength will be if the third stress

component, interlaminar shear, is added to the above stress state. This can be achieved by modifying the C-specimen so as to shift the failure zone away from the apex. Therefore a waisted C-specimen is designed by reducing the width at one side of the apex of a plain C-specimen (Fig. 3.4(a)). In this way, it is possible to localise the failure away from the apex to the waisted position. Ignoring the stress concentrations induced by the waist, the state of stress can be described by the elasticity solution like a plain C-specimen and thus an interlaminar shear stress τ_{rt} is added to the radial through-thickness tension σ_r and the tangential tension or compression σ_t (Fig. 3.4(b)).

3.2 WAISTED C-SPECIMEN

Only C/epoxy material system was used in the waisted C-specimen test. The specimens consisted of 12 layers of 0°/90° woven carbon fibre prepreg and were manufactured by putting prepregs over a mandrel, which was made of a semi-circular aluminium rod bolted on top of a rectangular aluminium bar of the same width as the diameter of the rod. Steel tube inserts were put at the ends of the specimen, where the tensile loads were applied. The laminate was cured for 1 hour at 175°C with 100 psi pressure. The post-cure cycle was 190°C for 4 hours.

The finished specimen had a thickness of 3.2 mm. The width of the specimen was 6mm, the minimum width at the waist was 3mm, the inner radius was 15.7mm, the waist radius 20mm and the *e* value 5.52mm (Fig.3.4). The waist was carefully machined by grinding, with much attention being paid to minimise any mechanical damage. The dimensions and waist configuration were the same for all specimens, except for the position of the waist, which is defined by the angle θ in Fig.3.4. Six groups of specimens were tested, with the angular

position of the waisted region between 30^0 and 70^0.

3.3 STRESS ANALYSIS

A detailed finite element stress analysis using ABAQUS (HKS Inc.,1992) was carried out in order to assess the possible stress concentration induced by the waist in the waisted C-specimen. The analyzed specimen had the waist position at $\theta = 60°$ (Fig.3.5). Due to symmetry in the width direction, only one-half of the specimen was modelled (Fig.3.6). Since the numerical modelling of the matrix and each fibre bundle was not feasible, a linear elastic orthotropic material was assumed, viz. the laminate was considered as an orthotropic homogeneous continuum where the elastic contributions from fibres and matrix were averaged bulk properties. The material properties of eight-harness satin C/epoxy woven fabric (MSRR 9411) are listed in Table 3.1.[1] The element type was a 20-node quadratic brick solid element (C3D20 in ABAQUS). Forty-one elements were used along the hoop direction, where twelve elements were within the waist length to make the mesh there finer. Six elements were used through the thickness, giving 2 plies per element, and two elements through the width, although the symmetry condition made the effective number of elements through the width four. The load was applied as a "line load" along the width direction (CLOAD in ABAQUS).

Fig. 3.6 presents the tangential stress distribution contours by FEM analysis. In Fig.3.7, the distribution of the three stress components along the through-thickness direction at the sections of $\theta = 49°$ (the lower edge of the waist), $\theta = 60°$ (the middle of the waist), $\theta = 70.4°$ (the

[1] Materials properties from Rolls-Royce plc.

upper edge of the waist) and $\theta = 90^{\circ}$ (the apex of the specimen) are compared with Timoshenko's analytical solution (Eqn.1-10). It is found that the numerical results are generally in very good agreement with the analytical solution for the plain C-specimen. Figs. 3.8(a) and (b) show the variation of tangential stress along the width of the specimen at the middle of the waist on the outer surface and the inner surface respectively. The stress is compressive (tensile) and the maximum value is at the edges, and in both situations the stress concentration factor is no more than 10%. This confirms that the additional stresses induced by the curvature of the waist are very low and can be neglected.

In the numerical analysis, the shape of the waist is idealized as conical for ease of meshing. However, due to the difficulty in machining the waist, the real shape was cylindrical instead of conical. Based on the above numerical analysis that the conical waist has not caused considerable difference from the analytical solution for a plain C-specimen (without waist) and considerable stress concentration, it should be safe to say that the small difference in the shape will have no effect on the above conclusions.

Table 3.1 Elastic Engineering Constants for C/Epoxy Woven Laminate

E_1	52.8E3 MPa	ν_{12}	0.05	G_{12}	5.16E3 MPa
E_2	52.8E3 MPa	ν_{13}	0.05	G_{13}	2.58E3 MPa
E_3	8.44E3 MPa	ν_{23}	0.05	G_{23}	2.58E3 MPa

3.4 TEST AND RESULTS

The specimens were loaded in an Instron testing machine and the tests were monitored using a video tape recorder which permitted the identification of the instant of failure. The loading rate was 1 mm/min. The alignment was secured by a pair of parallel steel tubes which were inserted into the two ends of a C-specimen during manufacture, and the use of universal fixtures.

Table 3.2 summarises the results of the tests. In each specimen the plies are numbered from 1 to 12 starting on the inside ply. In any given specimen geometry, delamination did not always occur between the same plies. For example, for the first two tests, with $\theta=30^{o}$, delamination occurred in one case between plies 3 and 4, on the tension side of the section (towards the inside face) while in the other case it was between plies 11 and 12, i.e., near the outside face and in compression. This was expected from the results of plain C-specimen tests and is due partly to the unavoidable variability of the mechanical properties of the material, but the main reason is the presence of at least two competing modes of failure, one in which the fibres are in tension and the other in which fibre buckling under compressive stress is possible. Fig.3.9 shows the recorded load-displacement curves, which display a linear elastic deformation up to failure.

The results are plotted in Fig.3.10 together with those obtained from plain C-specimens(no shear) (Fig.3.3). Note that the three axes have different scales reflecting the relative magnitude of the three stress components. The composite is much weaker in the through-thickness direction (in tension or in shear) than along the fibres. The experimental variability is

indicated by the scatter between the results and the best fit curve for the no-shear case, i.e., about $\pm$ 10MPa. In absolute terms this is a fairly small magnitude but it is, of course, of large relative importance when compared to the value of the radial stress, which is below 40MPa, and of the shear stress, which is below 20 MPa. This means that it is not possible to draw any firm quantitative conclusions from a single experiment and that all the experimental data must be considered together. For simplicity, all the results have been projected onto the σ_r - σ_t plane, against the no-shear data, Fig.3.11. An obvious observation is that while the shear stress τ_{rt} has very little effect on failure in the negative σ_t quadrant, it has a pronounced effect in the positive quadrant.

The fracture surfaces of the specimen were carefully examined using scanning electron microscopy(SEM). In order to prevent charging, the surfaces were coated with gold prior to SEM examination. The SEM pictures taken are shown in Fig.3.12 and Fig.3.13, which reveal distinctive features for the two stress states. A discussion of these results is found in Chapter 5.

3.5 PLAIN G/EPOXY C-SPECIMEN TEST

G/epoxy material system was used to try to repeat the C-specimen test and find the onset of delamination. The materials and curing cycle were the same as those described in Chapter 2 and the mandrel used for the manufacture was that used for the C/epoxy C-specimen.

The first batch of specimens were made of 12 plies with a finished thickness of 2.46 mm, and V_f=54%. Failure was found to occur as a result of buckling on the outer surface and there was

no delamination. It was thought that the specimen was too thin to have any delamination failure and therefore a thicker C-specimen was made.

The second batch of specimens were made of 24 plies with finished thickness of 4.94 mm, V_f=66% and sliced into 10 mm in width. For these specimens, delamination was found only near the outer surface, viz, failure occurred in the compressive in-plane stress quadrant, as shown in Table 3.3. This was very different from what was expected. The real reasons why G/epoxy C-specimen does not delaminate as randomly as C/epoxy need to be investigated further. One of the possible reasons could be the different epoxy system. This indicates a further complicated failure mechanism of polymer composite, which might depend on the matrix.

Although no quantitative data are to be drawn from these tests, this specimen gave a vivid illustration of the process of delamination. Fig.3.14 (a)(b) show the aspect of the inner surface and of the outer surface of the C-specimen after being loaded. The white spots are microcracks. It was very noticeable that, as soon as delamination happened, some large white spots appeared on the outer surface, indicating local micro-buckling failure (Fig.3.15). Fig.3.16 shows that the load just before delamination (with large white spots), 1.018 kN, is nearly the same as the load at delamination, about 1.013 kN. These pictures indicate that when interlaminar tension interacts with in-plane compression, failure results from microbuckling (in-plane compression), which triggers and augments the delamination by interlaminar tension.

3.6 CONCLUSION

Although the detailed interpretation of results is found in Chapter 5, some conclusive remarks at this point are still appropriate.

- Manufacturing of the C-specimen, particularly the one with the waist, is not a simple operation. Residual stress may arise during curing which will affect the strength. Even more important, the specimens are finished by cutting with a diamond impregnated slitting wheel and plunge grinding the waist. It is very difficult to avoid some damage of the outer surfaces and hence it is expected that the strength of the finished product will suffer.

- In contrast with the strength of tension or compression tests, the state of stress exhibits high gradients. Comparison in terms of the peak stress at failure may not be correct, since, as will be shown when studying the Weibull statistical approach, the material may respond to average stresses over a volume rather than to peak values.

- It will be noted that the variation in ply number, which reflects a change in state of stress at the initiation of failure, highlights a scatter of properties that must be considered when interpreting the results.

Table 3.2 Waisted C/Epoxy C-Specimen Test Results

Waisted Position (θ^0)	Specimen No.	Failure Load (N)	Failure Position (Ply No.)	Calculated Stresses		
				σ_t (MPa)	σ_r (MPa)	τ_{rt} (MPa)
30	a	145.6	3-4	225.58	16.23	17.21
	b	210.2	11-12	-501.5	7.66	8.0
40	a	94.4	3-4	175.93	12.62	10.08
	b	81.1	3-4	151.15	10.84	8.66
	c	153.3	10-11	-355.78	12.48	9.85
50	a	132.3	3-4	276.79	19.82	11.77
	b	90.6	5-6	59.03	16.59	9.82
55	a	166.7	7-8	-126.6	31.22	15.68
	b	182.8	7-8	-138.8	34.24	17.2
60	a	89.8	4-5	135.12	17.09	7.21
	b	101.2	3-4	234.0	16.74	7.08
70	a	114.5	3-4	280.5	20.05	5.46
	b	65.1	5-6	49.92	13.92	3.78
	c	122.8	3-4	300.8	21.5	5.86
	d	114.9	9-10	-265.24	16.94	4.58

Table 3.3 Plain G/Epoxy C-Specimen Test Results

Specimen No.	Failure Load (N)	Failure Position (Ply No.)	Average Load(N) and Standard Deviation	Calculated Stresses		
				σ_t (MPa)	σ_r (MPa)	τ_{rt} (MPa)
1	1037	20	1013 (4%)	-371.22	19.15	0
2	951.7	20		-340.68	17.57	0
3	1049	20		-375.51	19.37	0

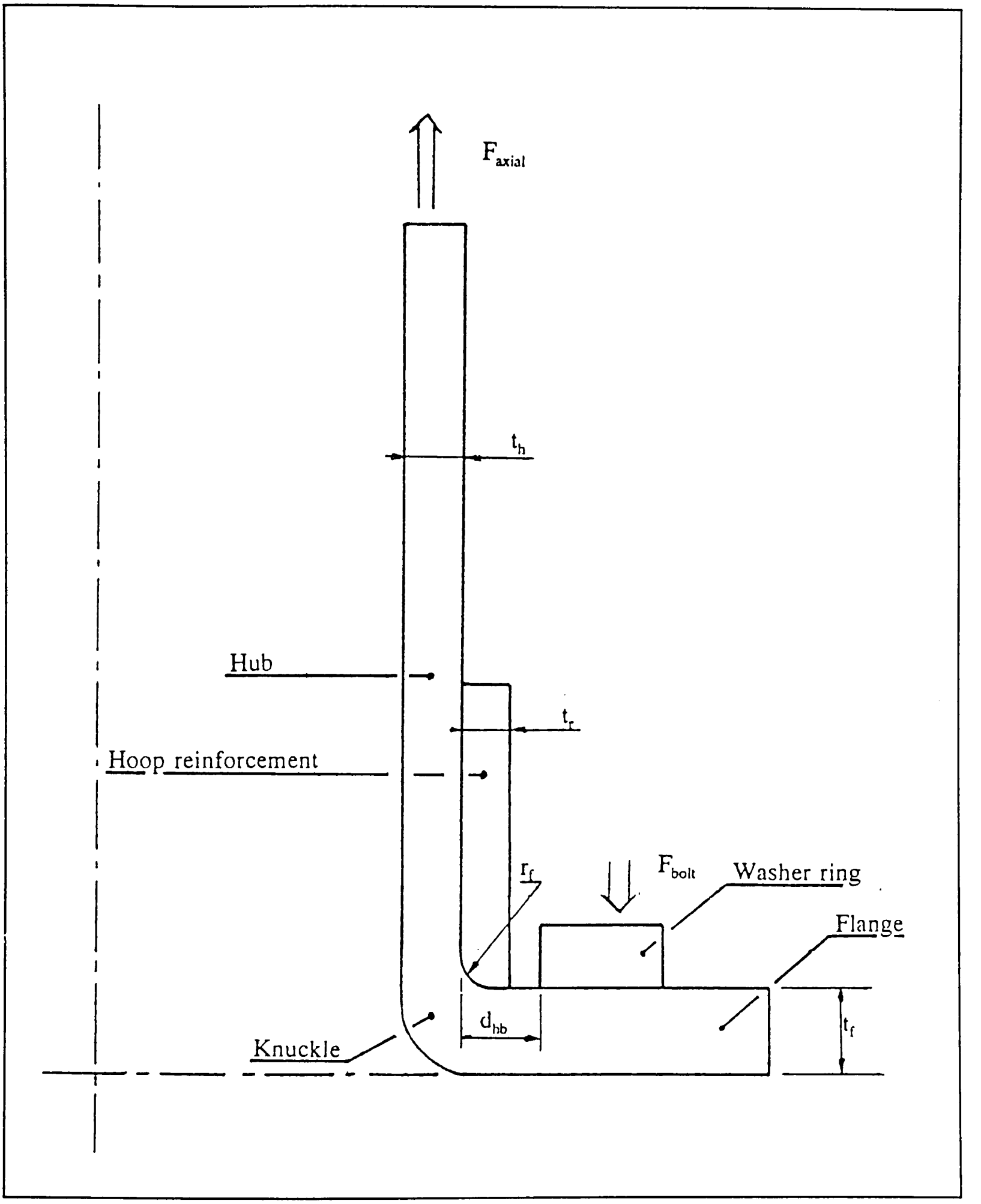

Figure 3.1 Flange geometry and nomenclature (Hognestad, 1993)

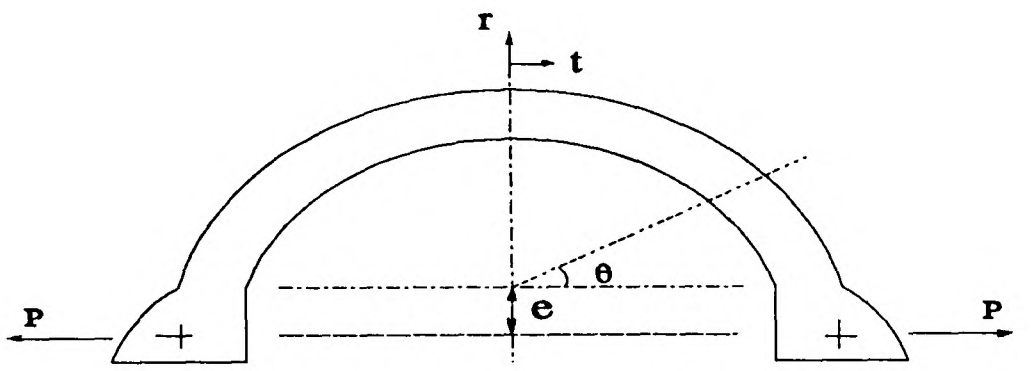
r
t
θ
e
P
P

(a)

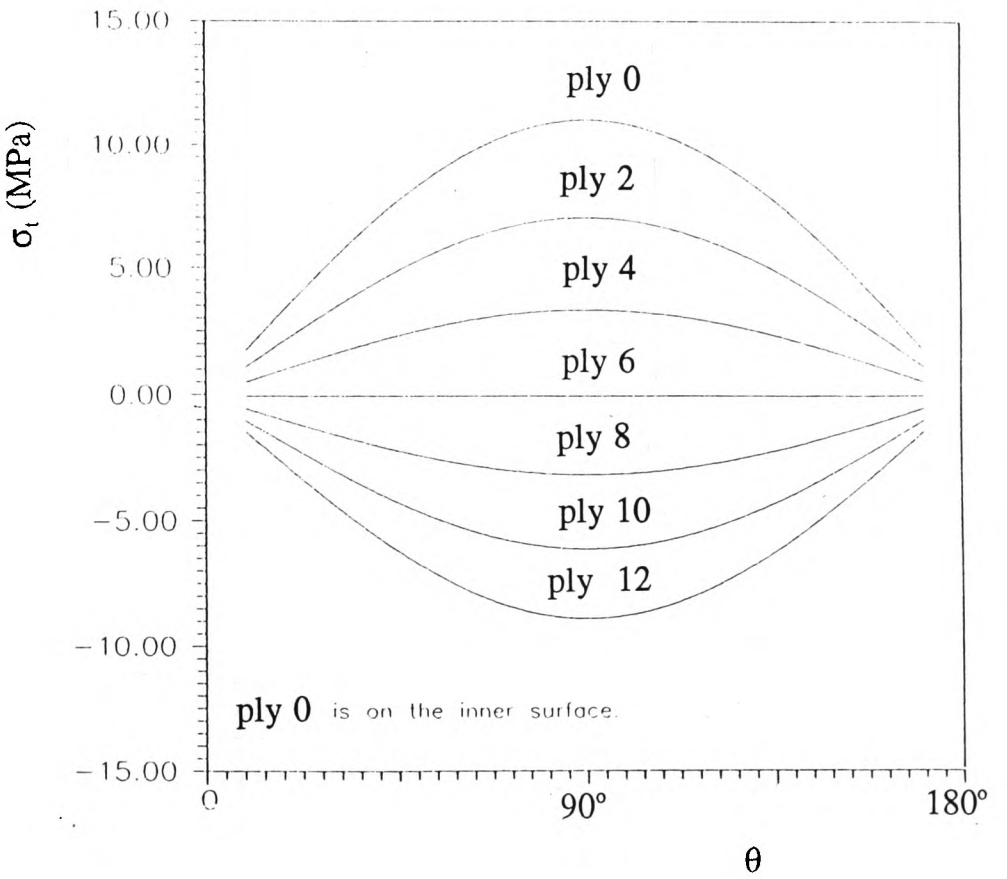
15.00
10.00
5.00
0.00
−5.00
−10.00
−15.00
σt (MPa)
ply 0
ply 2
ply 4
ply 6
ply 8
ply 10
ply 12
ply 0 is on the inner surface.
0
90°
180°
θ

Figure 3.2

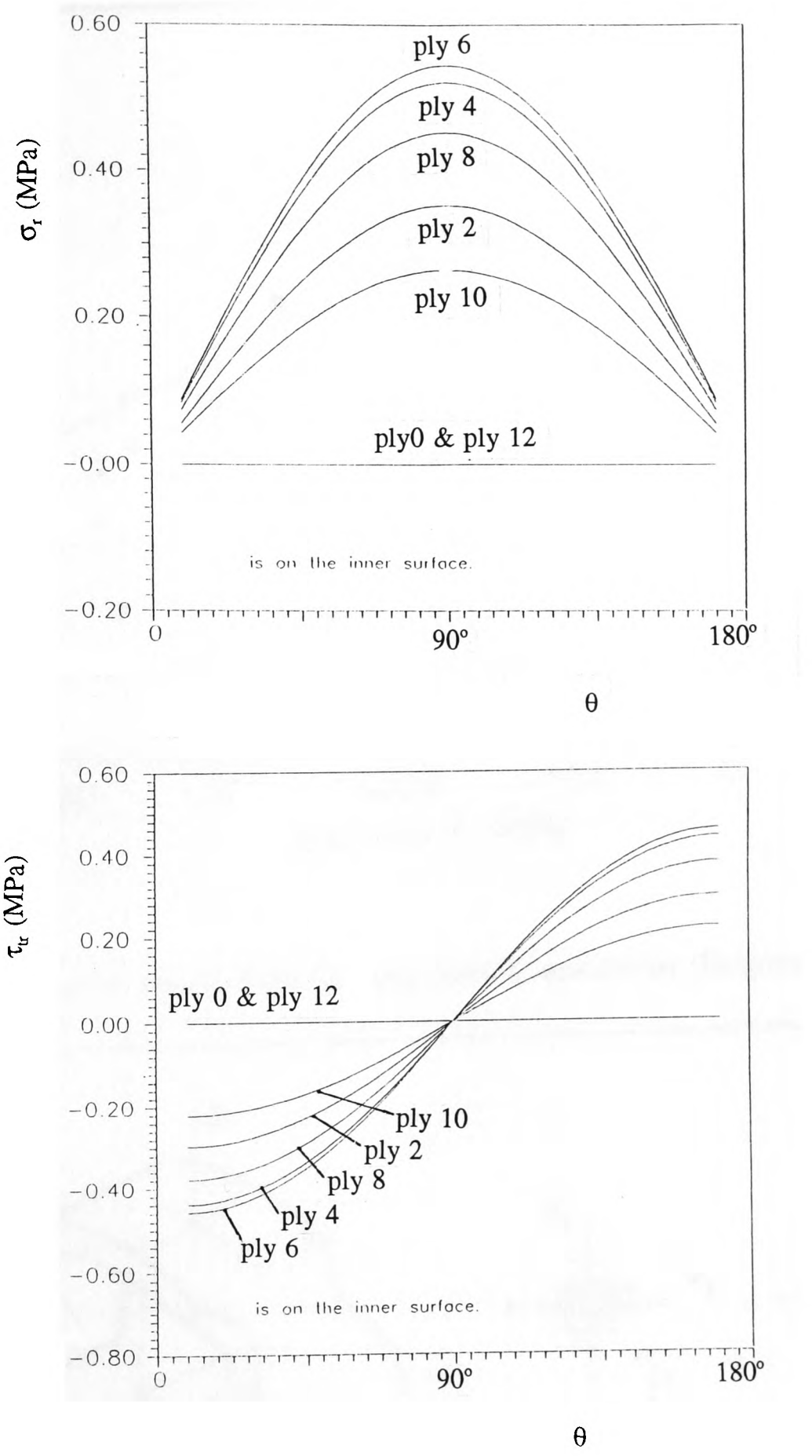

(b)

Figure 3.2 A plain C-specimen subjected to tensile load and its stress distribution following classical continuum mechanics (Eqn.1-8).

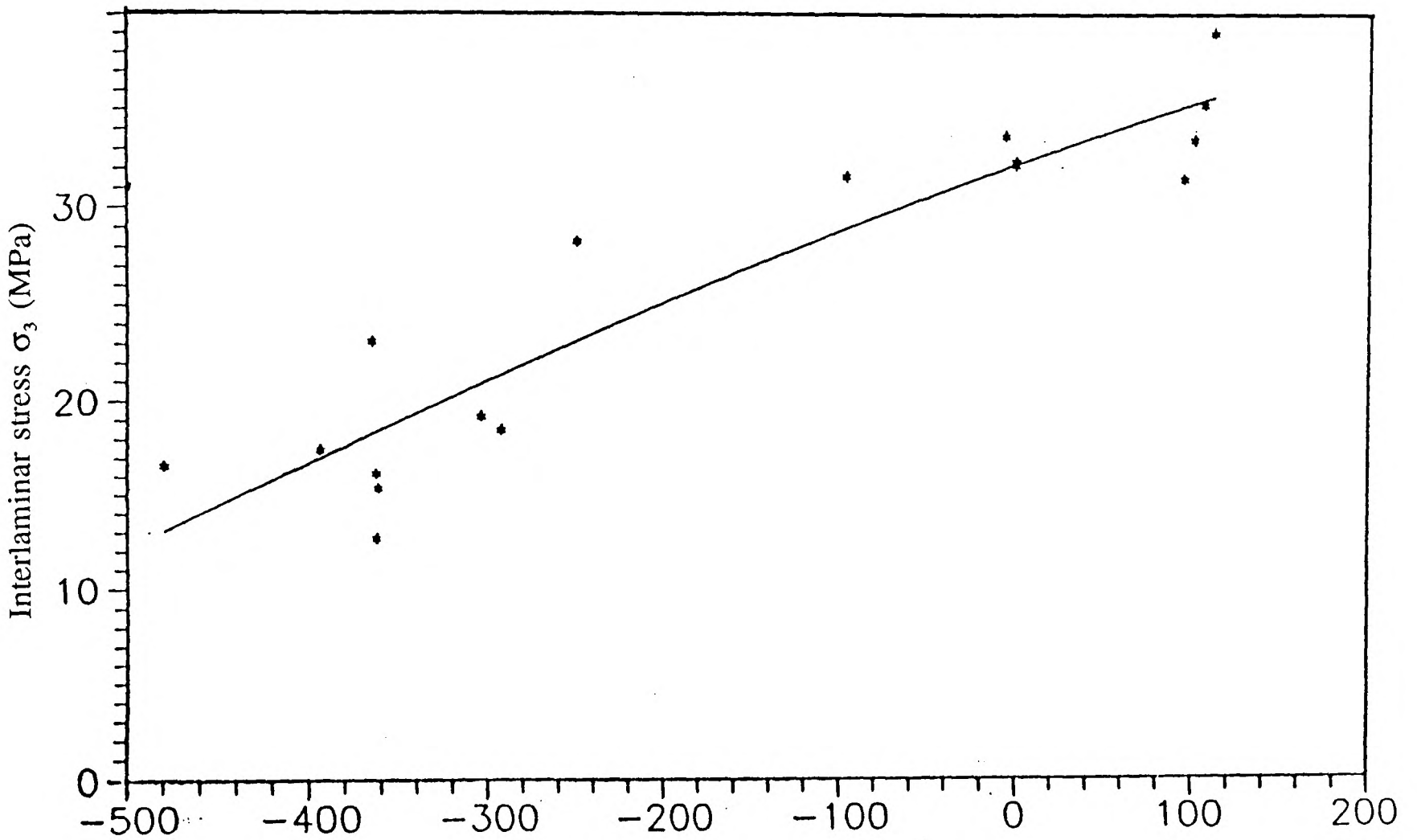

Figure 3.3 Experimental results from C/epoxy plain C-specimens (Hognestad, 1993).

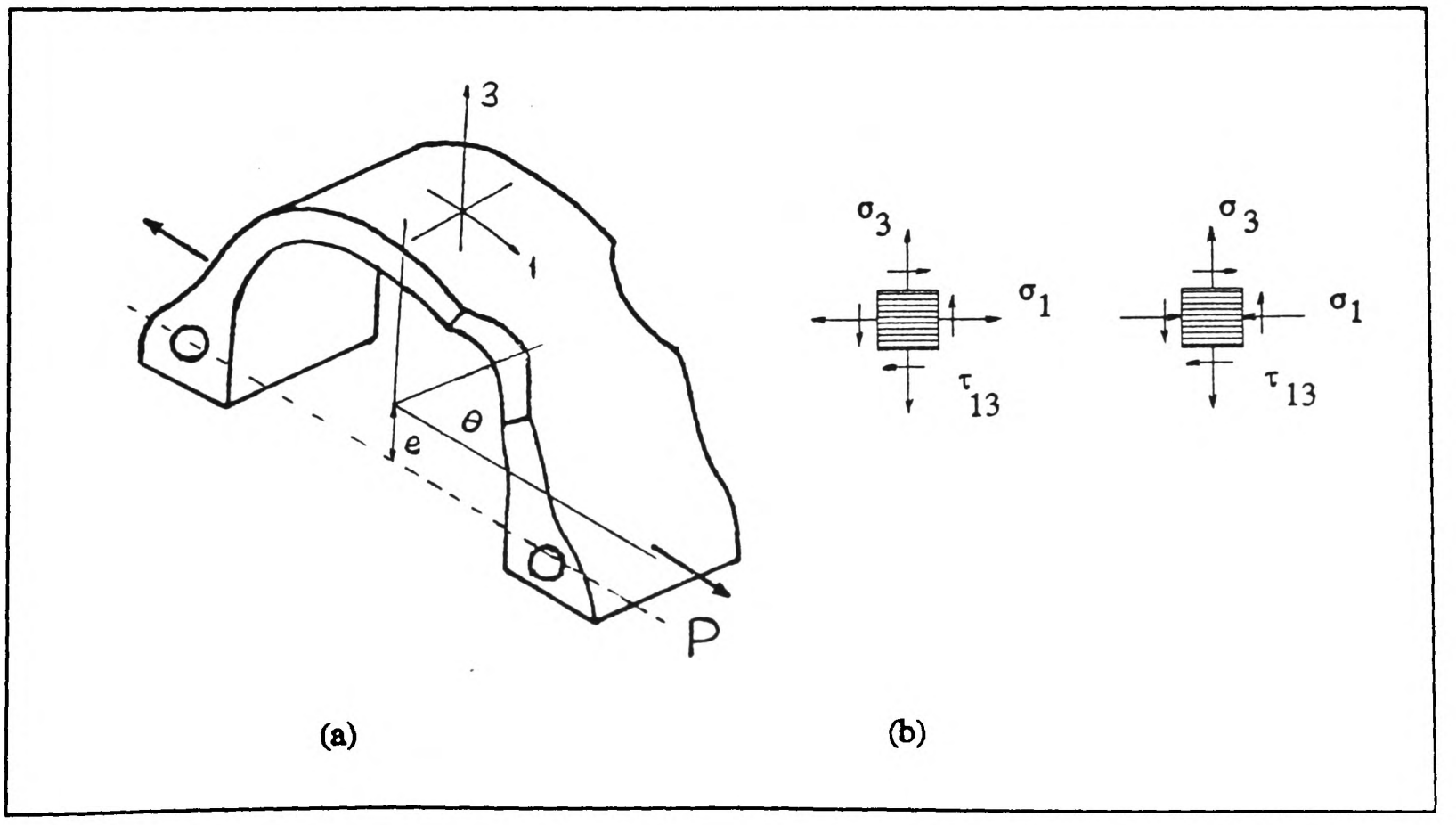

Figure 3.4

(c)

Figure 3.4 The waisted C-specimen.

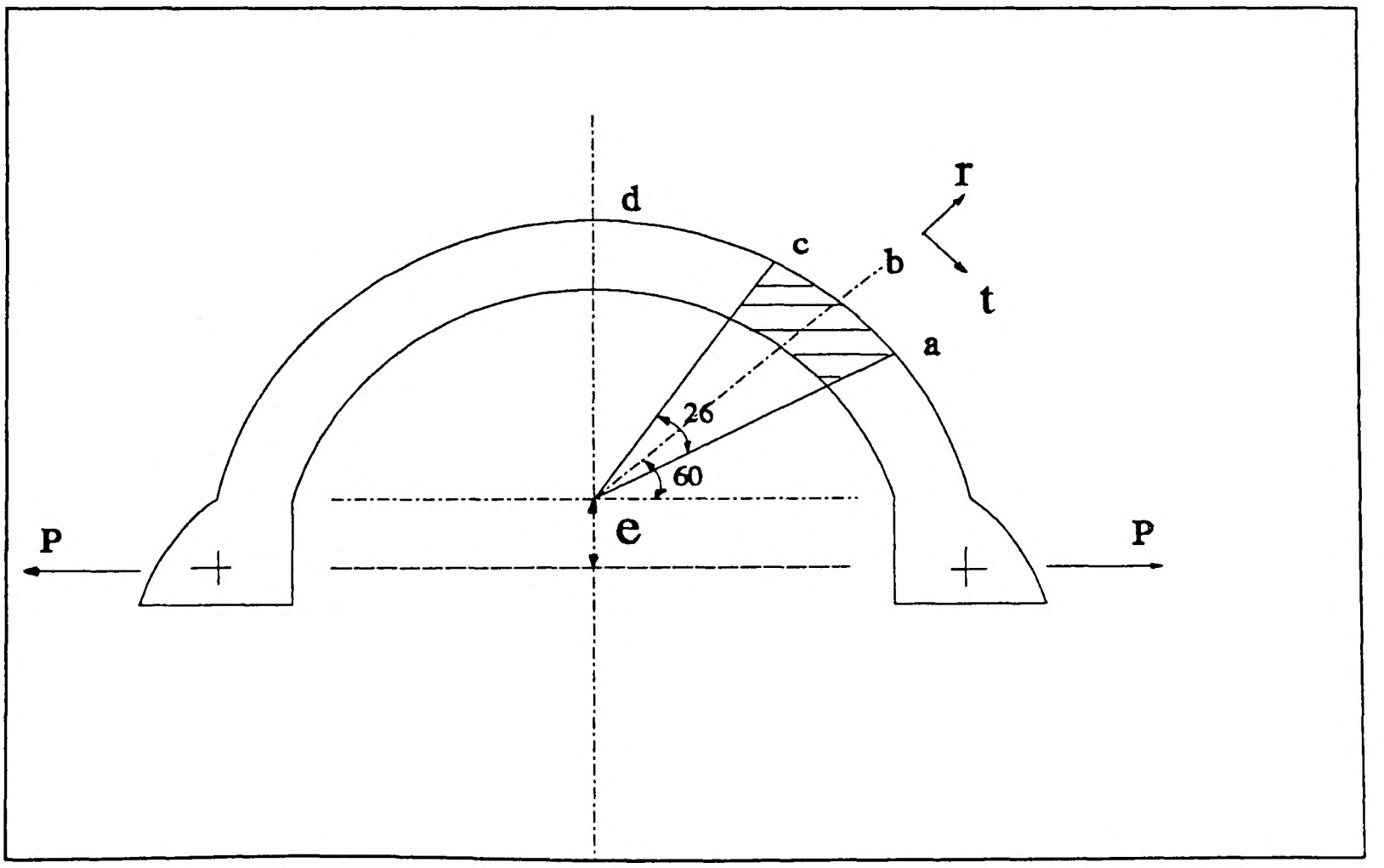

Figure 3.5 Dimensions of the waisted C-specimen for FE analysis.

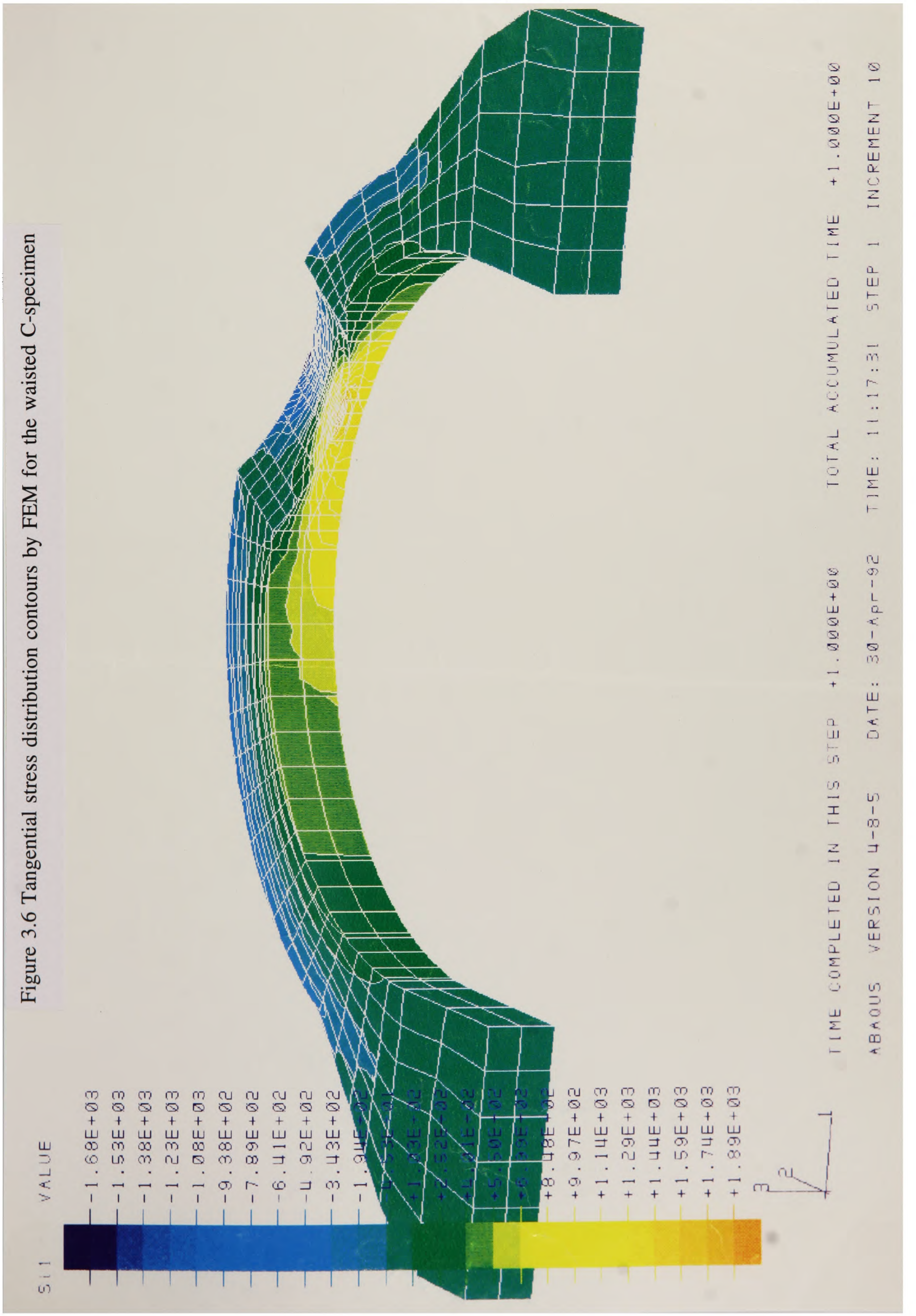

Figure 3.6 Tangential stress distribution contours by FEM for the waisted C-specimen

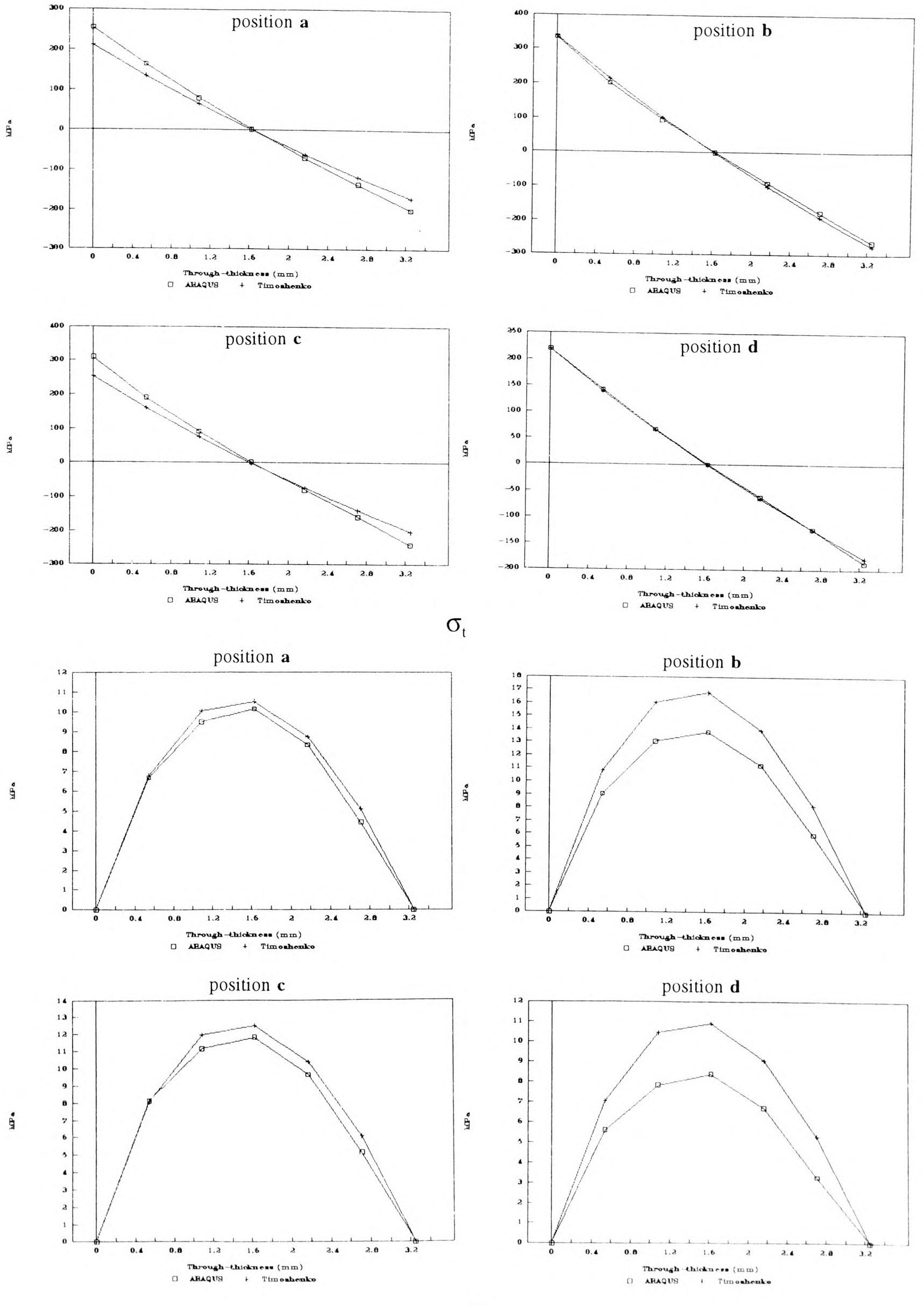
position a
position b
position c
position d
MPa
Through-thickness (mm)
ABAQUS
Timoshenko
σ_t
σ_r

Figure 3.7

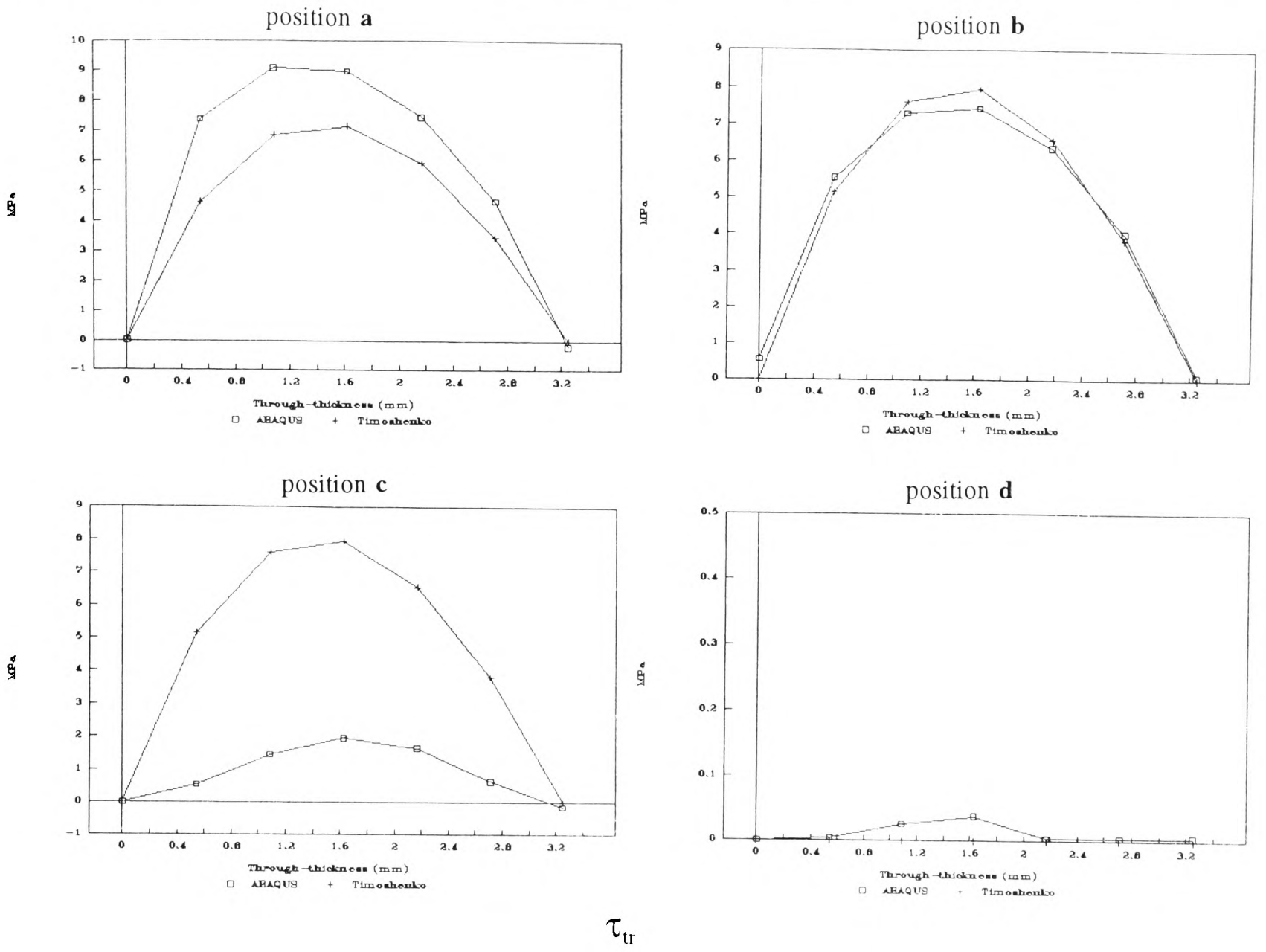

Figure 3.7 FE analysis results and comparison with Timoshenko

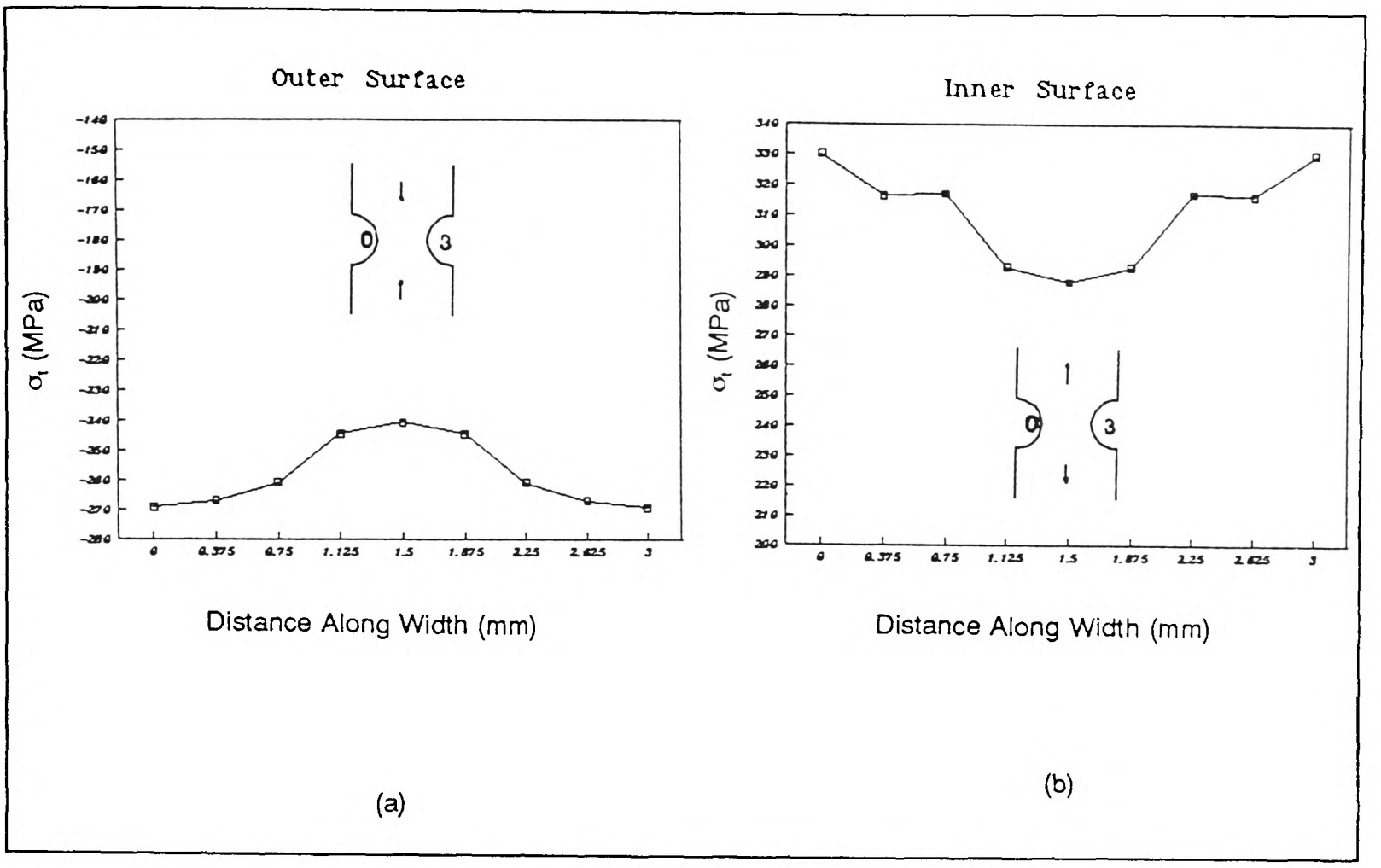

Figure 3.8 Tangential stress distribution along width of the specimen at the waist. (a) on the outer surface (b) on the inner surface.

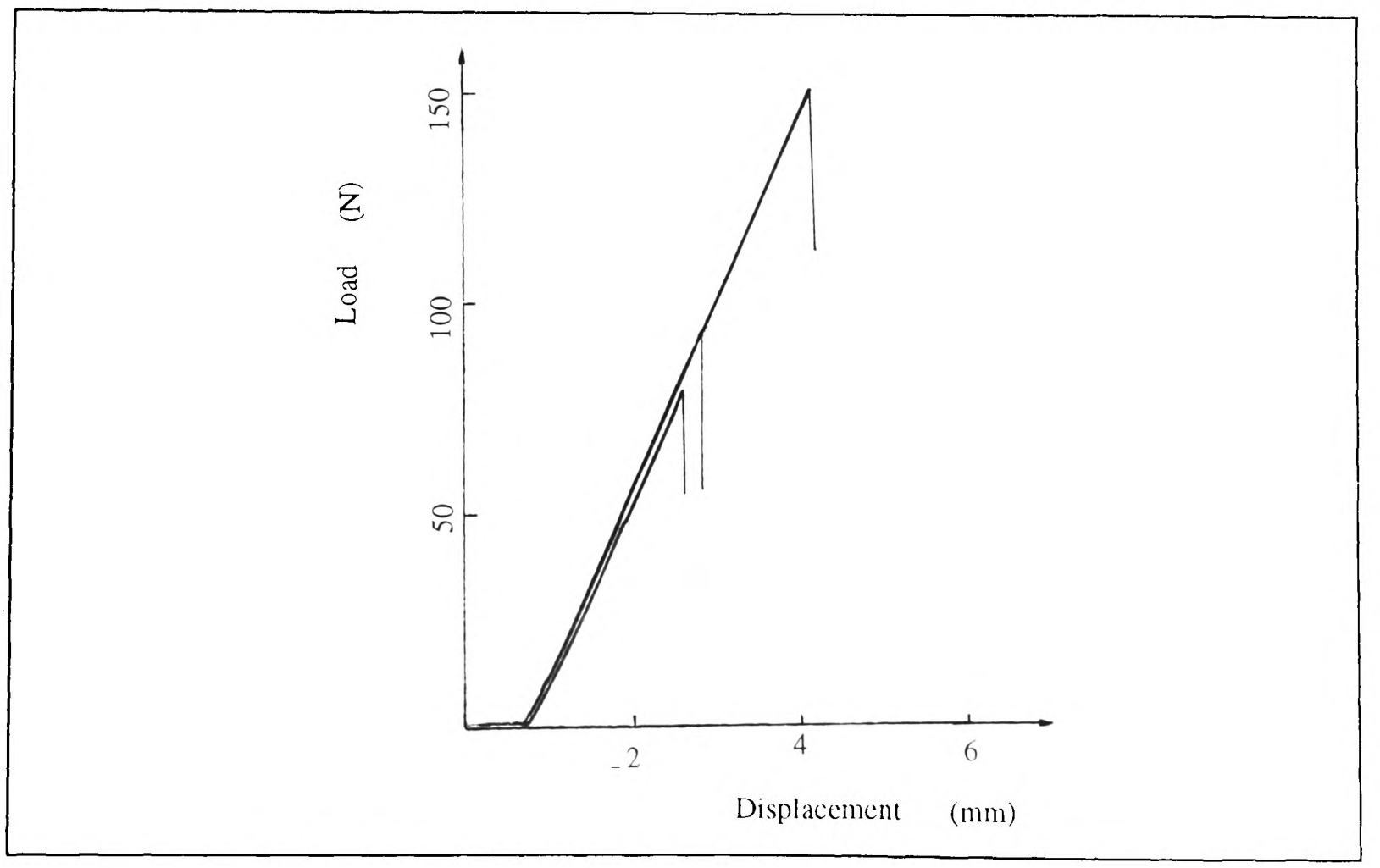

Figure 3.9 The load-displacement curves for waisted C-specimen tests. (for θ=40°)

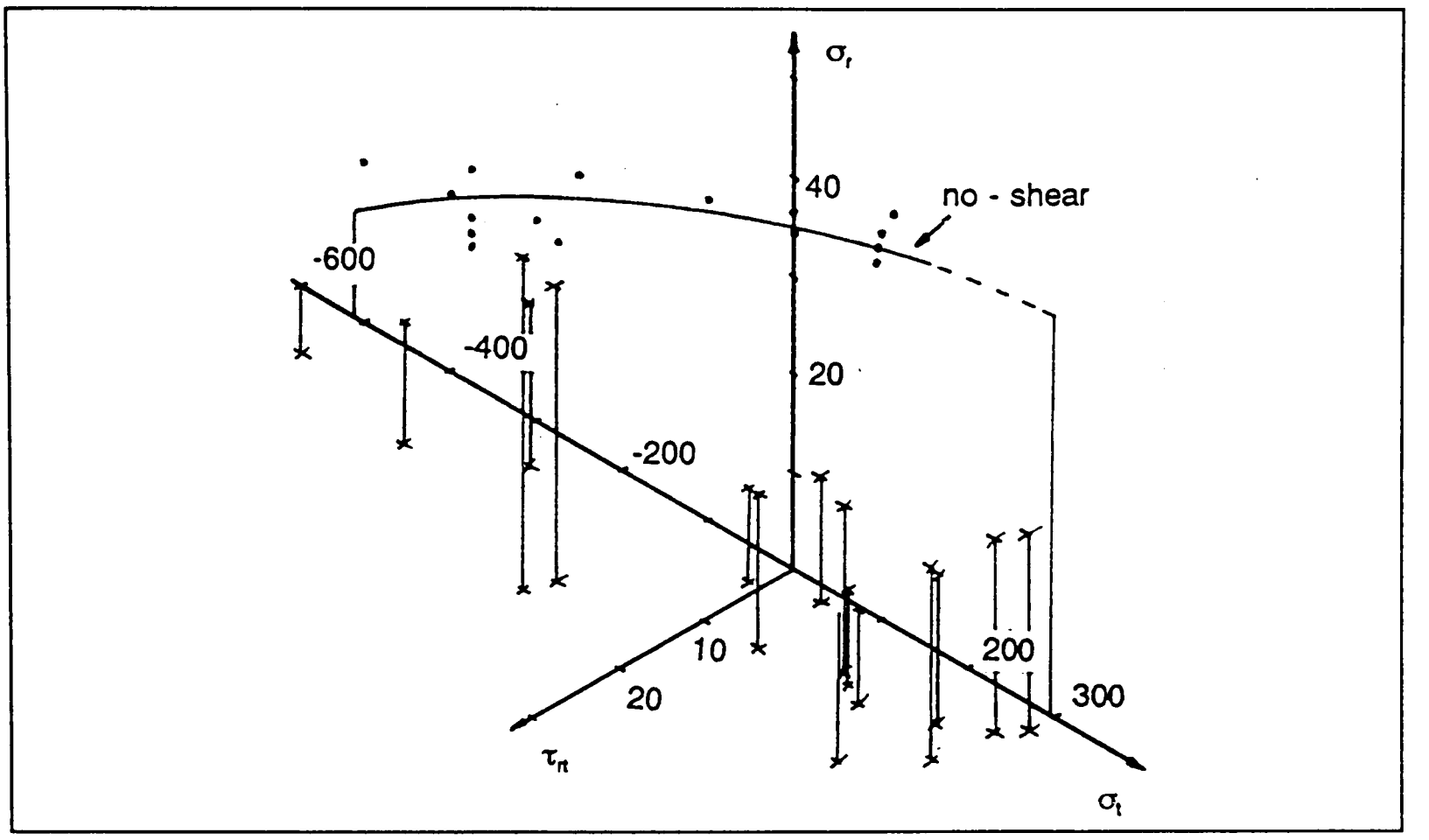

Figure 3.10 Waisted C-specimen test results, together with the data from the plain C-specimen test (no-shear, *ref.*Fig. 3.3).

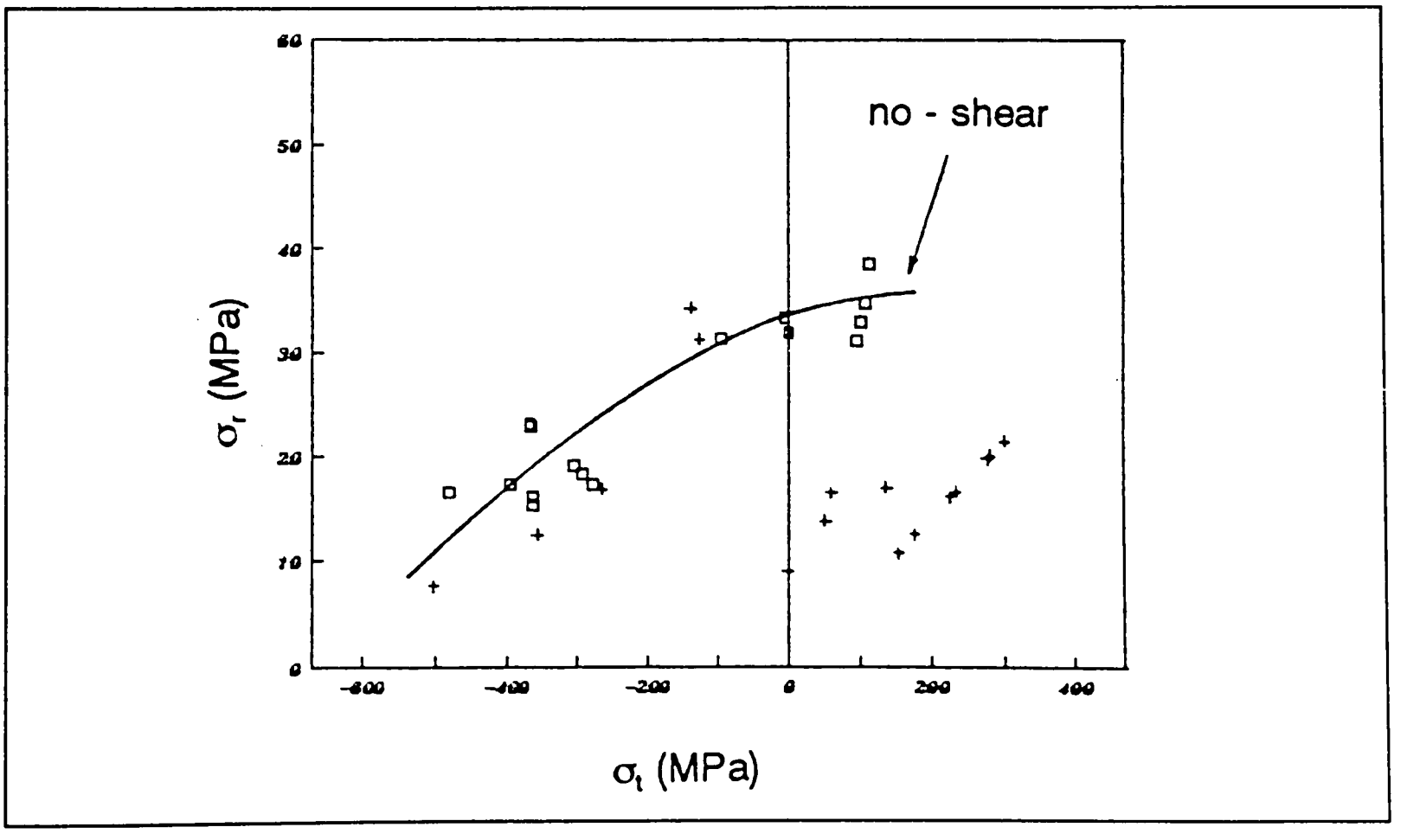

Figure 3.11 Effect of shear stress on failure by comparing the results possessing shear with no-shear data in σ_t-σ_r plane.

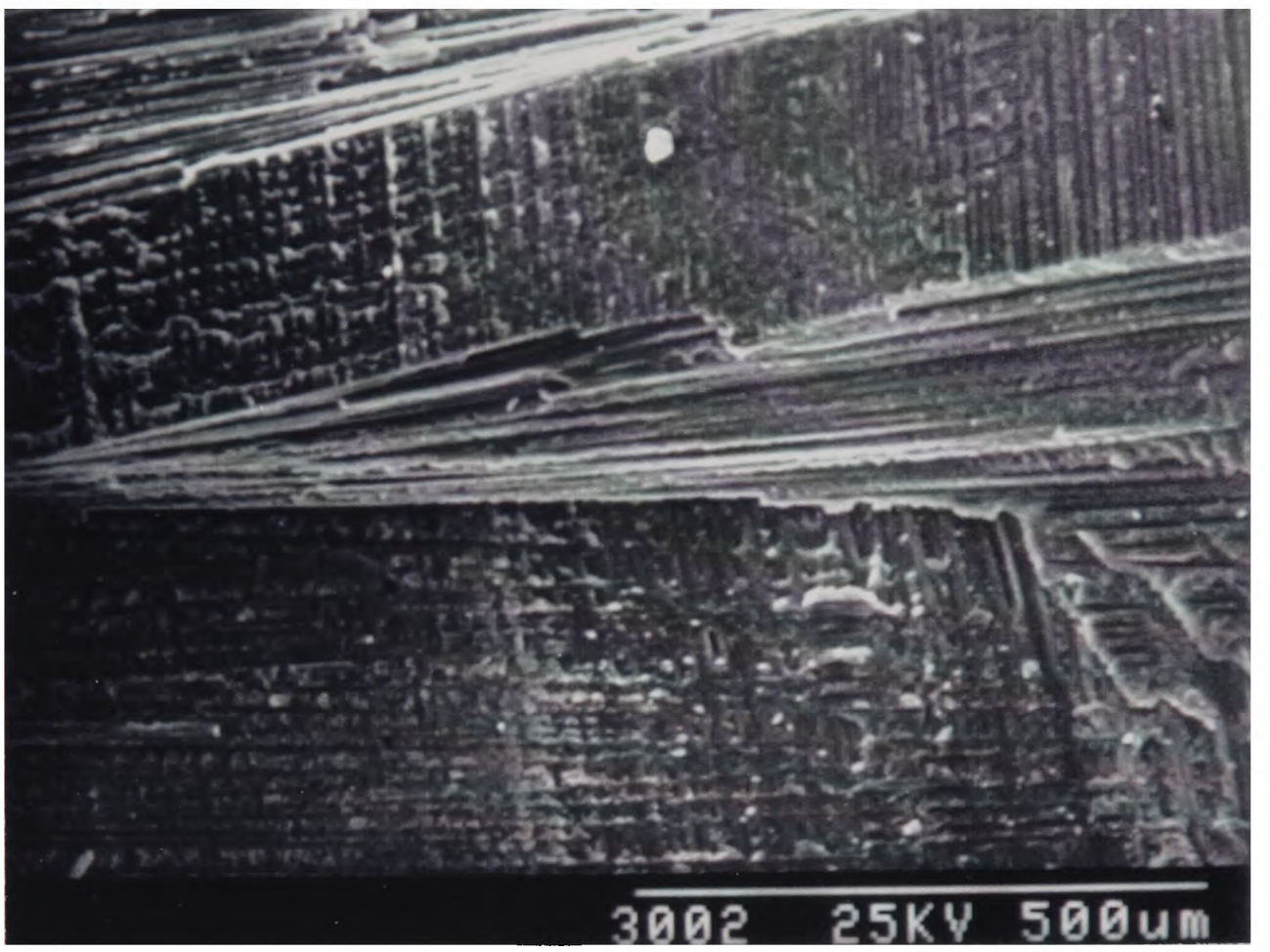

Figure 3.12 (a)

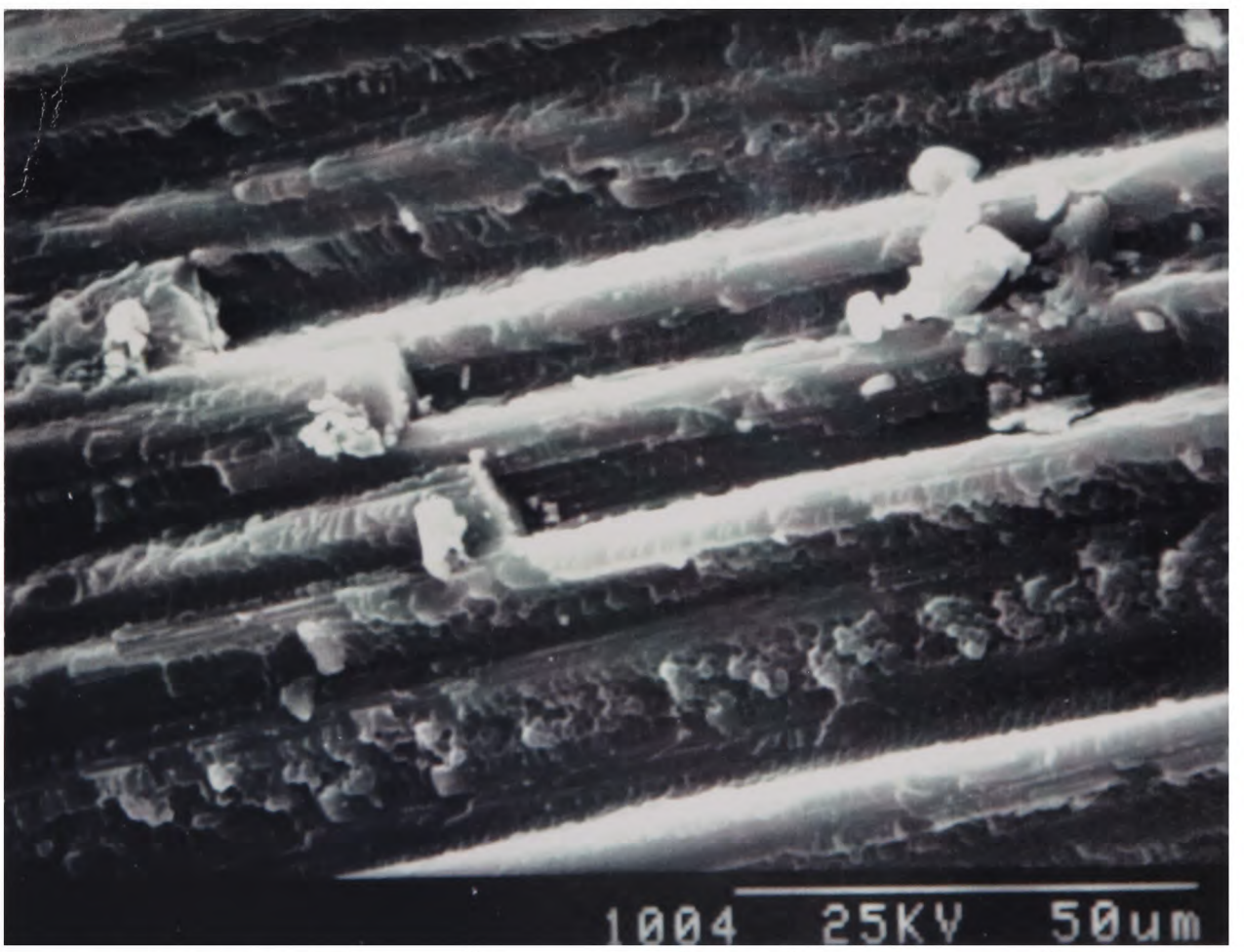

Figure 3.12 (b)

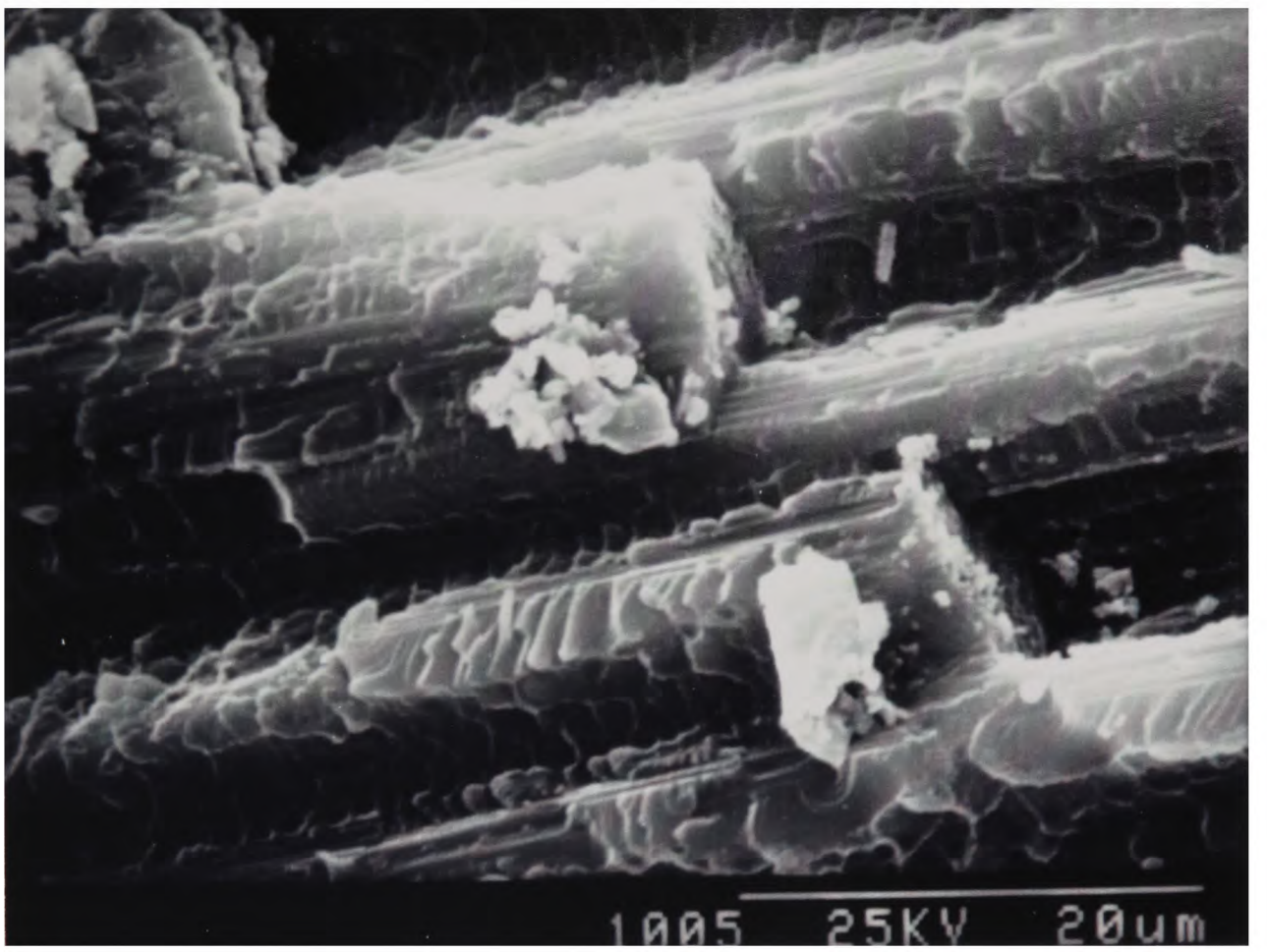

Figure 3.12 (c)

SEM fractographs of delamination layer caused by $\sigma_t(-)$ - $\sigma_r(+)$ - τ_{tr} stress state for C/epoxy.

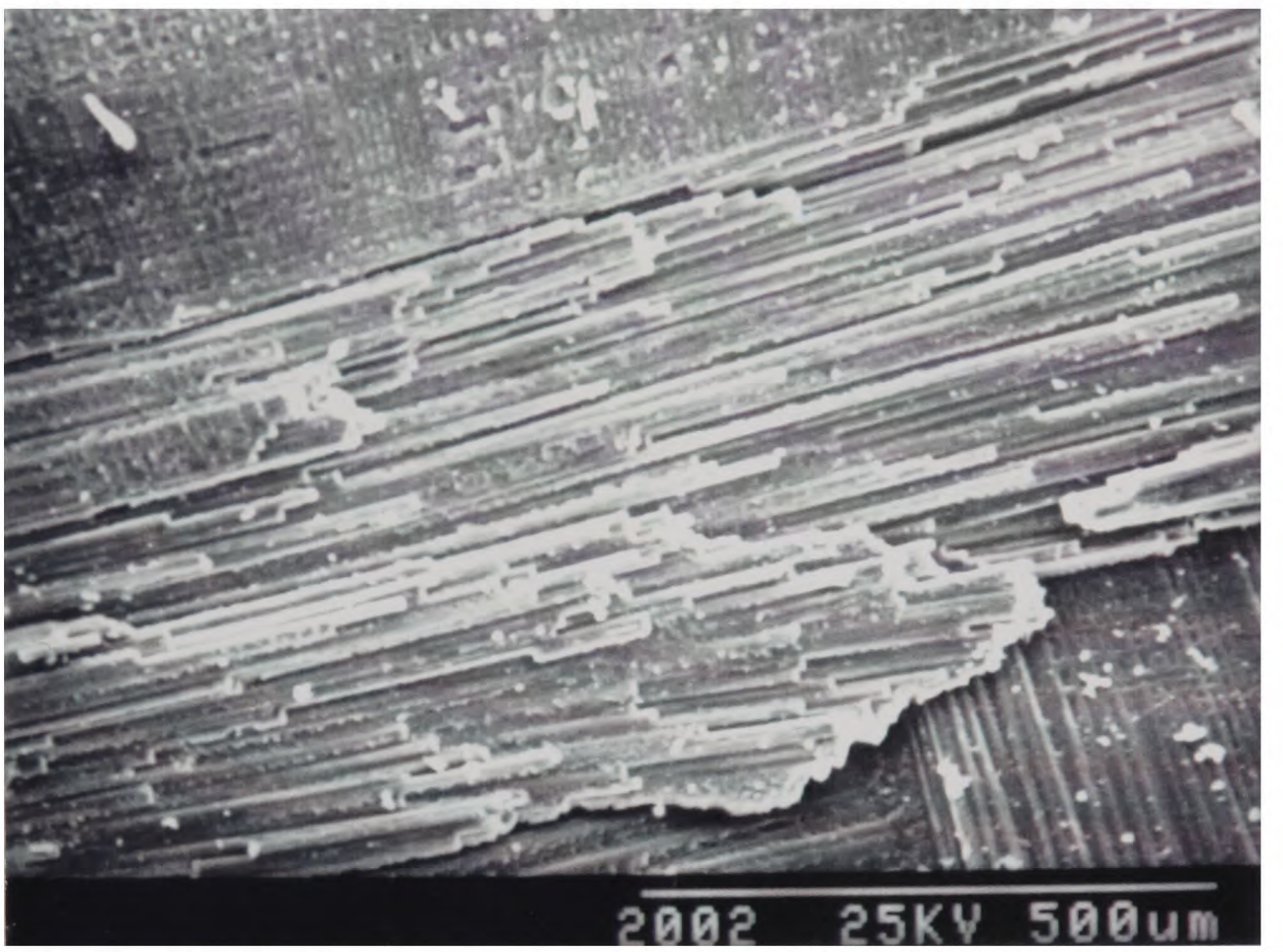

Figure 3.13 (a)

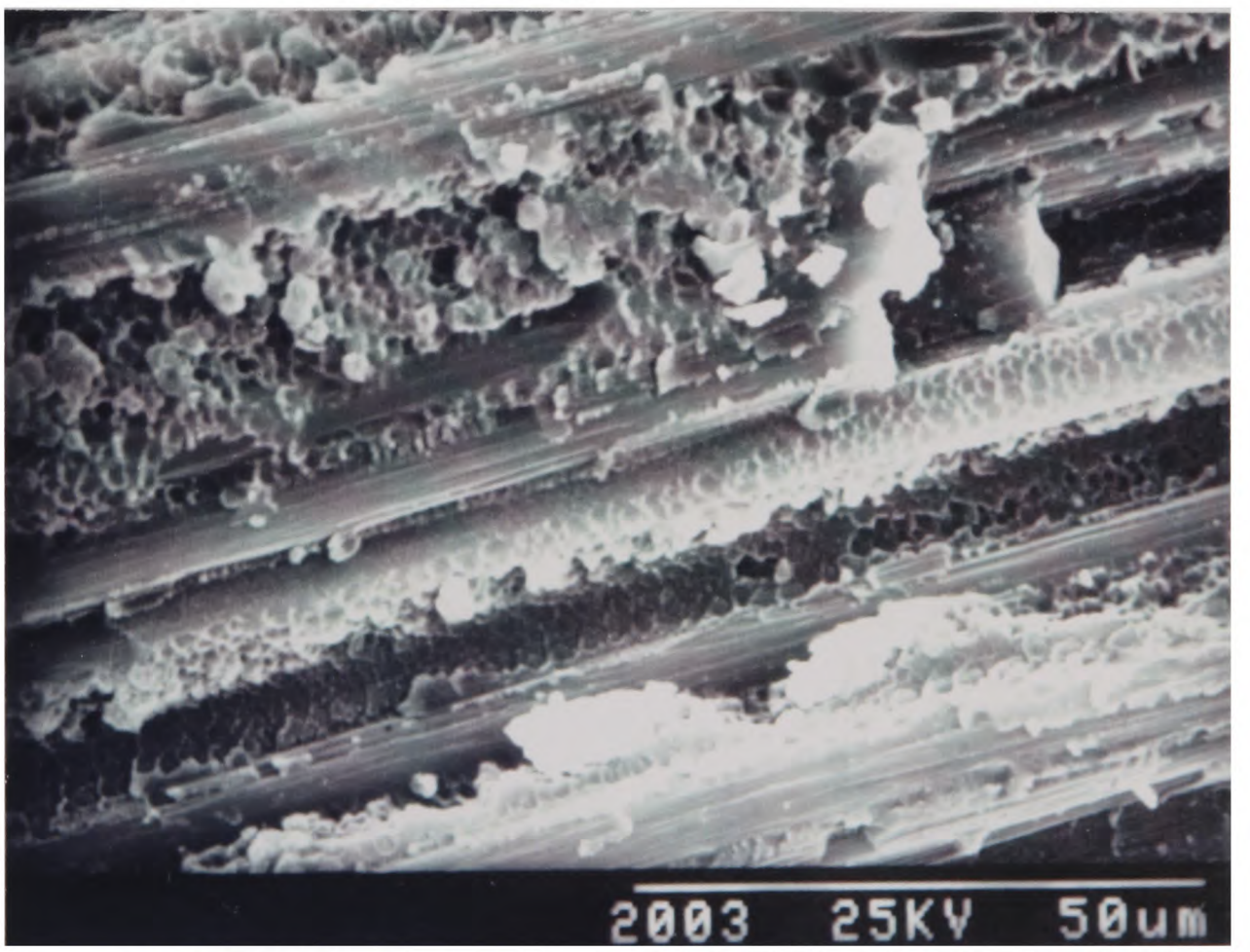

Figure 3.13 (b)

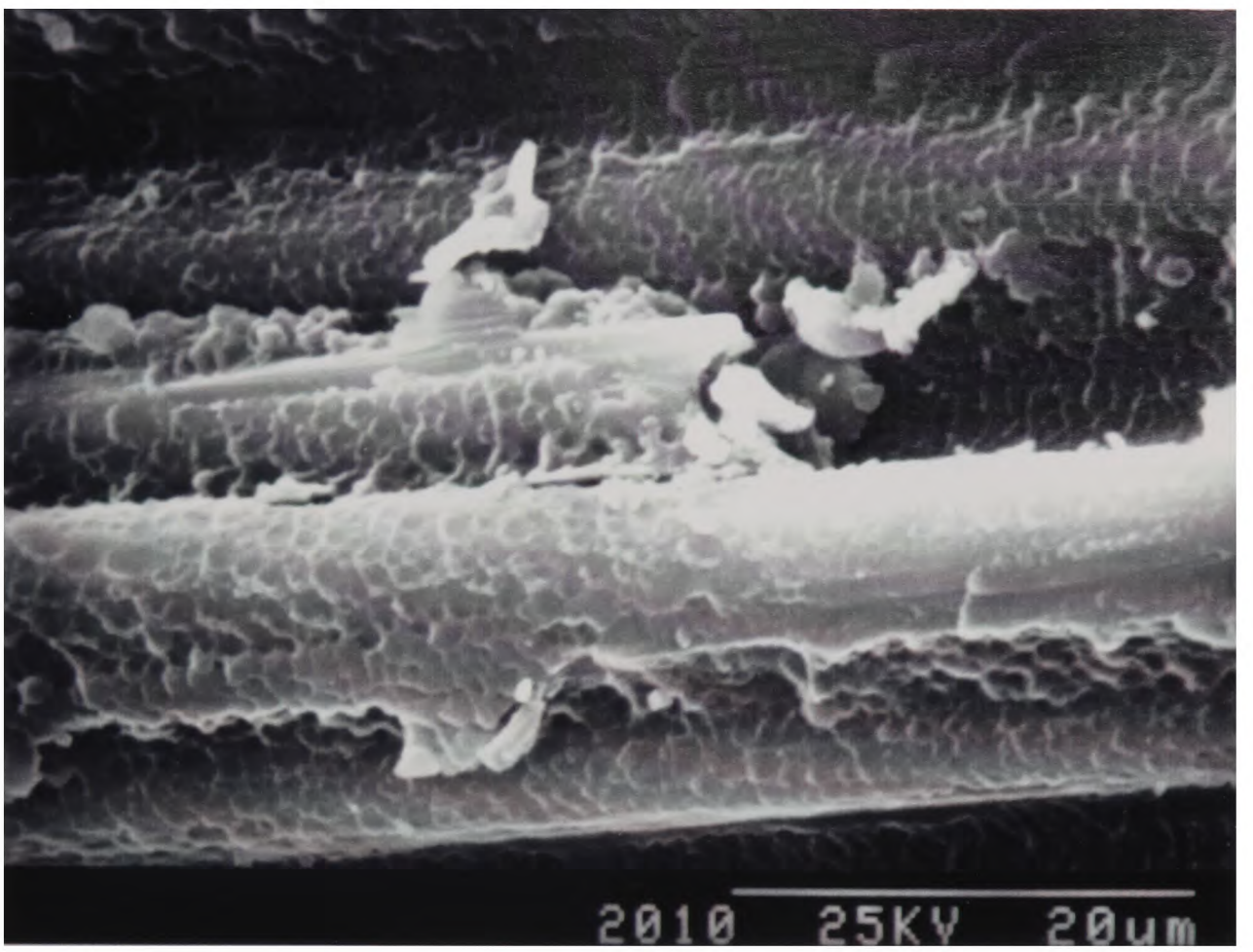

Figure 3.13 (c)

SEM fractographs of delamination layer caused by $\sigma_t(+)$ - $\sigma_r(+)$ - τ_{tr} stress state for C/epoxy.

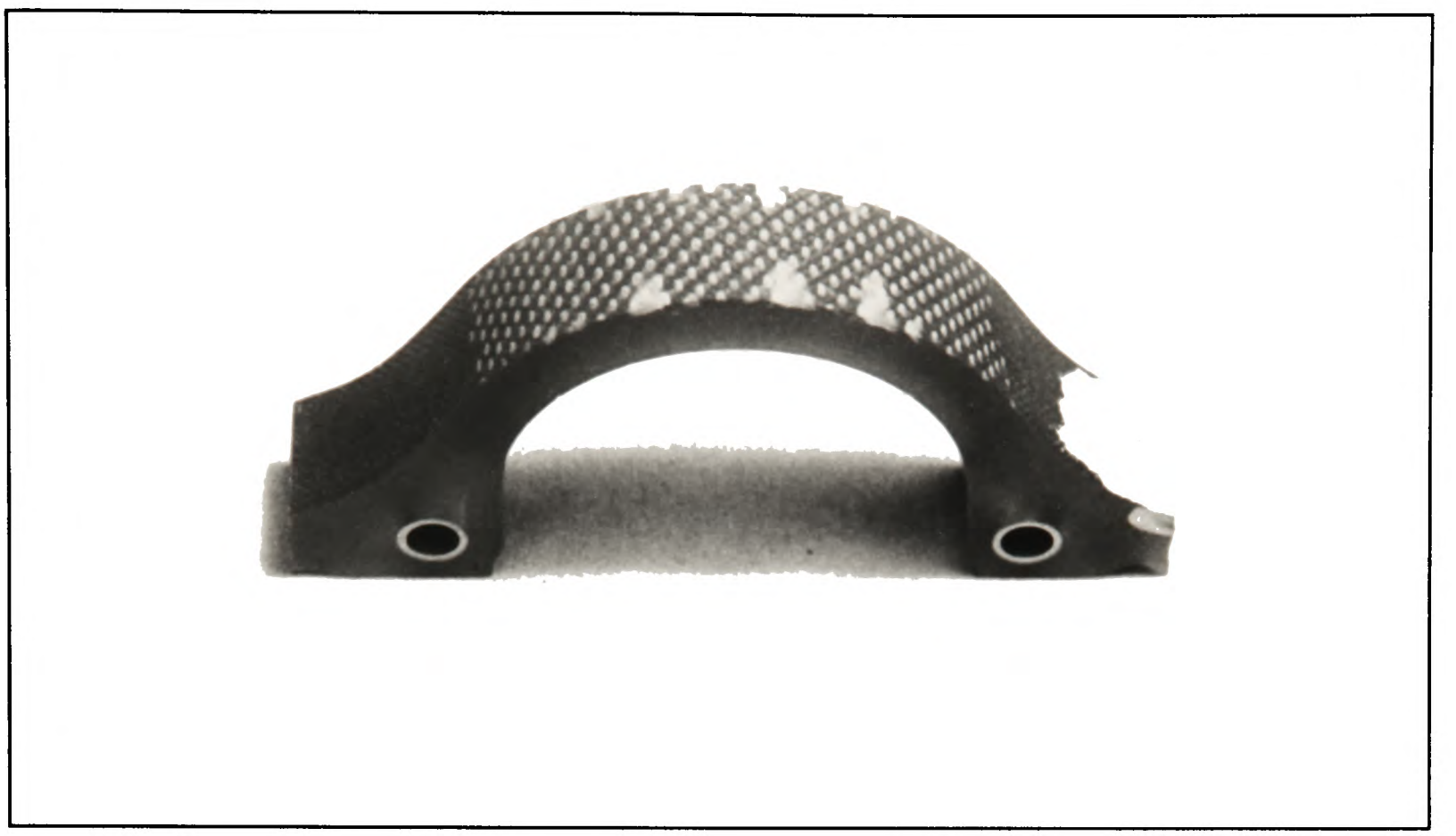

(a) outer surface.

(b) inner surface.

Figure 3.14 Pictures from G/epoxy plain C-specimen, showing the micro-buckling on the outer (a) and inner (b) surfaces before delamination.

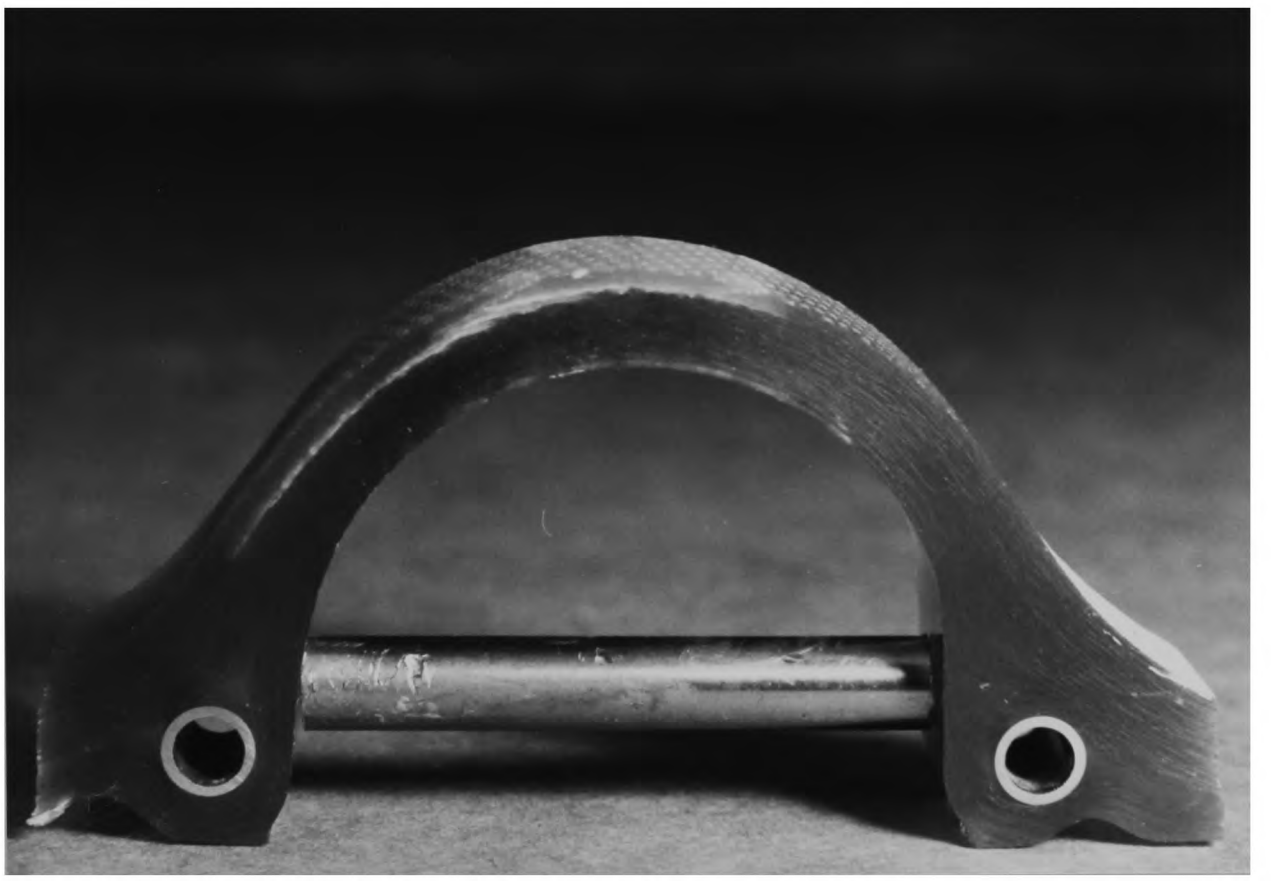

Figure 3.15 Pictures from G/epoxy plain C-specimen, showing the relationship between the micro-buckling and delamination.

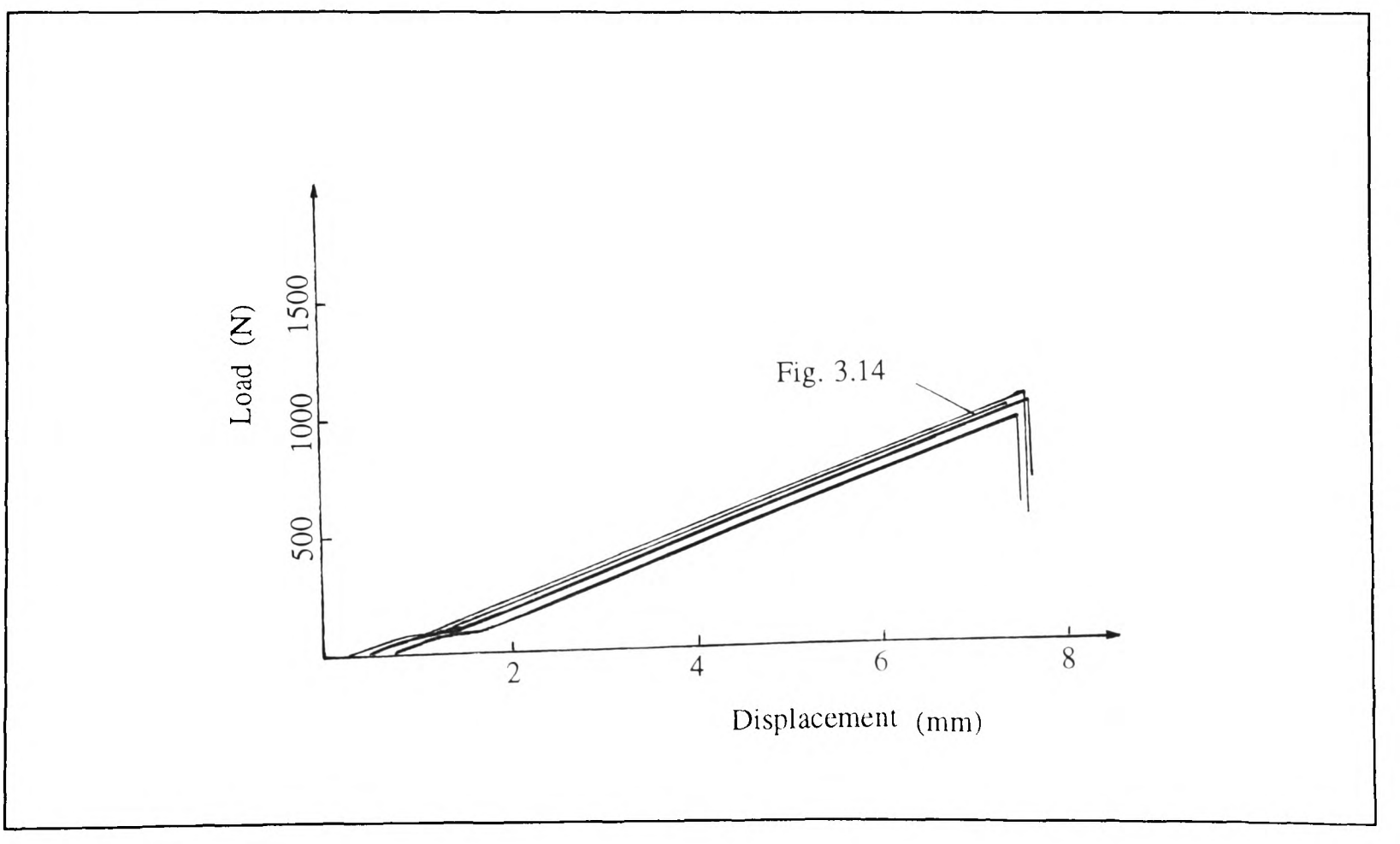

Figure 3.16 The load-displacement curves for the situations in Fig.3.14 and Fig.3.15.

Chapter 4

CENTRAL NOTCHED FOUR-POINT BENDING BEAM TESTS

4.1 GENERAL DESCRIPTION OF THE TEST

Through-thickness stresses can be obtained by making a through-thickness notch in a specimen. Cui, Wisnom & Jones (1992) designed a notched uniaxial tensile specimen as shown in Fig.4.1. The FEM analysis showed that a combined interlaminar tension and shear, and in-plane tension stress state existed on the notched surface. However it can also be seen that with this geometry it is easy to apply a bending moment if there is a small difference in size between the upper and lower notches, which will make the specimen non-symmetric.

A rectangular section beam with a central notch on one side and under four-point bending is shown in Fig. 4.2 (a). As it is known that, without the notch, the stress distribution on the upper surface of the specimen is a constant tension according to classical beam theory (Fig.4.2(b)), the existence of the notch diverts the stress flow line into the notch shape and hence, on the surface of the notch, through-thickness tension and interlaminar shear will be added to in-plane tension (Fig.4.2 (c)). The stress distribution along the notch surface obviously depends on the size and shape of the notch. If a circular notch is chosen and only the depth is changed, different combinations of the stresses will be obtained.

4.2 MATERIALS AND GEOMETRY OF THE SPECIMEN

Both C/epoxy and G/epoxy material systems as described in chapter 2 were used.

a) C/Epoxy

The specimen was made of 20 fabric prepregs with a finished thickness of 5.47 mm and 148x10 mm in the other dimensions. The fibre volume fraction was 45%. Three kinds of specimen geometries were tested and the radius of the central notch was 70mm for all three groups with only the bottom thickness h (or the depth of the notch) changing. The notch was carefully machined by grinding and according to preliminary numerical analysis, h = 2, 3 and 4 mm was chosen.

b) G/Epoxy

The specimen was also made of 20 layers, however, with a finished thickness of 4.4 mm. The fibre volume fraction was 50%. Plates were cut into 148x10 mm with a fixed notch radius of 70mm for all three groups of specimens, which were designed as h = 1.5, 2.5 and 3.5 mm. The notch was also machined by grinding and visual examination did not detect any mechanical defects.

4.3 STRESS ANALYSIS BY FEM

A three-dimensional stress analysis has been carried out by ABAQUS (HKS Inc., 1992). The finite element model is shown in Fig.4.3. Note that only half of the specimen has been modelled due to symmetry. A linear elastic orthotropic material was assumed both for the C/epoxy and for the G/epoxy materials. The material properties of the C/epoxy were the same as those in Table 3.1. For G/epoxy, they were calculated based on the properties of glass fibre

and resin (Appendix 4A). Table 4.1 shows the calculated results. 20-node quadratic brick solid elements (C3D20 in ABAQUS) were used and there were 36 elements along the longitudinal direction, 8 through-the-thickness and 2 along the width. Fig.4.3 shows the numerical analysis for the C/epoxy specimen with h=2 mm. It can be seen that in-plane bending still prevails in the specimen with a maximum tensile stress 754 MPa and maximum compressive stress 694 MPa at the very bottom section. Shear stress, as an induced stress, is mainly on the notch surface. Through-thickness tension is generally quite small even compared with the nominal strength (36 MPa) and the maximum value is 7 MPa, also on the notch. Reducing notch radius may increase the value of σ_3, but this will cause stress concentration especially for in-plane tension. For the current geometry, Fig.4.4 shows the distribution of σ_1 along the through-thickness at the very bottom of the notch, which presents little stress concentration caused by the notch. The distributions of σ_1, τ_{13} and σ_3 along the notch surface are shown in Fig.4.6. Notice that the relative stresses are presented, i.e. each stress component is divided by its respective nominal strength, i.e. σ_1^*=473 MPa (Rolls-Royce), τ_{13}^*=48 MPa (Hognestad, 1993) and σ_3^*=36 MPa (Table 2.5).

Table 4.1 Elastic Engineering Constants for G/Epoxy Woven Laminate

E_1	24.61E3 MPa	ν_{12}	0.123	G_{12}	3.96E3 MPa
E_2	24.61E3 MPa	ν_{13}	0.38	G_{13}	3.21E3 MPa
E_3	11.51E3 MPa	ν_{23}	0.38	G_{23}	3.21E3 MPa

4.4 TEST

Tests were done using a Instron machine and monitored by a load-displacement recorder. The cross-head speed was 1.0 mm/minute. The test rig was a standard 4-point bending rig, where the loading point is a ball on the centre of upper loading plate. This is a very efficient way to secure alignment.

4.5 EXPERIMENTAL RESULTS

a) C/Epoxy

All tests show linear load-displacement relations (Fig.4.5). The failure load and delamination position are shown in Table 4.2. The recorded failure load and specimen geometry were put into ABAQUS code and the stress components at failure along the notch surface are shown in Fig.4.7, with the x-axis scaled by ply number.

Two things can be easily observed from the test results. Firstly, the delamination happened where expected by calculation, as shown in Fig.4.6, for h=2 mm there is a peak of σ_1 between ply 0 and 1 and for h=3mm a quite large combination of σ_1 and τ_{13} appears there as well, therefore in both of the two situations failure should happen between ply 0 and 1; for h=4mm there is a close-to-strength shear stress between ply 2 and 3 where failure did happen. The failure stresses are listed in Table 4.3. Secondly it is noticed that when h=2 mm, the peak value of σ_1, 753 MPa, is much higher than quoted in-plane tensile strength, 473 MPa. It seems that the in-plane strength under this stress state should be higher. Actually by replacing σ_1^*=473 MPa with 753 MPa, or multiplying all in-plane stress by a ratio 473/753 = 1/1.59,

Fig.4.6 is modified into Fig.4.7, which can be found more close to experimental results. The first reason for the discrepancy might be that the strength comes from the average value among a lot of experimental data while the calculated stress here is the maximum. Considering that the strength is measured by means of a standard tensile test in which a uniform stress distribution prevails, the stress gradient in the current test might be another reason to explain this result.

Fractographic examination by SEM has been done for the three geometries (Fig. 4.8). The pictures reveal very different features reflecting corresponding failure mechanisms.

Table 4.2 Failure Load and Delamination Position for C/Epoxy

Group	Bottom Thickness(mm)	Specimen no	Failure Load (kN)	Average Load (kN) and Deviation	Delamination Position (between plies) *
1	2	1-1	0.483	0.467 (3%)	0 - 1
		1-2	0.453		0 - 1
		1-3	0.465		0 - 1
2	3	2-1	0.809	0.773 (5%)	0 - 1
		2-2	0.737		0 - 1
3	4	3-1	1.482	1.442 (9%)	2 - 3
		3-2	1.270		2 - 3
		3-3	1.575		2 - 3

* Only notched plies are numbered and started from bottom to top.

Table 4.3 Failure Stresses for C/Epoxy

Group	Bottom Thickness(mm)	Stress Components at Failure (MPa)		
		σ_1	τ_{13}	σ_3
1	2	752.81	0	0
2	3	484.12	31.58	2.18
3	4	325.41	43.35	4.45

b) G/Epoxy

The load-displacement curves are in Fig.4.9, the failure load and the delamination position in Table 4.4 and the calculated failure stress along the notch surface in Fig.4.10. Again relative stresses are presented and the strengths are calculated by an empirical formula (Appendix.4A) as, σ_1^*=712 MPa, τ_{13}^*=39.3 MPa and σ_3^*=44.3 MPa. However it should be mentioned that these calculated material strengths are only used to plot the stresses in a non-dimensional form in the same graph and not as a basis for further analysis. As Harris (1991) points out, although the current ability to predict the elastic properties of a given composite is sufficiently accurate for most practical purposes, accurate prediction of strength is still much more difficult because it depends not only on the properties of the constitutive materials but also on the mechanisms of failure, therefore reliable mechanical properties for polymer laminate can only be obtained experimentally.

In Fig.4.10, features similar to those in the C/epoxy material are found. As h changes from 1.5, 2.5 to 3.5 mm, the failure stress distribution along the notch surface shows peak values of σ_1, σ_1 & τ_{13} and τ_{13} respectively. It was also found that the failure positions coincided with

the predictions from calculation. The failure stresses are listed in Table 4.5. The transparent material also clearly showed that cracks initiated at both sides of the notch and propagated uniformly along the width of the specimen (Fig.4.11), and propagated very quickly. SEM pictures for the fracture surfaces are in Fig. 4.12.

Table 4.4 Failure Load and Delamination Position for G/Epoxy

Group	Bottom Thickness(mm)	Specimen no	Failure Load (kN)	Average Load(kN) and Deviation	Delamination Position (between plies) *
1	1.5	1-1	0.2099	0.1945 (5%)	0 - 1
		1-2	0.1663		0 - 1
		1-3	0.2073		0 - 1
2	2.5	2-1	0.5670	0.5242 (7%)	0 - 1
		2-2	0.5230		0 - 1
		2-3	0.4827		0 - 1
3	3.5	3-1	1.258	1.138 (8%)	2 - 3
		3-2	1.104		2 - 3
		3-3	1.051		2 - 3

* Only notched plies are numbered and started from bottom to top.

Table 4.5 Failure Stresses for G/Epoxy

Group	Bottom Thickness(mm)	Stress Components at Failure (MPa)		
		σ_1	τ_{13}	σ_3
1	1.5	571.0	0	0
2	2.5	465.8	26.56	1.64
3	3.5	390.4	49.19	6.42

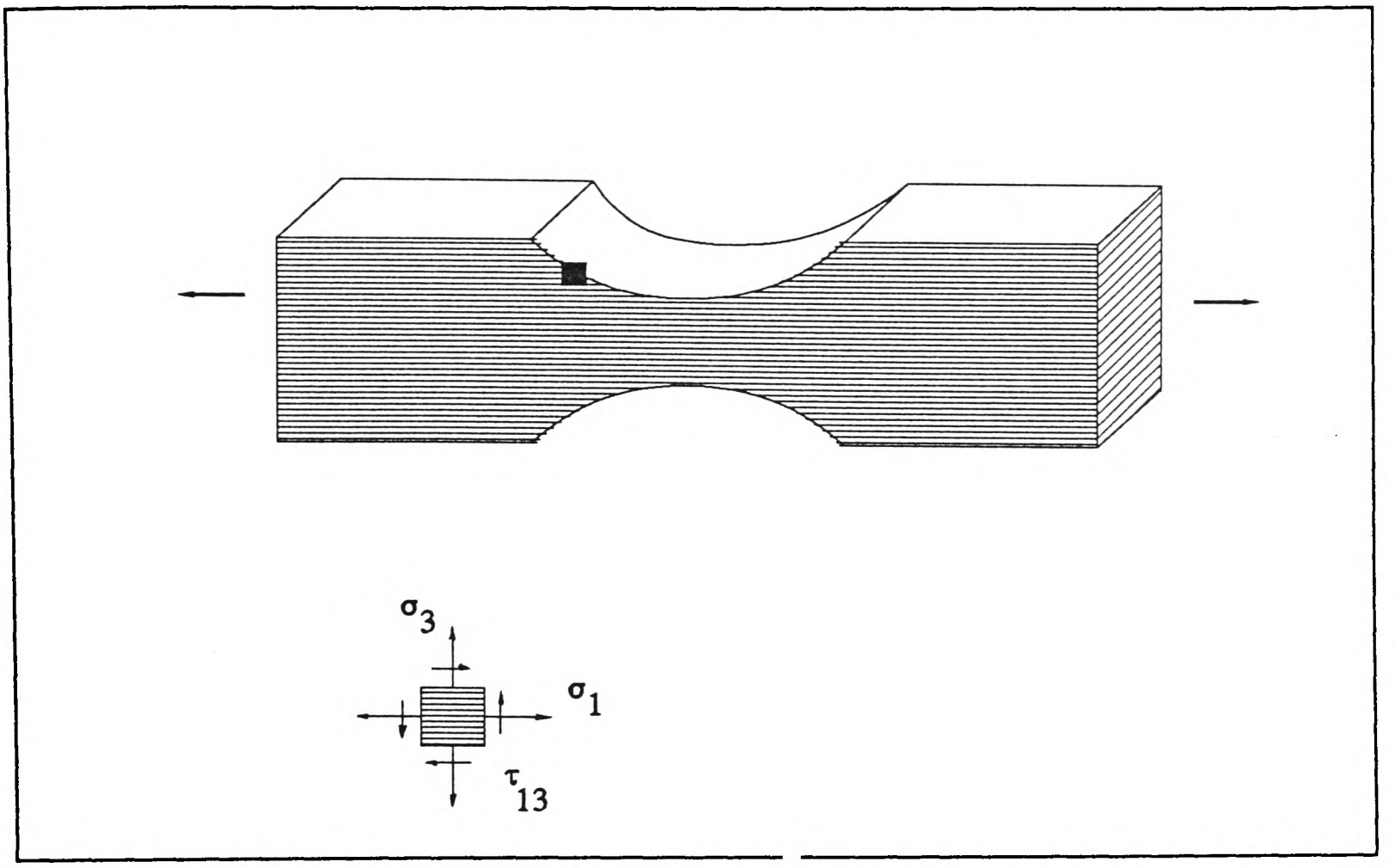

Figure 4.1 The notched uniaxial tensile specimen (Cui, Wisnom & Jones, 1992).

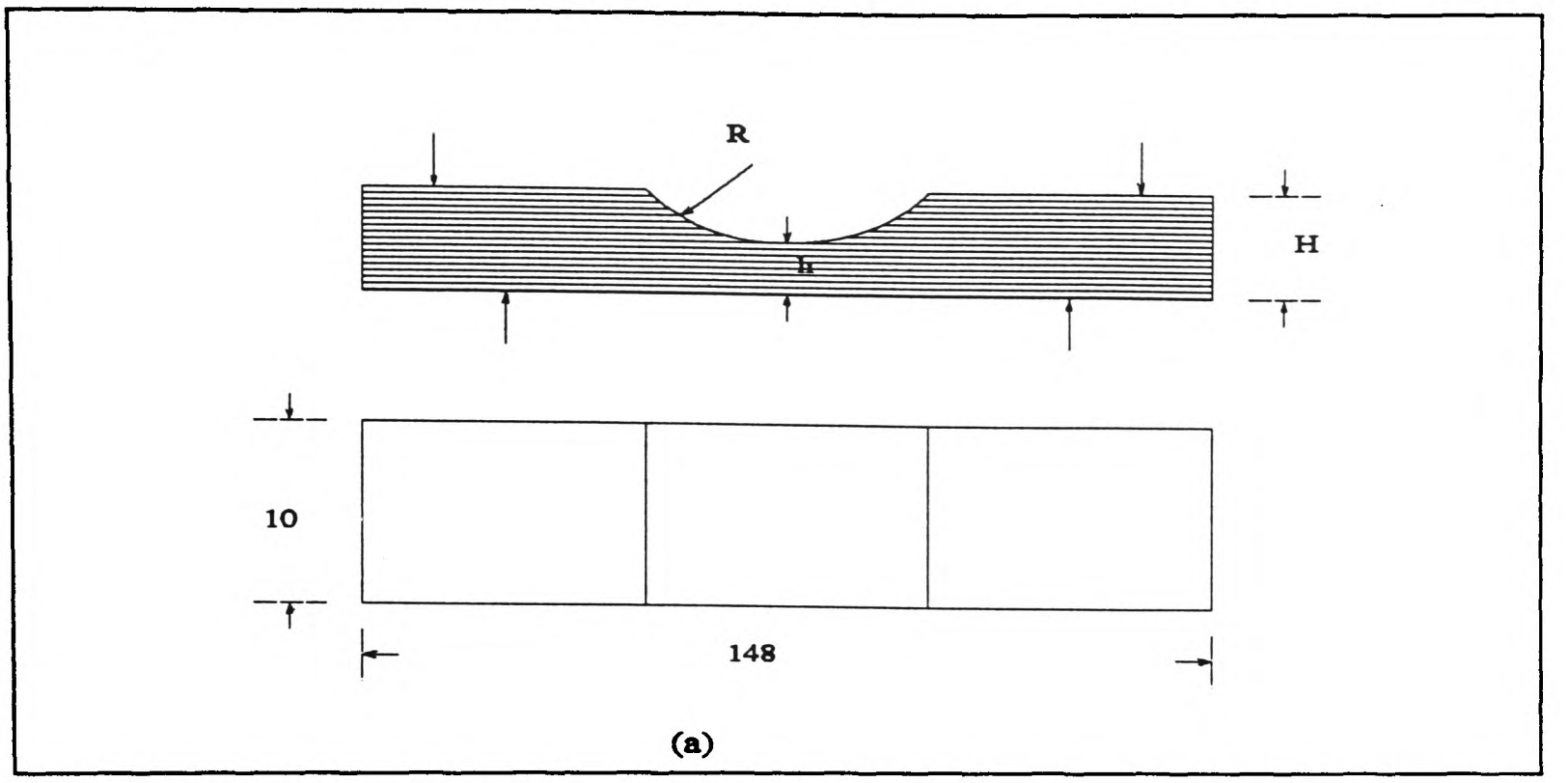

Figure 4.2 The central notched four-point bending beam test.

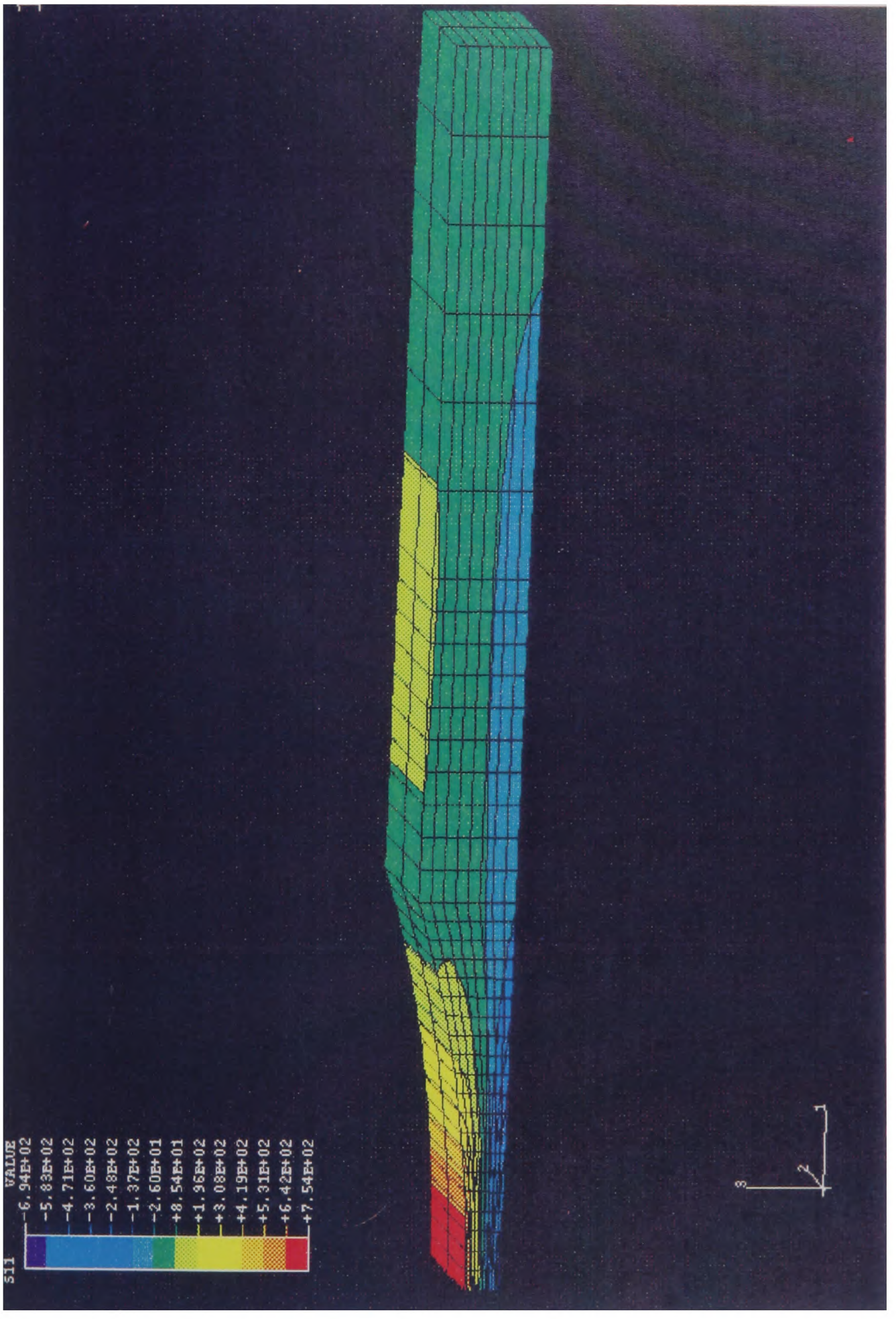

Figure 4.3 (a) σ_1

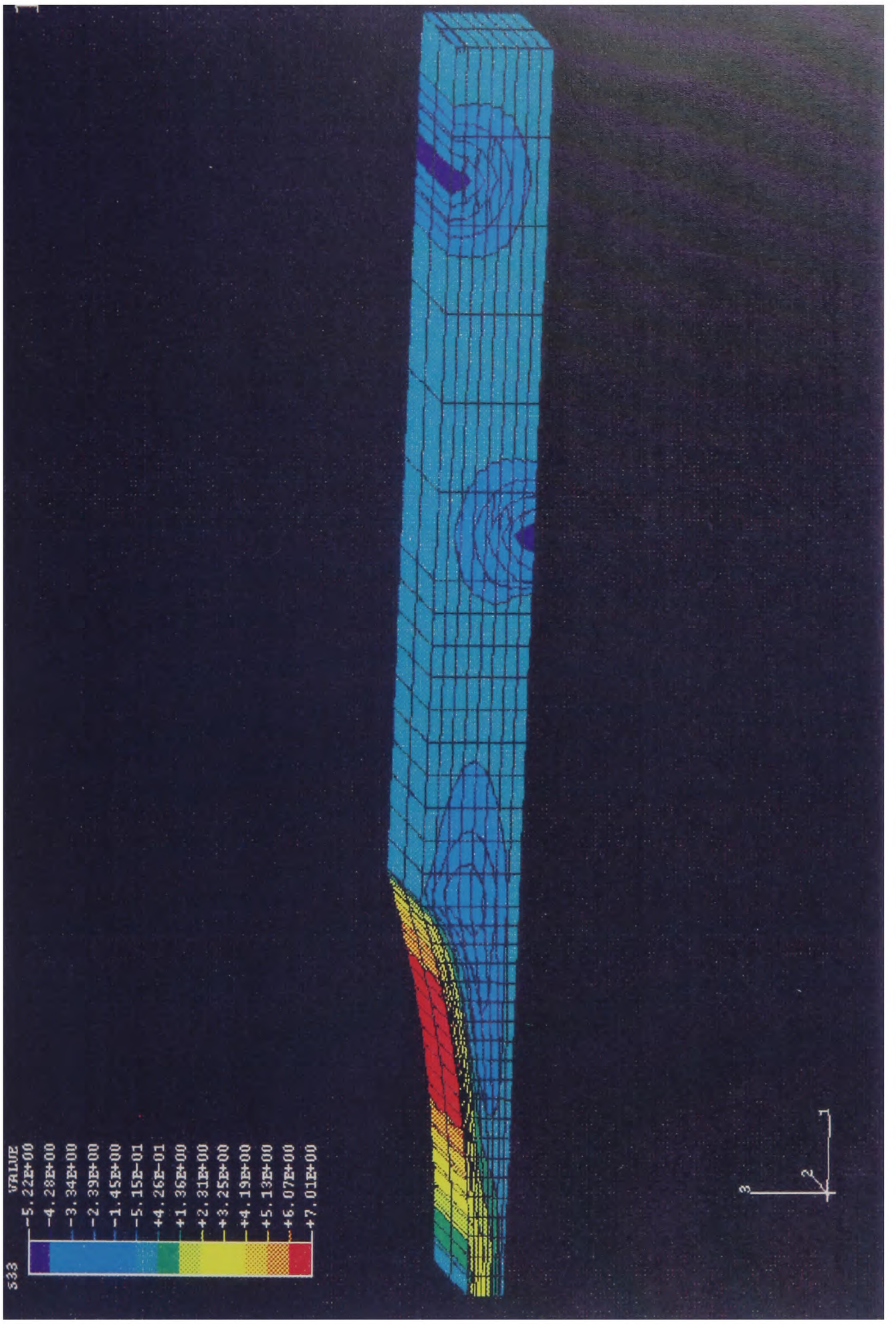

Figure 4.3 (b) σ_3

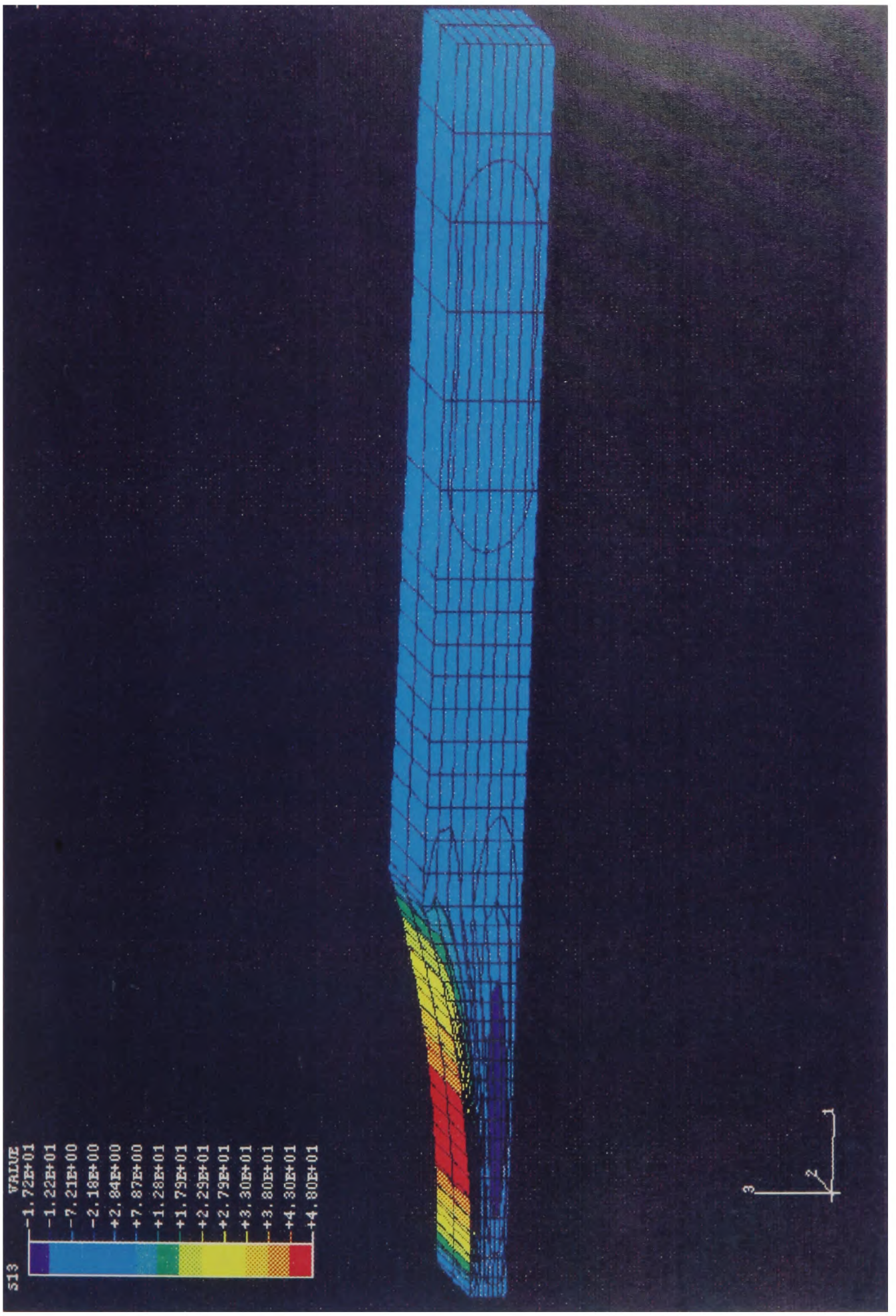

Figure 4.3 (c) τ_{13}

Stress distribution contours by FEM for the h=2 mm geometry of C/epoxy.

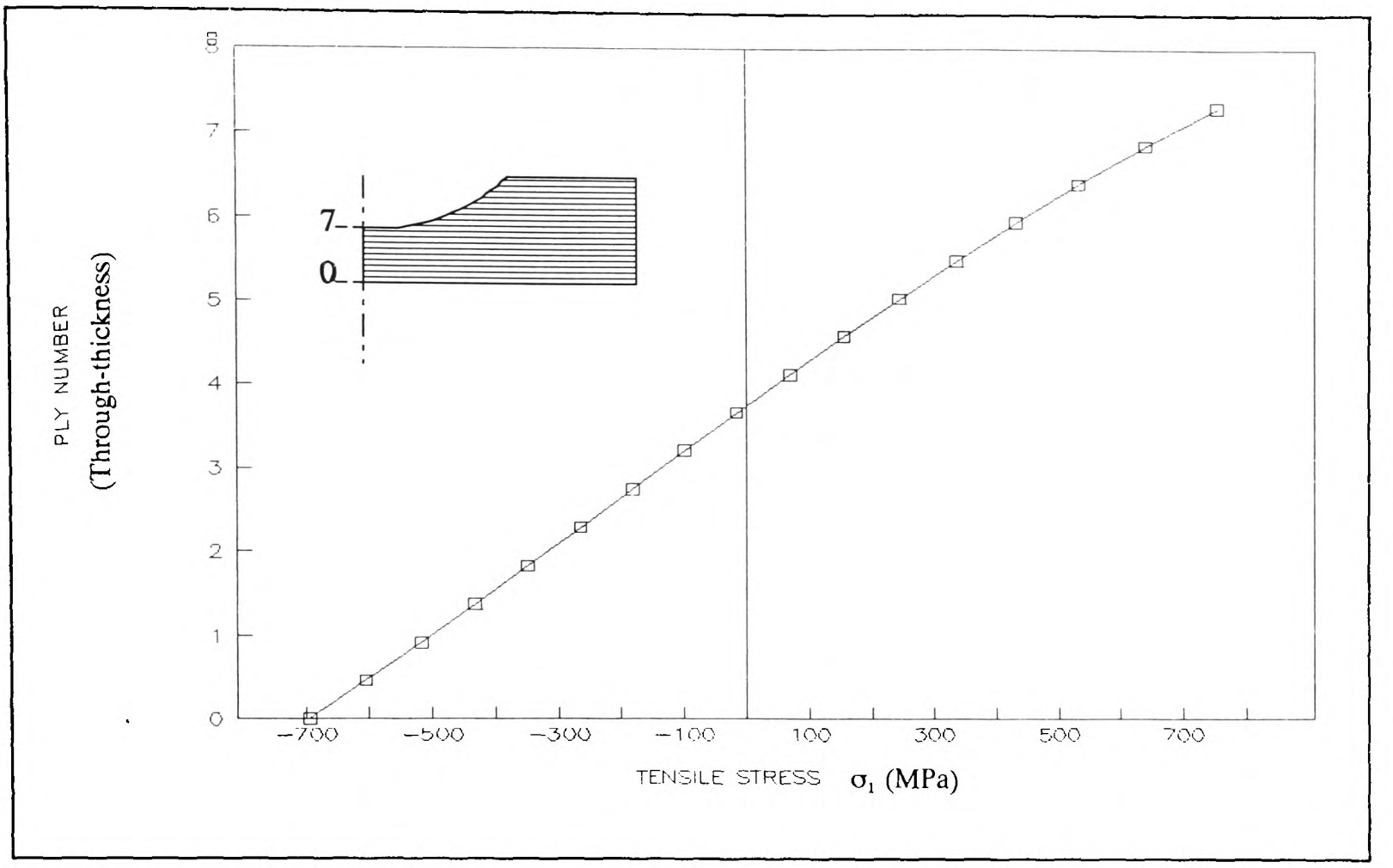

Figure 4.4 The distribution of σ_1 along the through-thickness at the very bottom of the notch for the h=2 mm geometry.

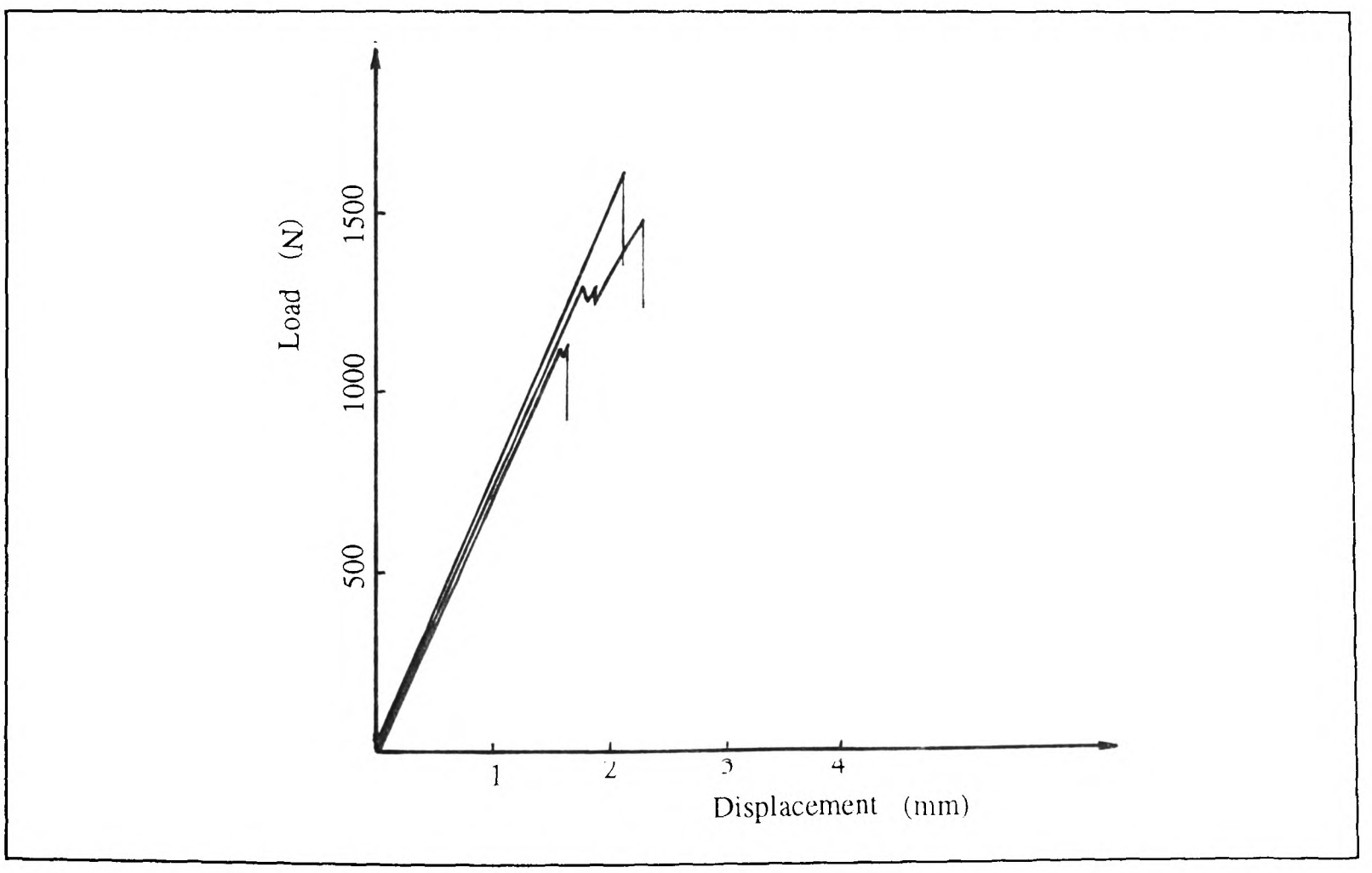

Figure 4.5 The load-displacement curves for C/epoxy notched beam tests. (Table 4.2 Group 3)

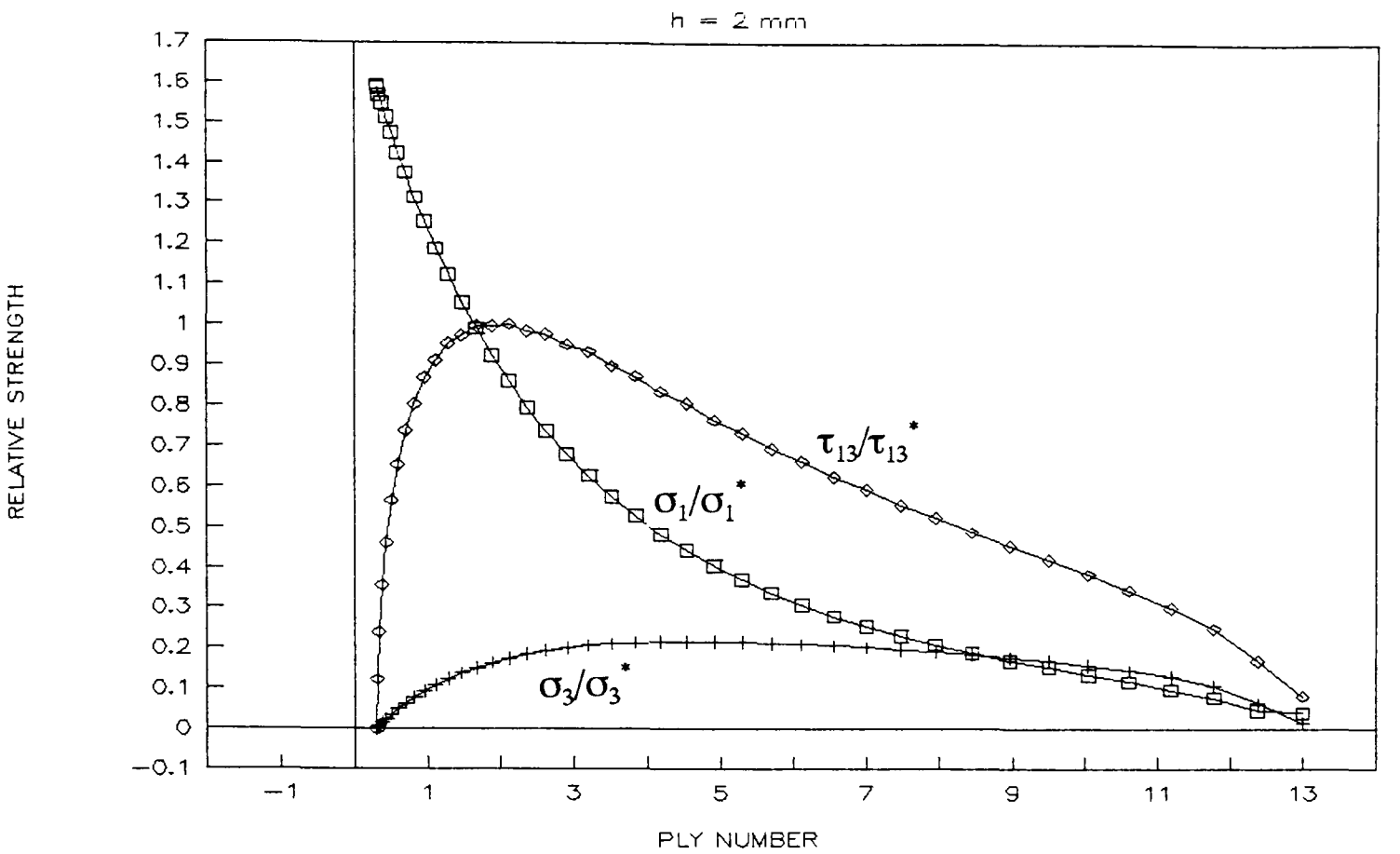
h = 2 mm
RELATIVE STRENGTH
PLY NUMBER
τ_{13}/τ_{13}^*
σ_1/σ_1^*
σ_3/σ_3^*
h = 3 mm
RELATIVE STRENGTH
PLY NUMBER
τ_{13}/τ_{13}^*
σ_1/σ_1^*
σ_3/σ_3^*

Figure 4.6

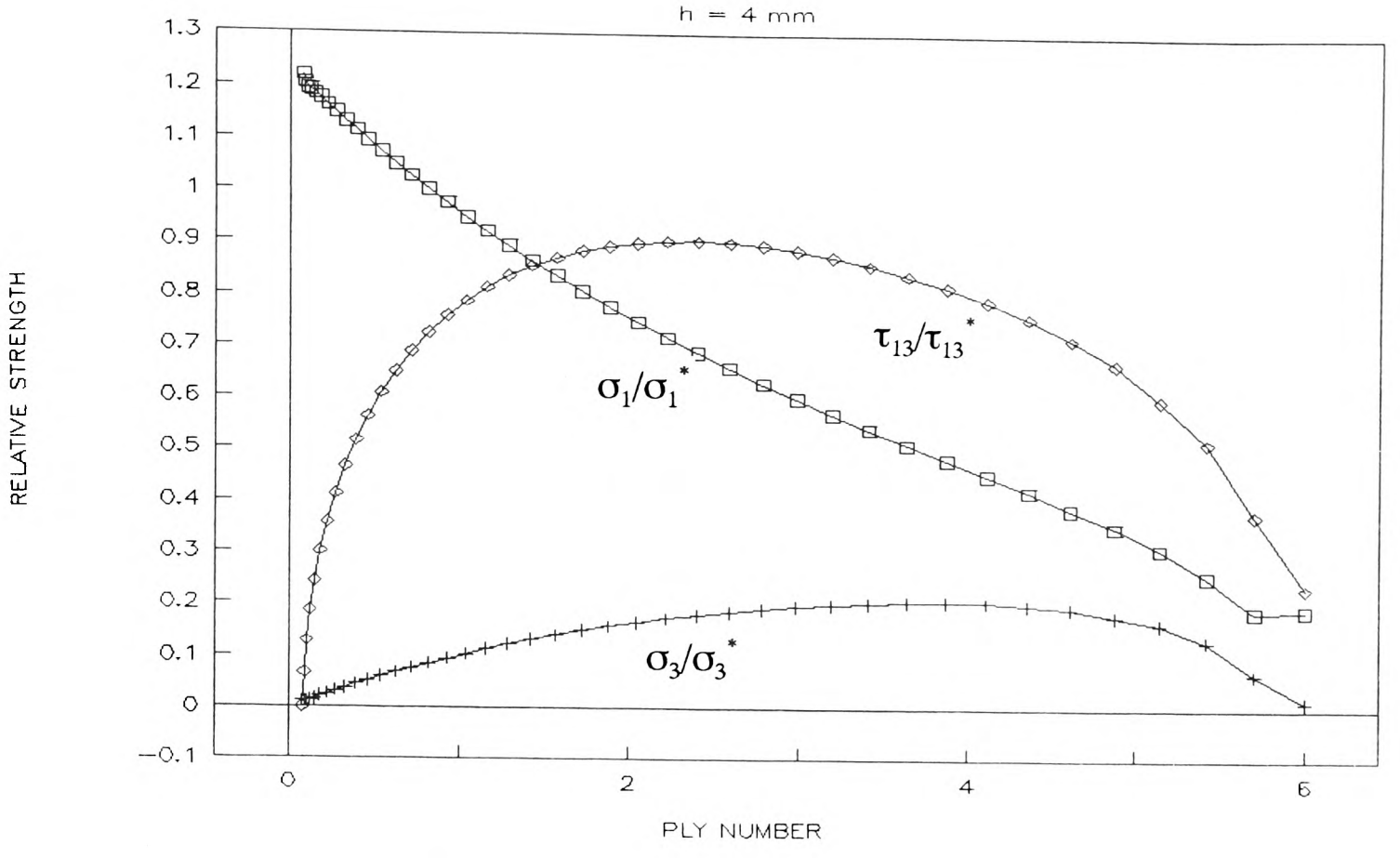

Figure 4.6 Stress distribution along the notched surface, calculated by FEM.

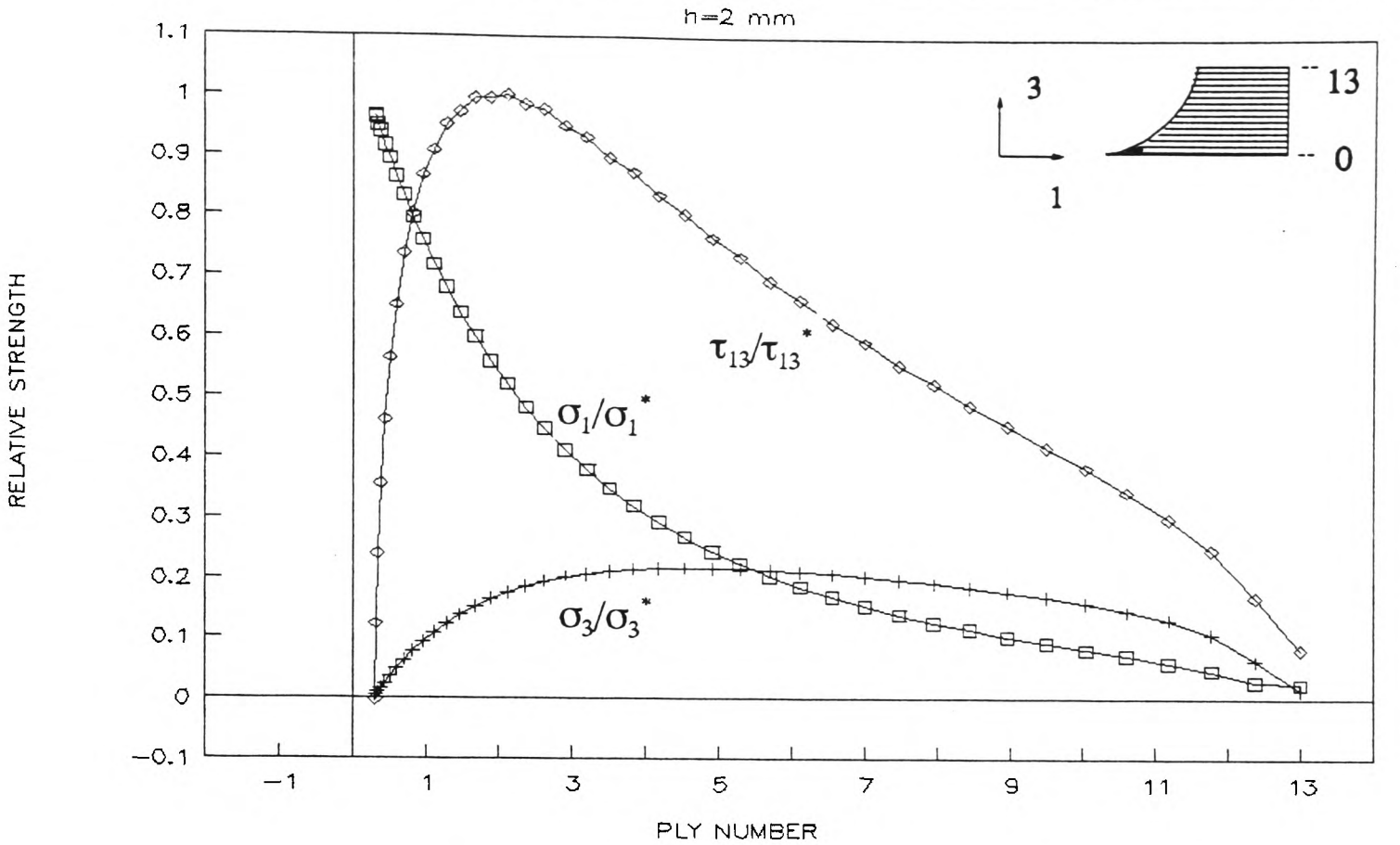
h=2 mm
RELATIVE STRENGTH
PLY NUMBER
τ_{13}/τ_{13}^*
σ_1/σ_1^*
σ_3/σ_3^*
3
1
13
0
h=3 mm
RELATIVE STRENGTH
PLY NUMBER
τ_{13}/τ_{13}^*
σ_1/σ_1^*
σ_3/σ_3^*
3
1
9
0

Figure 4.7

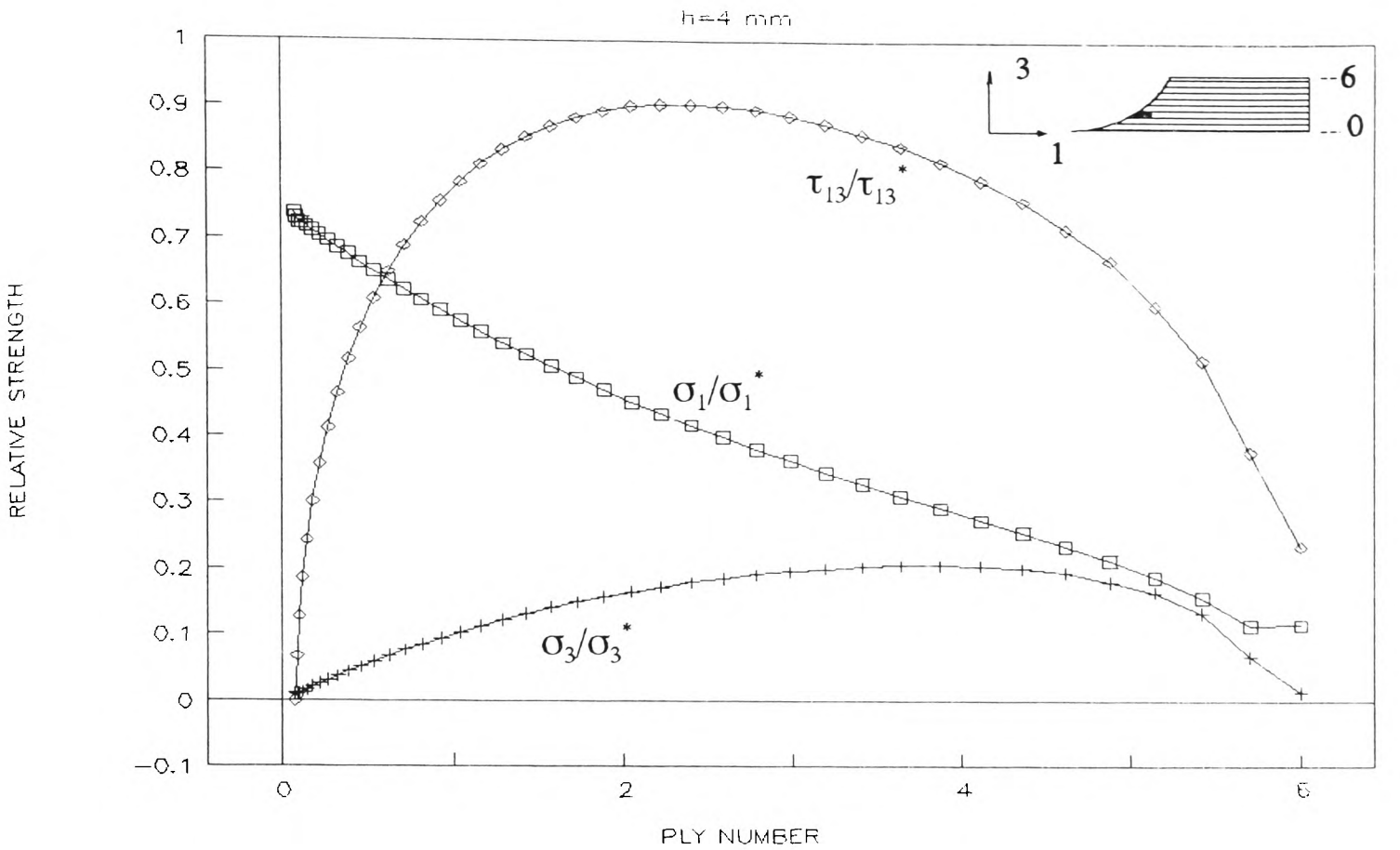

Figure 4.7 Numerical analysis by FEM based on experimental results for C/epoxy specimens.

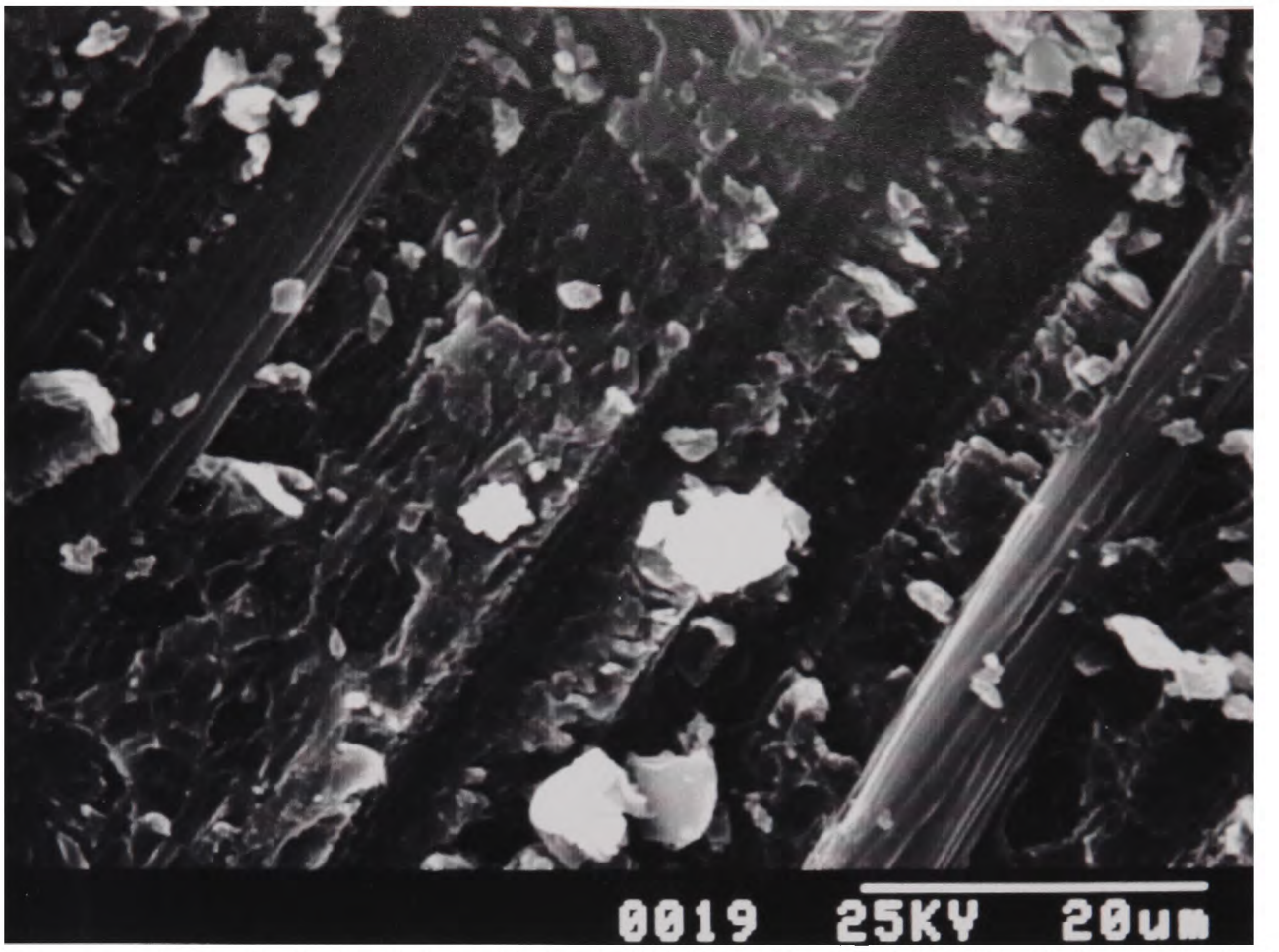

Figure 4.8 (a) h=2 mm

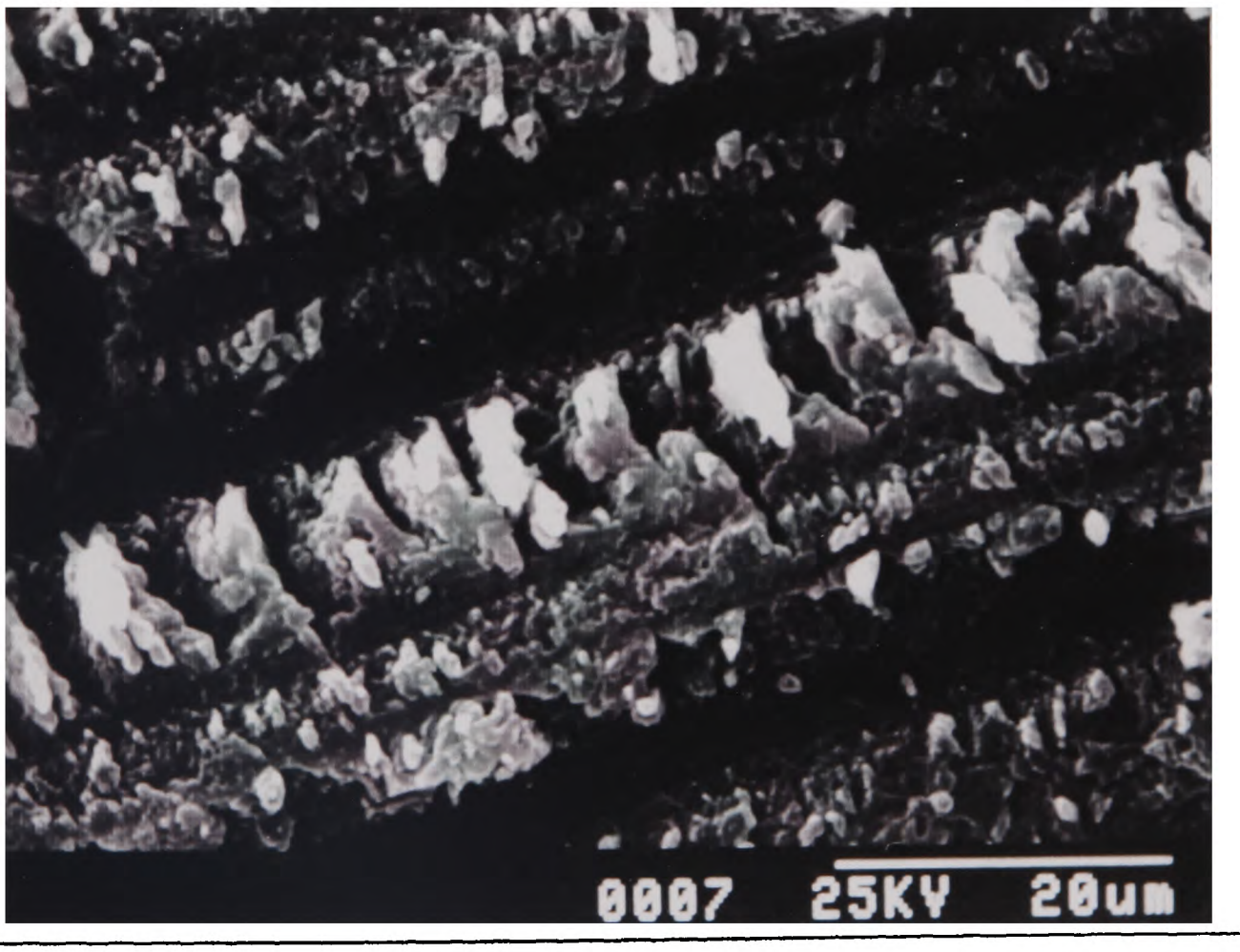

Figure 4.8 (b) h=3 mm

Figure 4.8 (c) h=4 mm

SEM fractographs from C/epoxy notched beam specimens.

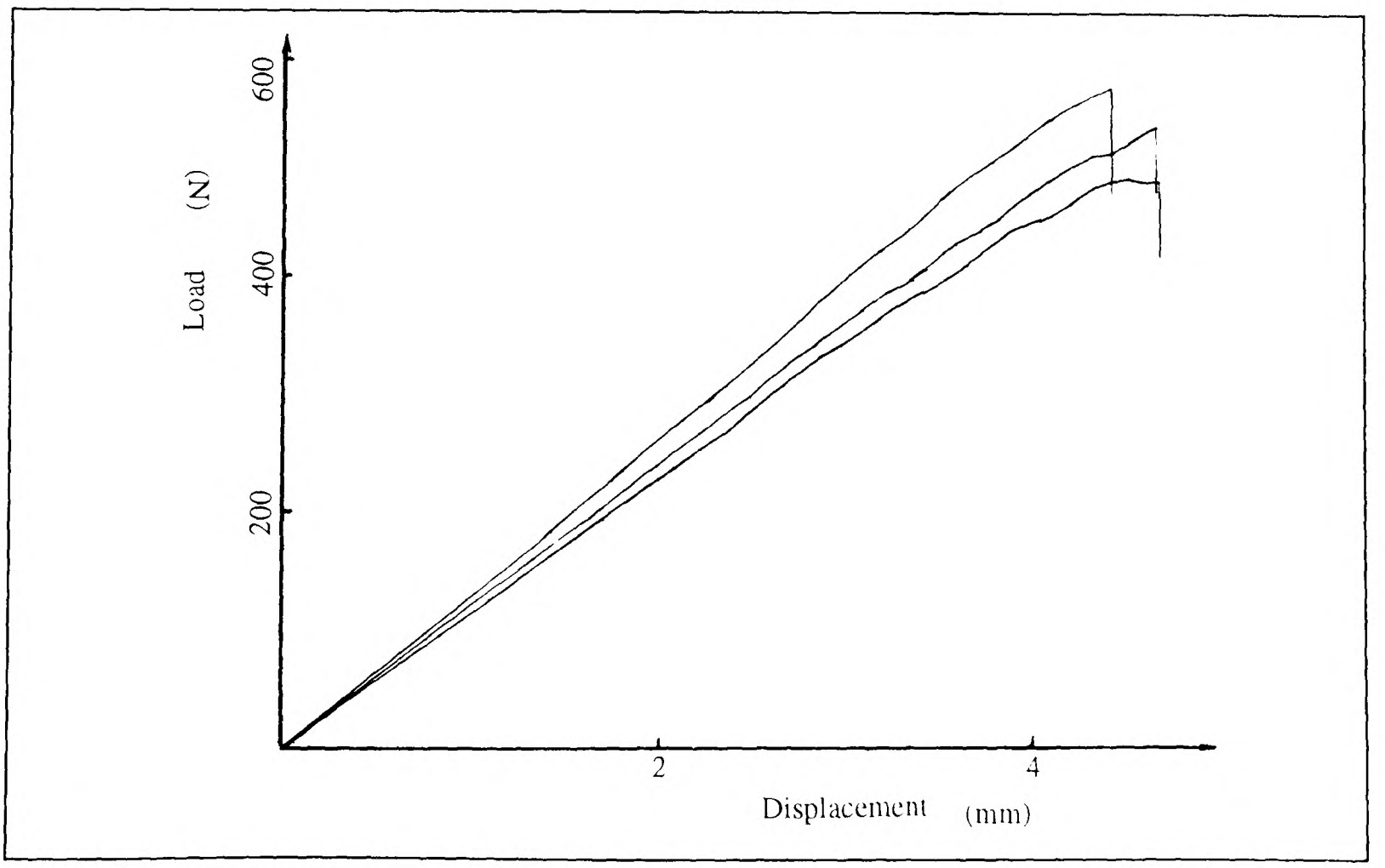

Figure 4.9 The load-displacement curves for G/epoxy notched beam tests(Table 4.4, group 2).

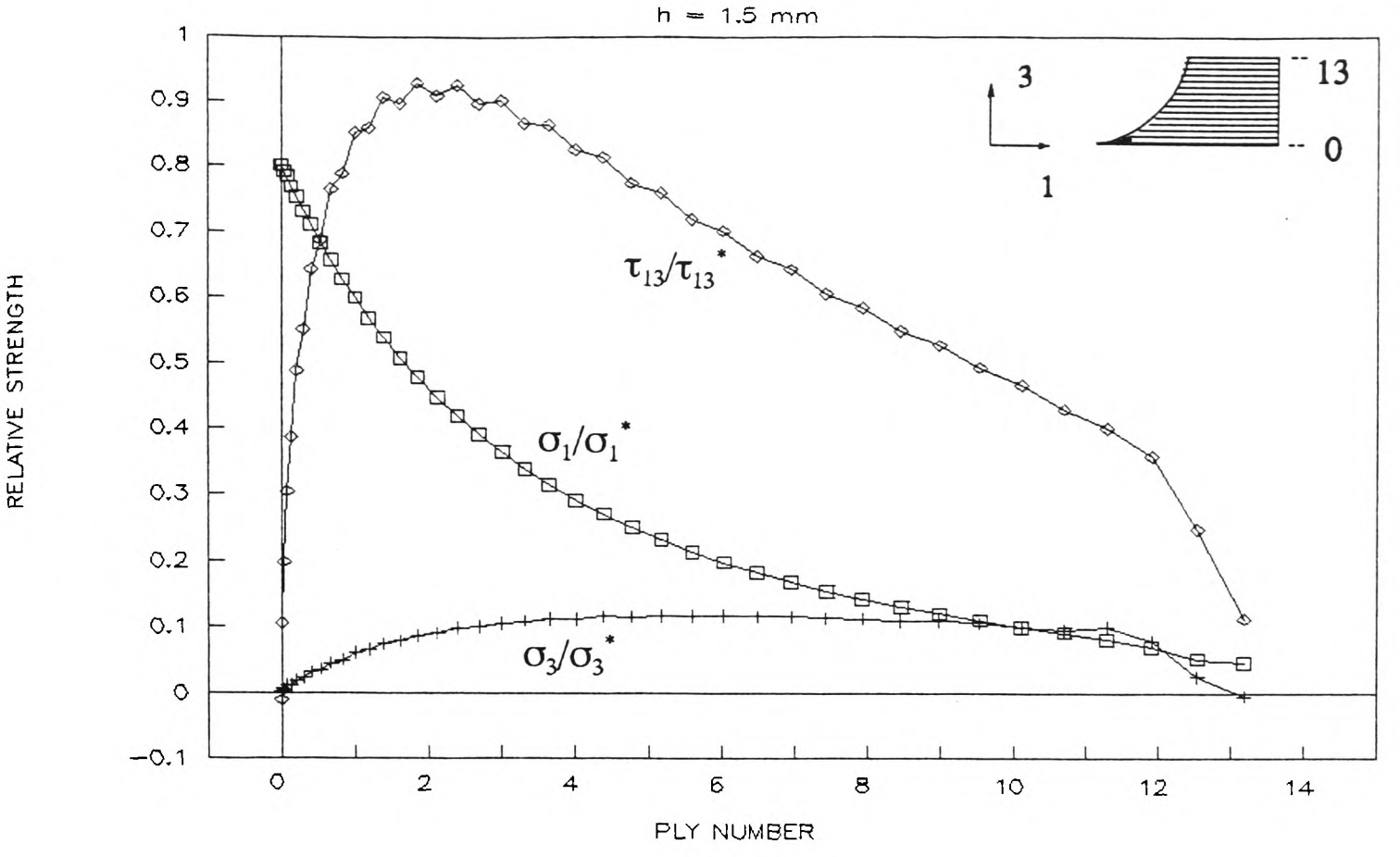
h = 1.5 mm
RELATIVE STRENGTH
PLY NUMBER
τ_{13}/τ_{13}^*
σ_1/σ_1^*
σ_3/σ_3^*
3
1
13
0
h = 2.5 mm
RELATIVE STRENGTH
PLY NUMBER
τ_{13}/τ_{13}^*
σ_1/σ_1^*
σ_3/σ_3^*
3
1
8
0

Figure 4.10

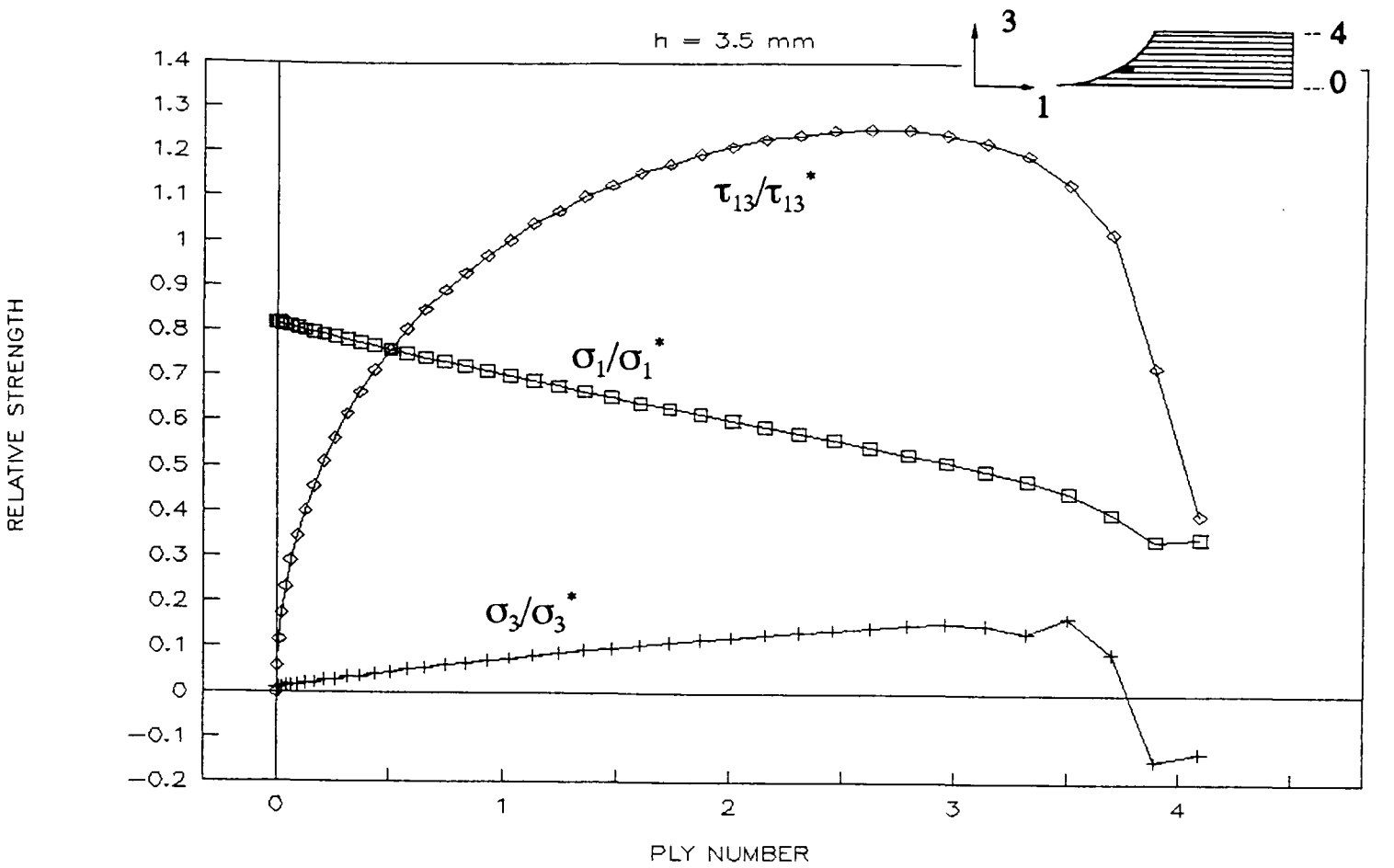

Figure 4.10 Numerical analysis by FEM based on experimental results for G/epoxy specimens.

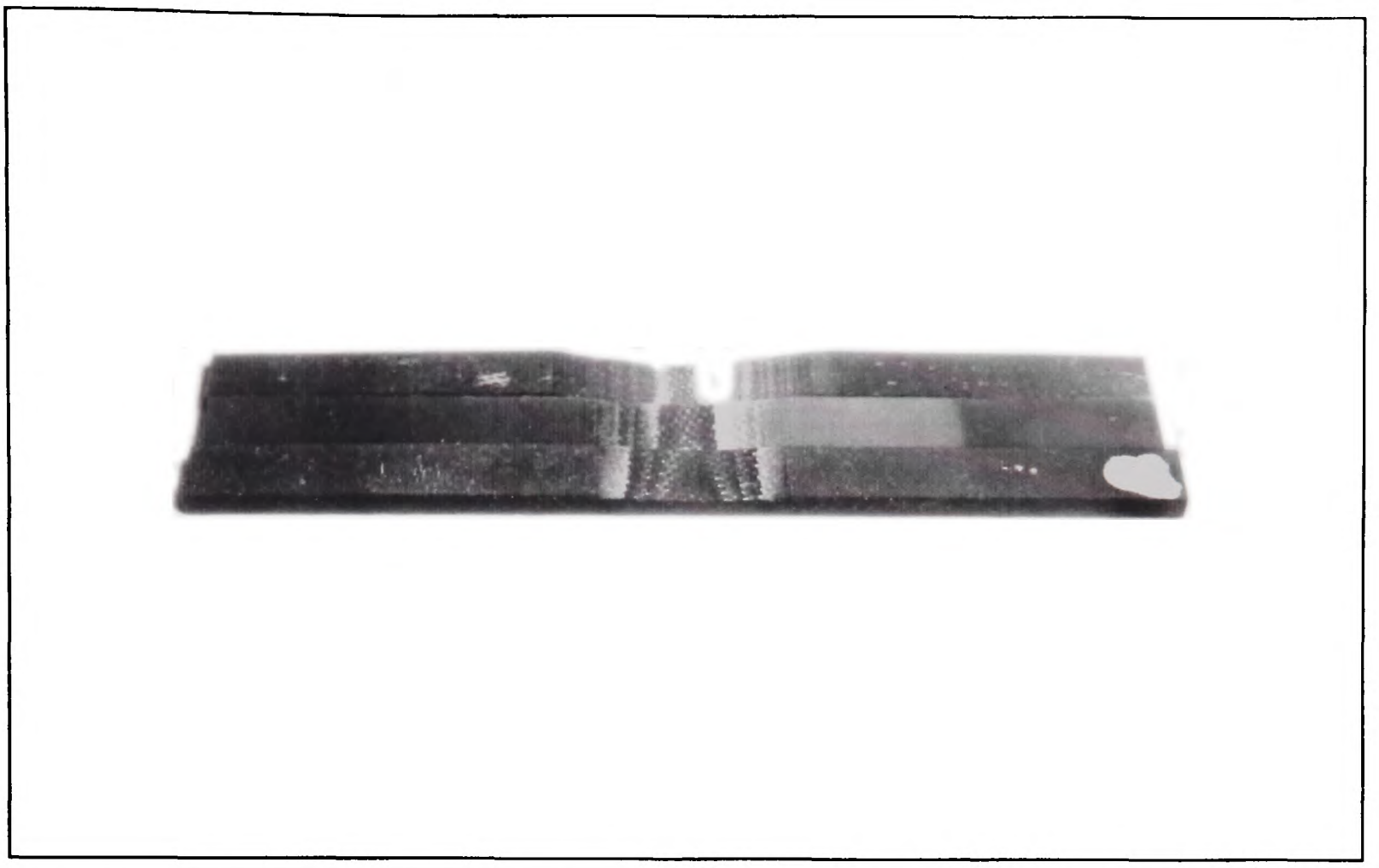

Figure 4.11 Delaminated G/epoxy notched beam specimens; h=1.5, 2.5 and 3.5 mm respectively downwards.

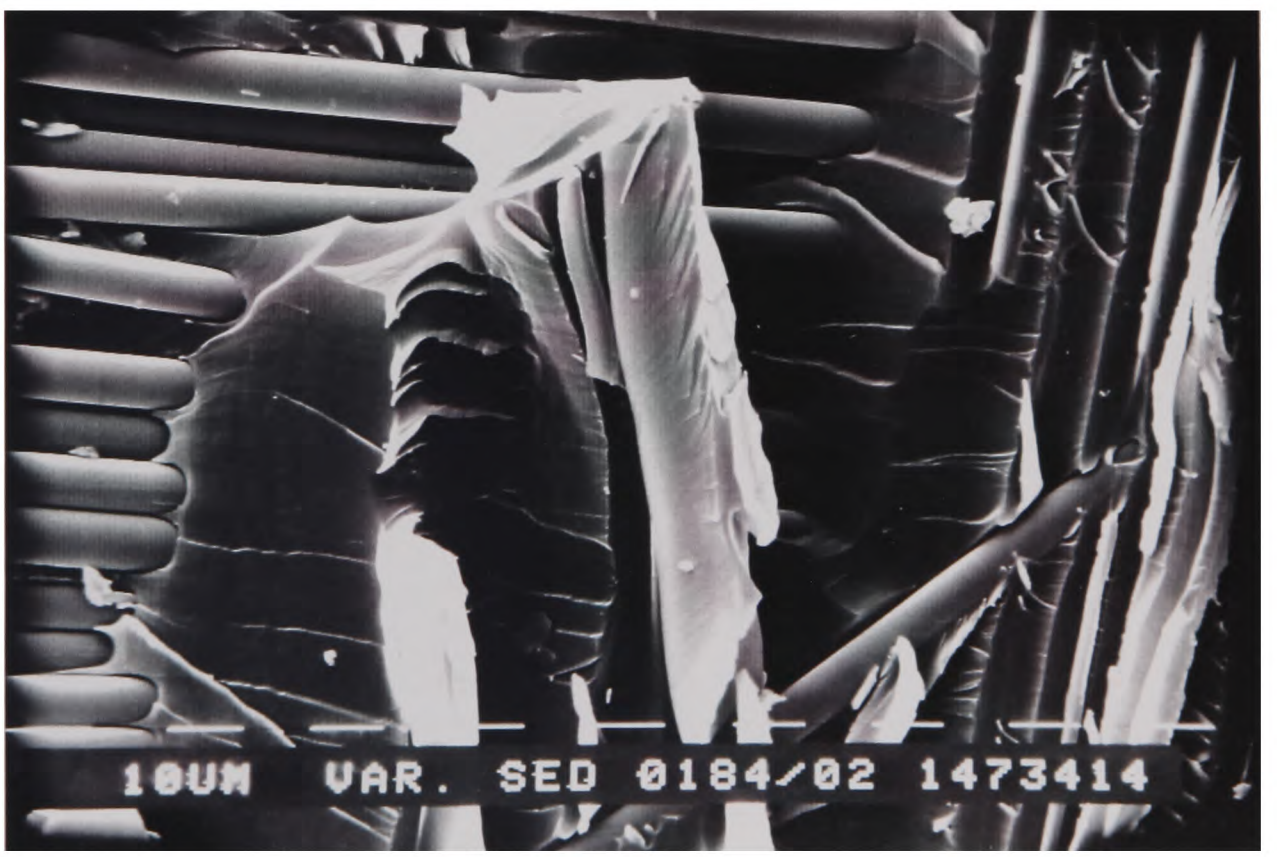

Figure 4.12 (a) h=1.5 mm

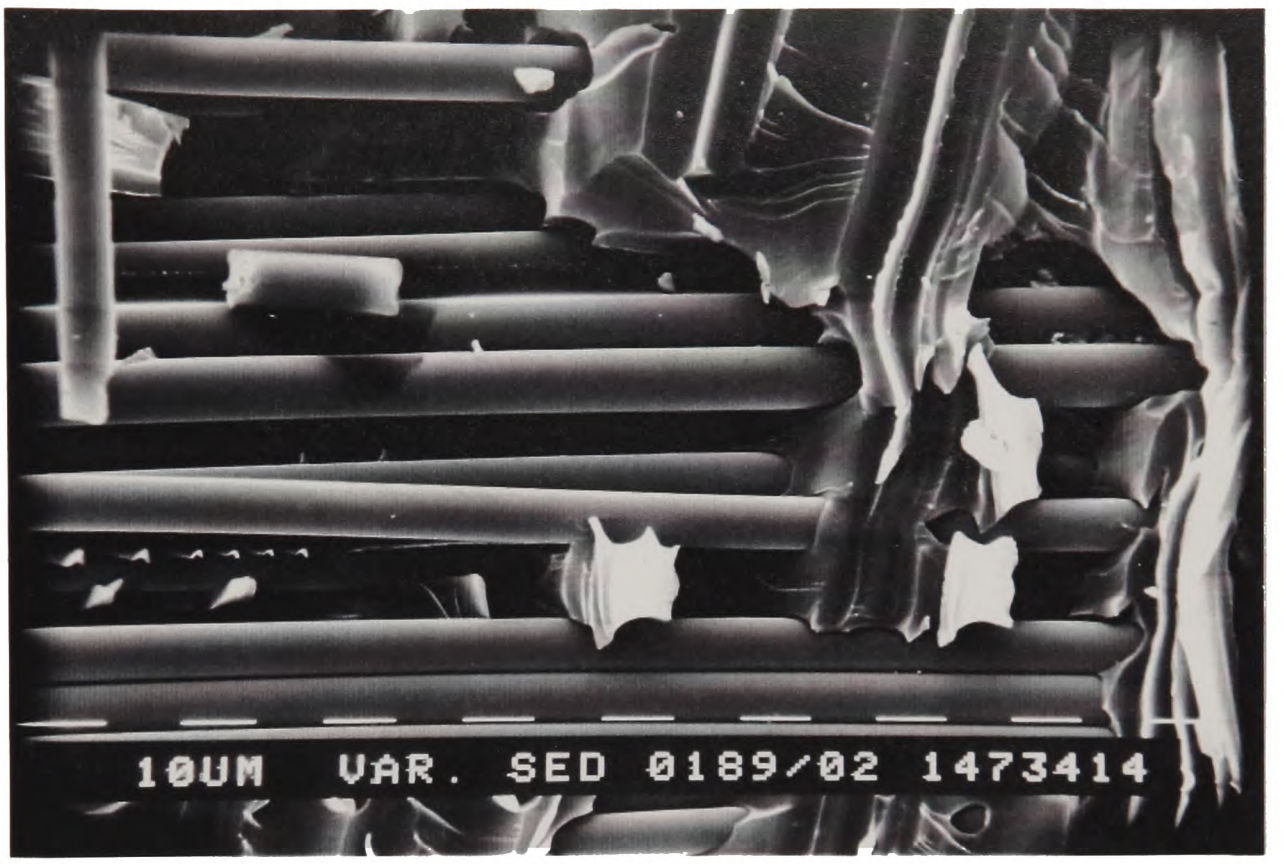

Figure 4.12 (b) h=2.5 mm

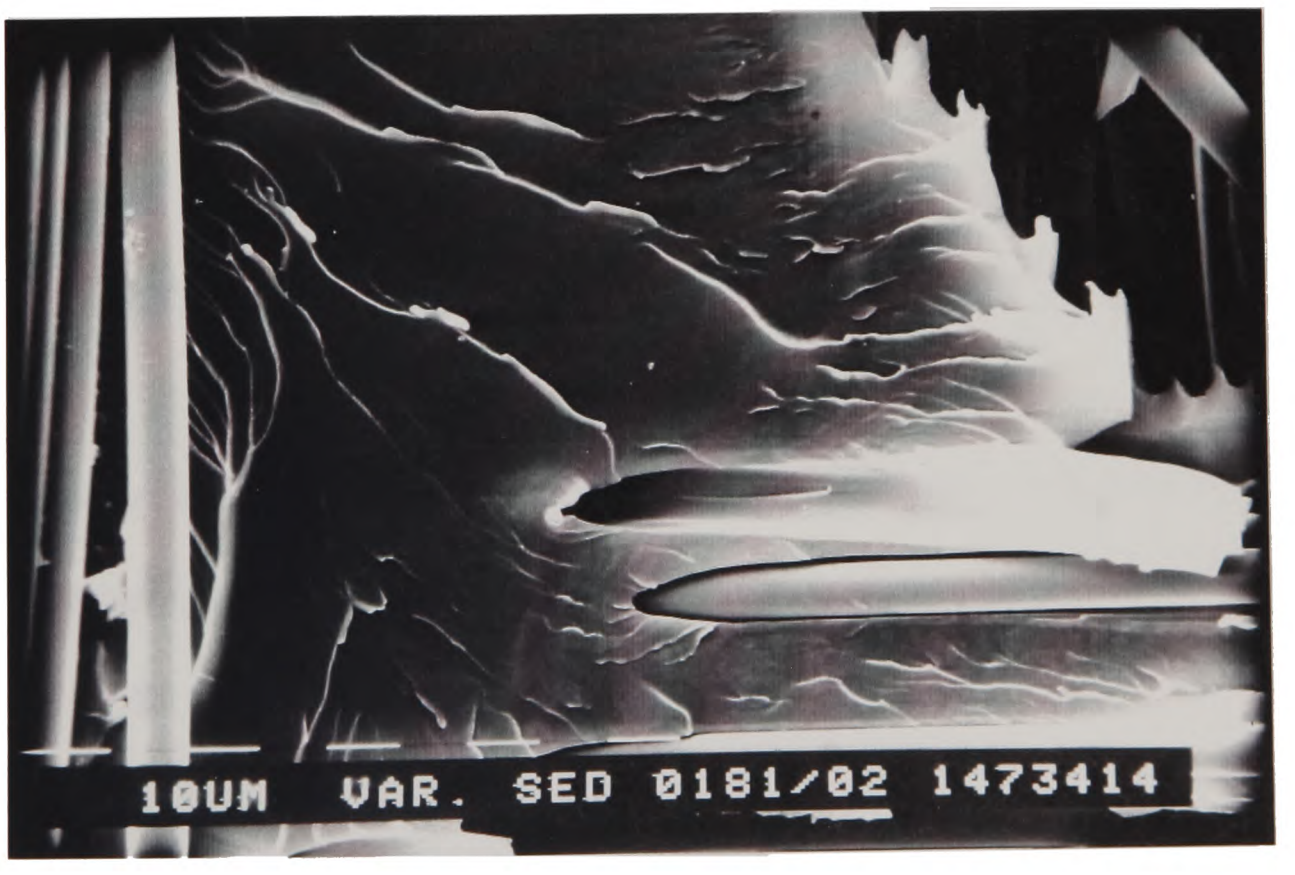

Figure 4.12 (c) h=3.5 mm

SEM fractographs from G/epoxy notched beam specimens.

Chapter 5

INTERPRETATION OF RESULTS

5.1 GENERAL OBSERVATIONS

Three tests -- uniaxial oblique, waisted C-specimen and central notched four-point bending beam, have been done in order to establish the through-thickness failure map (Fig.1.13) for C/epoxy woven laminate, which is one of the most widely used industrial materials. Transparent G/epoxy woven laminate, as a laboratory material, is basically used to repeat the tests. It was expected that the transparency of G/epoxy would help to detect the onset of any cracks so as to verify not only that the failures are caused by the known stress state rather than mechanical or any other defects, but also to reveal visually the failure mechanisms.

All tests have been analyzed numerically by the ABAQUS code except the oblique test, in which a simple uniform stress state prevails as shown by Moiré interferometry.

Tensile oblique and notched beam tests using G/epoxy transparent material system reveal visually the failure process. In the tensile oblique test, transparent specimens show that the failure is an abrupt breakdown and no edge cracks are detected. In the notched beam test, cracks are found to start and propagate uniformly through the width. The failure positions are well predicted by the stress analysis and coincide with those found in C/epoxy specimens. It is concluded that the failures are caused by the known stress state. The experimental results from G/epoxy plain C-specimens are not quite as expected. It is found that, unlike C/epoxy

specimens, the failure in G/epoxy always happens at one layer rather than randomly at each layer across the through-thickness. Although the reason why the delamination behaviour of the G/epoxy C-specimen is different from the C/epoxy is still not clear, and needs to be further investigated.

The purpose of the experimental results is to fill quadrants I ($\sigma_1(+)$-τ_{13}-$\sigma_3(+)$), II ($\sigma_1(-)$-τ_{13}-$\sigma_3(+)$) and III ($\sigma_1(-)$-τ_{13}-$\sigma_3(-)$) of the failure map. In quadrant I, the tensile oblique test provides data of in-plane tension σ_1 from 0 to 95.8 MPa, which is quite a narrow range when compared with the uniaxial strength of 473 MPa, and of shear τ_{13} from 0 to 34.8 MPa, which is quite an extensive range when compared with the pure shear strength of 48 MPa. On the other hand, data from waisted C-specimen exhibit a wide range of σ_1 from 49.92 to 300.8 MPa but a narrow range of shear from 3.78 to 17.21 MPa. Notched beam tests provide only three points of either a dominant σ_1 or τ_{13}, or combined σ_1 & τ_{13}, all with very small σ_3. Therefore the data from the three tests are positioned separately near the τ_{13}-σ_3 plane (tensile oblique), σ_1-σ_3 plane (waisted C-specimen) or σ_1-τ_{13} plane (notched beam) in quadrant I.

Waisted C-specimens provide data for quadrant II also with a narrow range of shear from 4.58 to 17.2 MPa, but quite extensive σ_1 from -126.6 to -501.5 MPa, which is beyond its nominal compressive strength of -388 MPa.

The existence of compressive through-thickness stress makes quadrant III the most complicated area. It is found from the compressive oblique test that the compressive through-thickness strength, -936 MPa, is very large compared with the interlaminar tension, shear and even the in-plane strength. The test provides data with a very extensive range both for σ_1,

from 0 to -306.9 MPa, and for τ_{13}, from 0 to 167.5 MPa, which is far beyond the value of pure interlaminar strength.

The results of both the oblique test and the notched beam test show very good consistency. The standard deviation of the recorded failure loads for each test group are generally within 10% with only one exception of group 2 in the compressive oblique test, which is 19%. The uncontrollable random failure positions of waisted C-specimen make it difficult to assess the test accuracy from only a few results. Instead, both plain C-specimen and waisted C-specimen results will be considered together and compared with other tests. For example, the pure interlaminar tensile strength from the C-specimen is 32 MPa compared with 36.5 MPa from the tensile oblique test. This also indicates good correlation between the tests.

The effect of interlaminar shear on failure in quadrants I and II is assessed in Fig.3.11 by comparing the results from waisted C-specimen and plain C-specimen. It is found that shear has little effect on failure in quadrant II while causing a significant drop of σ_3 in quadrant I. More comprehensively, the results from tensile oblique and notched beam tests are put into Fig.3.11, as shown in Fig.5.1 and it is found that the results still fit the conclusion.

The experimental results from G/epoxy specimens also show very good consistency with the standard deviation of the recorded failure loads for each test group within 10%. Although there are not as many experimental results as those for C/epoxy, some general laws can still be found to be the same with those in C/epoxy. For example, that in-plane compressive stress reduces the interlaminar tension strength can be concluded by comparing the interlaminar tensile strength 36.5 MPa from tensile oblique test with the failure point of a compressive in-

plane stress (-370 MPa) and an interlaminar tensile stress (19 MPa) from plain C-specimen test.

5.2 FAILURE MECHANISMS

Delamination is a very complicated failure mode which may consist of matrix cracking, apparent fibre/matrix interfacial failure, fibre breakage and fibre bridging etc. depending on the state of stress (Bascom, 1987). In order to recognize the failure mechanism for a specific situation, much work has been done on the fracture surface micromorphology since it depends strongly on the deformation mechanisms that are active prior to failure (Hertzberg, 1987).

Arcan et al (1987) characterized the morphology of interlaminar fractures in UD graphite/epoxy composites in order to correlate characteristic fractographic patterns for different pure and mixed mode loadings with fracture mechanisms. The tests were conducted with a specially designed loading system which allows the application of pure Mode I or Mode II loadings or any combination thereof. It was found by SEM fractographs that the fibres were, in general, covered with a film of matrix and the matrix fracture surface consisted of hackles resulting from interfacial tensile or shear failure. The hackle density increased from Mode I to Mode II (Fig.5.2), which was explained by the proposed physical models (Fig. 5.3). Similar work for UD graphite/epoxy laminates by Hibbs et al (1987) and Smith et al (1987) has also shown that for Mode I(pure tension) the fracture surface was relatively smooth and featureless while for Mode II(pure shear) the surface revealed numerous inclined hackles of epoxy oriented normal to the direction of resolved tension. Mixed mode failures showed a good consistency between the two extremes, e.g. the number of hackles increased as the

percentage of Mode II or shear loading increased. Since all the work described above is concerned with the 0/0 laminate stacking sequence, Smith et al (1987) also examined the fracture surface of laminate with a 0/90 stacking sequence and found that it still follows the general trend of the 0/0 laminate (Fig.5.4).

However, Mode I, Mode II and mixed-mode I & II are still quite simple through-thickness failure modes, which are referred to the τ_{13}-σ_3 plane in the failure map (Fig.1.13). In practice failure usually follows a much more complicated mode -- which is caused by interlaminar stress (mixed mode I & II) combined with in-plane stress. It is generally accepted (ESDU, 1986) that a UD laminate under in-plane tension may fail in a clean failure mode or bush type mode (Fig.5.5), or if it is under in-plane compression, the failure modes may be brittle fibre failure, kink band failure or fibre microbuckling (Fig.5.6). Therefore for a combined stress state in the failure map space, the interaction between interlaminar failure modes and in-plane failure modes will make it more difficult to draw a clear distinction from fracture patterns. This might be the reason why there is little work published on this aspect. In the following section the SEM pictures taken from the oblique, the waisted-C and the notched beam tests, of which all failures are caused by combined interlaminar stress and in-plane stress, will be discussed.

C/Epoxy Material System:

Quadrant I:

Fig. 2.19 from tensile oblique test, Fig. 3.13 from waisted C-specimen test and Fig. 4.8 from

notched beam test revealed the fracture features caused by a stress state in quadrant I. Generally speaking the fracture is in the form of a split between matrix and fibres. There is a thin sheathing of resin adhering to fibres, indicating a very good interfacial strength of the C/epoxy material system.

The tensile oblique test produced data with relatively low σ_1 values (near τ_{13}-σ_3 plane) and therefore showed features very similar to those found by Arcan (1987). Fig.2.19(a) is a picture from a θ=90° specimen, which is in a pure mode I stress state. However unlike the classical mode I test, it exhibits a very smooth, cleavage-type fracture without any hackles on the resin. According to the hackle formation physical model in Fig.5.3, this may mean that the failure is not caused by a pre-existing crack but an overall break-down in the surface because of a uniform applied stress. In Fig.2.19(b) and (c), the resin is characterized by many ductile voids which indicate the existence of shear stress.

The waisted C-specimen test produced data with relatively low shear stress (near σ_1-σ_3 plane). However, as shown in Fig.3.13, the resin on the fracture surface exhibited a large number of round dimples of the type associated with failure as a result of microvoid growth and coalescence as found by Arcan (1987) for Mode II failure, which indicated that even a small shear stress here may have a strong effect on failure.

The notched beam specimen test produced data with relatively low values of σ_3 (near τ_{13}-σ_1 plane). As expected by calculation, Fig.4.8(a) showed a σ_1 dominated fracture surface with broken bare fibres and brittle resin fragments. The inclined resin cracks in Fig.4.8(b)(c) revealed the dominant shear or combined shear and in-plane tension stress state.

Quadrant II:

The waisted C-specimen test also revealed the fracture features caused by a stress state in quadrant II (Fig.3.12). It was very interesting to find that the resin imprints on fibres exhibited hackles with very sharp faces, contrasted to the round dimples when σ_1 is tensile (Fig.3.13). Clearly two different failure mechanisms existed there, being reflected by different functions of τ_{rt} in these two stress states. A possible further explanation for that is as follows.

When σ_t is compressive, the micro-buckling of fibres results in micro-cracks in the interface, which quickly invoke Mode I failure because of the existence of tensile through-thickness stress. Therefore the interlaminar shear contributes very little to the failure. Figs. 3.14 & 3.15 show how delamination was initiated by micro-buckling under combined compressive tangential and tensile radial stress.

Nevertheless, since the tensile strength of fibres is higher than their buckling strength, the effect of a tensile tangential stress is basically to maintain the plies straight and aligned, and therefore to inhibit the Mode I opening and to increase delamination strength. But an introduction of interlaminar shear to this situation will make the single Mode I failure into a combined Mode I and Mode II failure which shows a significant drop of strength.

Quadrant III:

The compressive oblique test exhibited a very different and complicated fracture surface. When angle θ approaches 90°, the failure is actually not delamination but the combined break-

down of fibres and resin (Fig.2.15(a)(b), Fig.2.17(a)). When θ becomes smaller, delamination appears (Fig.2.15(c)). Instead of hackles or dimples of resin, many resin particles on the fracture surface are noticed (Fig.2.17(b)(c)), indicating the existence of a compressive interlaminar normal stress which constrained the shear deformation of resin.

G/Epoxy Material System:

Generally speaking the SEM pictures from the tensile oblique and the notched beam tests using G/epoxy material reflect nearly the same features as those from C/epoxy material (Fig.2.21, Fig.4.12). The two specific points for G/epoxy are, firstly that fibres are nearly bare with little resin on them, indicating a very poor interfacial strength between fibres and resin, secondly that larger resin particles appear on the fracture surfaces, indicating that the matrix is more easily stretched and is less brittle than in the C/epoxy system.

It is very interesting to recall the observation that the C-specimen made of G/epoxy is less likely to suffer from delamination failure under tensile loading although the micrographs clearly show the poor interfacial strength between matrix and fibres of the G/epoxy system. It seems that better interfacial strength does not necessarily mean better delamination strength.

5.3 APPLICATION OF PHENOMENOLOGICAL STRENGTH CRITERIA

5.3.1 Introduction

Phenomenological strength criteria are very efficient in predicting in-plane strength as discussed in Section 1.2.2 although they do not explain the failure mechanisms at all. Therefore, although it is agreed that the delamination of composite laminates follows very complicated failure mechanisms, it is still hoped that some phenomenological strength criteria can be established in terms of through-thickness strength. In the following, a criterion based on the Tsai-Wu theory will be established and compared to the experimental results.

Some assumptions for structuring a through-thickness failure criterion include: First of all, the laminate will be made of fabric laminae only with $0^0/90^0$ or $0^0/0^0$ stacking sequence, so as to get average uniform interlaminar properties. Secondly, as stated in Chapter 1, the stresses in the through-thickness plane, which are σ_1, σ_3 and τ_{13}, are predominant for delamination. Therefore 2-D lamina failure criteria can be adapted to describe through-thickness strength.

5.3.2 Establishment of a Through-Thickness Failure Criterion Based on the Tsai-Wu Theory

As a phenomenological failure criterion, the Tsai-Wu(1971) tensor theory seems more reasonable than other in-plane failure criteria as described in Chapter 1 because all of its strength tensors are determined by a comprehensive series of tests. So the Tsai-Wu theory is chosen to structure the through-thickness criterion, which is,

$$F_1\sigma_1+F_3\sigma_3+F_5\sigma_5+F_{11}\sigma_1^2+F_{33}\sigma_3^2+F_{55}\sigma_5^2+2F_{13}\sigma_1\sigma_3=1 \qquad (5-1)$$

Some of the components of the strength tensors can be defined in terms of the engineering strength,

$$F_1=\frac{1}{X_t}+\frac{1}{X_c} \qquad F_5=0$$

$$F_{11}=-\frac{1}{X_tX_c} \qquad F_{55}=\frac{1}{ST^2} \qquad (5-2)$$

$$F_3=\frac{1}{Z_t}+\frac{1}{Z_c}$$

$$F_{33}=-\frac{1}{Z_tZ_c}$$

wherein, X_t (X_c) and Z_t (Z_c) are tensile (compressive) engineering strengths in 1 and 3 directions respectively, and ST is the shear strength in the 1-3 plane.

For T300/914 fabric laminate with 0°/90° layup, the engineering strength components are shown in Table 5.1. Therefore the parameters in Equation (5-2) are,

$F_1=-4.63 \times 10^{-4}$, $F_{11}=5.45 \times 10^{-6}$

$F_3=3.02 \times 10^{-2}$, $F_{33}=3.25 \times 10^{-5}$

$F_{55}=4.34 \times 10^{-4}$, $F_5=0$

TABLE 5.1 Materials Properties of Fabric Laminate

X_t [1] (MPa)	X_c [1] (MPa)	Z_t [2] (MPa)	Z_c [3] (MPa)	ST [2] (MPa)
473	-388	32	-961	48

Now the only unknown is the interactive tensor strength F_{13} , which can be determined by a through-thickness biaxial test. However, from Eqn.(5-1), it is readily seen that any biaxial state of stress which has non-zero σ_1 and σ_3 may be used to determine F_{13}. Hence it is necessary to find a methodology to make the determined F_{13} as reasonable as possible. One of the theories is that the experimental accuracy in the determination of the interactive parameter is a governing factor in establishing the failure criterion and therefore the determined F_{13} should be the one which is the least sensitive to the experimental scatter (Wu, 1972).

From Equation(5-2), the relative resolutions $|\Delta F_i/F_i|$ and $|\Delta F_{ij}/F_{ij}|$ may be related to the variability in the original strength measurements, i.e.,

$$\left|\frac{\Delta F_1}{F_1}\right| = \Psi_1 \left|\frac{\Delta X_t}{X_t}\right| \qquad \left|\frac{\Delta F_{11}}{F_{11}}\right| = \Psi_{11} \left|\frac{\Delta X_t}{X_t}\right|$$

$$\left|\frac{\Delta F_3}{F_3}\right| = \Psi_3 \left|\frac{\Delta Z_t}{Z_t}\right| \qquad \left|\frac{\Delta F_{33}}{F_{33}}\right| = \Psi_{33} \left|\frac{\Delta Z_t}{Z_t}\right| \qquad (5-3)$$

[1] Materials Properties from Rolls-Royce plc

[2] Hognestad, 1993.

[3] Refer to Table 2.2

$$\left|\frac{\Delta F_{55}}{F_{55}}\right| = \Psi_{55}\left|\frac{\Delta ST}{ST}\right|$$

where Ψ_i, Ψ_{jj} are magnifying factors that will be determined later.

Assume $A = X_t/X_c$ (5-4)

Substitution of Equation (5-4) in Equation(5-2) yields,

$$F_1 = \frac{1-A}{X_t} \qquad (5-5)$$

So,

$$\frac{\Delta F_1}{F_1} = \frac{\partial F_1}{\partial X_t}\frac{\Delta X_t}{F_1} = -\frac{(1-A)}{X_t^2}\frac{\Delta X_t}{F_1} = -\frac{\Delta X_t}{X_t} \qquad (5-6)$$

Therefore, in Equation (5-3) $\Psi_1 = -1$ and similarly all the other magnifying factors Ψ_i and Ψ_{ij} can be derived as,

$$\Psi_1 = \Psi_3 = -1$$

$$\Psi_{11} = \Psi_{33} = \Psi_{55} = -2 \qquad (5-7)$$

Equations (5-3) and (5-7) imply that the evaluation of F_1 and F_3 has the same scatter as the experiments; and that of F_{11}, F_{33}, F_{55} has twice the scatter of the experiments. Now the relation between actual and experimental sensitivity in the case of F_{13} will be explored.

For the normal biaxial stresses ($\sigma_5 = 0$), Equation (5-1) becomes,

$$F_{11}\sigma_1^2+2F_{13}\sigma_1\sigma_3+F_{33}\sigma_3^2+F_1\sigma_1+F_3\sigma_3=1 \qquad (5-8)$$

Geometrically, the failure surface defined by Equation (5-8) is an ellipse in the σ_1, σ_3 plane. If it is assumed that the components of the strength tensors -- F_1, F_3, F_{11}, F_{33} -- have been measured from previously described tests, then the intersections of the ellipse with the axis (σ_1, σ_3) are known. The remaining constant F_{13} determines the inclination and semi axes of the ellipse. Thus the relative resolution of F_{13} may be interpreted as the accuracy with which the inclination of the ellipse can be measured. This is schematically illustrated in Figure 5.7 where the biaxial stress ratio B is defined as:

$$B = \frac{\sigma_1}{\sigma_3}$$

In Figure 5.7, σ_i are the failure strengths under a complex state of stress and β is defined as the radial intercept between a biaxial ratio B and the failure surface defined by Equation (5-8). The relative resolution of F_{13} can be expressed as

$$\left|\frac{\Delta F_{13}}{F_{13}}\right|=\Psi_{13}\left|\frac{\Delta\beta}{\beta}\right|=\Psi_{13}\left|\frac{\Delta\sigma_3}{\sigma_3}\right| \qquad (5-9)$$

In order to evaluate the scatter magnification factor Ψ_{13}, Equation (5-8) may be expressed in terms of the unknowns B, σ_3 and F_{13}:

$$B^2F_{11}\sigma_3^2+2BF_{13}\sigma_3^2+F_{33}\sigma_3^2+BF_1\sigma_3+F_3\sigma_3 = 1 \qquad (5-10)$$

Ψ_{13} in Equation (5-9) can be evaluated by a similar operation as performed above,

$$\frac{\Delta F_{13}}{F_{13}} = \frac{1}{F_{13}} \frac{\partial F_{13}}{\partial \sigma_3} \Delta \sigma_3 \qquad (5\text{-}11)$$

Differentiating Equation (5-10) and evaluating for $\sigma_3 = \bar{\sigma}_3$ (intercept of the failure surface) yields:

$$\left.\frac{\partial F_{13}}{\partial \sigma_3}\right|_{\bar{\sigma}_3} = -\left(F_{11}B + 2F_{13} + \frac{F_{33}}{B} + \frac{F_1}{2\bar{\sigma}_3} + \frac{F_2}{2B\bar{\sigma}_3}\right) \frac{1}{\bar{\sigma}_3} \qquad (5\text{-}12)$$

Thus, by Equation (5-9),

$$\Psi_{13} = -\frac{1}{F_{13}} \left(F_{11}B + 2F_{13} + \frac{F_{33}}{B} + \frac{F_1}{2\bar{\sigma}_3} + \frac{F_3}{2B\bar{\sigma}_3}\right) \qquad (5\text{-}13)$$

$\bar{\sigma}_3$ in Equation (5-13) can be solved from Equation (5-10)

$$\bar{\sigma}_3 = \frac{-(F_1B + F_3) + [(F_1B + F_3)^2 + 4(F_{11}B^2 + 2F_{13}B + F_{33})]^{1/2}}{2(F_{11}B^2 + 2F_{13}B + F_{33})} \qquad (5\text{-}14)$$

Combining Equations (5-13) and (5-14), it can be seen that, contrary to the non-interactive tensor components, the relative scatter $\Delta F_{13}/F_{13}$, as characterized by the magnifying factor Ψ_{13}, is dependent on the magnitude of the strength measurement $\bar{\sigma}_3$ and on the magnitude of the strength tensor F_{13} itself.

Hence the determination of F_{13} is an optimization procedure which needs to make the ψ_{13} minimum by choosing σ_r (B) and F_{13} itself.

As discussed in chapter 3, C-specimen test is a good biaxial test containing σ_1 and σ_3, which will be employed to decide F_{13}. Table 5.2 shows the experimental results of tests with C/epoxy plain C-specimens by Hognestad (1993) and it can be found that most failures happen in the symmetric section with $\tau_{rt}=0$, i.e. under a normal biaxial stress state. It can also be found that nearly all results fall into three categories, B=$\pm$15.9, B=$\pm$22.55 and B=$\pm$3.06.

According to Equation (5-13) the "best" value of F_{13} should be the one which makes the experimental scatter Ψ_{13} "minimum". Therefore the curves of $\left|\Delta F_{13}/F_{13}/\Delta\sigma_3/\sigma_3\right|$ (Ψ_{13}) vs F_{13} with different values of B are plotted in Fig. 5.8. Then it is found that when $F_{13} > 0$ and $F_{13} < 0$, B=-15.9 and B=15.9 minimize the scatter of F_{13}.

That means that in the experiment here B=-15.9 is a "better" value to determine F_{13}. Putting the test results with B=-15.9 in Table 5.2 into Equation (5-8), F_{13} is obtained as shown in Table 5.3.

From Fig. 5.8 it is obvious that among the five values of F_{13} in Table 5.3, F_{13}=0.000036 is the "best". Hence a through-thickness failure criterion for C/epoxy based on Tsai-Wu is obtained as,

$$F_1\sigma_t + F_3\sigma_r + F_{11}\sigma_t^2 + F_{33}\sigma_r^2 + F_{55}\tau_{rt}^2 + 2F_{13}\sigma_t\sigma_r = 1 \qquad (5\text{-}15)$$

where,

F_1=-4.63 x 10^{-4}, F_{11}=5.45 x 10^{-6}

F_3=3.02 x 10^{-2}, F_{33}=3.25 x 10^{-5}

F_{55}=4.34 x 10^{-4}, F_{13}=3.6 x 10^{-5}

TABLE 5.2 The Data of Failure Points With C-Specimen (Hognestad,1993)

	σ_r (MPa)	σ_t (MPa)	τ_{rt} (MPa)	$B=\sigma_t/\sigma_r$
GROUP 1	16.1	-363	0	-22.55
	38.5	112	0	2.91
	31.8	0	0	0
	17.4	-394	0	22.64
	32	0	0	0
	31.3	-96.2	0	-3.07
	30.4	-93.6	7	
	22.6	-342	6	
GROUP 2	15.32	-362	0	-23.63
	32.96	101	0	3.06
	34.76	106.5	0	3.06
	31.02	95.0	0	3.06
GROUP 3	17.4	-276.8	0	-15.91
	16.4	-261.3	6.74	
	17.5	-278.3	4.15	
	16.6	-479.7	0	-28.90
	18.4	-292.5	0	-15.90
	19.1	-303.8	0	-15.90
	23.0	-365.4	0	-15.89
	33.3	-5.7	0	-0.17
	23.1	-366.9	0	-15.88

TABLE 5.3 F_{13} CALCULATED FROM TEST RESULTS

B	σ_r (MPa)	F_{13}
-15.91	17.4	0.000008
-15.90	18.4	0.000019
-15.90	19.1	0.000015
-15.89	23.0	0.000036
-15.88	23.1	0.000036

5.3.3 Comparison With Experimental Results

The failure criterion that has been established from the plain C-specimens of Hognestad (1993) will now be tried to see whether it predicts the failure map corresponding to all the C/epoxy experimental results. As shown in Table 5.4, the test results for the three stress components are listed and the theoretical prediction of interlaminar tension σ_3 for the given experimental results of σ_1 and τ_{13} is compared with the test result.

It should be pointed out first that since all the experimental results are actually separate data in a 3-D space, a firm quantitative assessment for the failure criterion requires a large amount of test data. Given that the number of the experimental results in Table 5.4 is somewhat limited, the following discussion can only provide an indication of a general trend rather than any detailed conclusions.

The failure criterion in quadrant I generally agrees with the experimental results reasonably well. The average scatter is 23% for the tensile oblique test and 22% for the plain C-specimen. Two of the three test data from the notched beam test can not be predicted by the theory and the last one fits the theory with a scatter of 36%. These discrepancies are expected because of the effect of the stress gradient in the test and will be further discussed in Chapter 6. There are two test data from waisted C-specimen, which disagree with the theory with a scatter greater than 100%. Although it is not easy to decide whether this is caused by experiment or theory, the disparity between these results and the rest make it more likely that these two points might be erroneous. If these two points are excluded, the average scatter is 34%. This is slightly larger than that for the other tests except for the notched beam. A possible reason

may be the presence of machining damage, difficult to avoid in the manufacture of a relatively complex specimen, and error in geometry.

Quadrant II shows complex results. Between -261.3 to -303.8 MPa of σ_1, the prediction is very poor with scatter of around 100%, while in other ranges of σ_1, the prediction is very good with average scatter about 20%. It is very clear from the results of the plain C-specimen, where there is no shear stress and therefore all results are on the σ_1-σ_3 plane, that the theory predicts the test very well as σ_1 starts from 0 till -96.7 MPa, then as σ_1 reaches -261.3 MPa, the theory predicts much higher σ_3 than the test, and finally as σ_1 approaches in-plane compressive strength (-388 MPa), the theory and the test are in good agreement again. Therefore the theory in quadrant II does not predict a correct trend with experiment.

Finally, it is easy to understand that the theory can not predict the results of quadrant III because the compressive oblique test finds that compressive interlaminar stress will cause the interlaminar shear to increase to a very high value at failure, viz, the compressive interlaminar stress inhibits delamination, while the theory does not consider any interaction between σ_1 and τ_{13}.

5.4 CONCLUSIONS

The three tests have proved able to provide data for establishing a through-thickness failure map. Being verified experimentally or numerically, the uniaxial oblique test and the notched beam test have also shown very consistent experimental results, with a standard deviation less than 10%, both for G/epoxy and C/epoxy material systems. For the C/epoxy C-specimen test,

the uncontrollable failure positions make it very difficult to obtain repeatable results although, on the other hand, this supplies a wide range of stress states at failure and therefore somewhat justifies the shortcoming. The reliability is verified by numerical analysis as well as by comparing the experimental results with those from other tests. It is found that the interlaminar tensile stress from the C-specimen (32 MPa) is very close to that from tensile oblique tests (36.5 MPa), with a difference of about 12%. This also indicates the good correlation within each test. The transparency of G/epoxy system provides further evidence that the failures are caused by the known stress state and are not the result of minor imperfections. Further support comes from the SEM micrographic examination for the delaminated surfaces, which reveals micro-features corresponding to the stress state.

A phenomenological failure criterion approach has been tried to describe the failure space. A through-thickness failure criterion based on Tsai-Wu theory has been established for the C/epoxy system and compared with the experimental results. It is found that the theory is in broad agreement with the tests in quadrant I, but there is a large discrepancy in quadrants II and III. This could be explained by the complicated failure mechanisms in quadrants II and III, which have not been considered in the criterion. The failure mechanisms might be more complicated for the G/epoxy system since for the C-specimen the observation that the failure happens randomly between each layer through the thickness for the C/epoxy system has not been detected for the G/epoxy. This clearly indicates a very complicated through-thickness failure mechanism for a polymer laminate, which not only depends on the stress state but also on its constitutive components. Therefore the final description of the delamination failure, i.e. the establishment of a 3-D through-thickness failure map can only be fulfilled by many more tests under a variety of stress states.

A question of comparability then arises, i.e. are the data from the tests with a stress gradient comparable with those from the tests with uniform stress distributions in a failure map?

As discussed before, the oblique test specimen has a uniform stress state while both the waisted C-specimen and the notched beam tests exhibit a stress gradient. It was found that in a notched beam test, the stress gradient has caused the failure stress to be much higher than the nominal tensile strength. A correction factor to take into account the stress gradient should be introduced when comparing the results of different tests. In particular, the data from notched beam tests should be corrected before presenting it in the form of failure map together with the results of quadrant I. For this purpose, the Weibull statistical approach will be discussed in the following chapter.

TABLE 5.4 Comparison of experimental results with the prediction by Tsai-Wu criterion

QUADRANTS	TESTS	EXPERIMENTAL RESULTS (MPa)			PREDICTION BY TSAI-WU THEORY (MPa)		ERROR
		σ_1	τ_{13}	σ_3	σ_3	τ_{13}	
I	TENSILE OBLIQUE	0	0	36.5	32		12%
		2.9	10.9	40.9	30.25		26%
		13.8	24.9	40.6	23.1		43%
		32.1	32.1	32.1	17.0		47%
		57.2	30.6	19.1	17.35		9%
		95.8	34.8	12.7	12.5		2%
	WAISTED C-SPECIMEN	49.92	3.78	13.92	28.89		-108%
		59.03	9.82	16.59	27.35		-65%
		135.12	7.21	17.09	23.12		-35%
		151.15	8.66	10.84	21.84		-101%
		175.93	10.08	12.62	19.96		-58%
		225.58	17.21	16.23	14.89		8%
		234.0	7.08	16.74	16.59		1%
		276.79	11.77	19.82	12.87		35%
		280.5	5.46	20.05	13.54		32%
		300.8	5.86	21.5	12.08		44%
	NOTCHED BEAM	325.41	43.35	4.45		27.75	36%
		484.12	31.58	2.18		ERR [1]	
		752.81	0	0		ERR	
	PLAIN C-SPECIMEN	0	0	31.8	32.0		-0.6%
		0	0	32	32.0		0%
		95.0	0	31.02	26.3		15%
		101	0	32.96	25.9		21%
		106.5	0	34.76	25.5		26%
		112	0	38.5	25.2		34%

II	WAISTED C-SPECIMEN	-126.6	15.68	31.22	33.69		-8%
		-138.8	17.2	34.24	33.01		4%
		-265.24	4.58	16.94	39.16		-131%
		-355.78	9.85	12.48	19.77		-58%
		-501.54	8.0	7.66	ERR		
	PLAIN C-SPECIMEN	-5.7	0	33.3	32.3		3%
		-93.6	7	30.4	36.0		-18%
		-96.2	0	31.3	37.0		-18%
		-261.3	6.74	16.4	38.5		-134%
		-276.8	0	17.4	39.3		-125%
		-278.3	4.15	17.5	38.6		-120%
		-292.5	0	18.4	38.3		-108%
		-303.8	0	19.1	37.3		-95%
		-342	0	22.6	31.0		-37%
		-362	0	15.32	24.0		-56%
		-363	0	16.1	23.5		-45%
		-365.4	0	23.0	22.4		3%
		-366.9	0	23.1	21.6		6%
		-394	0	17.4	ERR		
		-479.7	0	16.6	ERR		
III	COMPRESSIVE OBLIQUE	0	0	-961	-961		0%
		-20.5	121.9	-725.9	-607.8		16%
		-87.6	167.5	-321.3	ERR		
		-124.1	124.1	124.1	ERR		
		-132.2	59.2	-22.4	-34.6		-54%
		-233.8	62.39	-20.8	-62.7		-226%
		-306.9	57.4	-10.8	ERR		

[1] ERR means that the theory can not predict σ_3 (or τ_{13}) for the given experimental results of σ_1 and τ_{13} (or σ_3).

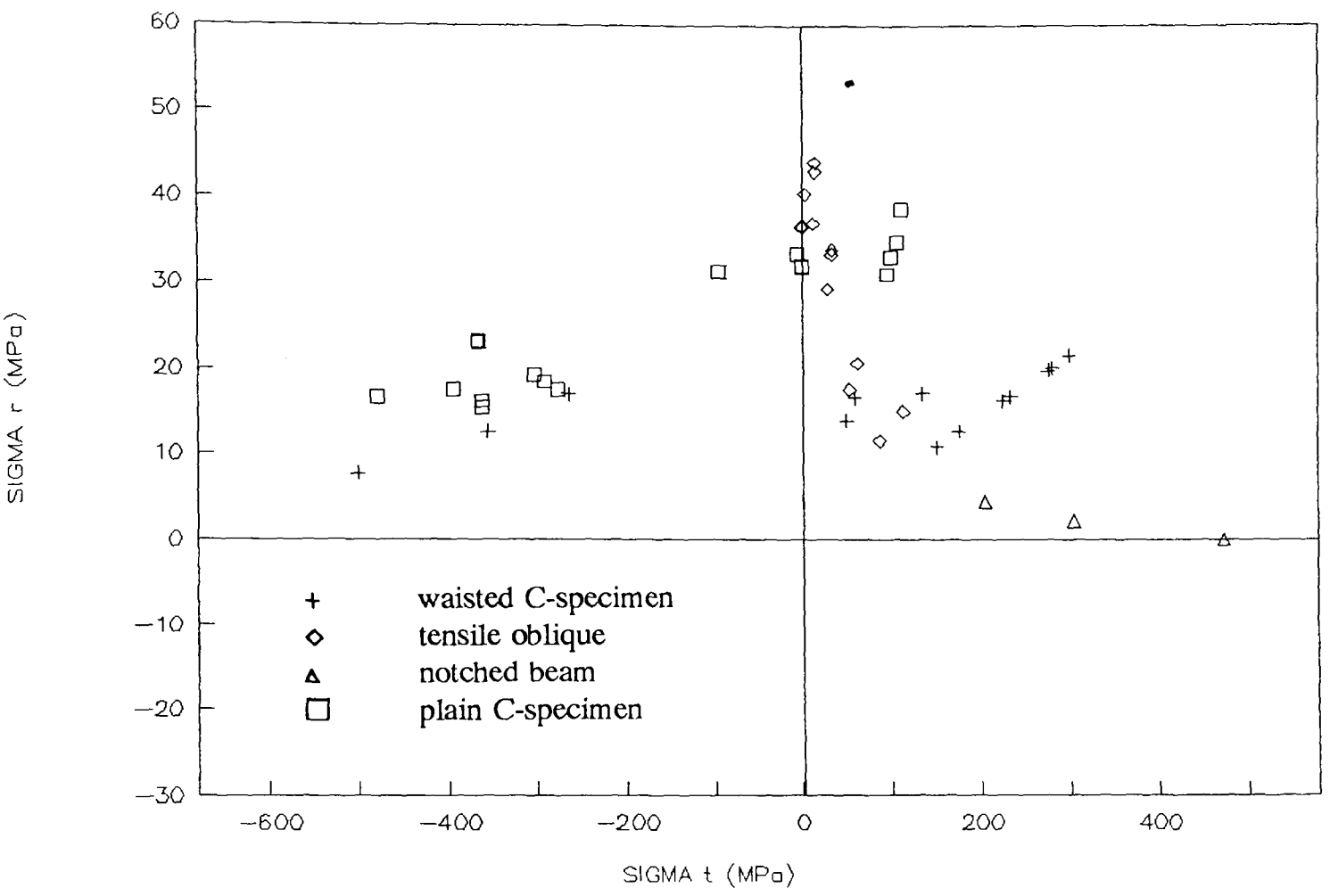

Figure 5.1 The effect of shear on failure.

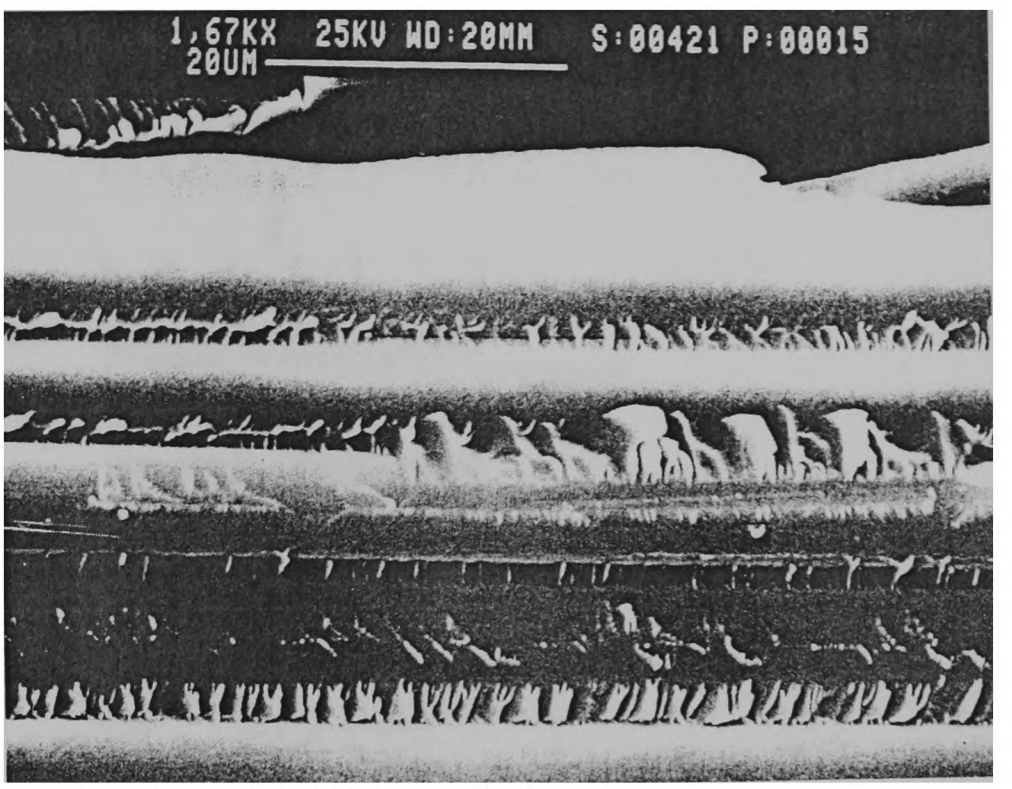

(a) Mode I fracture in AS4/3501-6 graphite/epoxy.

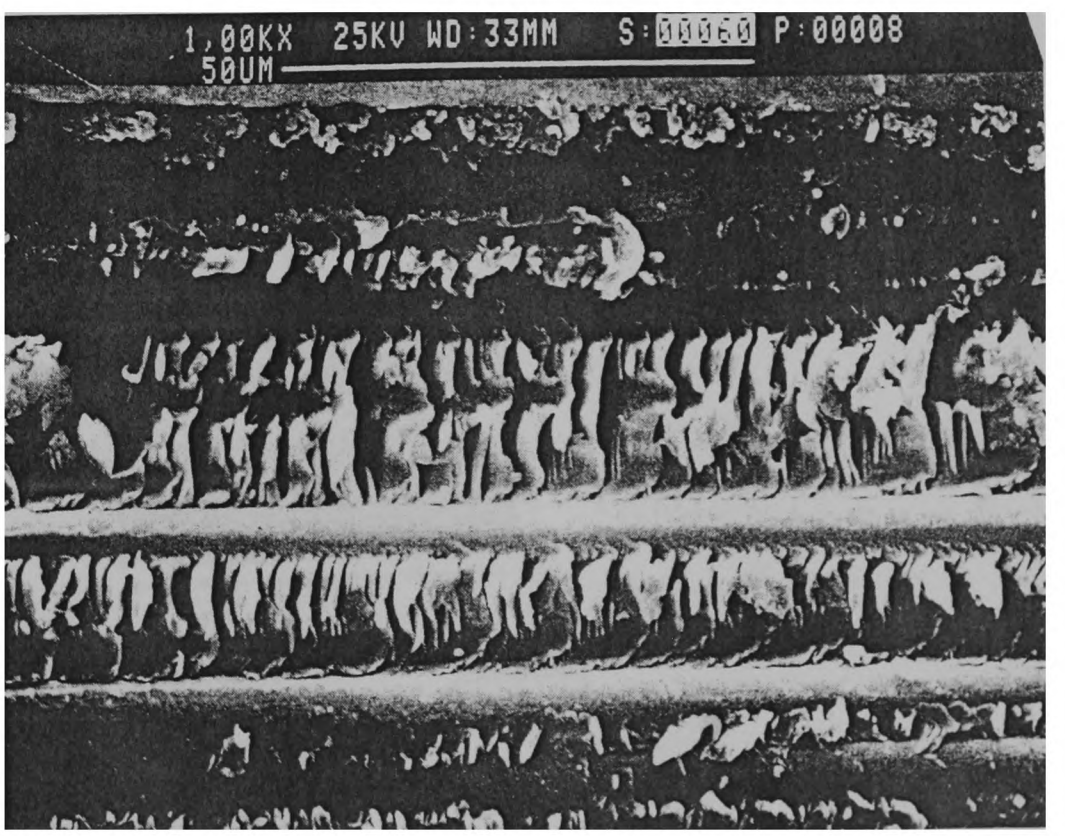

(b) Mode II fracture in unidirectional AS4/3501-6 graphite/epoxy.

Figure 5.2 Typical morphology of interlaminar fracture in UD graphite/epoxy composites (Arcan, 1987).

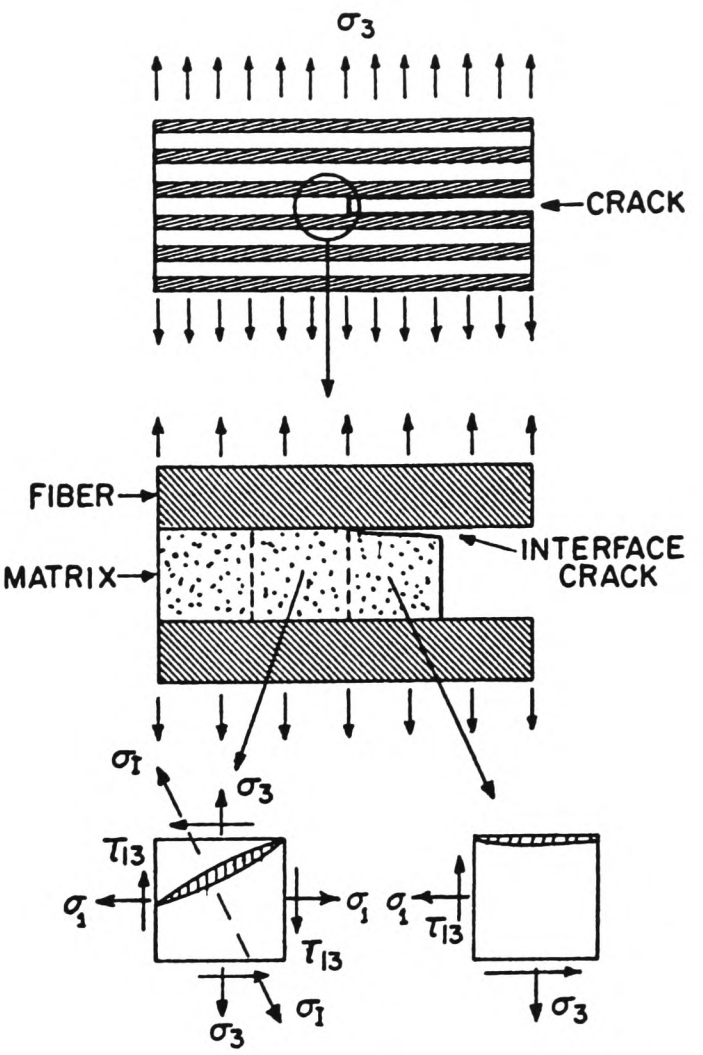

(a) Physical model explaining crack branching under Mode I loading.

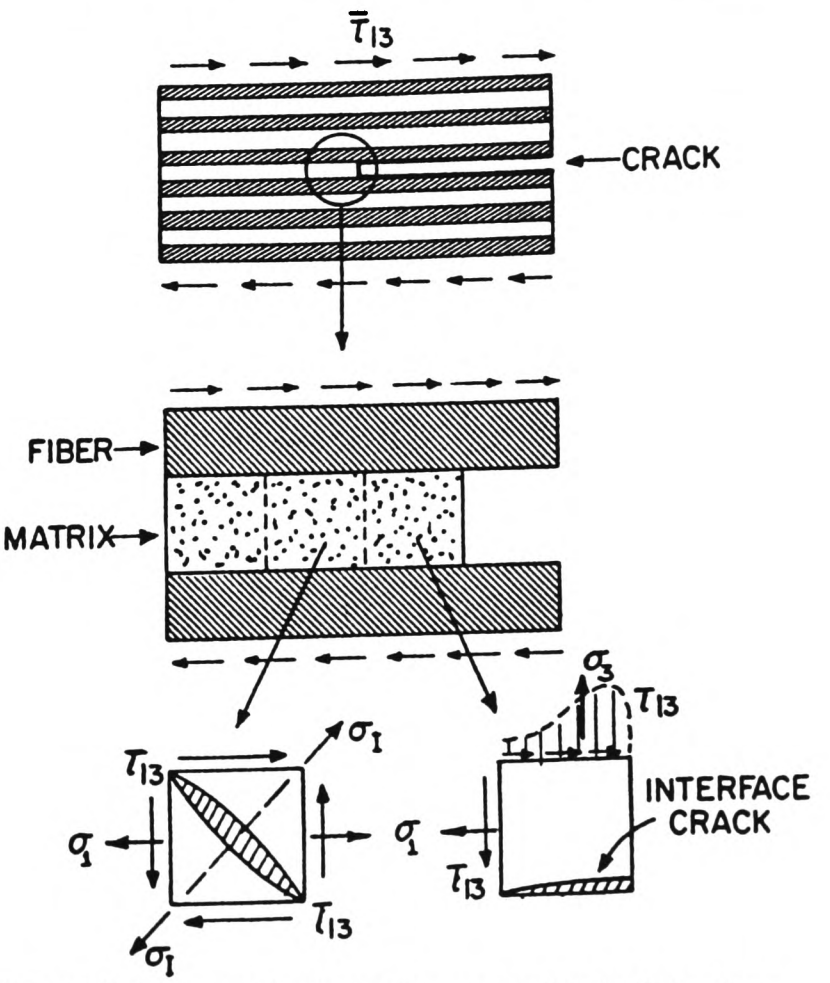

(b) Physical model explaining crack formation under Mode II loading.

Figure 5.3 Physical model explaining resin hackle formation (Arcan, 1987).

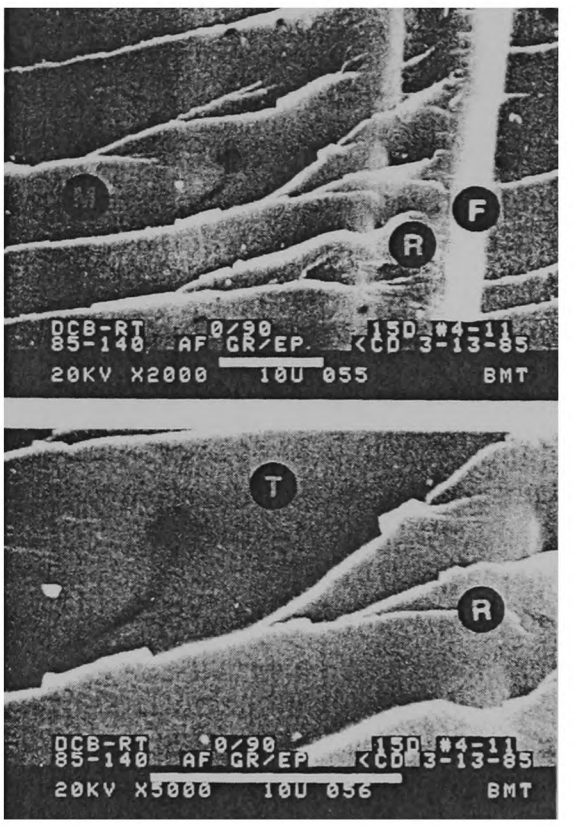

(a) Fracture topography typical of Mode I delamination between 0 and 90° plies.

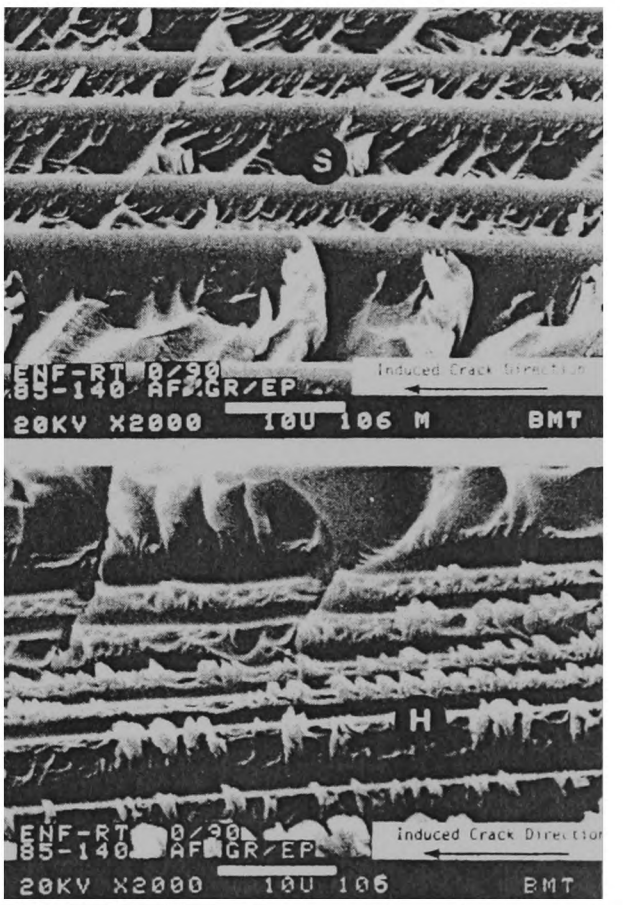

(b) Topography of mating fracture surfaces produced under Mode II between 0 and 90° ply orientations.

Figure 5.4 Fracture topography of delamination between 0 and 90° plies (Smith, 1987).

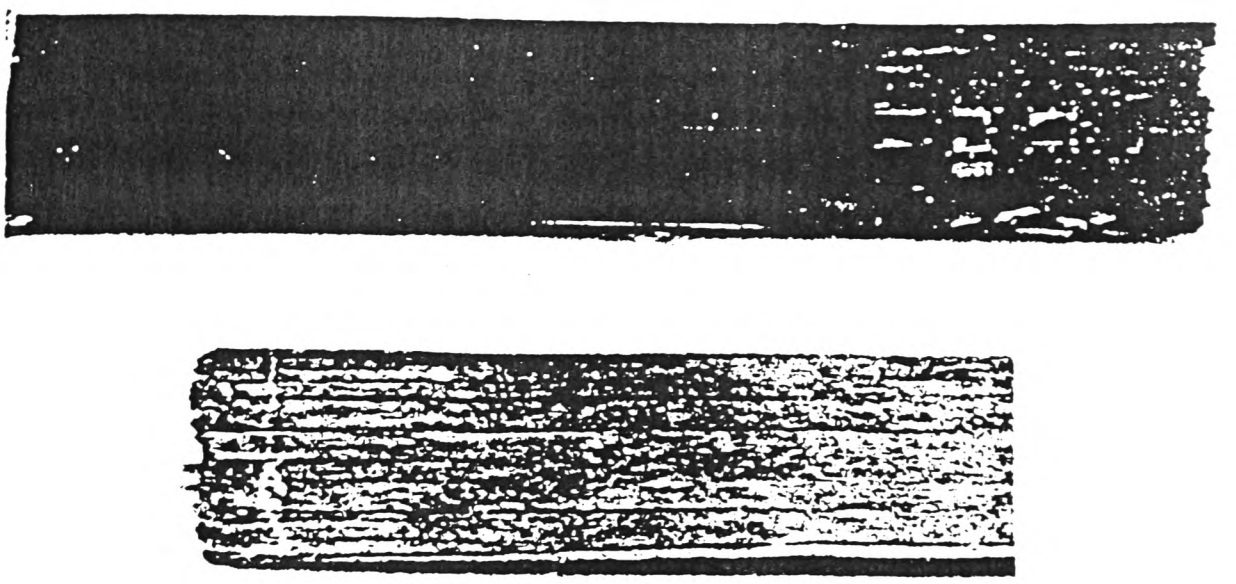

Clean failure (CFRP)

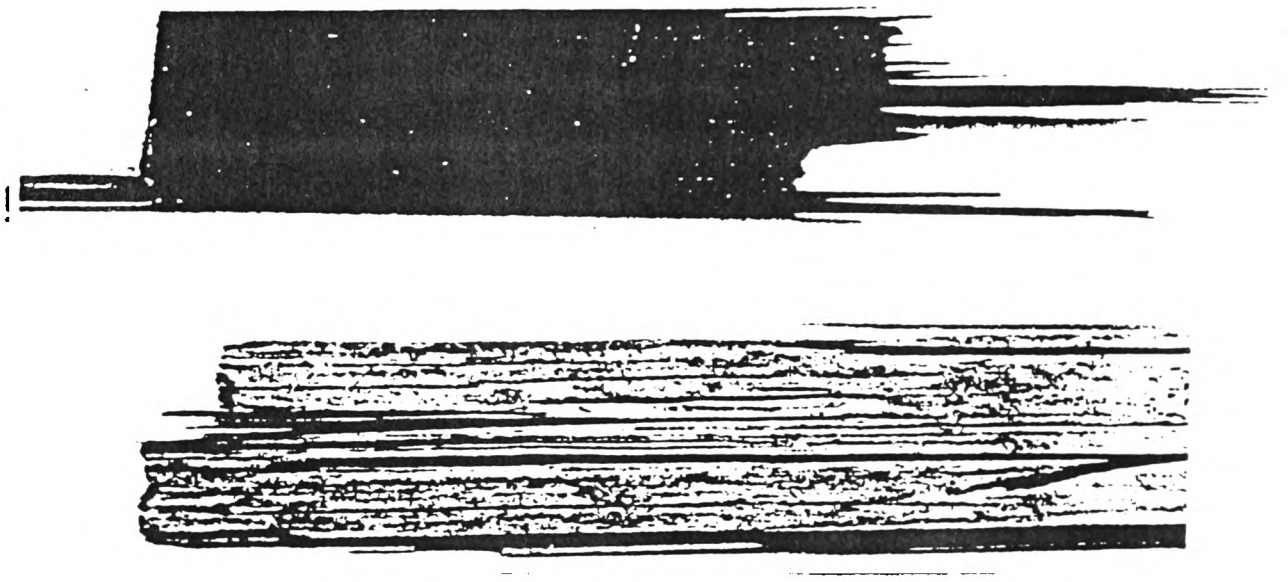

Bush type failure (CFRP)

Figure 5.5 Tensile failure modes in fibre reinforced unidirectional laminates under uniaxial load (ESDU, 1986).

(a) Diagonal shear failure form for individual layer in longitudinal compression.

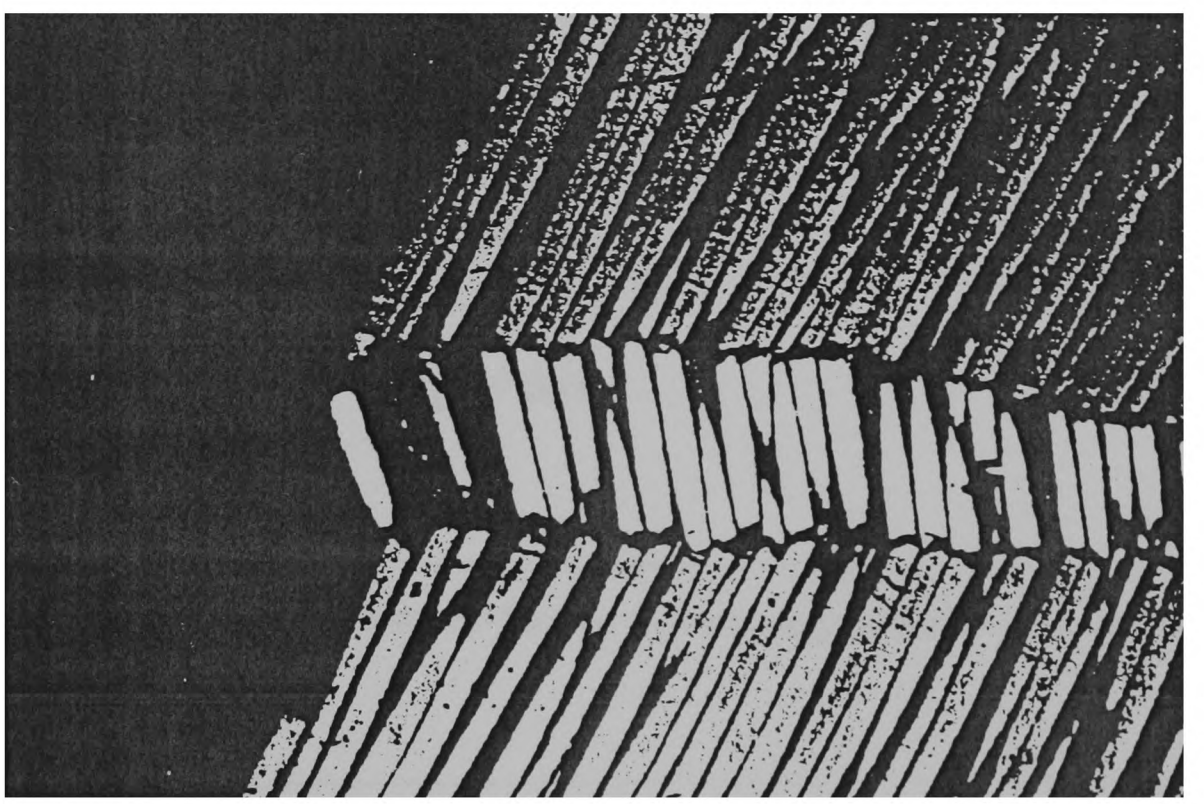

(b) "Kind band" failure of individual layer or unidirectional laminate compression.

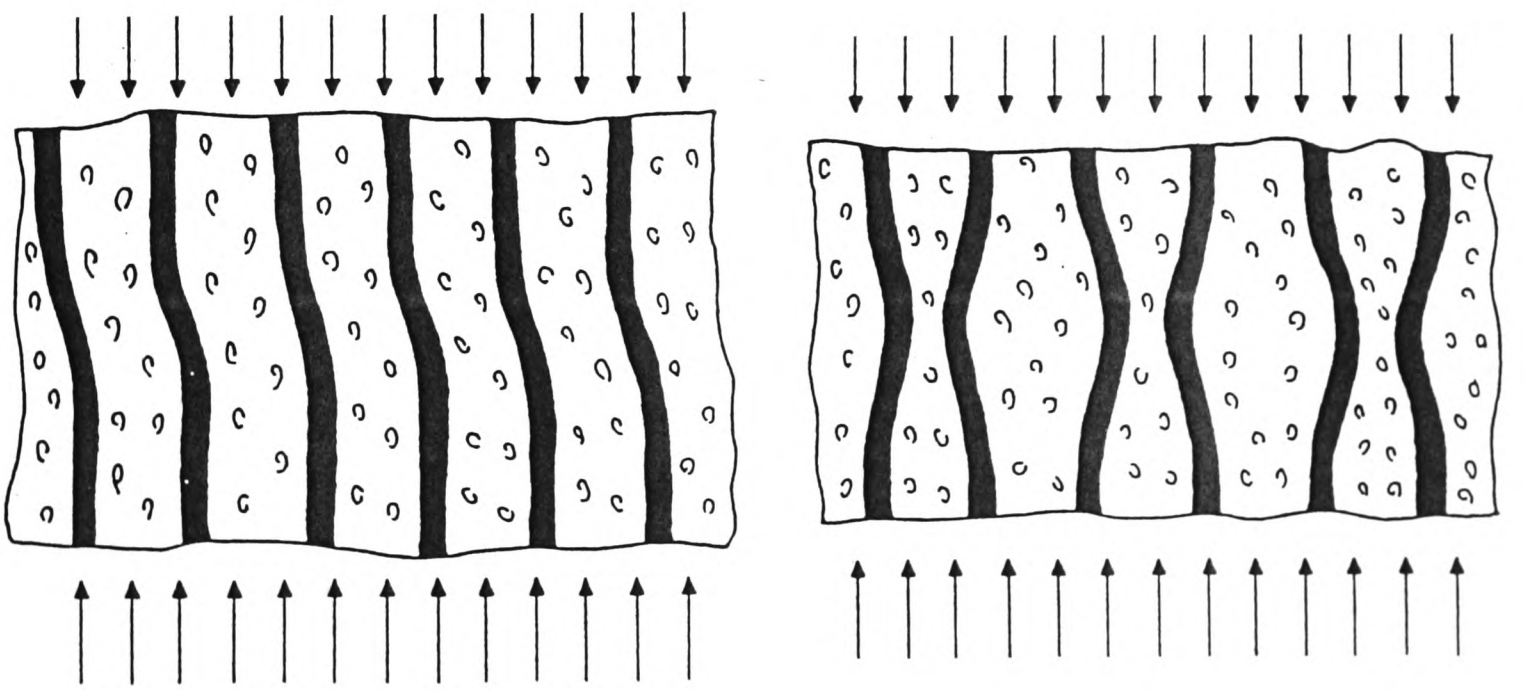

(c) Fibre microbuckling.

Figure 5.6 Compression failure modes in UD laminates under uniaxial load (ESDU, 1986).

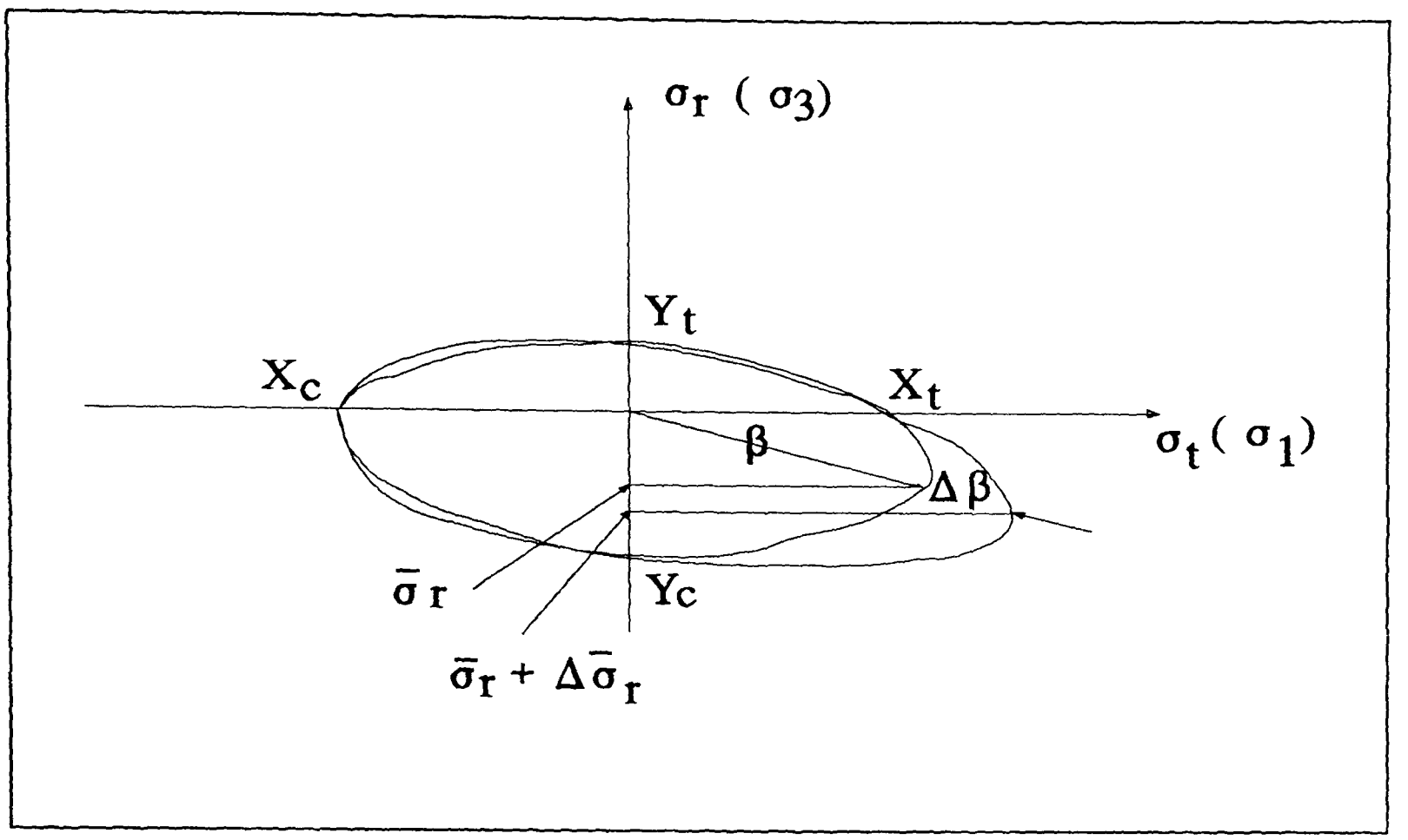

Figure 5.7 Schematic of failure surface in σ_1-σ_3 (σ_t-σ_r) domain with variation of F_{13}.

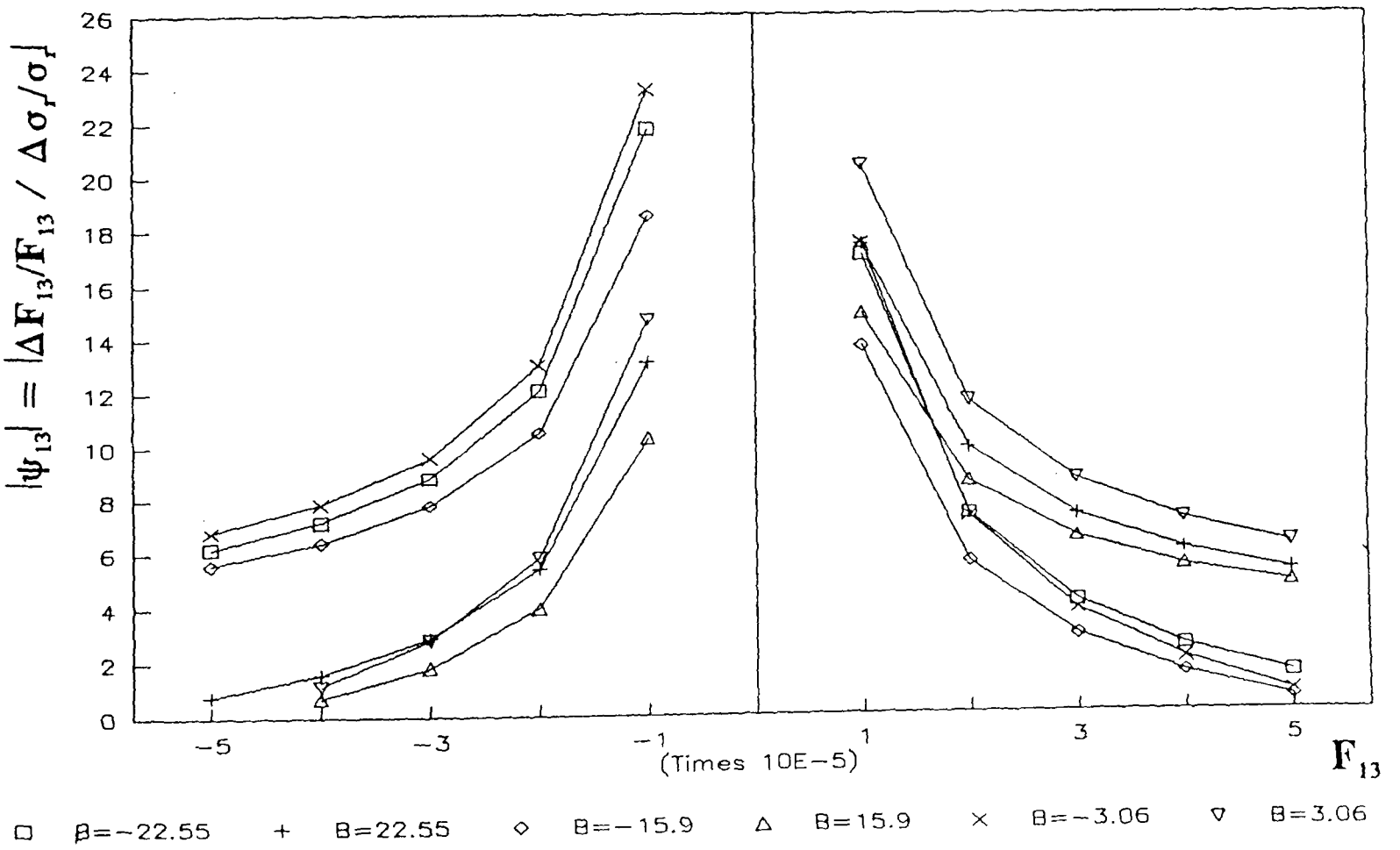

Figure 5.8 ψ_{13} vs F_{13} with variation of B.

Chapter 6

APPLICATION OF WEIBULL STATISTICS

6.1 INTRODUCTION

The effect of stress gradient on failure in brittle materials like ceramics has been well described by Weibull statistics, as it is assumed that all the stress-limiting defects are distributed uniformly throughout the brittle body and they are generally statistical in nature. A typical example is that when a rectangular-section ceramic bar is tested in three-point bending, the strength (σ_{bend}) will always exceed the mean strength of the bar in tension(σ_{ten}). This observation could be described by the Weibull statistical method, which predicts that, for the material with Weibull modulus m=20, the ratio of $\sigma_{ten}/\sigma_{bend}$ = 0.577 (Derby, 1992).

Polymer-matrix composites (PMCs) reinforced with continuous fibres have a number of characteristics that are typical of brittle materials. One of the most important similarities to ceramics is that PMCs lack plasticity to reduce the influence of stress concentrations arising from defects (Zweben, 1994). Actually the three tests conducted in the previous chapters have already shown the features of linear elastic deformation and brittle failure both for C/epoxy and G/epoxy material systems. These make it possible to use the statistical method in the interpretation of the stress gradient effect in PMCs.

6.2 WEIBULL STATISTICS

A statistical distribution first proposed by Weibull in 1951 is currently the most favoured technique used in design with brittle materials. This approach reflects the fact that the strength

of a brittle material is limited by the size of the largest flaw present. A simple mechanical analogy is that of a long chain, the strength of which will be determined by the weakest link. If the strength of individual links follow some probability distribution we can clearly see that the longer the chain, the more links are present, and hence the greater the likelihood of a weak link. This type of behaviour is seen in brittle materials, where a large specimen usually fails at a lower strength than a small one.

In order to model the behaviour of these materials, consider a chain of length λ under a load F with a probability of failure $P_f(\lambda)$. There will be a complementary probability that the chain survives of $P_s(\lambda)=1 - P_f(\lambda)$. If the length of chain is now doubled to 2λ, then the probability of survival will be that of two chains of length λ joined together, i.e.

$$P_s(2\lambda) = P_s(\lambda) \cdot P_s(\lambda) \qquad (6-1)$$

If instead of a chain it is a piece of a brittle material of unit volume V under a stress σ, a similar survival probability of $P_s(V)$ can be defined. Using the same arguments as those used to calculate the probability of failure of the chain, the probability that a piece of a brittle material of volume xV will fail at the same stress is:

$$P_s(xV) = [P_s(V)]^x \qquad (6-2)$$

For ease of manipulation later, the above equation can be rewritten as:

$$P_s(xV) = \exp\{x \ln[P_s(V)]\} \qquad (6-3)$$

In Weibull's terminology the risk of fracture is defined as:

$$R = -x \ln[P_s(V)] \qquad (6-4)$$

and at infinitesimally small volumes of ceramic this is taken to depend solely on the stress

experienced by that volume, i.e.

$$dR = f(\sigma)\, dV \tag{6-5}$$

Weibull then proposed a simple three-parameter expression for f(σ) of:

$$f(\sigma) = \left(\frac{\sigma - \sigma_c}{\sigma_o} \right)^m \tag{6-6}$$

where σ_c is a critical stress below which no failure is observed and σ_o is a normalising reference stress of no physical significance. Combining the above equations, a failure probability as a function of stress and volume can be calculated by:

$$\begin{aligned} P_f(V) &= 1 - P_s(V) \\ &= 1 - \exp\left[-\int_V \left(\frac{\sigma(V) - \sigma_c}{\sigma_o} \right)^m \frac{dV}{V_o} \right] \end{aligned} \tag{6-7}$$

where σ(V) is the stress of an element dV as a function of its position in the stressed volume and V_o is some normalising reference volume. If the volume of material tested is stressed uniformly, Eqn.(6-7) becomes:

$$P_f(V) = 1 - \exp\left[-\left(\frac{V}{V_o} \right) \left(\frac{\sigma - \sigma_c}{\sigma_o} \right)^m \right] \tag{6-8}$$

the magnitude of *m*, known as the Weibull modulus, determines the width of this probability distribution in σ. If *m* is large the distribution becomes narrow and the material behaves as if there is a very narrow range of σ over which failure might occur. Conversely, if *m* is small there will be a large range of possible failure stresses. The extreme situations are that $m=\infty$, corresponding to the ultimate precise definition of a unique failure stress, and m=0 which defines a totally random fracture behaviour. Clearly all materials lie between these limits, with most ceramics having values in the range $5 < m < 25$ (Derby, 1992) and a well-made polymer

composite around 24 (Zweben, 1994). In contrast, metals would have *m* values in the 100s.

6.3 THE EFFECT OF STRESS DISTRIBUTION IN A LAMINATED COMPOSITE

In most engineering applications the stress within a component will not be constant and approximate solutions such as Eqn.(6-8) will not be valid. Instead, the complete volume integral of the stress distribution in Eqn.(6-7) must be considered. It is easier to consider the evaluation of this volume integral if some measurable reference stress is used to define the stress distribution, i.e. $\sigma(V) = f(V)\sigma_{ref}$, where f(V) is some function of the position of a volume element dV. This stress σ_{ref} might be, for example, the maximum tensile stress observed on the surface of a specimen tested in bending. This can now be included into Eqn.(6-7) to give the probability distribution function for a volume V which contains some stress distribution $\sigma(V)$:

$$P_f(V) = 1 - P_s(V)$$
$$= 1 - \exp\left[-\left(\frac{V}{V_o}\right)\left(\frac{\sigma_{ref}}{\sigma_o}\right)^m \int_V \left(\frac{\sigma(V)}{\sigma_r}\right)^m \frac{dV}{V}\right] \qquad (6\text{-}9)$$

The volume integral in the above equation has the normalising constants σ_0 and V_o removed and is known as the stress-volume integral. Because $\sigma(V)$ will be a linear relation with the reference stress, the stress-volume integral will be independent of the load on the specimen. This integral can be determined analytically or numerically but it is still needed to replace the normalising constants by physically meaningful terms.

The constant-stress probability distribution function with $\sigma_c = 0$ (Eqn. 6-8) is considered first. This probability is a cumulative probability of failure and from it the mean failure stress $\bar{\sigma}$

may be determined:

$$\overline{\sigma}=\int_o^{\infty}\exp\left[-\left(\frac{V}{V_o}\right)\left(\frac{\sigma}{\sigma_o}\right)^m\right]d\sigma$$
$$=\Gamma\left(\frac{1}{m}+1\right)\left(\frac{V_o}{V}\right)^{\frac{1}{m}}\sigma_o \qquad (6\text{-}10)$$

where $\Gamma(1/m + 1)$ is the numerically evaluated gamma function, given by:

$$\Gamma(q)=\int_o^{\infty}x^{q-1}e^{-x}dx \qquad (6\text{-}11)$$

which can be referred to in tables of mathematical constants. From this σ_0 can be replaced by a measured average stress $\overline{\sigma}$ to give:

$$P_f(V)=1-\exp\left[-\left(\frac{1}{m}!\right)^m\left(\frac{\sigma}{\overline{\sigma}}\right)^m\right] \qquad (6\text{-}12)$$

where 1/m! is conventionally used to replace the gamma function in Eqn (6-10).

Using the above equation, the behaviour of some real reference volume V^*, which is uniformly stressed (σ^*) and has a mean failure stress $\overline{\sigma}^*$, is now considered. This mean failure stress is given by:

$$\overline{\sigma^*}=\int_o^{\infty}\exp\left[-\left(\frac{V^*}{V_o}\right)\left(\frac{\sigma_{ref}}{\sigma_o}\right)^m\int_V\left(\frac{\sigma^*(V)}{\sigma_{ref}}\right)\frac{dV}{V^*}\right]d\sigma_r \qquad (6\text{-}13)$$

Note that the asterisk here denotes a reference value. In the case of a uniformly stressed volume the stress distribution will be constant and must be equal to the system's reference stress, i.e. $\sigma^*(V) = \sigma_{ref}$ and the stress-volume integral in Eqn(6-13) will be equal to 1. Thus the above equation gives:

$$\overline{\sigma^*}=\left(\frac{V_o}{V^*}\right)^{\frac{1}{m}}\left(\frac{1}{m}!\right)\sigma_o \tag{6-14}$$

If this is now substituted into Eqn. (6.9),

$$\begin{aligned} P_f(V) &= 1-P_s(V) \\ &= 1-\exp\left[-\left(\frac{V}{V_*}\right)\left(\frac{\sigma_{ref}}{\overline{\sigma_*}}\right)^m\left(\frac{1}{m}!\right)^m\int_v\left(\frac{\sigma(V)}{\sigma_{ref}}\right)^m\frac{dV}{V}\right] \end{aligned} \tag{6-15}$$

Now all the undefined normalizing constants have been replaced by well-defined or measurable stresses and volumes. The average failure stress for any specimen is then given by:

$$\begin{aligned} \overline{\sigma} &= \int_o^\infty \exp\left[-\left(\frac{V}{V^*}\right)\left(\frac{\sigma_{ref}}{\overline{\sigma^*}}\right)^m\left(\frac{1}{m}!\right)^m\int_v\left(\frac{\sigma(V)}{\sigma_{ref}}\right)\frac{dV}{V}\right]d\sigma_{ref} \\ &= \overline{\sigma^*}\left[\frac{V^*}{V\ I(V)}\right]^{1/m} \end{aligned} \tag{6-16}$$

where I(V) represents the stress-volume integral.

A typical testing geometry is shown in Fig. 6-1(a), where the strength of a rectangular-section carbon/epoxy woven laminate bar is tested under four-point bending. The maximum tensile stress occurs on the top surface and is given by,

$$\sigma_{max}=\frac{3Pl'}{bh^2} \tag{6-17}$$

If the reference stress is taken as this maximum stress (i.e. $\sigma_{ref}=\sigma_{max}$), and only considering half of the bar because of the symmetry, the stress distribution in the bar is given by,

$$\sigma(V) = \frac{2y}{h}\sigma_{ref} \qquad for \quad x > l' \tag{6-18.a}$$

$$\sigma(V) = \frac{2y}{h}\frac{x}{l'}\sigma_{ref} \qquad for \quad x < l' \tag{6.18.b}$$

i.e., the stress distributions in a four-point bending bar are that, in the middle part it only changes along the height direction while in the two ends it changes along both axis and height directions. Therefore the stress volume integral is,

$$I(V) = \int_V \left(\frac{\sigma(V)}{\sigma_{ref}}\right)^m \frac{dV}{V}$$

$$= 2\int_0^{l'}\int_0^{\frac{h}{2}} \left(\frac{2yx}{hl'}\right)^m \frac{dxdy}{hl} + \int_0^{h/2}\left(\frac{2y}{h}\right)^m \frac{(l-2l')}{hl}dy \tag{6-19}$$

$$= \frac{l}{l'}\frac{1}{(m+1)^2} + \frac{(l-2l')}{l}\frac{1}{2(m+1)}$$

From Eqn. (6-16) the relationship between the four-point bending mean failure stress $\bar{\sigma}_{bend}$ and the reference stress $\bar{\sigma}^*$ will be,

$$\frac{\bar{\sigma}^*}{\bar{\sigma}_{bend}} = \left[\frac{V_{bend}}{V^*}\left(\frac{l'}{l(m+1)^2} + \frac{l-2l'}{2l(m+1)}\right)\right]^{1/m} \tag{6-20}$$

Assuming $V_{bend} = V^*$, Eqn.(6-20) will predict the ratio between the mean tensile stress and mean four-point bending strength for a given laminate specimen depending on the value of m and the assembly of the test rig (l & l').

6.4 DETERMINATION OF WEIBULL MODULUS m

Rearranging Eqn.(6-8) and taking logarithms twice, the following equation is obtained,

$$lnln(\frac{1}{1-P_f})=mln(\sigma_f-\sigma_c)+ln(\frac{V}{V_0})-mln\sigma_0 \qquad (6-21)$$

The physical meaning of the term σ_c is a maximum stress below which no fracture can occur. Usually σ_c is taken as zero. Hence Eqn.(6-21) can be plotted graphically giving a gradient of *m* and an intercept of $\ln(V/V_o)-m\ln(\sigma_o)$.

If the N test values are placed in ascending order of strength, the *n*th ranked sample can be assigned a nominal probability of failure defined by,

$$P_f=\frac{n}{N+1} \qquad (6-22)$$

Then,

$$\frac{1}{1-P_f}=\frac{N+1}{N-n+1} \qquad (6-23)$$

In order to obtain a reliable value for Weibull modulus *m*, it is necessary to have at least 20 test points (Creyke,1982).

Table 6.1 shows the test results from four-point bending of C/epoxy specimen. The panel was made of 11 plies C/epoxy woven fabric with total thickness of 3mm and was cut into a 148 x 10 mm beam. The test rig assembly was l=120 mm and l'=20 mm. According to Eqn.(6-21), $\ln(\sigma)$ vs. $\ln\ln(1/(1-P_f))$ from Table 6.1 can be plotted in Fig. 6.2. The least squares method is used to fit the data and *m* is measured as 21.

The Weibull modulus can also be estimated from the coefficient of variation, $C_{v,}$, about the mean of a set of results,

$$m \approx \frac{1.2}{C_v} \qquad (6\text{-}24)$$

This is derived by comparing the width of normal and Weibull distributions. Hence,

$$m \approx \frac{1.2 \times \bar{\sigma}}{s} \qquad (6\text{-}25)$$

where,

$$s = \sqrt{\frac{\sum_i (\sigma_i - \bar{\sigma})^2}{(n-1)}} \qquad (6\text{-}26)$$

From data in Table 6.1, m is estimated as 24.6 by Eqn.(6-24), which is quite close to 21.

Table 6.1 Results for Strength Measurement

Ascending Order No.	Flexural Strength (MPa)	Nominal Probability of Failure P_f=n/(N+1)	Specimen No.
1	699.9	1/21	1
2	703.9	2/21	9
3	748.5	3/21	16
4	757.7	4/21	20
5	766.8	5/21	17
6	767.1	6/21	10
7	768.2	7/21	14
8	773.2	8/21	4
9	774.1	9/21	2
10	793.1	10/21	19
11	795.3	11/21	13
12	797.3	12/21	18
13	808.7	13/21	11
14	810.2	14/21	5
15	810.3	15/21	7
16	813.8	16/21	3
17	824.1	17/21	8
18	831.5	18/21	12
19	838.0	19/21	15
20	839.2	20/21	6

According to Eqn.(6-20), it can be predicted that the ratio ($\bar{\sigma}^*/\bar{\sigma}_{bend}$) between the mean tensile strength and mean four-point bending strength for C/epoxy woven laminate is 0.820.

The experimental result of the ratio can be calculated, with $\bar{\sigma}^*$ = 473 MPa in Table 5.1 and $\bar{\sigma}_{bend}$ from Table 6.1 which is 786 MPa with a standard deviation of 38.4 MPa(less than 5%), as 0.602 which is much lower than the theoretical prediction.

The discrepancy might come from two sides. On the one hand, all the data in Table 6.1 was taken as the maximum value to failure for simplicity and ease to handle the experimental data. Actually, micro failures happened before final breakdown as shown in Fig. 6.3. Hence 786 MPa may overestimate the real flexural strength and this may cause a lower experimental result of $\bar{\sigma}^*/\bar{\sigma}_{bend}$. On the other hand, the scatter may be less than in a real situation since the data in Table 6.1 corresponded to the maximum values, i.e. the so calculated Weibull modulus may be larger than the real one according to Eqn.6-24. This may cause the theoretical prediction of $\bar{\sigma}^*/\bar{\sigma}_{bend}$ to have a higher value.

In the following the Weibull modulus m = 21 will still be used with the assumption that the accuracy of m can cause only a systematic error.

6.5 Manipulation of Results Using Weibull Statistics

The real situation in practical structures will not be as simple as the example of four-point bending in Section 6.3, i.e. a function f(V) independent of σ_{ref} to form the relation between $\sigma(V)$ and σ_{ref}, $\sigma(V) = f(V)\,\sigma_{ref}$, in the integral in Eqn.(6-9) is usually difficult to obtain. Some

hypotheses, therefore, are assumed in order to deal with complicated stress distributions. Since the stress gradient in the vicinity of a failure position should have a much larger effect on the failure, for the case of a complicated stress state, a linear stress distribution with the stress gradient equal to that at the position concerned is assumed to manipulate the test results by using Weibull statistics. Then reference stress σ_{ref} is taken as the stress at the position concerned and a relationship between $\sigma(V)$ and σ_{ref} can be obtained.

6.5.1 Notched Beam Test

The whole-field stress contours are shown in Fig.4.3. It can be seen that the stress gradients are mainly along the through-thickness direction. Therefore the integral I(V) in Eqn.(6-16) can become a stress-line integral. As the normalized value of σ_3 is too small to be considered, the stress distributions of σ_1 and τ_{13} along the through-thickness direction for the three geometries at their corresponding failure positions are shown in Figs. 6.4 and 6.5.

Fig. 6.4 shows the distributions of in-plane stress σ_1 along the through-thickness direction at their corresponding failure position for the three geometries. It can be seen that for all of them, the effect of the notch is very small, i.e. they are still nearly linear with the neutral point at the middle of the section. Take the stress at the upper surface (notch surface) as the reference stress and ignore the compressive stress, the stress distribution is,

$$\sigma(V)=\frac{2y}{h_f}\sigma_{ref} \qquad (6\text{-}27.a)$$

where h_f is the height of the section where failure happens and y from 0 to $h_f/2$. The stress integral is,

$$\int_V \left(\frac{\sigma(V)}{\sigma_{ref}}\right)^m \frac{dV}{V} = \int_0^{\frac{h}{2}} \left(\frac{2y}{h_f}\right)^m \frac{dy}{h_f} = \frac{1}{2(m+1)} \tag{6-27.b}$$

Therefore, according to Eqn.(6-16), the ratio between the failure stress at a uniform stress state and the average failure stress when there is a stress gradient, $\bar{\sigma}_{uniform}/\bar{\sigma}_{gradient}$, is 0.835.

Fig.6.5 shows the distribution of interlaminar shear stress τ_{13} along the through-thickness direction at the corresponding failure positions for the geometries of h=3 and h=4 mm. For h=2 mm, τ_{13} is zero along the thickness in the failure position and hence not considered. It can be seen that for both geometries, there is a very sharp stress gradient near the notch surface, where failure happened. As discussed above, a linear stress gradient is assumed near the notch surface (see the dotted line in Fig.6.5) while the stress elsewhere does not affect the failure. Take the stress at the notch surface as reference stress, the stress distributions are, for h=3 mm,

$$\tau_{13}(V) = \frac{y}{0.22h_f}\tau_{13ref} \tag{6-28.a}$$

for h=4 mm,

$$\tau_{13}(V) = \frac{y}{0.25h_f}\tau_{13ref} \tag{6-28.b}$$

where y from 0 to $0.22h_f$ and from 0 to $0.25h_f$ respectively for h=3 and h=4 mm, and again h_f is the height of the section where failure happens.

Then the stress volume integrals are,

for h=3 mm,

$$\int_V \left(\frac{\tau_{13}(V)}{\tau_{13ref}}\right)^m \frac{dV}{V} = \int_0^{0.22h} \left(\frac{y}{0.22h_f}\right)^m \frac{dy}{h_f} = \frac{0.22}{(m+1)} \tag{6-29.a}$$

for h=4 mm,

$$\int_V \left(\frac{\tau_{13}(V)}{\tau_{13ref}}\right)^m \frac{dV}{V} = \int_0^{0.25h} \left(\frac{y}{0.25h_f}\right)^m \frac{dy}{h_f} = \frac{0.25}{(m+1)} \tag{6-29.b}$$

Putting the results of the above equations into Eqn.(6-16), the ratios of $\bar{\tau}_{uniform}/\bar{\tau}_{gradient}$ are 0.803 for h=3 mm and 0.808 for h=4 mm geometry.

Then the experimental results from notched beam tests in Table 4.3 can be modified by multiplying by an appropriate ratio in order to put them onto the failure map, as shown in Table 6.2.

Table 6.2 Modified Failure Stresses from C/Epoxy Notched Beam Tests

Group	Bottom Thickness(mm)	Stress Components at Failure (MPa)		
		σ_1	τ_{13}	σ_3
1	2	628.60	0	0
2	3	404.24	25.35	2.18
3	4	271.72	35.03	4.45

6.5.2 C-Specimen Test

The stress gradient in a C-specimen exists both along the hoop direction (Fig.3.7) and along the radial direction (Fig.3.7) for all three stress components. However the "C" shape of the specimen makes the stresses along the hoop direction change not only in value but also in direction. This makes the effort to obtain a ratio of $\bar{\sigma}_{uniform}/\bar{\sigma}_{gradient}$ meaningless because in practice a stress with uniform value but changing direction is impossible to obtain. Therefore for the C-specimen, only the stress gradients along the through-thickness direction are considered.

From Fig.3.7, it can be seen that the distribution of σ_1 along the through-thickness direction is linear with the neutral point at about the middle. An enlarged figure from Fig.3.7 for a section at θ=60° (the middle of the waist) is shown in Fig.6.6. It is clear that for either tensile stress gradient or compressive gradient, it is the same as the four-point bending example in Section 6.3, therefore the ratio is 0.835.

The distributions of σ_3 and τ_{13} have similar features in that they have a relatively flat part in the middle of the thickness and sharp gradients near the two surfaces. It is therefore assumed that the effect of the stress gradient in the middle part could be ignored. For the specimens tested in Chapter 3, it is found from Fig.3.7 that regardless of the section in the specimen, the distributions of both σ_3 and τ_{13} are nearly the same in terms of the stress gradient. Enlarged figures from Fig.3.7 for θ=60° and 90° are shown in Fig.6.7, noting that τ_{13} is zero at θ= 90° section. For ease of manipulation, it is assumed that the middle flat part includes plies 4 to 7. For the part near the inner surface, take the stress at ply 3 as the reference stress (see

Fig.6.7), the stress distribution is,

$$\sigma_3(V)=\frac{y}{0.25h}\sigma_{3ref} \tag{6-30.a}$$

or

$$\tau_{13}(V)=\frac{y}{0.25h}\tau_{13ref} \tag{6-30.b}$$

where h is the through-thickness height and y from 0 to $0.25h$. According to Eqns.(6-19) and (6-20), the ratio is 0.808. For the part near the outer surface, take the stress at ply 8 as reference stress (see Fig.6.7), the stress distribution is,

$$\sigma_3(V)=\frac{y}{0.33h}\sigma_{3ref} \tag{6-31.a}$$

or

$$\tau_{13}(V)=\frac{y}{0.33h}\tau_{13ref} \tag{6-31.b}$$

where h is the through-thickness height and y from 0 to $0.33h$. The calculated ratio is 0.819.

Therefore, for C-specimens, the experimental results of σ_1, either tensile or compressive, should be multiplied by a ratio of 0.835. For the experimental results of σ_3 and τ_{13}, if the failure happened within plies 4 to 7, the results do not need to be modified; if the failure happened within plies 0 to 3 or 8 to 12, the results need to be modified by multiplying by a ratio of 0.808 or 0.819 respectively.

6.5.3 Modified Table 5.4

In Chapter 5, the experimental results were compared with the predictions by Tsai-Wu criterion as shown in Table 5.4. Table 6.3 presents the results modified by the Weibull analysis.

In quadrant I the tensile oblique specimens show a consistently higher result than predicted, by between 2% and 47%, as in Table 5.4 since the Weibull correction does not apply. The waisted C-specimens, for which the errors previously varied from 44% to -108%, are now more in line with the prediction, with the exception of three results that are less than -111%. It is not unreasonable to accept that these low results are in fact explained by machining damage. The notched beam data show a distinct improvement. There is a good agreement between the predicted and the corrected experimental results for the C-specimens.

Table 5.4 found complex results in quadrant II in that the theory predicts the experimental data very well as σ_1 starts from 0 to a certain value and σ_1 approaches in-plane compressive strength while a very large discrepancy was found in other ranges of σ_1. This is, however, very difficult to explain. The modified test results show a different trend in that as σ_1 starts from 0 to -115.9 MPa, the theory predicts experiments very well; as σ_1 increases further to the in-plane compressive strength, the experimental results of σ_3 decrease dramatically while the theory does not predict this trend and leaves a very large discrepancy. This corresponds to the failure mechanism in quadrant II as discussed in Chapter 5 in which the interaction between in-plane compression and interlaminar tension will greatly reduce the through-thickness strength. Although there is a term in Tasi-Wu theory which considers the interaction

between σ_1 and σ_3, it seems that it cannot well describe quadrant II as it does in quadrant I.

6.5.4 An Empirical Criterion for Quadrant II

As the effect of compressive in-plane stress not only causes a big drop in through-thickness tensile strength but also greatly suppresses the effect of interlaminar shear, a simple equation is proposed to describe the failure in quadrant II, which contains only the effect of σ_1 on σ_3. According to the distribution of the experimental results, an exponential function is assumed,

$$\sigma_3 = a\, e^{b\sigma_1} \tag{6-32}$$

A linear curve fitting can be conducted by assuming,

$$\begin{aligned} X &= \sigma_1 \\ Y &= \ln\sigma_3 \end{aligned} \tag{6-33}$$

then,

$$Y = \ln a + bX \tag{6-34}$$

and using the least squares method to determine a and b, based on the data in quadrant II in table 6.3, regardless of shear stress.

The calculated results are,

a = 35.1 b = 0.003151

and the comparison between experiment and Eqn.(6-32) is shown in Fig.6.8. It can be seen that Eqn.(6-32) shows a very good trend with experiments although a fairly large discrepancy still exists, which is inevitable because of the shortcomings of the C-specimen test.

TABLE 6.3 Comparison of modified experimental results with the prediction by theory

QUADRANTS	TESTS	EXPERIMENTAL RESULTS (MPa)			PREDICTION BY TSAI-WU THEORY (MPa)		ERROR
		σ_1	τ_{13}	σ_3	σ_3	τ_{13}	
I	TENSILE OBLIQUE	0	0	36.5	32		12%
		2.9	10.9	40.9	30.25		26%
		13.8	24.9	40.6	23.1		43%
		32.1	32.1	32.1	17.0		47%
		57.2	30.6	19.1	17.35		9%
		95.8	34.8	12.7	12.5		2%
	WAISTED C-SPECIMEN	41.68	3.78	13.92	29.38		-111%
		49.29	9.82	16.59	27.92		-68%
		112.83	7.21	17.09	24.54		-43%
		126.21	7.0	8.76	23.72		-167%
		146.90	8.15	10.20	22.20		-114%
		188.36	13.91	13.13	18.25		-37%
		195.39	5.72	13.53	19.33		-40%
		231.12	9.51	16.01	16.39		-1%
		234.22	4.41	16.20	16.82		-2%
		251.17	4.74	17.37	15.63		11%
	NOTCHED BEAM	271.72	35.03	4.45		33.99	3%
		404.24	25.35	2.18		19.64	22%
		628.60	0	0		ERR [1]	
	PLAIN C-SPECIMEN	0	0	31.8	32.0		-0.6%
		0	0	32	32.0		0%
		79.33	0	31.02	27.24		12%
		84.34	0	32.96	26.93		19%
		88.93	0	34.76	26.64		23%
		93.52	0	38.5	26.35		31%

II	WAISTED C-SPECIMEN	-105.21	15.68	31.22	33.09		-6%
		-115.90	17.2	34.24	32.50		5%
		-221.48	3.75	13.87	40.11		-180%
		-297.08	8.07	10.22	35.45		-235%
		-418.79	6.55	6.27	ERR		
	PLAIN C-SPECIMEN	-4.76	0	33.3	32.28		3%
		-78.16	5.73	24.9	35.61		-38%
		-80.74	0	25.64	36.26		-37%
		-218.19	5.52	13.43	39.68		-186%
		-231.13	0	14.25	40.46		-175%
		-232.38	3.4	14.33	40.14		-171%
		-244.24	0	15.07	40.34		-159%
		-253.67	0	15.64	40.16		-149%
		-285.57	0	18.51	38.83		-103%
		-302.27	0	12.55	37.50		-190%
		-303.11	0	13.19	37.41		-175%
		-305.11	0	18.84	37.21		-91%
		-306.36	0	18.92	37.08		-90%
		-328.99	0	14.25	33.86		-130%
		-400.55	0	13.6	ERR		
III	COMPRESSIVE OBLIQUE	0	0	-961	-961		0%
		-20.5	121.9	-725.9	-607.8		16%
		-87.6	167.5	-321.3	ERR		
		-124.1	124.1	124.1	ERR		
		-132.2	59.2	-22.4	-34.6		-54%
		-233.8	62.39	-20.8	-62.7		-226%
		-306.9	57.4	-10.8	ERR		

[1] ERR means that the theory can not predict σ_3 (or τ_{13}) for the given experimental results of σ_1 and τ_{13} (or σ_3).

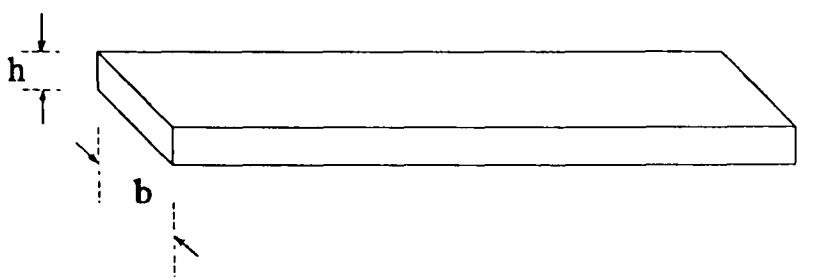

(a)

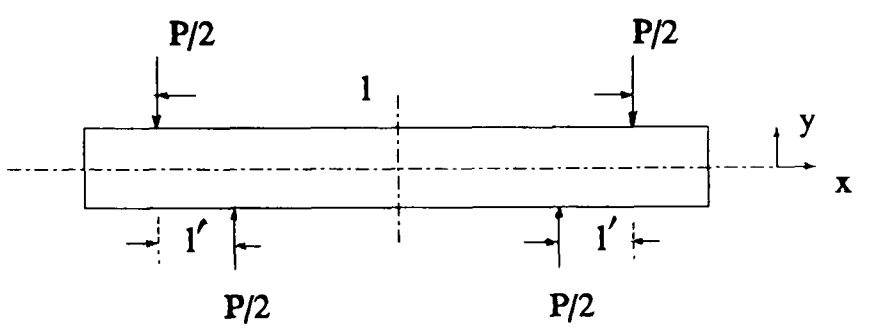

(b)

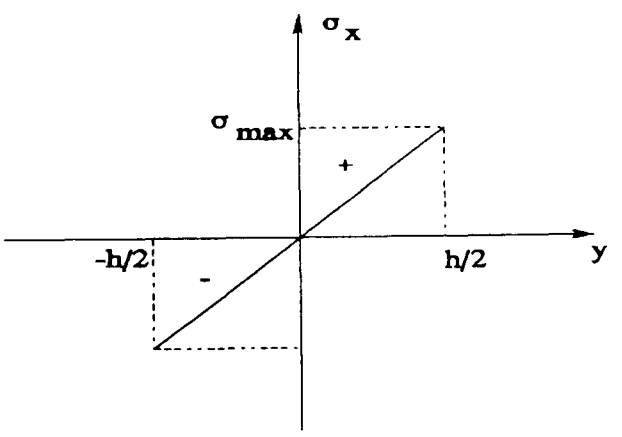

(c)

Figure 6.1 A rectangular-section bar under four-point bending.

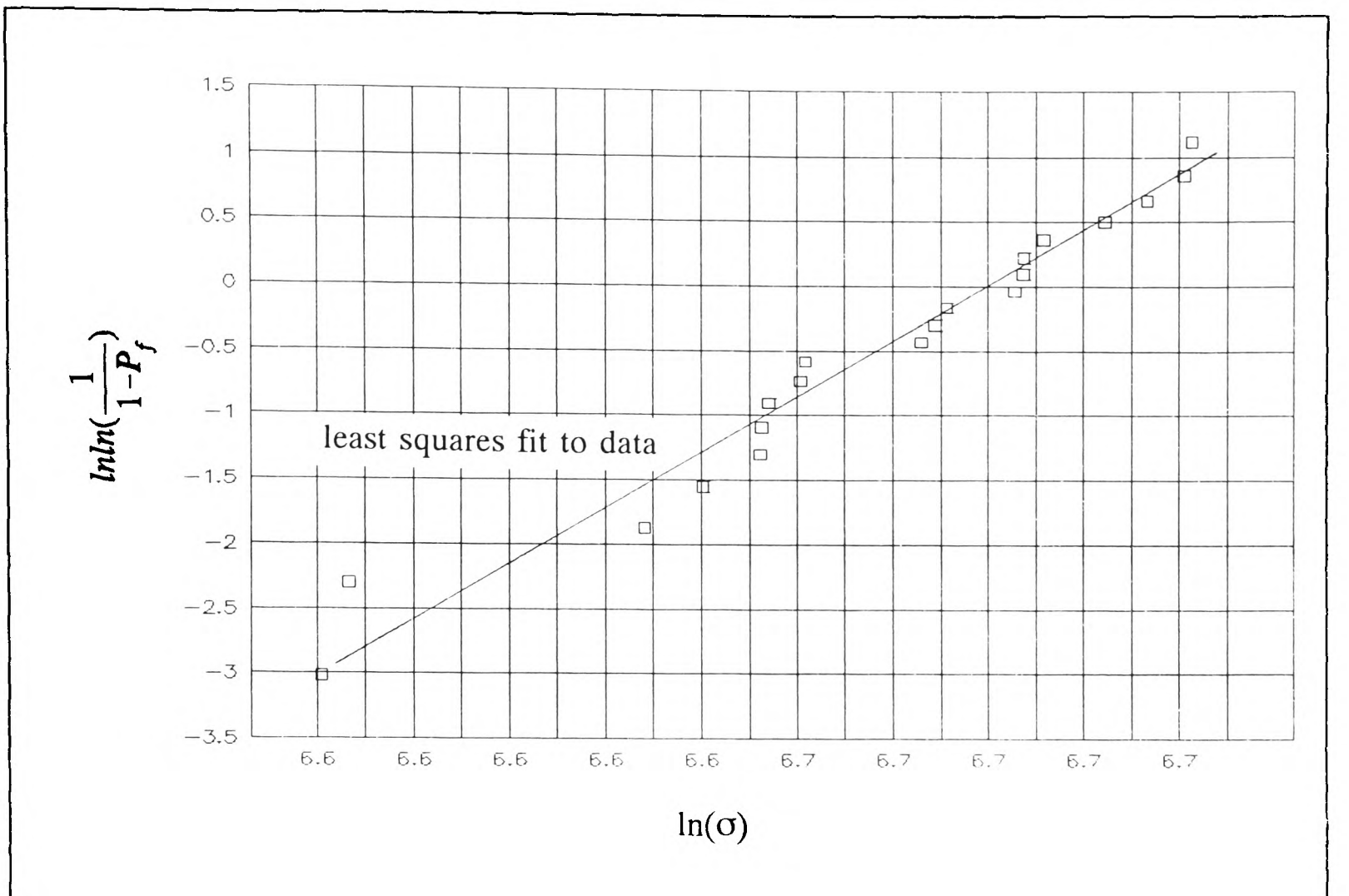

Figure 6.2 Determination of Weibull modulus *m*.

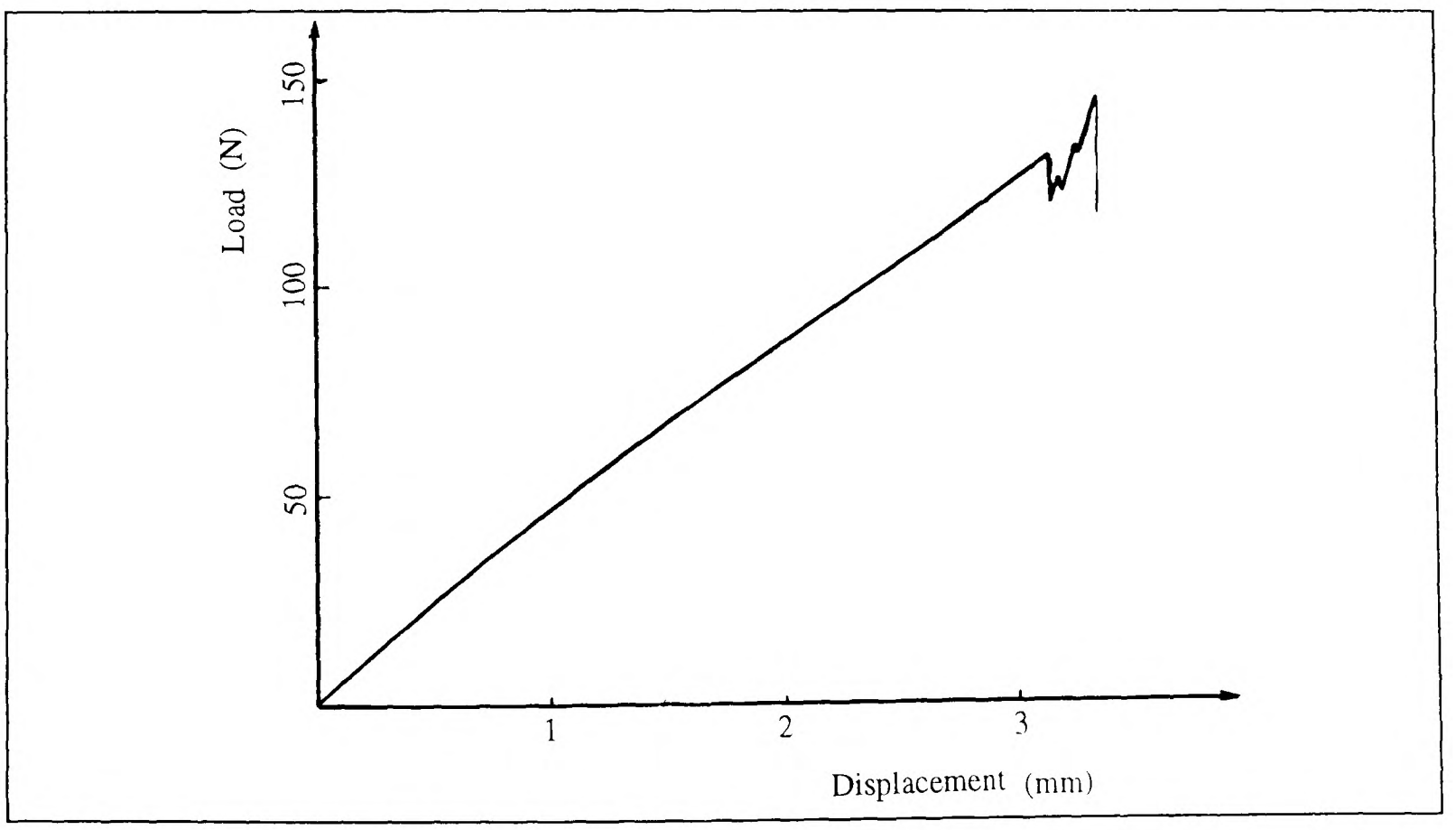

Figure 6.3 The load-displacement curve for specimen No.17 in Table 6.1.

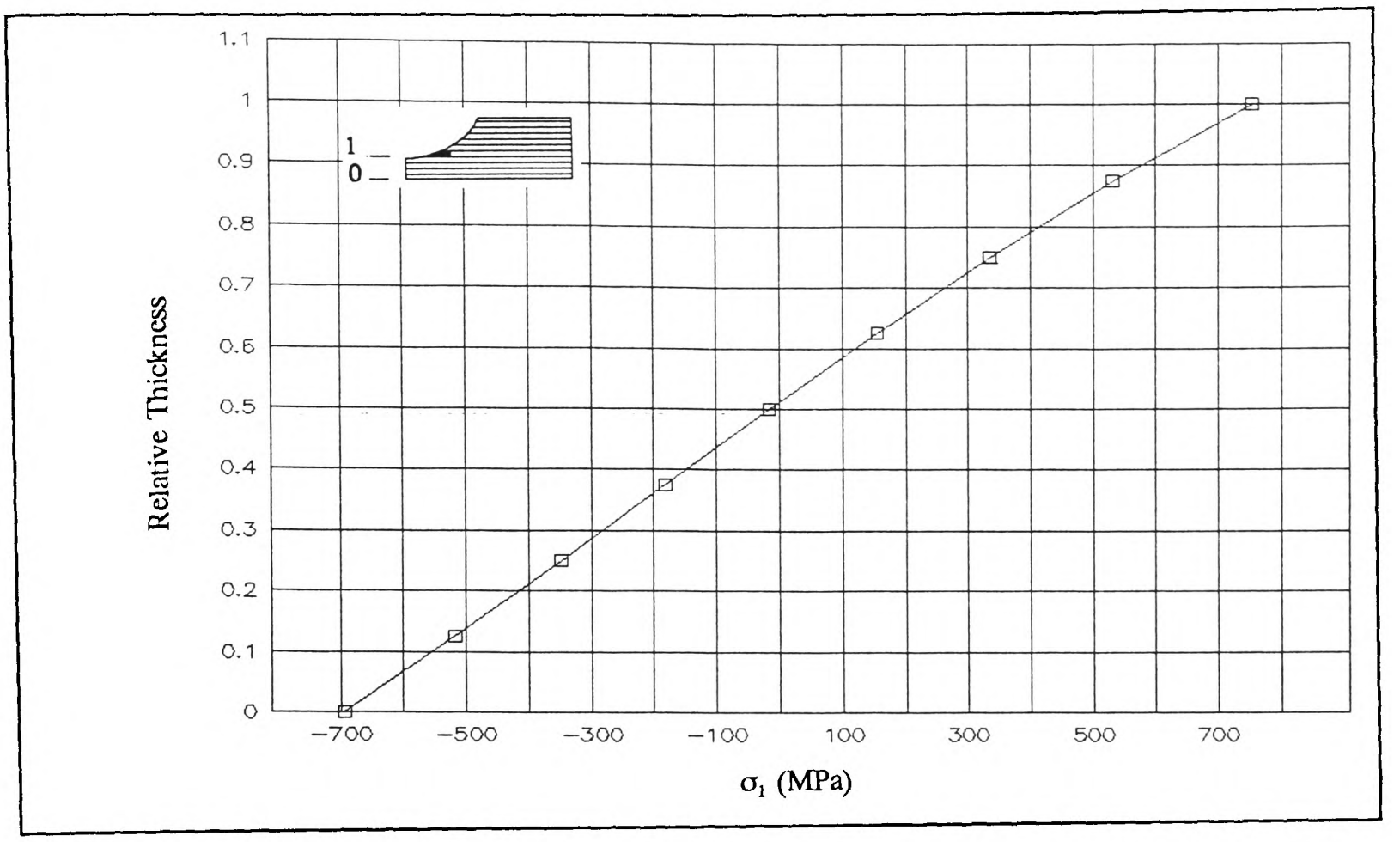

Figure 6.4 (a) The distribution of σ_1 along the through-thickness direction at the failure position for h=2 mm geometry of the notched beam specimen.

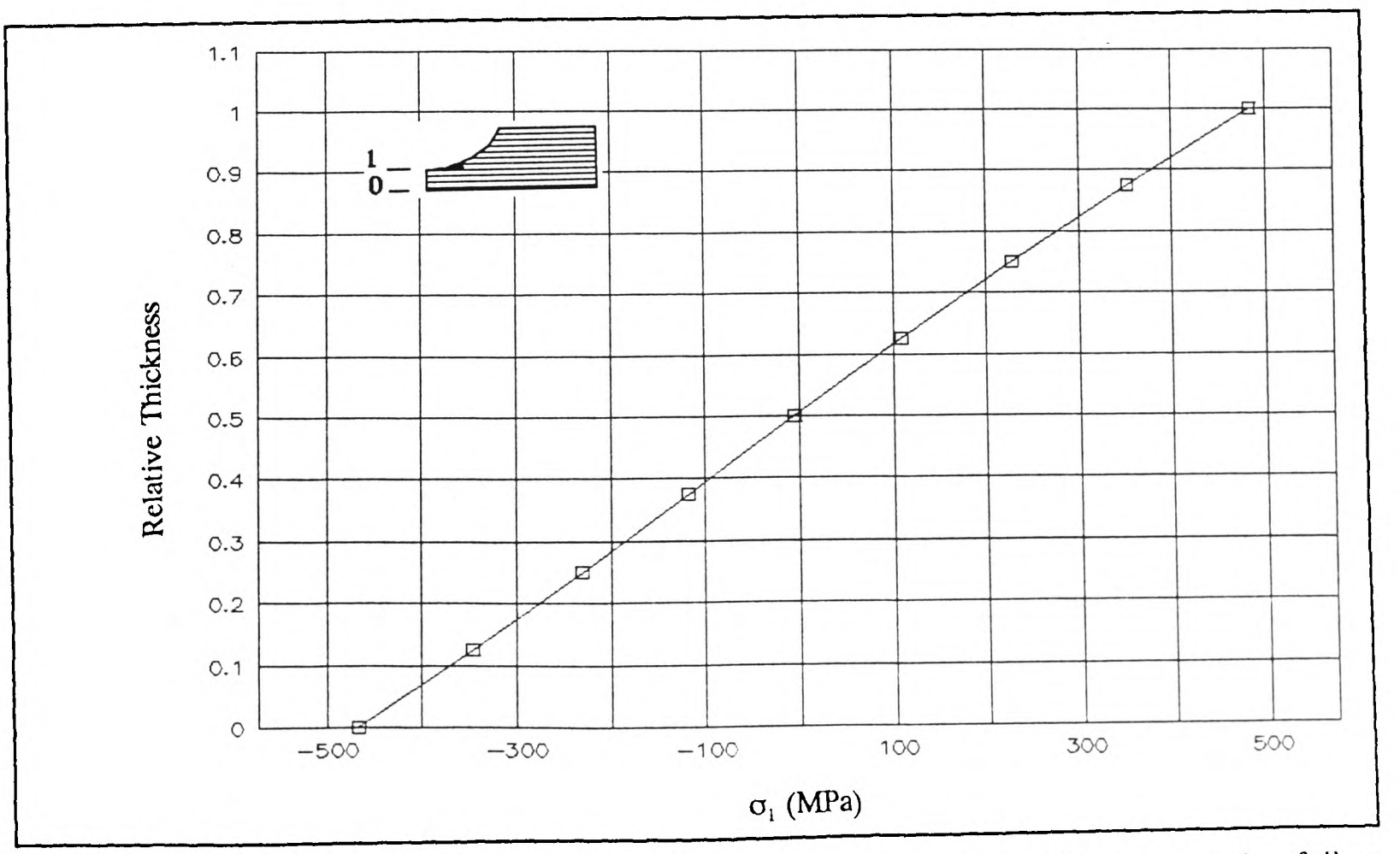

Figure 6.4 (b) The distribution of σ_1 along the through-thickness direction at the failure position for h=3 mm geometry of the notched beam specimen.

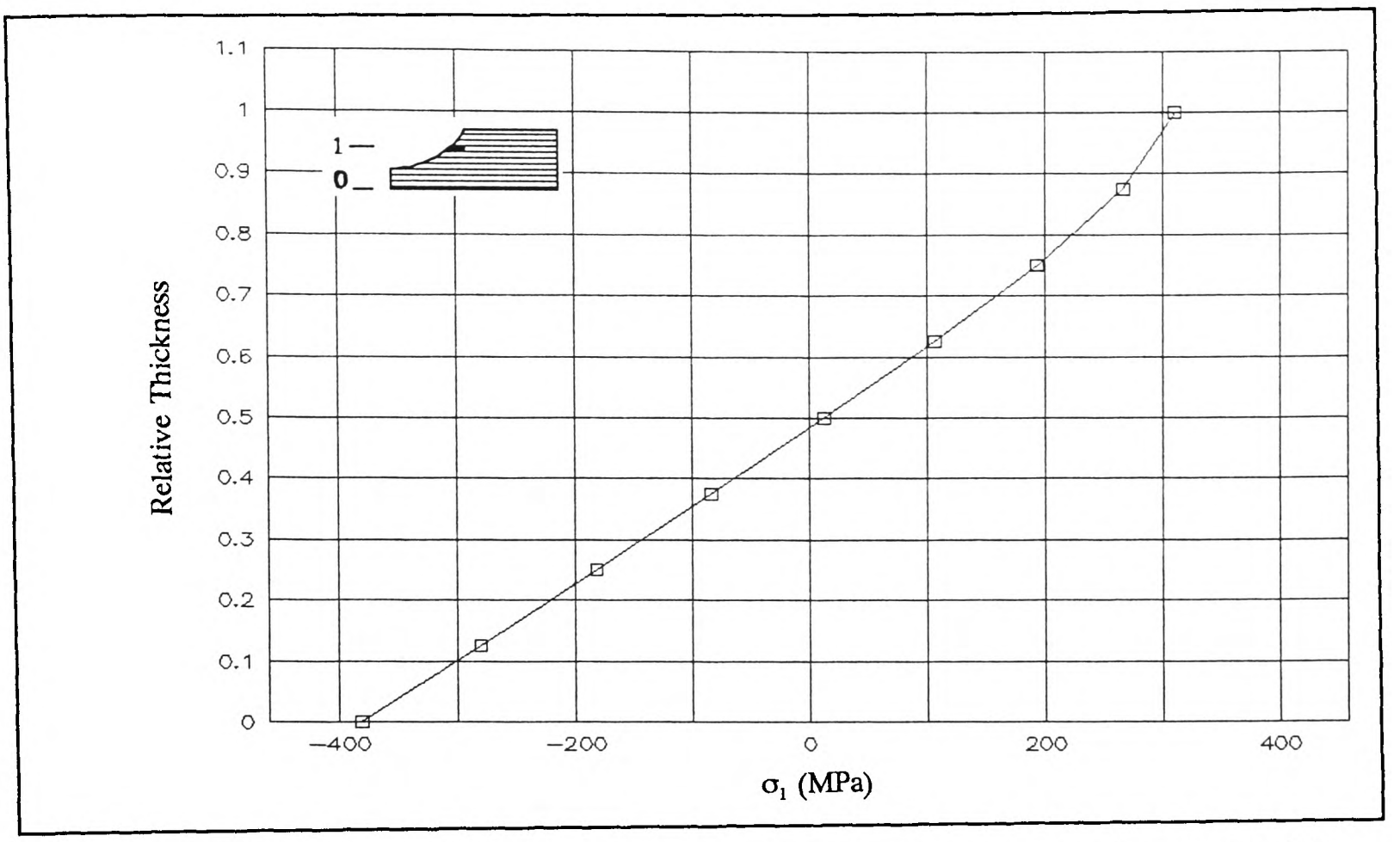

Figure 6.4 (c) The distribution of σ_1 along the through-thickness direction at the failure position for h=4 mm geometry of the notched beam specimen.

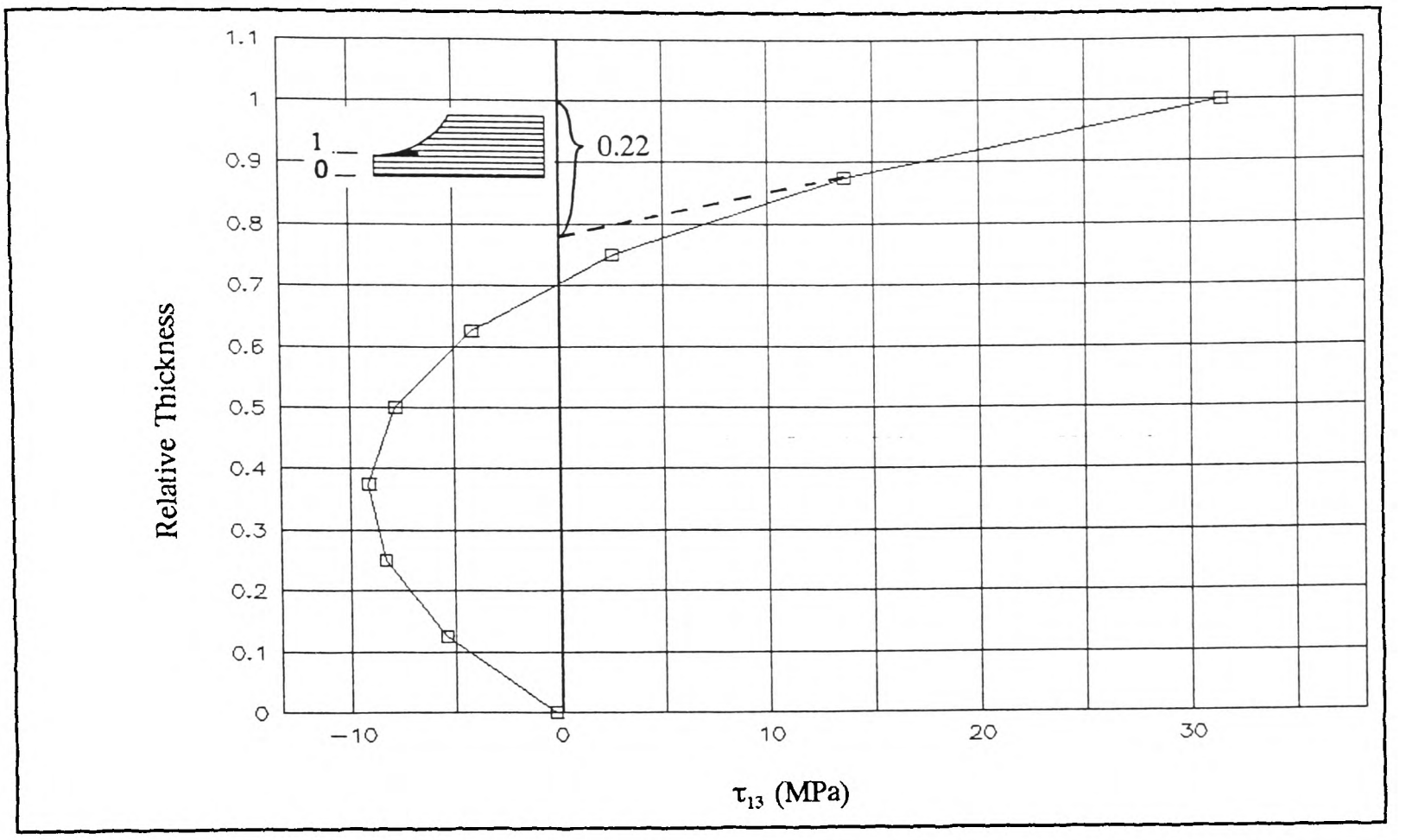

Figure 6.5 (a) The distribution of τ_{13} along the through-thickness direction at the failure position for h=3 mm geometry of the notched beam specimen.

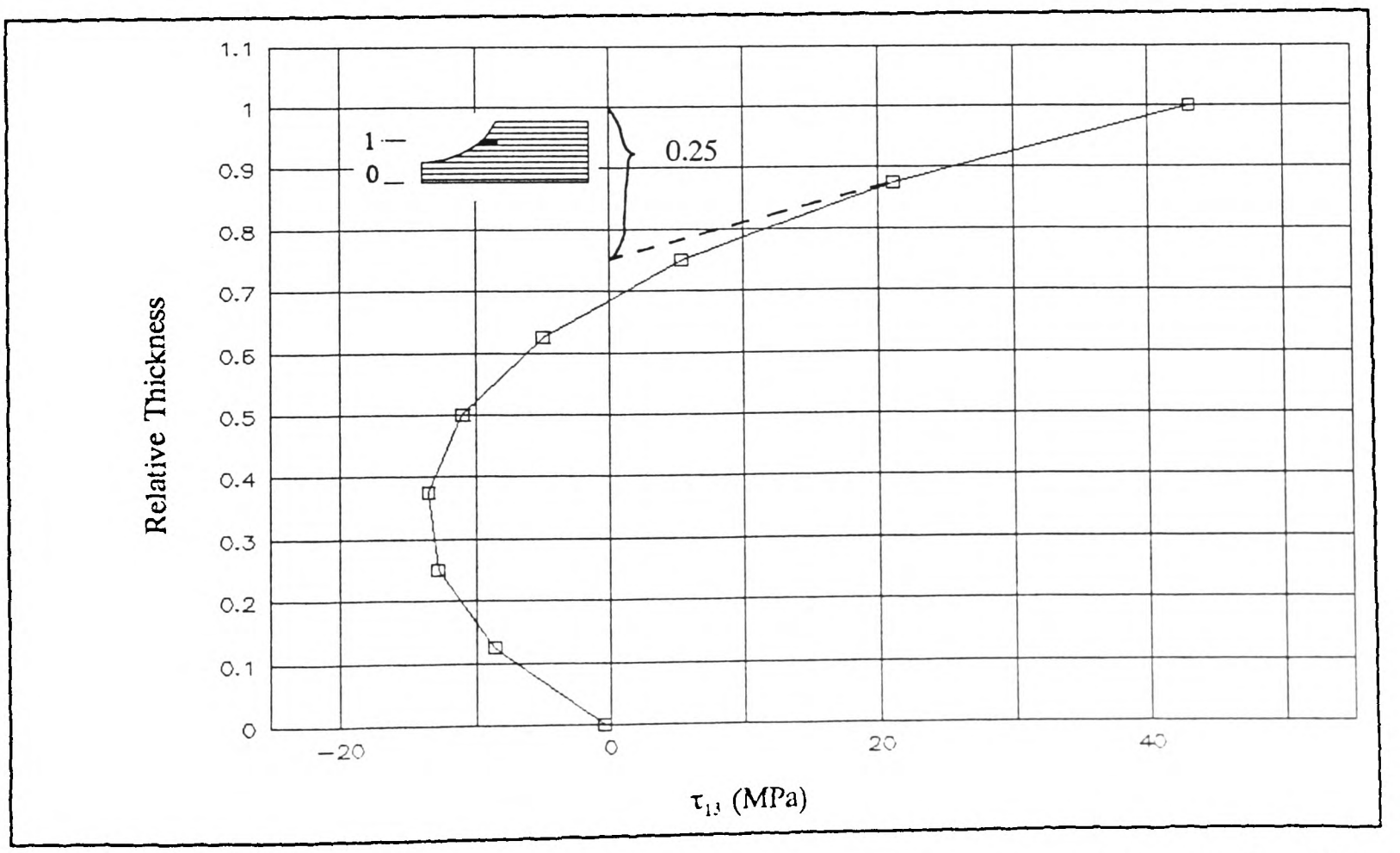

Figure 6.5 (b) The distribution of τ_{13} along the through-thickness direction at the failure position for h=4 mm geometry of the notched beam specimen.

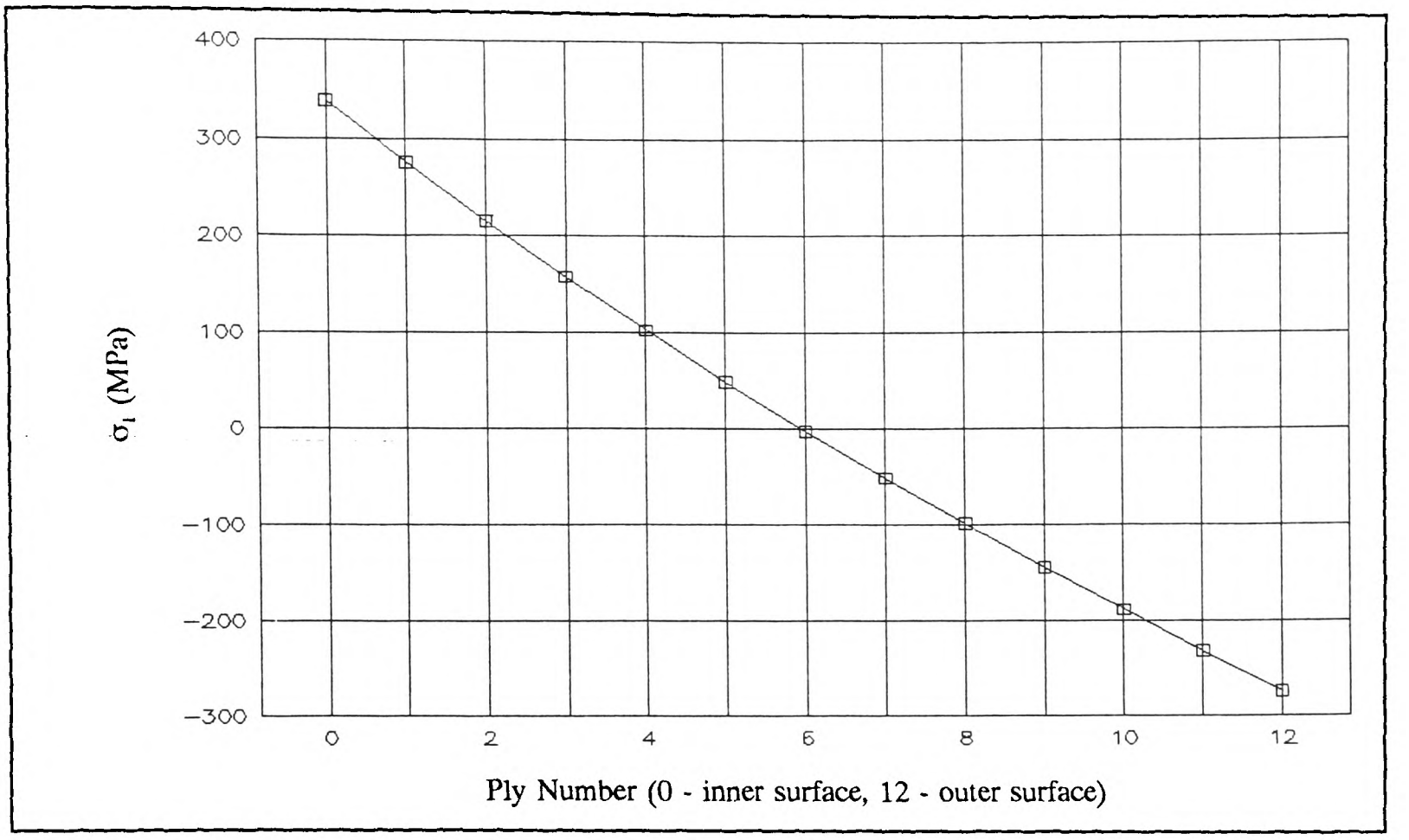

Figure 6.6 The distribution of σ_1 along the through-thickness direction at θ=60° section of the waisted C-specimen.

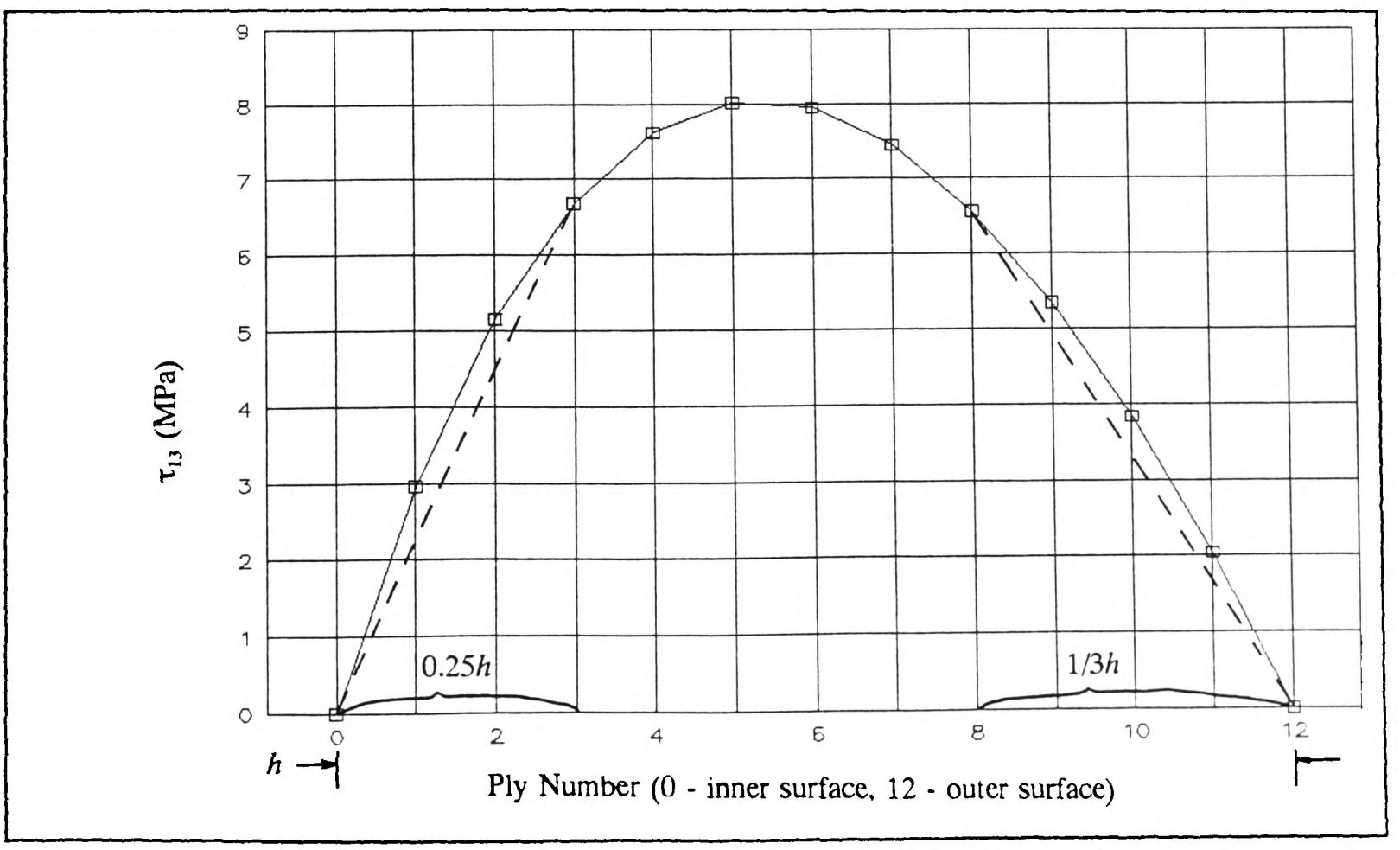

Figure 6.7 (a) The distribution of τ_{13} along the through-thickness direction at θ=60° section of the waisted C-specimen.

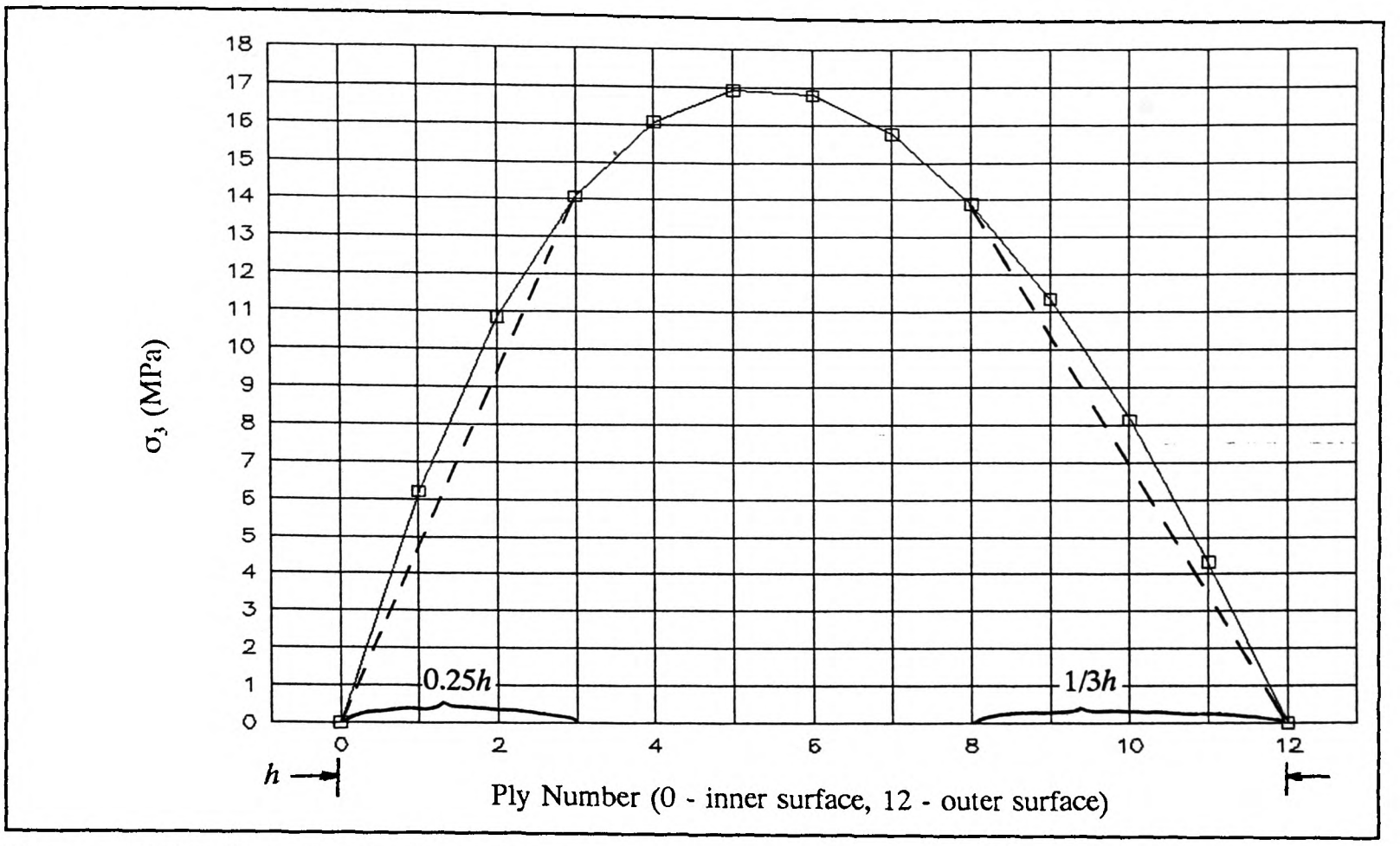

Figure 6.7 (b) The distribution of σ_3 along the through-thickness direction at θ=60° section of the waisted C-specimen.

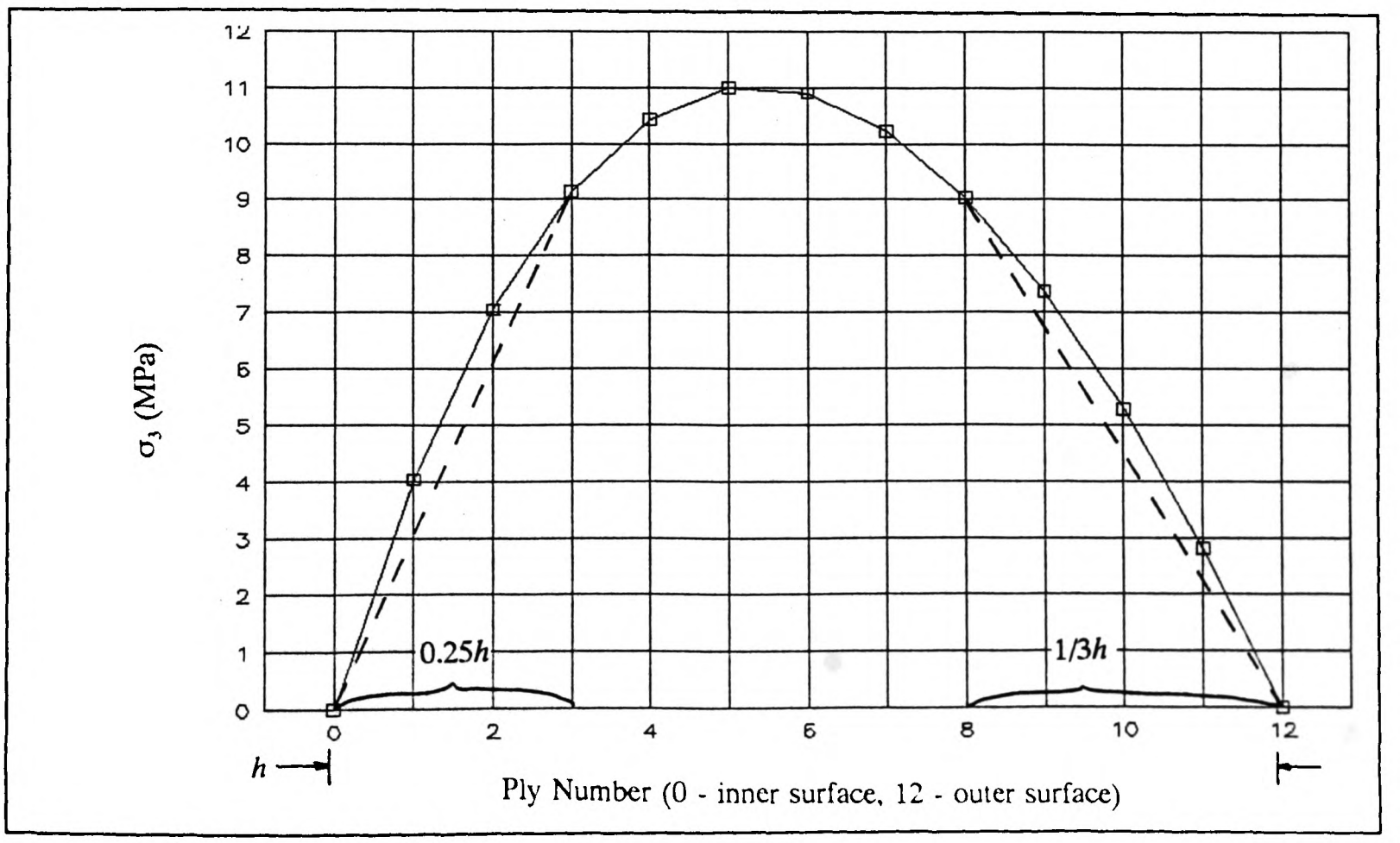

Figure 6.7 (c) The distribution of σ_3 along the through-thickness direction at θ=90° section of the waisted C-specimen.

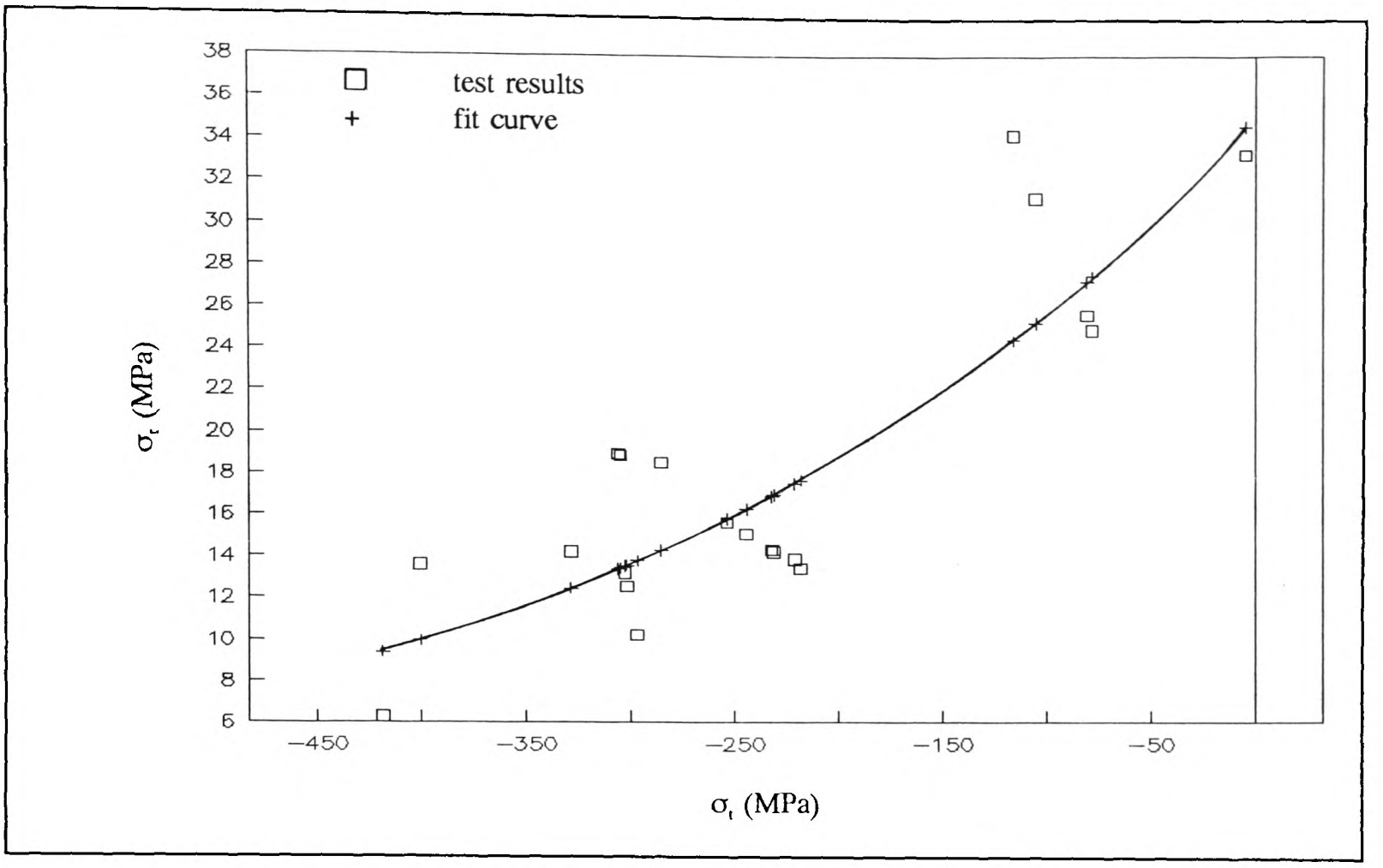

Figure 6.8 The comparison between the experimental results in quadrant II in Table 6.3 and the proposed empirical criterion.

Chapter 7

CONCLUSIONS AND SUGGESTIONS FOR FURTHER WORK

7.1 DISCUSSION AND CONCLUSIONS

The improved properties have already allowed laminated polymer composites to replace metals and alloys in many fields mainly in the form of flat plates, e.g. in the McDonnel-Douglas AV8B (Harrier Mk.II) composites are used in 25% of the structural mass, whereas fighter planes made today contain in the region of 40% composites in the structural mass, covering around 80% of the surface area of the aircraft (Kelly, 1989). Further application of laminates to more complicated components and structures, however, will depend on the through-thickness strength of laminates since it is much lower than the strength in in-plane directions, and hence delamination, a main through-thickness failure mode, usually happens at a much lower stress than that for an in-plane failure. A method is therefore required to predict the through-thickness strength of a laminate.

This project started by the experimental investigation of the through-thickness tensile ($\sigma_3(+)$) and interlaminar shear strength (τ_{13}) of a carbon fabric reinforced epoxy matrix laminate (C/epoxy) commonly used industrially, and its failure strength under combined interlaminar tensile $\sigma_3(+)$ and in-plane normal stress σ_1. It was found that a positive σ_1 increases the strength $\sigma_3(+)$ and a negative σ_1 will greatly reduce the strength $\sigma_3(+)$ (Hognestad, 1993). This

discovery partially revealed the complicated failure mechanisms of laminates under a combined stress state, but since this test considers only two stress components, it can only be used for two-dimensional design.

Further to the previous 2-D investigation and assuming that the stress components σ_1, σ_3 and τ_{13} are the most important factors contributing to delamination, the investigation reported in this thesis has covered the following ground:

- design of tests which can reveal failure under a 3-D state of stress.
- understanding of the failure mechanisms corresponding to the stress state.
- establishment of a three-dimensional failure map in the coordinates of σ_1, σ_3 and τ_{13}.

Three tests, namely uniaxial oblique, waisted C-specimen and central notched four-point bending beam, have been designed to study the delamination under the combined through-thickness stress state of σ_1, σ_3 and τ_{13}. All tests have been analyzed numerically by the ABAQUS code except the oblique test, in which a simple uniform stress sate prevails as shown by Moiré interferometry. The experimental material is mainly C/epoxy woven laminate, whilst transparent G/epoxy woven laminate, as a laboratory material, is also used to repeat the tests so as to detect the onset of any cracks and reveal visually the failure mechanisms. The Scanning Electronic Microscope (SEM) technique is used extensively to examine failure surfaces.

All the experiments have produced very consistent results with the standard deviation of recorded failure loads within 10%. For the uniaxial oblique test, tensile oblique specimens using transparent G/epoxy show that the failure is an abrupt breakdown and no edge cracks

are detected visually. In the notched beam test, cracks are found to start and propagate uniformly through the width. The failure positions are predicted well by the stress analysis and coincide with those found in C/epoxy specimens. The three tests, therefore, have proved able to provide data for establishing a through-thickness failure map.

As was discussed in Chapter 5, the current tests cover only a quite narrow part of the failure map. However some conclusions can still be drawn from the current tests which partially fill quadrants I, II and III. In quadrants I and II, the results from plain C-specimen tests (Hognestad, 1993) show that in-plane tensile stress ($\sigma_1(+)$) increases the through-thickness tensile strength ($\sigma_3(+)$) while in-plane compressive stress ($\sigma_1(-)$) greatly reduces the ($\sigma_3(+)$), whilst current tests reveal that the failure under the combined stress state including interlaminar shear (τ_{13}) involves more complicated mechanisms in that the shear causes a substantial drop of stress in quadrant I while it has very little effect in quadrant II. SEM examination has identified ductile fracture features in quadrant I and brittle fracture features in quadrant II and the plain C-specimen made from the G/epoxy transparent material system reveals visually the failure process caused by the combined stress state of in-plane compression and interlaminar tension. Based on these observations, the failure mechanisms involved are that when σ_1 is compressive, the micro-buckling of fibres results in micro-cracks in the interface, which quickly invoke Mode I failure because of the existence of tensile through-thickness stress. Therefore the interlaminar shear contributes very little to the failure. Since the tensile strength of fibres is higher than their buckling strength, the effect of a tensile tangential stress is basically to maintain the plies straight and aligned, and therefore to inhibit the Mode I opening and to increase delamination strength. An introduction of interlaminar shear to this situation will make the single Mode I into a combined Mode I and Mode II

failure which shows a significant drop of strength. In quadrant III, it is found that failure is caused by a combined stress state with much higher shear stress than pure interlaminar shear strength. The high shear stress is believed to be due to the existence of a high compressive interlaminar normal stress which constrains the shear deformation of resin. This is verified by SEM photographs which reveal many resin particles and bare fibres on the fracture surface.

These observations further support the need for a failure map as a design criterion for structures requiring through-thickness strength since these failure mechanisms are never encountered in metallic materials, on which most of the current design guidelines are based. Phenomenological strength criteria are the most commonly used methods to describe failure maps such as von Mises and Tresca criteria for metallic materials and Tsai-Wu and Tsai-Hill etc. for the in-plane strength of laminates. The question is whether or not a phenomenological criterion can be used to describe the through-thickness strength of laminates. A through-thickness failure criterion based on Tsai-Wu theory has been developed and compared with the experimental results. It is found that there is only good agreement in quadrant I and the failures in other quadrants can not be described by the criterion. This again confirms that a failure map can only be obtained by extensive experiments.

The stress gradient effect is very important to establish experimentally the through-thickness failure map. The Weibull statistics method has been used to treat the failure stress under a state of stress gradient into an equivalent value with uniform stress. The results show that the Weibull method is an efficient means for this purpose.

7.2 FURTHER WORK

An attempt has been made to describe the experimental results by a phenomenological approach. It has been found, as shown in Table 6.3, that in quadrant I, the experimental results have a good agreement with the prediction, except for the results from the waisted C-specimen, in which several data show a quite high discrepancy from the prediction. These have been regarded as mainly due to the test itself since, on the one hand, the specimens were manufactured by plunge grinding and therefore some machining damages were inevitable, from which the strength will suffer; on the other hand, due to the small size and relatively complicated shape of the waisted C-specimen, some experimental errors might arise from misalignment while applying load. Hence, further work for the waisted C-specimen test are to make better specimens, to control the experiment by a better way and to carry out more tests to obtain repeatable results. In quadrant II, there is a big divergence between the tests and the prediction. It is believed that since the experimental results are self-consistent and reproducible, the theory is inadequate in this quadrant. The question is, therefore, if the theory can be improved. Some ideas for further work include approaches of FE analysis of ply-by-ply, damage mechanics etc. although the most ideal way is to take into account the mode of failure.

The tests described in this thesis cover only a relatively small part of the stress and material system. Since the establishment of a failure map can have only an empirical basis, it is essential to extend the range of the tests. Other states of stress, achieved by designing other types of test, and other materials of industrial interest must be tested.

In terms of the experimental results obtained from different tests, it has been found already that the effect of stress gradient must be considered in order to make the failure envelope meaningful. The Weibull method has been used and satisfactory results have been achieved. However, since a linear stress distribution is required when applying the method, it makes the processing of results very inconvenient. As described in chapter 6, a simplified graphical method has been used. A more accurate and convenient method to apply Weibull statistics should be developed.

DETERMINATION OF FIBRE VOLUME FRACTION

If the densities of fibre (ρ_f), matrix (ρ_m) and composite laminate (ρ_{spec}) are known, the fibre volume fraction can be determined by,

$$V_f = \frac{\rho_{spec} - \rho_m}{\rho_f - \rho_m}$$

Usually ρ_f and ρ_m can be obtained from manufacturer's data sheet while ρ_{spec} could be measured by hydrostatic method (Glazebrook, 1923).

Data for the material systems used in this thesis are,

G/Epoxy	ρ_m=1.2162 kg/dm^3
	ρ_f=2.4876 kg/dm^3
C/Epoxy	ρ_m=1.30 kg/dm^3
	ρ_f=1.80 kg/dm^3

Hydrostatic method for measuring density:

The specimen is first weighed in air (W_{air}) and then weighed in distilled water (W_{water}). An approximate value of its density can be obtained in accordance with Archimedes' principle,

$$\rho_{spec} = \frac{W_{air}}{W_{air} - W_{water}}$$

CALCULATIONS OF G/EPOXY COMPOSITE PROPERTIES

1. Elastic Constants

To calculate accurately the elastic constants of glass fabric reinforced epoxy matrix lamina following Naik (1992) is a quite complicated job. Here a relatively simple and approximate way is used.

Assume that a fabric lamina is simply composed of two cross-plied UD laminae. The elastic constants of the fabric lamina can be obtained by supposing that the stiffness matrix of the fabric lamina is the arithmetic mean of those of the two UD laminae.

A simplified micromechanics approach to calculate elastic constants of a UD lamina is expressed as (Weeton, 1987) (Fig. 4A.1),

$$E_{l11} = V_f E_{f11} + V_m E_m$$

$$E_{l22} = \frac{E_m}{1-\sqrt{V_f}\left(1-\frac{E_m}{E_{f22}}\right)} = E_{l33}$$

$$G_{l12} = \frac{G_m}{1-\sqrt{V_f}\left(1-\frac{G_m}{G_{f12}}\right)} = G_{l13} \qquad (4A\text{-}1)$$

$$G_{123} = \frac{G_m}{1-V_f(1-\frac{G_m}{G_{f23}})}$$

$$\upsilon_{112} = V_f\upsilon_{f12}+V_m\upsilon_m = \upsilon_{113}$$

$$\upsilon_{123} = V_f\upsilon_{f23}+V_m(2\upsilon_m-\frac{\upsilon_{112}}{E_{111}}E_{122})$$

where *l* represents lamina's properties, *f* fibre's properties and *m* matrix's, V_f and V_m are fibre and matrix volume ratios respectively.

Since (from manufacturer's data sheet),

E_{f11}=73.1 GPa E_{f22}=73.1 GPa G_{f12}=30.14 GPa

G_{f23}=30.14 GPa υ_{f12}=0.22 υ_{f23}=0.22

E_m=3.45 GPa $G_m=E_m/2(1+\upsilon_m)$=1.28 GPa υ_m=0.35

V_f=50%

The elastic constants of a G/epoxy UD lamina are,

E_{l11}=38.28 GPa E_{l22}=10.57 GPa=E_{l33} G_{l12}=3.96 GPa=G_{l13}

G_{l23}=2.46 GPa υ_{l12}=0.285=υ_{l13} υ_{l23}=0.42=υ_{l32}

$\upsilon_{l21}=\upsilon_{l12} * E_{l22}/E_{l11}$=0.079=$\upsilon_{l31}$

For an orthotropic material, the governing constitutive equations in terms of the principal material directions are,

$$\begin{pmatrix}\sigma_1\\ \sigma_2\\ \sigma_3\\ \tau_{23}\\ \tau_{31}\\ \tau_{12}\end{pmatrix} = \begin{bmatrix}C_{11}C_{12}C_{13} & 0 & 0 & 0\\ C_{12}C_{22}C_{23} & 0 & 0 & 0\\ C_{13}C_{23}C_{33} & 0 & 0 & 0\\ 0\ 0\ 0 & C_{44} & 0 & 0\\ 0\ 0\ 0 & 0 & C_{55} & 0\\ 0\ 0\ 0 & 0 & 0 & C_{66}\end{bmatrix} \begin{pmatrix}\epsilon_1\\ \epsilon_2\\ \epsilon_3\\ \gamma_{23}\\ \gamma_{31}\\ \gamma_{12}\end{pmatrix} \qquad (4A\text{-}2)$$

where, C_{ij} is the stiffness matrix which can be expressed in terms of the engineering constants,

$$C_{ij} = \begin{bmatrix} \frac{(1-\upsilon_{23}\upsilon_{32})}{E_2E_3} & \frac{(\upsilon_{21}+\upsilon_{31}\upsilon_{23})}{E_2E_3\Delta} & \frac{\upsilon_{31}+\upsilon_{21}\upsilon_{32}}{E_2E_3\Delta} & 0 & 0 & 0\\ C_{12} & \frac{(1-\upsilon_{13}\upsilon_{31})}{E_1E_3\Delta} & \frac{(\upsilon_{32}+\upsilon_{12}\upsilon_{31})}{E_1E_3\Delta} & 0 & 0 & 0\\ C_{13} & C_{23} & \frac{(1-\upsilon_{12}\upsilon_{21})}{E_1E_2\Delta} & 0 & 0 & 0\\ 0 & 0 & 0 & G_{23} & 0 & 0\\ 0 & 0 & 0 & 0 & G_{31} & 0\\ 0 & 0 & 0 & 0 & 0 & G_{12}\end{bmatrix} \qquad (4A\text{-}3)$$

where,

$$\Delta = \frac{1-\upsilon_{12}\upsilon_{21}-\upsilon_{23}\upsilon_{32}-\upsilon_{31}\upsilon_{13}-2\upsilon_{21}\upsilon_{32}\upsilon_{13}}{E_1E_2E_3}$$

Likewise the compliance matrix in $\varepsilon_{ij} = S_{ij}\,\sigma_{ij}$ can be expressed in terms of the engineering constants,

$$S_{ij} = \begin{bmatrix} \frac{1}{E_1} & -\frac{\upsilon_{21}}{E_2} & -\frac{\upsilon_{31}}{E_3} & 0 & 0 & 0 \\ -\frac{\upsilon_{12}}{E_1} & \frac{1}{E_2} & -\frac{\upsilon_{32}}{E_3} & 0 & 0 & 0 \\ -\frac{\upsilon_{13}}{E_1} & -\frac{\upsilon_{23}}{E_2} & \frac{1}{E_3} & 0 & 0 & 0 \\ 0 & 0 & 0 & \frac{1}{G_{23}} & 0 & 0 \\ 0 & 0 & 0 & 0 & \frac{1}{G_{31}} & 0 \\ 0 & 0 & 0 & 0 & 0 & \frac{1}{G_{12}} \end{bmatrix} \qquad (4A-4)$$

where,

$$\frac{\upsilon_{ij}}{E_i} = \frac{\upsilon_{ji}}{E_j} \qquad i,j = 1,2,3$$

The relationship between C_{ij} and S_{ij} is,

$$\begin{aligned} S_{11} &= \frac{C_{22}C_{33}-C_{23}^2}{C} & S_{12} &= \frac{C_{13}C_{23}-C_{12}C_{33}}{C} \\ S_{22} &= \frac{C_{33}C_{11}-C_{13}^2}{C} & S_{13} &= \frac{C_{12}C_{23}-C_{13}C_{22}}{C} \\ S_{33} &= \frac{C_{11}C_{22}-C_{12}^2}{C} & S_{23} &= \frac{C_{12}C_{13}-C_{23}C_{11}}{C} \\ S_{44} &= \frac{1}{C_{44}} & S_{55} &= \frac{1}{C_{55}} & S_{66} &= \frac{1}{C_{66}} \end{aligned} \qquad (4A-5)$$

where,

$$C = C_{11}C_{22}C_{33} - C_{11}C_{23}^2 - C_{22}C_{13}^2 - C_{33}C_{12}^2 + 2C_{12}C_{23}C_{13}$$

If the fibre direction of UD lamina A is with axis 1 and that of UD lamina B is with axis 2, each stiffness matrix of the UD laminae is,

$\Delta^A=0.76/E_1E_2E_3$

$C_{11}^A=41.48$	$C_{22}^A=13.59$	$C_{33}^A=13.60$
$C_{12}^A=5.63$	$C_{13}^A=5.63$	$C_{23}^A=6.15$
$C_{44}^A=2.46$	$C_{55}^A=3.96$	$C_{66}^A=3.96$

$\Delta^B=0.76/E_1E_2E_3$

$C_{11}^B=13.59$	$C_{22}^B=41.48$	$C_{33}^B=13.59$
$C_{12}^B=5.63$	$C_{13}^B=6.15$	$C_{23}^B=5.63$
$C_{44}^B=3.96$	$C_{55}^B=2.46$	$C_{66}^B=3.96$

The stiffness matrix of the woven lamina is supposed to be the arithmetic mean, viz. $C_{ij} = (C_{ij}^A+C_{ij}^B)/2$. Hence,

$C_{11}=27.54$	$C_{22}=27.54$	$C_{33}=13.59$
$C_{12}=5.63$	$C_{13}=5.89$	$C_{23}=5.89$
$C_{44}=3.21$	$C_{55}=3.21$	$C_{66}=3.96$

According to Eqn.(4A-5), the compliance matrix is,

$S_{11}=0.04063$	$S_{22}=0.04063$	$S_{33}=0.0869$
$S_{12}=-0.005$	$S_{13}=-0.01543$	$S_{23}=-0.01543$
$S_{44}=1/3.21$	$S_{55}=1/3.21$	$S_{66}=1/3.96$

Then the engineering elastic constants can be deduced from the compliance matrix,

$E_{11}=24.61$ GPa	$E_{22}=24.61$ GPa	$E_{33}=11.51$ GPa
$G_{12}=3.96$ GPa	$G_{13}=3.21$ GPa	$G_{23}=3.21$ GPa
$\upsilon_{12}=0.123$	$\upsilon_{13}=0.38$	$\upsilon_{23}=0.38$

2. Mechanical Properties

Weeton (1987) gave the formula for calculating mechanical properties of a UD lamina as follows (Fig.4A.2),

Longitudinal tension:

$$\sigma_{111T} = V_f \sigma_{fT}$$

Transverse tension:

$$\sigma_{122T} = [1-(\sqrt{K_f}-K_f)\,(1-\frac{E_m}{E_{f22}})]\,\sigma_{mT}$$

Interlaminar shear:

$$\tau_{113} = \left[1-(\sqrt{K_f}-K_f)\,(1-\frac{G_m}{G_{f12}})\right]\tau_m$$

$$\tau_{123} = \left[\frac{1-\sqrt{K_f}(1-\frac{G_m}{G_{f23}})}{1-K_f(1-\frac{G_m}{G_{f23}})}\right]\tau_m$$

Again we assume a woven lamina is simply composed of two cross-ply UD lamina and therefore,

$\sigma_{1T} = (\sigma_{111T}+\sigma_{122T})/2 = 712.2$ MPa

$\sigma_{3T} = \sigma_{122T} = 44.3$ MPa

$\tau_{13} = (\tau_{113}+\tau_{123})/2 = 39.3$ MPa

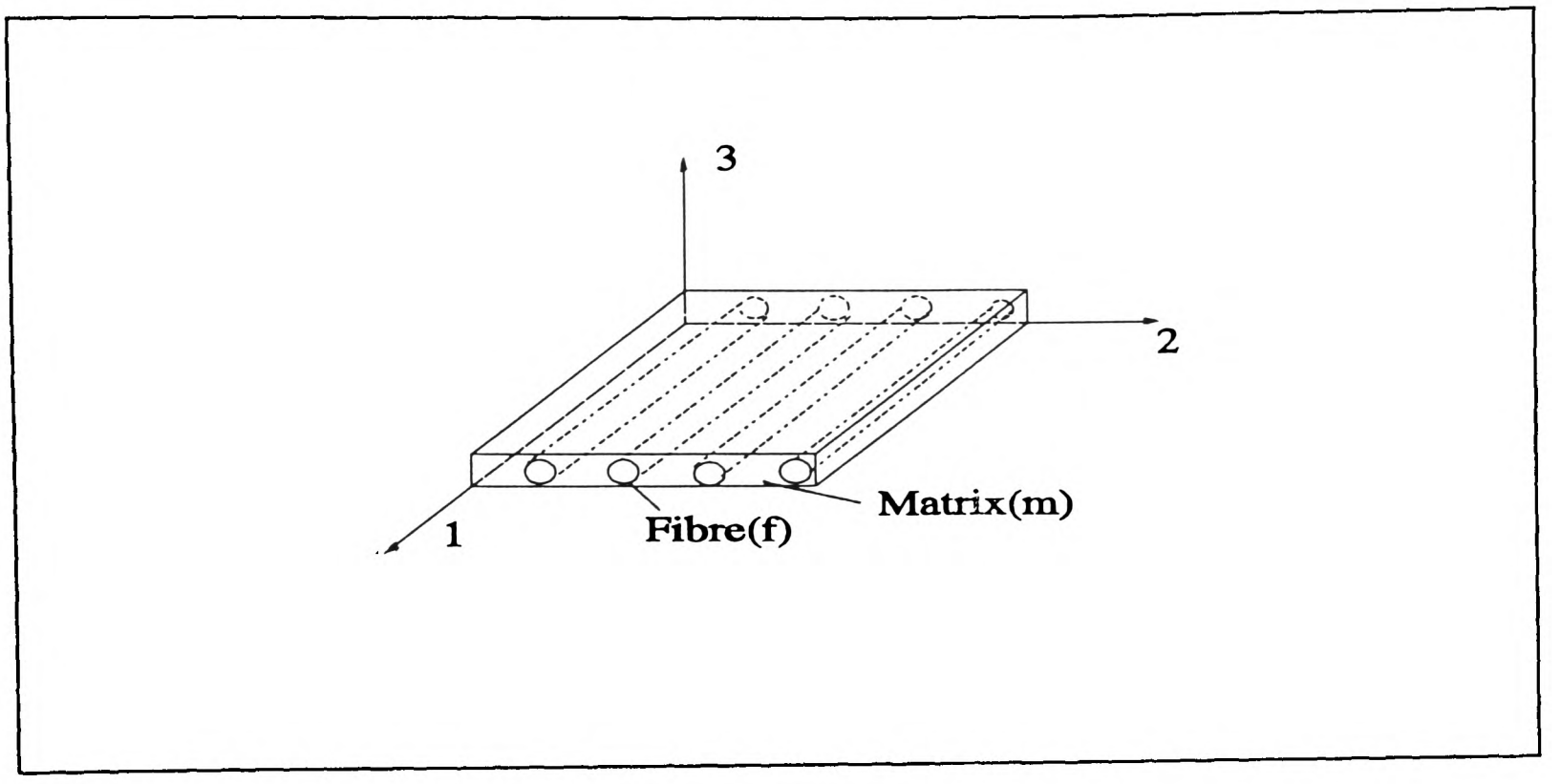

Figure 4A.1 The model used for calculating elastic constants. (Weeton, 1987)

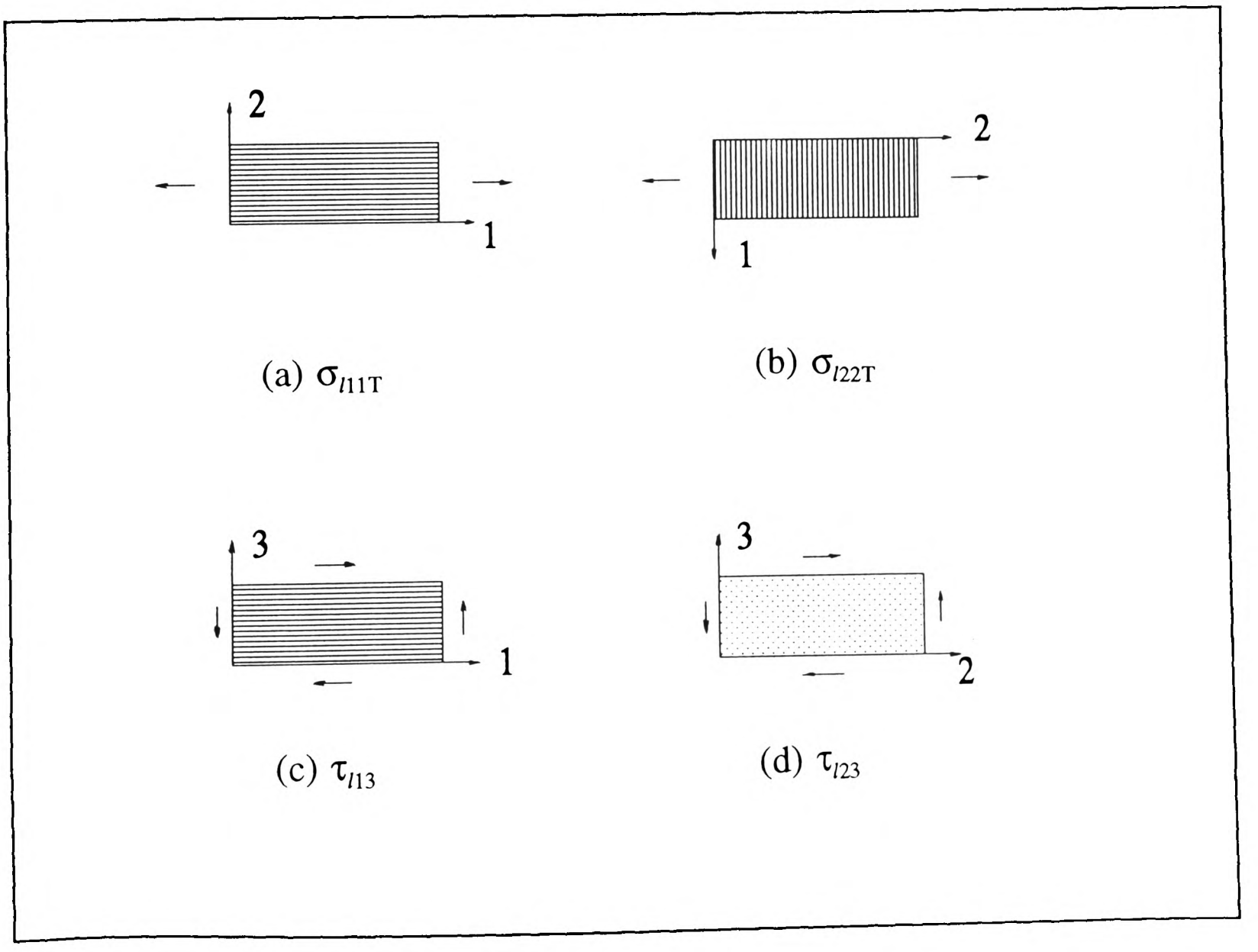

Figure 4A.2 The models used for calculating mechanical properties. (Weeton, 1987)

References

Arcan, L., Arcan, M. & Daniel, I.M., "SEM Fractography of Pure and Mixed Mode Interlaminar Fractures in Graphite/Epoxy Composites", Fractography of Modern Engineering Materials: Composites and Metals, ASTM STP 948, J.E.Masters and J.J.Au, Eds., ASTM, Philadelphia(1987), p41.

Barsoum, R.S., "Finite element application in the fracture analysis of composite materials - delamination", Key Engineering Materials, Vol 37,1989, p35.

Bascom, W.D., Boll, D.J., Hunston, D.L., Fuller, B. & Phillips, P.J., "Fractographic analysis of interlaminar fracture", Toughened Composites, ASTM STP 937, N.M. Johnston ed., ASTM, Philadelphia, 1987, p131.

Berry, J.P., "Determination of fracture surface energy by the cleavage technique", J. Appl. Phys. **34**, 1963, p62.

Boniface, L., Dept. of Materials Science & Engineering, University of Surrey, Guildford, England, Private Communication, 1993.

Carlsson, L.A., Gillespie, J.W. Jr. & Pipes, R.B., "On the analysis and design of end notched flexure(ENF) specimen for mode II testing", J. Compos. Mater. **20**, 1986, p594.

Chang, F.K., Perez, J.L. & Chang, K.Y., "Analysis of thick laminated composites", J. Composite Materials, Vol.24, August 1990, p801.

Creyke, W.E.C., Sainsbury, I.E.J. & Morrell, R., "Design with Non-ductile Materials", Applied Science Publishers Ltd, 1982.

Cui, W.C., Wisnom, M.R. and Jones, M., "A comparison of failure criteria to predict delamination of unidirectional glass/epoxy specimens waisted through the thickness", Composites, **23**, No.3, 1992.

Davies, P. & Benzeggagh, M.L., "Interlaminar mode I fracture testing" in Application of Fracture Mechanics to Composite Materials, ed. K.Friedrich, Elsevier Science Publisher 1989, ch3.

Davies, P., Moulin, C., Kausch, H.H. & Fischer, M., "Measurement of G_{Ic} and G_{IIc} in carbon/epoxy composites", Composites Sci. Tech., **39**, 1991.

Derby, B., Hills, D. & Ruiz, C., "Materials for Engineering - A fundamental Design Approach", Longman Scientific & Technical, 1992.

Doherty, J.E., "Nondestructive evaluation", SEM Handbook on Experimental Mechanics, ed. A.S. Kobayashi, Prentice-Hall Inc., 1987.

ESDU, Data item 83025, "Failure modes of fibre reinforced laminates", ESDU International plc, 27 Corsham Street, London, 1986.

Glazebrook, R., "A Dictionary of Applied Physics", Vol.III, MacMillan and Co. Ltd., 1923.

Griffith, A.A., "The phenomena of rupture and flow in solids", Phil. Trans. R. Soc. A221 1920, p163.

Guedra, D., Lang, D., Rouchon, J., Marais, C. & Sigety, P., "Fracture toughness in Mode I : a comparison exercise of various test methods", Proc. ICCM & ECC M 6, Elsevier Appd. Science, 1987, London, p3.346.

Harris, B., "A perspective view of composite materials development", Materials & Design, Vol.12, No.5, October 1991.

Hashemi, S., Kinlock, A.J. & Williams, J.G., "Mixed mode fracture in fibre polymer composite laminate", Composite Materials: Fatigue and Fracture, Vol.3 ed. T.K.O'Brien, ASTM-STP 1110, 1991, p143.

Hertzberg, R.W., "Fracture surface micromorphology in engineering solids", Fractography of Modern Engineering Materials: Composites and Metals, ASTM STP 948, J.E.Masters and J.J.Au, Eds., ASTM, Philadelphia(1987).

Hibbs, M.F. and Bradley, W.L., "Correlations between micromechanical failure processes and the delamination toughness of graphite/epoxy systems", Fractography of Modern Engineering Materials: Composites and Metals, ASTM STP 948, J.E.Masters and J.J.Au, Eds., ASTM, Philadelphia(1987), p68.

Hiel, C.C., Sumich, M. & Chappell, D.P., "A curved beam test specimen for determining the interlaminar tensile strength of a laminated composite", J. Composite Materials, Vol 25, 1991.

Hill,R., "The Mathematical Theory of Plasticity", Oxford University Press, 1956

HKS Inc. ABAQUS User's Manual, Version 5.2, 1992.

Ho, H., Tsai, M.Y., Morton, J. & Farley, G.L., "An experimental investigation of Iosipescu specimen for composite materials", Experimental Mechanics, Vol 31, No. 4, 1991, p328.

Hognestad, G., DPhil Thesis, Oxford University, 1993.

Hutchinson, J.W. and Suo, Z., "Mixed mode cracking in layered materials", Advance in Applied Mechanics, Vol.28, ed. T.Wu and J.W.Hutchinson, 1992, p81.

Iosipescu, N., "New accurate procedure for single shear testing of metals", J. Materials, **2**, No.3, 1967, p537.

Jiang, Z. & Tennyson, R.C., "Closure of the cubic tensor polynominal failure surface", J. Composite Materials, vol.23, March 1989, p208.

Johnson, W.S. and Mangalgiri, P.D., "Influence of the resin on interlaminar mixed-mode fracture", Toughened Composites, ed. N.J.Johnston, ASTM-STP 937, 1987, p295.

Jones, R.M., "Mechanics of Composites Materials", Hemisphere Publishing Corporation, 1975

Kanninen, M.F., "A dynamic analysis of unstable crack propagation and arrest in the DCB test specimen", Int. J. Fract. **10**, 1974, p415.

Kedward, K.T., "University of Delaware Composites Design Guide Encylopedia", **5**, June 1980, section 5.1.2.

Kedward, K.T., Wilson, R.S. and Mclean, S.K., "Flexure of simply curved composite shapes", Composites, **20**, 1989, p527.

Kelly, A. ed., "Concise encyclopedia of composite materials", Pergamon Press, 1989.

Kinloch, A.J., Wang, Y., Williams, J.G. & Yayla, P., "The mixed-mode delamination of fibre composite materials", Compos. Sci. & Technol. **47**, 1993, p225.

Latter, R.E. and Santare, M.H., "Analysis of mode I and mode II interlaminar fracture specimens by a comparative F.E.M.", Composites Sci. Tech., **40**, 1991, p87.

Lee, S. & Munro, M., "Evaluation of Testing Techniques for the Iosipescu Shear Test for Advanced Composite Materials", J. of Composite Materials, **24**, April 1990, p419.

Lu, X. & Liu, D., "Interlayer Shear Slip Theory for cross-Ply Laminates With Nonrigid Interfaces", AIAA J., **30**, NO.4, April 1992, p1063.

Naik, N.K. & Shembekar, P.S., "Elastic behaviour of woven fabric composites: I-lamina analysis", J. Composite Materials, **26**, No.15, 1992, p2196.

Noor, A.K. & Burton, W.S., "Assessment of Shear deformation theories for multilayered composite plates", Appl. Mech. Rev., **42**, No.1, Jan. 1989, p1.

Pipes, R.B., "Moire Analysis of the Interlaminar Shear Edge Effect in Laminated Composites", J. Composite Materials, **5**, April 1971, p255.

Poon, C.Y., "In-plane strain measurement using Moire interferometry combined with automated fringe pattern analysis", Oxford UTC Report No. 20, 1991.

Post. D., "Moire interferometry", SEM Handbook on Experimental Mechanics, ed. A.S. Kobayashi, Prentice-Hall Inc., 1987.

Post, D., "Moire Interferometry : Advances and Applications", Experimental Mechanics, **31**, No. 3, 1991, p276.

Reddy, J.N., "A Review of Refined Theories of Laminated Composite Plates", Shock and Vibration Digest, **22**, No.1, 1990

Reeder, J.R. & Crews, J.H.Jr., "Mixed-Mode Bending Method for Delamination Testing", AIAA Journal, **28**, No 7, 1990, p1270.

Ruiz, C., "Application of fracture mechanics to interlaminar fracture of carbon fibre/epoxy composites", Oxford University UTC Report No. 46, 1994

Russell, A.J., "On the Measurement of Mode II Interlaminar Fracture Energies", Defence Research Establishment Pacific, Victoria, Canada, DREP Materials Rept. 82-0, Dec. 1982.

Singer, F.L., "Strength of Materials", Harper & Row Publishers Inc. 1951.

Smith, B.W. and Grove, R.A., "Determination of Crack Propagation Directions in Graphite/Epoxy Structures," Fracture of Modern Engineering Materials: Composites and Metals, ASTM STP 948, J.E. Masters and J.J. Au, Eds., American Society fro Testing and Materials, Philadelphia, 1987, p154.

Tennyson,R.C., MacDonald, D. & Nanyaro, A.P., "Evaluation of the tensor polynominal failure criterion for composite materials", J. Composite Materials, **12**, Jan. 1978, p63.

Timoshenko, S. and Goodier, J.N., "Theory of Elasticity", McGraw-Hill, 1970.

Tsai, S.W., "Strength theories of filamentary structures", Fundamental Aspects of Fibre Reinforced Plastic Composites, ed. R.T.Schwartz et al, Wiley Interscience, 1968.

Tsai, S.W. and Wu, E.M., "A general theory of strength for anisotropic materials", J. Composite Materials, **5**, Jan. 1971, p58.

Weeton, J.W., "Engineer's Guide to Composite Materials", American Society for Metals, 1987.

Whitcomb, J.D. & Raju, I.S., "Superposition Method for Analysis of Free-Edge Stresses", J. Composite Materials, **17**, Nov. 1983, p492.

Williams, J.G., "End corrections for orthotropic DCB specimens", Compos. Sci. & Technol. **35**, 1989, p367.

Wu,E.M., "Optimal experimental measurements of anisotropic failure tensors", J. Composite Materials, **6**, Oct. 1972, p472.

Wu, Y.S. et al, " Delamination of Curved Composite Shells due to Through-Thickness Tensile Stresses", Plastics, Rubber and Composites Processing and Applications, **19**, 1993, p39.

Xing, Y.M., Poon, C.Y. & Ruiz, C., "A whole-field strain analysis of the Iosipescu specimen and evaluation of experimental errors", Oxford University UTC Report No.26, 1992.

Zhu, X.Y., Li, Z.X. & Jin, Y.X., "Laminar fracture behaviour of carbon/glass hybrid FRL I - Laminar fracture process", Eng. Fracture Mechanics, **44**, 1993, p545.

Zweben, C., "Is there a size effect in composites?", Composites, **25**, No.6, 1994, p451.